Electrodeposition of Cu-Sn Alloys from Methanesulfonate Electrolytes

A Thesis submitted by

Naray Pewnim

For the Degree of Doctor of Philosophy

School of Chemical Engineering and Advanced Materials

Newcastle University

December 2012

ABSTRACT

The most commonly used alloy in the electronics industry has been the ubiquitous tin-lead alloy. As the demand for electronic devices continues to increase, there have been concerns about the continued use of lead and its long term environmental impact. In the last decade there has been a push to ban the use of lead in electronic products. Legislation from various governments around the world limiting the use of lead has given rise to the drive to find suitable lead-free alternatives.

The aim of this research project was to establish a systematic approach for the selection of electrochemical parameters for the electrodeposition of tin-rich copper-tin alloys from a single electroplating bath. By studying and understanding a model system such as copper-tin, one can then use the information obtained as a basis to successfully deposit various other tin binary alloys in the future. Tin-rich deposits were enabled by employing various strategies such as maintaining a high Sn to Cu ratio in the electrolyte and by using surface active agents that have been known to facilitate alloy co-deposition. The effect of surfactants on the tin content in the deposit was initially examined with the aid of a rotating cylinder Hull cell. It was found that the presence of fluorosurfactant was crucial in eliminating metal oxide formation.

Cyclic voltammetry at a rotating disk electrode showed that inclusion of surfactant in the electrolyte had no effect on the reduction potential of tin which remained at -0.45 V vs SCE. However, the reduction potential for copper shifted from approximately -0.13 to -0.18 V vs SCE, thereby facilitating alloy co-deposition. Chronoamperometry and anodic stripping voltammetry showed that current efficiency for copper-tin deposition ranged from 55-92% depending on the deposition time and deposit composition.

Results from voltammetry experiments were used in the next galvanostatic electrodeposition experiments at vitreous carbon electrodes. Deposits containing up to 96 wt.% tin were obtained from both direct current and pulse plating modes. It was found that an optimal current density of 22 mA cm^{-2} was needed to obtain desirable deposits. For pulse plating the peak current density should be set to 100 mA cm^{-2} with a duty cycle of 0.2. Cu-Sn alloys obtained consisted of two phases, tetragonal tin and a hexagonal Cu_6Sn_5 intermetallic compound. Deposit annealing showed that the Cu_3Sn intermetallic was not formed.

ACKNOWLEDGEMENTS

CONTENTS

LIST OF FIGURES

LIST OF TABLES

SYMBOLS

ΔG°	Gibbs standard free energy	kJ mol^{-1}
C_b	bulk concentration	mol cm^{-3}
D	diffusion coefficient	cm^{2}s^{-1}
E°	standard reduction potential	V
F	Faraday constant	C mol^{-1}
i	current density	mA cm^{-2}
i_{ave} / i_p	average/ peak applied current density	mA cm^{-2}
$i_{(x/h)}$	local current density	mA cm^{-2}
$i_{L,RCH}$ / $i_{L,DC}$ / $i_{L,PP}$	limiting current density	mA cm^{-2}
M	Molarity	mol L^{-1}
t_{on} / t_{off} / t_{total}	on-time / off-time / total plating time	ms
U	peripheral velocity	cm s^{-1}
z	number of electrons in electrode process	
η	overpotential	
β	instrumental line broadening	
δ	diffusion layer thickness	µm
θ	Bragg angle	rad
Θ	duty cycle	
ω	angular velocity	rad s^{-1}
λ	x-ray wavelength	nm
ν	kinematic viscosity	cm^2 s^{-1}

ABBREVIATIONS

ASV   anodic stripping voltammetry

BSE   backscatter electrons

BSI   backscatter electron image

CA   chronoamperometry

CV   cyclic voltammetry

DC   direct current plating

EDX   energy dispersive x-ray

FWHM   full width half maximum

HC   Hull cell

ICDD   International Centre for Diffraction Data

IHP   inner Helmholtz plane

IMC   intermetallic compound

ITRI   International Tin Research Institute

JEITA   Japan Electronics and Information Technology Industries Association

LSV   linear sweep voltammetry

MSA   Methanesulfonic acid

NEMI   National Electronics Manufacturing Initiative

OHP   outer Helmholtz plane

OPPE   iso-octyl phenoxy ethanol (Triton X-100)

PCB   printed circuit board

PDF   powder diffraction file

PFOS	Perfluorooctane sulfonic acid
POELE	polyoxyethylene laurylether
PP	pulse plating
PVD	physical vapour deposition
PTFE	Polytetrafluoroethylene
RCH	rotating cylinder Hull cell
RDE	rotating disk electrode
RPM	revolutions per minute
SAC	Sn-Ag-Cu, tin-silver-copper alloys
SCE	saturated calomel electrode
SEM	scanning electron microscopy
SHE	standard hydrogen electrode
SMD	surface mount device
UPD	underpotential deposition
XRD	x-ray diffraction

1. INTRODUCTION

1.1 Background

Some of the most important alloys historically have been those of tin. Early archaeological evidence found that the use of tin alloys can be dated back to the beginning of the Bronze Age c.a. 3500 BC [1, 2]. Tin alloys are very ductile and malleable making them suitable for creating tools and instruments of various shapes and sizes. Copper-tin (Cu-Sn) or bronze alloys were used to manufacture tools and weapons and can be found in many other ancient artefacts such as ornaments, statues, and musical instruments. The Greeks used lead-tin (Pb-Sn) solders to seal their bronze base water pumps, air pumps, and musical organs while the Romans used them extensively in the construction of aqueducts [2]. The advent of the Industrial Revolution in the 18th century saw the rising demand of tin for use in industrial soldering, plumbing, and tin-plate for food and beverage cans. Tin coatings on steel sheets can also provide a corrosion resistant finish and better cosmetic appearance. Cu-Sn coatings are used in metal sliding bearings as it provides anti-friction benefits, increasing the component lifetime. As technology advances, new uses for tin solders have been found. For instance the use of tin-lead solders in the electronics industry from the early 20th century to the present day [1-3].

The production of tin in the early 20th century was dominated by Indonesia, Malaysia, Thailand, Bolivia, and Nigeria whom together produce up to 93% of the world supply which was approximately 150,000 metric tons per year [1]. A century later the global output has increased to almost twice that amount. Table 1-1 shows that in 2009 the global production of tin from primary resources has increased to approximately 260,000 metric tons per year. Only three countries now dominate tin production namely China, Indonesia, and Peru whom together produce 99% of the world supply [4]. The production of secondary refined tin from scrap material in the same period has exceeded 60,000 metric tons [5].

Country	2009	2010e	Mine production reserves (metric tons)
Australia	1,400	2,000	180,000
Bolivia	19,000	16,000	400,000
Brazil	13,000	12,000	590,000
China	115,000	115,000	1,500,000
Congo (Kinshasa)	9,400	9,000	NA
Indonesia	55,000	60,000	800,000
Malaysia	2,380	2,000	250,000
Peru	37,500	38,000	710,000
Portugal	30	100	70,000
Russia	1,200	1,000	350,000
Thailand	120	100	170,000
Vietnam	3,500	3,500	NA
Other countries	2,000	2,000	180,000
World total (rounded)	260,000	261,000	5,200,000

Table 1-1 Global mine production and reserves of tin in 2009 and estimates for 2010 [4].

The four main uses of tin today are found in 1) chemicals, 2) production of brass (copper-zinc-tin) and bronze (copper-tin), 3) tin plating, and most importantly, 4) soldering. In chemicals tin is predominantly found in the form of organotin compounds and due to their high toxicity are used as biocides [3]. Other applications include the production of float glass through the Pilkington process where molten glass is floated on top of a bath of molten tin, producing a very flat glass sheet with uniform thickness [6]. Tin plating is often used to provide corrosion resistance to protect various base metals such as steel and due to their low toxicity, tin plates are suitable for use in food containers, hence the term tin cans [7].

1.2 Tin based solder alloys in electronics

There has been a shift in tin consumption over the past two decades which reflects the increasing demand for tin-based solders for microelectronics. Figure 1-1 shows the change in demand of tin for soldering applications in 2009 compared to 1988. A recent publication by ITRI, formerly known as the International Tin Research Institute, provides new information on global tin use and recovery in 2009 and initial estimates for 2010. Their 6th Annual Tin Use and Recycling Survey [5] reported that refined tin use in electronic and industrial solders was around 54% of total use in 2009. The proportion has been greater than 50% since 2005.
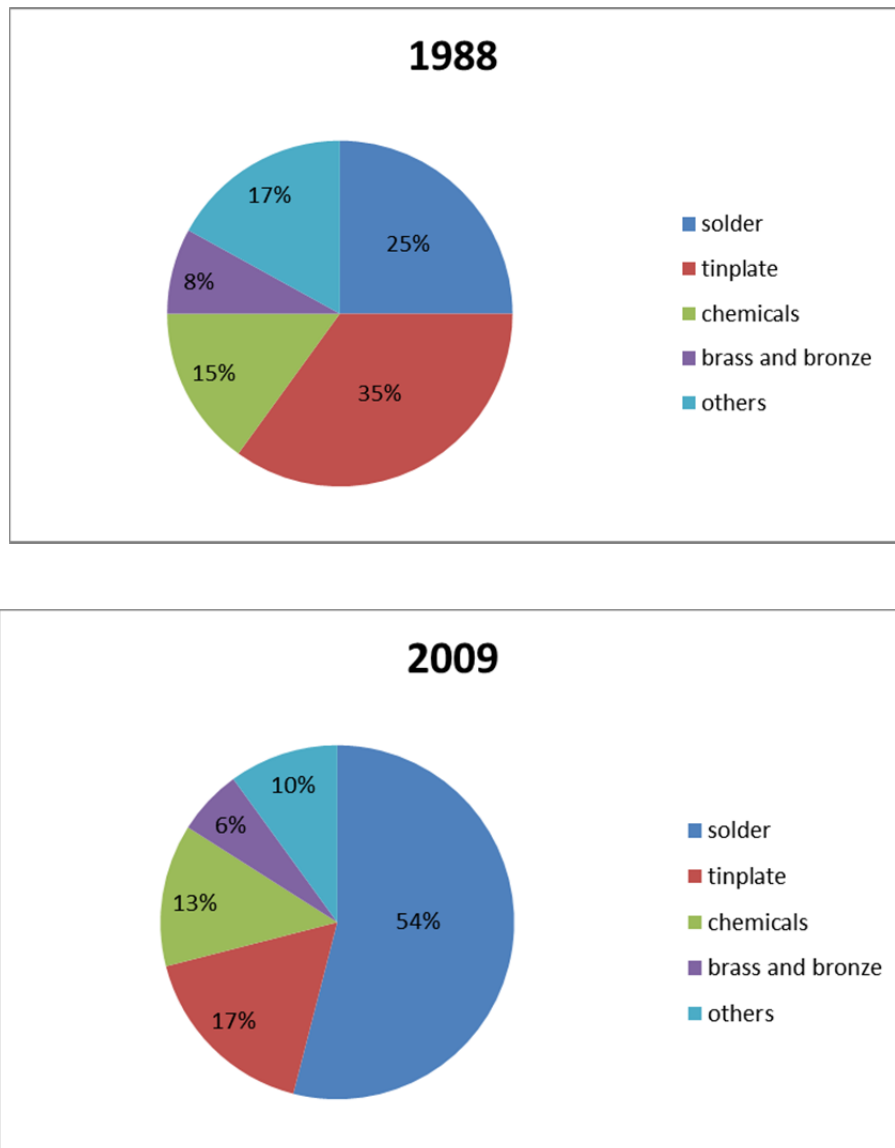
Figure 1-1 Change in tin consumption for various applications from 1988 to 2009 [5].

1.2.1 Lead-tin solder alloys

Since the emergence of consumer electronics in the 1950s, Sn-based solders have been used extensively to attach components to printed wiring board or printed circuit boards (PCB). While it is possible that pure tin can be used as a solder, one of the main disadvantages is the formation and growth of tin crystal filaments or tin whiskers [8]. These so-called whiskers can grow across the PCB surface creating multiple contact points which can result in short-circuits and equipment failures [1, 2]. Research carried out in the 1960s has shown that tin alloy finishes significantly suppress whisker growth when compared to pure tin [9]. Therefore, the addition of other metals such as lead has been standard practice in the electronics industry ever since. The addition of various metals to form an alloy gives the Sn-based solders many extra desirable characteristics. Tin alloyed with bismuth, cobalt, copper, gold, lead, nickel, and zinc have been chosen by commercial manufacturers to achieve various improvements such as better mechanical, thermal, and electrical properties. Figure 1-2 shows that the presence of lead in the solder also has other benefits such as lowering the solder melting temperature to 183°C (pure tin has a melting point of 232°C, pure lead 328°C) and decreasing the surface tension improving solder wetting into holes [2].
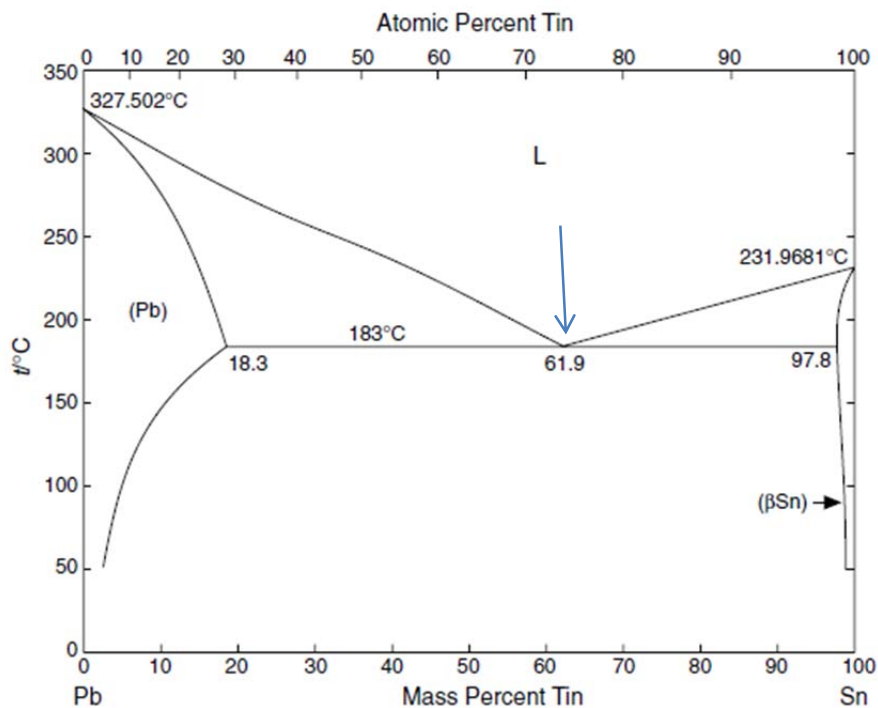
Figure 1-2 Pb-Sn phase diagram [10].

1.2.2 Lead-free solder alloys

Lead-tin has been the most commonly used alloy in the electronics industry for over 50 years, due to its low cost, availability, and good solderability. However, the drive for lead-free alternatives has become more important in the last few decades. This is due to the fact that lead is a highly toxic metal which has been increasingly found at higher concentrations in the environment from various sources such as paints, plumbing materials, and even gasoline. The United States, for example, has banned lead-based paints in 1978 and lead additives in gasoline were banned since 1996. As more electronic devices are disposed of every year there is also rising concern that the presence of lead in landfills will have a negative effect on human health and safety of the environment. There have been concerns that if not properly disposed of or recycled, lead in electronic components may leach into the environment such as natural water systems and inadvertently enter the food chain.

One of the first countries to make a push towards lead-free electronics was Japan. According to the Japan Electronics and Information Technology Industries Association (JEITA), the Japanese electronics industry started enforcing lead-free legislation in the late 1990s with goals to become completely lead-free by the end of 2005 [11]. In July 2006 the Directive on the Restriction of the Use of Certain Hazardous Substances in Electrical and Electronic Equipment 2002/95/EC, often referred to as the lead-free directive, was enforced within the European Union [12]. This effectively bans the use of lead-based solders in the manufacturing of all electronic equipment to be sold or imported to the EU with the exception of those used in components that require high reliability such as aerospace, military, and communication applications. By definition lead-free components are those that contain less than 0.1 wt% lead.

This has led to an increase in research to find a suitable non-toxic replacement for the ubiquitous tin-lead solder. Lead-free tin alloy systems in use by commercial manufactures and others that have been described in literature include [13-16]:

Binary systems – Ag-Sn, Au-Sn, Bi-Sn, Cu-Sn, In-Sn, Sn-Sb, Zn-Sn

Ternary systems – Sn-Ag-Cu, Sn-Ag-Bi, Sn-Zn-Bi

Quaternary systems – Sn-Ag-Bi-Cu, Sn-Ag-Bi-In, Sn-Ag-Bi-Ge

Relative costs of metals

Many factors have to be taken into account when considering a replacement for Pb-Sn. For example the relative costs of metals need to be considered. The binary alloys that have been proposed as the main lead-free alternatives are Ag-Sn, Bi-Sn, and Cu-Sn. Among these, Cu-Sn alloys are of particular interest due to the relatively low cost of the starting metal copper compared to bismuth or silver. Table 1-2 compares the typical price of various metals found on the London Metal Exchange in July 2011 [17]. The prices of precious metals silver and gold were only available in troy ounces (1 metric ton = 32,151 troy ounces). From Table 1-2, the most practical metals based on industrial scale economics would appear to be Cu and Zn.

Metal	Price (USD/metric ton)
Bismuth	27,011
Cobalt	35,500
Copper	9,606
Lead	2,650
Nickel	24,060
Tin	27,260
Zinc	2,320
Silver	1,227,203 (38.17/troy oz.)
Gold	51,023,637 (1,587/ troy oz.)

Table 1-2 Official reference price of selected metals in July 2011 [17].

Availability of metals

The availability of lead-free alternatives is another factor that must also be taken into consideration. Table 1-3 lists the global production and reserves of selected lead-free alternatives. Using the availability criteria, it can be seen that some metals such as bismuth would not be a suitable candidate as the main lead-free alternative. This is because global annual production of bismuth is relatively low compared to other metals and due to its low reserves would also be depleted at a relatively faster rate.

Metal	2009	2010e	Mine production reserves (metric tons)
Bismuth	8,200	7,600	320,000
Cobalt	72,300	88,000	7,300,000
Copper	15,900	16,200	630,000
Lead	3,860	4,100	80,000
Nickel	1,400,000	1,500,000	76,000,000
Tin	260,000	261,000	5,200,000
Zinc	11,200	12,000	250,000
Silver	21,800	22,200	510,000
Gold	2,450	2,500	51,000

Table 1-3 Global mine production and reserves for selected lead-free alternatives in 2009 and estimates for 2010 [4].

Melting point of metals

Another important consideration is the melting point of various lead-free solder alloys. The temperature of most soldering processes in industry was traditionally based on lead-tin and many electronic packaging and board materials usually can withstand a peak operating temperature of 260°C [15]. As shown in Table 1-4 the eutectic melting point of tin alloys varies depending on the secondary metal being added.

Tin alloy		Eutectic composition (wt %)	Melting point (°C)
Indium-Tin	(In-Sn)	In51.7-Sn	120
Bismuth-Tin	(Bi-Sn)	Bi57-Sn	139
Lead-Tin	(Pb-Sn)	Pb37-Sn	183
Zinc-Tin	(Zn-Sn)	Zn8.8-Sn	199
Tin-Silver-Copper (SAC)		Sn-Ag3.5-Cu0.9	217
Silver-Tin	(Ag-Sn)	Ag3.5-Sn	221
Copper-Tin	(Cu-Sn)	Cu0.7-Sn	227
Pure Tin	Sn	-	232
Gold-Tin	(Au-Sn)	Au80-Sn	278

Table 1-4 Eutectic composition and melting point of selected tin-based solder alloys [13, 18].

For low temperature applications Bi-Sn is a good candidate as it has a relatively low melting point of 139°C. The alloy exhibits good wettability and low propensity for whisker formation, but can be relatively brittle. For high temperature applications such as in microwave devices, laser diodes, or RF power amplifiers, solders such as Au-Sn are commonly used.

It is preferable for solder alloys to have a near eutectic composition as it would allow the solder to melt at a single temperature during soldering. Upon cooling, the alloy would also solidify at the single eutectic temperature forming a good solder joint. Non-eutectic alloys are composed of many different phases and will not completely melt and solidify at the same temperature which can affect the reliability of the solder joints.

Figure 1-3 shows the phase diagram for Cu-Sn. The eutectic composition is Cu0.7-Sn99.3 wt% which has a melting point of 227°C. Although the Cu-Sn phase diagram is relatively complex with many intermetallic compounds (IMC), for soldering purposes only the phases near the Sn-rich corner (bottom right) are important. At temperatures below 260°C, only two IMCs are found; ε-Cu_3Sn and η-Cu_6Sn_5. IMCs are defined as compounds that contain two or more metallic elements that produces a new phase with its own composition, crystal structure, properties, and are usually hard and brittle [19]. Due to Sn and Cu interdiffusion at the interface, IMC layers form between the bulk solder deposit and Cu substrates. Since IMCs are brittle, they are the weakest part of a solder joint and can cause fractures and joint failures if they become too thick.
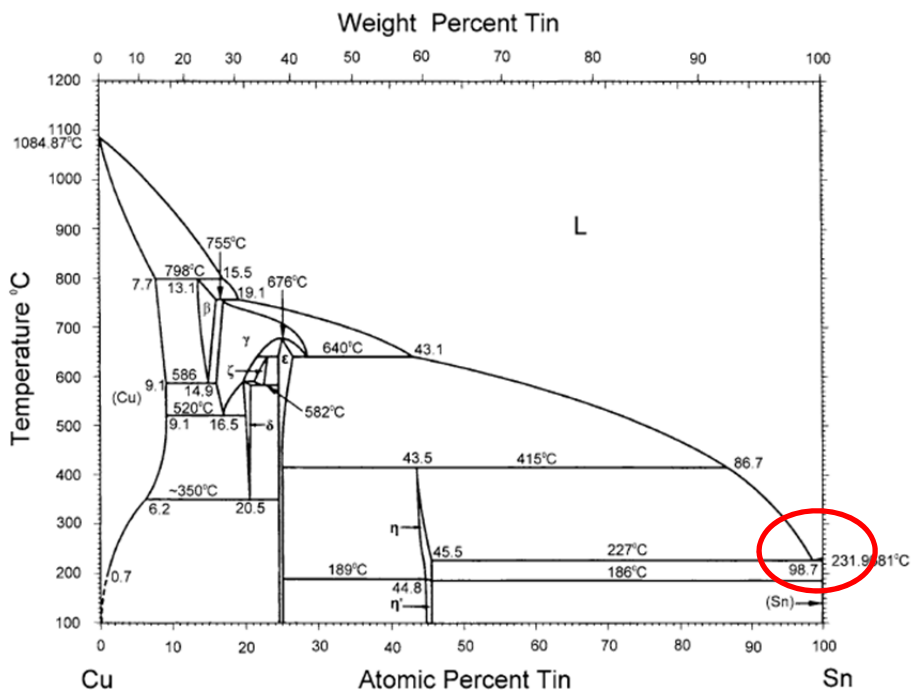
Figure 1-3 Cu-Sn phase diagram showing eutectic point at Cu0.7-Sn99.3 wt% [20].

1.3   Soldering Techniques

Soldering is defined as the metallurgical joining of two metal parts at temperatures below approximately 427°C (800°F) [21]. The term brazing is used for higher temperatures. In the soldering process a chemical compound called flux is needed to promote wetting of the molten solder and remove metal oxides and other contaminants from the surface [22]. A layer of metal oxide between the solder and the substrate would lead to weak bonding and joint failures. For electronic devices the solder not only provides a strong mechanical connection but it also needs to provide a good electrical connection.

1.3.1   Hand soldering

In the early days electronic components could be hand soldered onto PCBs. Although it is relatively time-consuming and labour-intensive, this technique was commonly used as the electronic packages were initially not very large. Fluxes were applied to clean the surface at points where soldering was to be performed. In the 1950s this technique was replaced by dip, drag, and wave soldering for mass soldering of through-hole components [23].

1.3.2   Wave soldering

As the number of electronic components increase and their size becomes smaller, hand soldering was no longer a feasible method for use in product assembly lines. This problem was addressed by wave soldering where there are three main zones that the electronic package has to pass through. In the first zone the PCB is usually sprayed with fluxes on the underside. The flux cleans and ensures proper solder adhesion to the PCB. In the second zone the PCB is preheated which serves to dry and activate the flux and minimize the effect of thermal shock as the PCB is passed through to the next stage. In the third stage the whole PCB package is moved across a bed of molten solder. The solder is melted in a pot and pumped to the assembly in waves hence the term wave soldering. The solder adheres to solder joints on the underside of the PCB by surface tension.

An atmosphere of nitrogen is usually used to minimize solder oxidation. For wave soldering the temperature must be maintained around 240 to 260°C to ensure low viscosity and suitable hydraulic flow needed for solder recirculation [22]. In the final

stage the electronic package is usually cleaned with deionized water. Wave soldering is mainly used for through-hole components but it can also be modified to be used with surface mount assemblies in which the components leads are attached on top of PCBs instead of going through.

1.3.3 Reflow soldering

As the use of surface mount devices (SMD) became more widespread in the 1980s, infrared reflow soldering became the preferred method to attach these devices on PCBs. Instead of running through a bath of molten solder, the SMDs are pre-attached to the PCB at solder pads or solder joints. Figure 1-4 shows the electronic packaging sequence in which solder pastes are initially applied at the solder joints of the SMD. The SMD is then flipped, placed on top of the substrate with the solder joints precisely aligned. This is the reason SMDs are sometimes referred to as "flip" chips. The whole package is then later heated and cooled to form a permanent solder bond. Reflow soldering is divided into four main zones; preheat, soak, reflow, and cooling zone.

The PCB initially enters the preheat zone to gradually heat up the assembly and minimize the risk of thermal shock which can cause cracks on the devices. The next zone is the thermal soak or soak zone where the flux is activated and solder paste volatiles evaporated. In the reflow zone the peak temperature is achieved in a period of approximately 30 to 90 seconds. The solder is said to "reflow" or liquefy once again. The last stage is the cooling zone where the whole assembly cools down and solder start to solidify joining the SMDs to PCB.

Automated deposition of solder
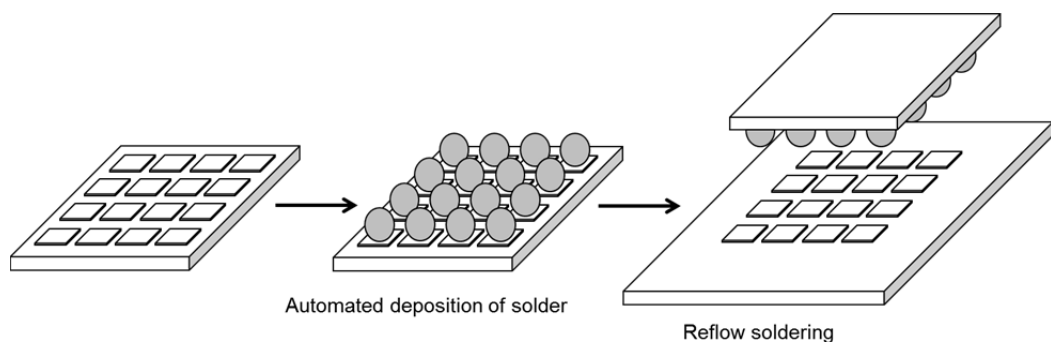
Reflow soldering

Figure 1-4 Attachment of an SMD on a PCB in preparation for reflow soldering.

It should be noted that as a rule of thumb, reflow and wave soldering peak temperature should be higher than the melting point of the solder alloy to ensure complete reflowing at an acceptable rate. The reflow soldering temperature is usually in the range of 210 to 240°C. The temperatures for reflow soldering are typically lower than wave soldering which reduces thermal shock and associated risks to the electronic package.

It must also be taken into account that usually more than two reflow steps occur in electronic manufacturing [24]. As shown in Figure 1-4, in some assemblies a first reflow step would be needed to form an array of solder balls on top of the solder joints. In the second reflow step, the SMDs are placed on top of the substrate and upon cooling the SMDs are attached securely to the substrate. Multiple reflowing may also be needed for testing purposes or when the SMDs need to be removed and repaired.

After much investigation from the late 1990s, the electronics industry has converged on tin-silver-copper (Sn-Ag-Sn or SAC) class of alloys as the main lead-free replacements for most soldering purposes. It has been recommended by JEITA and the National Electronics Manufacturing Initiative (NEMI) that SAC alloys should be used for reflow applications which accounts for at least 70% of all board assembly production [25]. For wave soldering applications that requires a larger amount of solder, the less expensive Cu-Sn alloys should be used [18].

As technology progresses SMDs with ever smaller dimensions are being fabricated. This means that the density of SMDs per unit area is also quickly increasing. To cope with this, an automated process is necessary in order to deposit a ball grid array (BGA) of solders seen in Figure 1-4. A small mechanical tip quickly moves from one solder joint to the next depositing exact amounts of soldering material. The precise deposition of soldering material at the solder joints of these microelectronic devices is an important factor affecting the reliability of these products. This is due to the fact that once cooled and solidified the solder joints are hidden and cannot be easily examined for quality control. Smaller SMDs also mean smaller solder joints and smaller amounts of soldering material needed. We must now explore the various solder microfabrication techniques in order to find the method which is most suitable for our needs.

1.4 Microfabrication of solders

Microfabrication of solders requires specialised processes due to the small size of the devices and large production volumes. Usually a typical solder coating is around 10 µm thick. Solders can be fabricated and applied to PCBs through techniques such as:

- pastes
- preforms
- physical vapour deposition
- electrodeposition

1.4.1 Solder Paste

Solder pastes are composed of fine metallic powders, fluxes, and chemical binders to hold everything together as they are applied to components. The inclusion of fluxes in the pastes makes this a cost-effective application method as fluxes do not need to be added separately. The paste also acts as a temporary adhesive keeping the surface mount components in the correct position before reflow soldering. However, one major drawback is that solder joints are susceptible to impurities arising from flux residues and other contaminations due to the decomposition of binders. These impurities may affect the quality and strength of the solder joints.

1.4.2 Solder preforms

Solder preforms are solders with specifically designed shape and sizes that are tailor-made depending on the shape of surface mount components [26]. This allows for precise targeted deposition based on the shape of the preforms and when only a small amount of solder is needed. Solder preforms are sometimes used in conjunction with solder paste and placed directly on the PCB. In some cases this is done in order to eliminate the need for wave soldering as the application of solder preforms are suitable for reflow soldering. The main problem with preforms is that they cannot be accurately applied to very small systems. As device dimensions continue to shrink, smaller amounts of solder are needed and novel solder application techniques are required in cases where pastes and preforms cannot be used.

1.4.3   Physical vapour deposition

Physical vapour deposition (PVD) refers to a technique in which material is transferred from a source to the component or substrate in a low pressure or vacuum chamber. The two most important PVD technologies are evaporation and sputtering [27]. Both processes share the same three main steps as shown in Figure 1-5:

1) evaporation phase — source material is converted in vapour

2) transport phase — particles are transferred in low pressure to the substrate

3) condensation phase — deposition of material onto the substrate
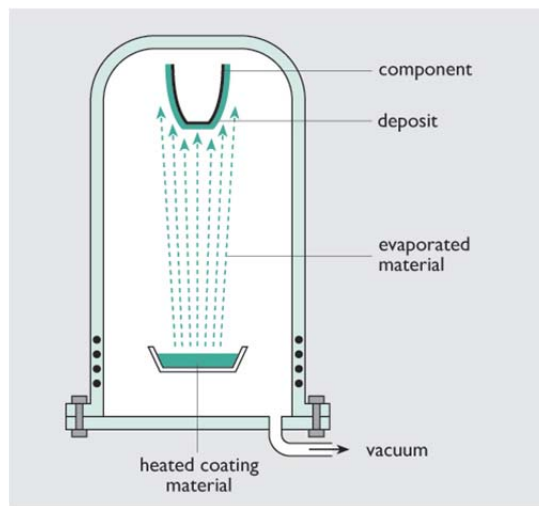
Figure 1-5 The PVD evaporation process used for metal deposition [28].

Evaporation is carried out at a temperature high enough to boil and evaporate the source material. The vacuum allows the material to be evaporated freely which then condenses on the substrate. However, PVD evaporation of alloys such as Cu-Sn can be problematic and not feasible as the melting and evaporation temperature for Cu (1083 and 2567 ^{o}C) and Sn (232 and 2270 ^{o}C) is very far apart.

Sputtering, on the other hand, can be carried out at a much lower temperature and differs from evaporation in that instead of heating the source material to boiling point, the source or target material is constantly bombarded by ions with high enough energy to eject the atoms from the target surface. These ions are said to "sputter" atoms from the target. In the final stage the sputtered atoms condense on the substrate and form a thin film.

The main advantage of sputtering over evaporation is that it is possible to deposit materials with very high melting points without having to completely boil and evaporate them. Low operating temperatures also mean that sputtering is the preferred technique used in the semiconductor industry where circuit boards cannot be exposed to very high temperatures. The thickness of PVD coatings can also be precisely controlled by fixing the operating parameters and adjusting the deposition time. Another advantage of PVD coatings is that they are sometimes physically stronger and more corrosion resistant when compared to electroplated deposits. However, PVD usually needs a direct line of sight in order to coat the substrate making the deposition of complicated structures unfeasible not to mention the high operational costs if high temperature or high vacuum is required.

1.4.4   Electrodeposition

Electrodeposition or electroplating in its simplest form is the process in which layers of material are coated on top of a substrate due to the application of an electric current to the system. The substrate is submersed in a plating bath containing metal salts which when dissolved is the source of the positively charged metal cations to be deposited. A negative charge is then applied to the substrate which acts as the cathode attracting the metal cations towards the substrate surface. The metal cations are reduced and deposited at the substrate surface. Electrodeposition is a relatively inexpensive technique that has the potential to solve the problems encountered with the application of solder in the form of pastes, preforms, and PVD techniques. Multilayers can be electroplated and later annealed to form the desired solder alloy. Targeted deposition across the surface through use of a patterned photomask can be carried out. This means that expensive metals such as gold in Au-Sn solders can be applied efficiently, lowering production costs.

Another major advantage of electrodeposition is that it is a flux-less process. With processes that require fluxes, they are heated along with the solder during soldering and can produce fumes which when inhaled can cause respiratory problems. The Health and Safety Executive consider prolonged exposure to Rosin-based solder flux fumes to be one of the most important causes of occupational asthma in the UK [29]. The absence of fluxes also eliminates the problem of additional chemicals and cleaning steps needed to remove flux residues, lowering costs and fabrication time.

The major drawback for electrodeposition is that in many cases bath composition needs to be strictly maintained in order to achieve the desired deposits. The plating bath parameters such as pH and applied current density also need to be tightly controlled in order to keep the alloy composition as close to the eutectic as possible. The ability of a plating solution to plate uniformly over a large area (covering power) and its ability to plate evenly into holes or surfaces with irregular shapes (throwing power) is also effected by the bath composition and plating parameters. Organic additives added to the electroplating bath such as brighteners and grain refiners can be co-deposited with the solder and needs to be carefully monitored as they can have detrimental consequences for solder performance.

Table 1-5 lists the main advantages and disadvantages of each solder microfabrication technique.

Fabrication technique	Advantages	Disadvantages
Paste	- Low cost - Rapid deposition	- Impurities from flux and binder residue
Pre-form	- High purity - Targeted deposition	- Cannot be applied to very small structures
Physical Vapour Deposition (PVD)	- Higher deposition rates - Uniform thickness	- Wide dispersion - Waste of material - High operation costs
Electrodeposition	- Low cost - Flux-less, no impurities	- Lower deposition rates - Precise plating parameters needed

Table 1-5 Main advantages and disadvantages of various solder fabrication techniques.

1.5   Electrodeposition of Tin

Since the major component of Pb-free solder alloys is Sn, we must first discuss what type of electrolytes have been used to electrodeposit Sn in order to compare the advantages and disadvantages that each plating system provide. It has been shown that plating parameters which determine the composition of the deposit include current density, agitation, operating temperature, pH, and the concentration of metal ions [2,

30-32]. Therefore, it is important that the combination of these variables be chosen carefully in order to obtain usable deposits.

1.5.1 Electrolyte systems

The most important decision before plating any metals is the selection of the electrolyte system. This section provides an overview of the various electrolytes options available. Although cyanide-based solutions are still being used in metal finishing, the industry has been actively moving away from these electrolytes due to its highly toxic nature which can affect worker health and safety. Environmental issues such as possible site contamination and waste disposal are also of concern as these factors increase the overall operational costs. Therefore, only non-cyanide baths are reviewed here.

Electrodeposition of tin is a well-established process. Over the years, commercial tin plating has been carried out using a variety of different electrolytes involving different chemistries which can be roughly divided, based on pH, into two categories: acidic and alkaline systems. In acid baths Sn^{2+} is the main metal cation while in alkaline baths Sn^{4+} is predominant. The exception is for mildly alkaline baths such as pyrophosphate where Sn is in the divalent state. Traditionally alkaline baths were extensively used as they provided very high throwing powers at the expense of the low current densities that can be passed. As technology advanced acid baths are now able to provide very high current densities and a much faster plating rate [1, 2].

Alkaline baths include:

- stannate
- pyrophosphate

Acid baths include:

- sulfate
- fluoroborate
- phenolsulfonic acid
- methanesulfonate

Alkaline baths

Alkaline stannate baths were originally based on $SnCl_2$ and KOH with the addition of other chemicals such as pyrophosphate, cyanide, or tartaric acid [33]. However, the first baths that were operated successfully on a commercial scale in the 1930s were based on sodium stannate [34-36]. Although initially additives such as malic acid, ethylene glycol, and tartaric acid [37] were added to improve the quality of the deposits it was found that they are not necessarily needed [33]. The alkaline stannate baths in use today are relatively simple as they contain only two main components, a stannate and an alkali hydroxide. Usually potassium stannate ($K_2Sn(OH)_6$) dissolved in potassium hydroxide solutions is preferred over sodium stannate ($Na_2Sn(OH)_6$) dissolved in sodium hydroxide solutions as the former bath allows operation at higher current densities and current efficiencies. The amount of Sn that is present in the solution can range from 40-180 g L^{-1}, depending on the current density applied [1].

The advantage of stannate baths is that they can be operated without additives and can have very high throwing power [1, 2]. However, stannate baths are currently not widely used as current densities that can be passed are much lower (3-40 mA cm^{-2}) compared to most acid counterparts (as high as 80 mA cm^{-2}) [2]. A minimum temperature of more than 70°C is also needed to allow higher current efficiencies and this requirement would increase operational costs [1]. The major disadvantage of alkaline baths is that they are not compatible with modern electronics as they can dissolve photoresists used during microfabrication.

Pyrophosphate baths are similar to stannate baths but usually need additives to improve the quality of deposits. They are composed of $Sn_2P_2O_7$ (8-15 g L^{-1}) dissolved in sodium or potassium pyrophosphate solutions (120-250 g L^{-1}) with potassium nitrate added to allow higher current densities [1]. The pH of the solution is usually maintained at around 8 [38]. Additives such as dextrin-gelatin [39] were added to influence Sn deposition such as increasing the brightness of the deposits, It must be noted that although pyrophosphate baths are still considered toxic plating baths, they were developed with the aim of replacing more corrosive and dangerous systems such as cyanide baths [1]. It is also used mainly in the electrodeposition of tin-alloys. The addition of additives such as formaldehyde [40] or poly ethylene glycol [38, 40] have been shown to change the reduction potential of Sn and facilitate alloy co-deposition.

Acid baths

There is a wider range of options available when plating from acid systems. The main added benefit of using acid baths over alkaline baths is that the amount of electric charge required to reduce Sn^{2+} à Sn is less than that required to reduce Sn^{4+} à Sn. Assuming 100% current efficiency, 2.214 g of Sn is deposited per ampere-hour from an acidic Sn^{2+} solution compared to 1.107 g from an alkaline Sn^{4+} solution [33].

Sulfate

Sulfate baths provide good throwing power, high cathode current efficiency, and low initial operating costs. These baths can be operated at room temperature and are relatively easy to control and maintain. The source of Sn in these baths are tin sulfate $SnSO_4$ (15-45 g L^{-1}) dissolved in sulfuric acid (135-210 g L^{-1}) [2]. The main advantage of this bath is very high current efficiency of almost 100%.

The major disadvantages of sulfate based electrolytes are anode passivation at high current densities (>30 mA cm^{-2}), corrosivity of the solution (pH below 1), and spontaneous oxidation of Sn^{2+} to Sn^{4+}. Therefore, in order to reduce the formation of tin sludge (SnO_2) which can aggregate at the bottom of plating tanks, antioxidants are an essential component of these baths [41].

Fluoroborate

In fluoroborate baths tin tetrafluobarate, $Sn(BF_4)_2$ (75-113 g L^{-1}) is dissolved in a solution containing fluoroboric acid (188-263 g L^{-1}) and boric acid (23-38 g L^{-1}). $Sn(BF_4)_2$ is very soluble in this bath allowing the use of high current densities up to 80 mA cm^{-2} in an operating temperature range of 30-50 °C [2]. Other advantages include high cathode current efficiencies and higher throwing power. There is a variety of additives that need to be added to this bath such as peptone[42] which is used to obtain smooth fine grained deposits while catechol and hydroquinone function as antioxidants [43].

The disadvantage of fluoroborate electrolytes is the high cost of waste management due to the presence of fluoride ions and boric acid not to mention that fact that it is the most corrosive among acid electroplating baths.

Phenolsulfonic

Phenolsulfonic acid baths are widely used in continuous tin plating of steel strips as they allow for operation at very high current densities (200-500 mA cm^{-2}). This bath system the most widely used in the "Ferrostan" tin-plate process and accounts for 70% of all the 130-140 continuous tin-plate lines around the world [1]. In this process the plating solution usually contains Sn (20-35 g L^{-1}) dissolved in a solution of phenol sulfonic acid (40-80 g L^{-1}) [2]. The operating temperature is around 40-50 °C with current densities of up to 300-350 mA cm^{-2}. Another advantage of this bath is that phenolsulfonic acid acts as an antioxidant and sludge formation is typically not a problem. However, the major disadvantage is the high toxicity of the phenol group.

Methanesulfonate

The toxicity of fluoroborate and phenol sulfonic acid baths resulted in environmental regulations promoting the use of more environmentally friendly electrolytes such as methanesulfonic acid (MSA), which has gained widespread acceptance [30, 44-47]. Up to 70 g L^{-1} of Sn can be used in MSA baths and current densities ranging from 25-700 mA cm^{-2} can be applied depending on the application [2]. Normal operating temperatures were in the range of 30-60 °C. The oxidation of Sn^{2+} to Sn^{4+} is much less of a problem compared to fluoroborate baths in which Sn^{4+} compounds such as the hexafluostannate ion (SnF$_6^{2-}$) is known to exist .

MSA has become the preferred choice for electroplating tin and tin alloys from the 1980s onwards. MSA, being an acid electrolyte, has the additional benefit of being compatible with photoresist materials used in microfabrication of electronic devices as photoresists are not dissolved in these baths. MSA is also an interesting supporting electrolyte with many desirable properties such as high metal salt solubility, high conductivity, low toxicity and lower corrosivity than sulfate or fluoroborate baths leading to better waste management [44, 45, 48, 49]. A simple MSA bath usually consists of metal sulfonate salts dissolved in MSA solutions containing bath additives such as antioxidants, brighteners, and surfactants (ionic or non-ionic depending on the specific bath formulation).

The advantages and disadvantages of various electroplating baths are summarized in Table 1-6.

Electrolyte	Advantages	Disadvantages
Stannate	- No additives	- High temperature - Lower current efficiency - not compatible with microfabrication
Pyrophosphate	- High throwing power	- Toxic effluent
Sulfate	- Low cost - High current efficiency - Room temperature operation	- Anode passivation at high current density - Needs antioxidant
Fluoroborate	- High current density - High current efficiency - High throwing power	- Toxic effluent - Needs antioxidant
Phenolsulfonic acid	- High current density - No antioxidant needed	- Toxic effluent
Methanesulfonate	- Environmentally friendly - High metal salt solubility - High conductivity	- Needs antioxidant

Table 1-6 Advantages and disadvantages of various electroplating baths.

1.5.2   Bath additives

The term additive refers to chemicals added to the plating bath which can influence the growth and structure of deposits. Additives or complexing agents such as antioxidants, brighteners, and surfactants are also commonly used to stabilize the bath and improve the quality of deposits [1, 2, 50]. Care must be taken to avoid adding too much additives as they may be incorporated into the deposits causing roughness and may result in deposits that do not adhere well to the surface. This would eventually lead to solderability and reflow problems.

Antioxidants

In acid solutions atmospheric oxygen can spontaneously oxidise Sn^{2+} to Sn^{4+}. This results in the loss of stannous tin in solution and can lead to lower deposition rates. A large amount of Sn^{4+} tin present in the electrolyte can also lead to unwanted sludge formation [51]. This also means that Sn^{2+} in the solution needs to be replenished more often, increasing the operational costs. Excessive amounts of oxygen in the electrolyte can be avoided by minimizing agitation of the solution or by adding antioxidants which is a component of most commercial tin plating processes. Antioxidants inhibit Sn^{4+} formation though one of three mechanisms [2]. The first involves the formation of stable complexes with Sn^{2+}. In the second mechanism the antioxidant reduces oxygen solubility in solution. In the last mechanism the antioxidant binds to soluble oxygen in the solution, reducing the oxidation rate. Table 1-7 shows a list of commonly used antioxidants and the effect they have on Sn^{2+} concentration.

Antioxidant	Sn^{2+} concentration (initial 50 g L^{-1})
None	20
Catechol	48
Hydroquinone	48
Citric acid	27
Phenol sulfonic acid	40
Glycolic acid	32
Lactic acid	29

Table 1-7 List of various antioxidants and the effect on Sn concentration in MSA electrolytes [2].

Brighteners

Brighteners, as its name suggests, are added to create a bright surface finish. While this is desirable for some applications such as creating a corrosion resistant coating, bright deposits are detrimental for soldering applications. This is due to the observation that bright finishes tend to have a higher propensity for tin whisker formation [24]. Tin whiskers are tin or tin alloy materials that extend from the surface which can then come into contact with nearby electronic components causing an electrical short-circuit. Whisker growth is less pronounced on matte deposits and is, therefore, the preferred type of deposit for soldering.

Surfactants

Surfactants are surface active agents that are usually added to help the dissolution of brighteners or grain refiners in the electrolyte. Surfactants lower the surface tension of liquids increasing the wetting ability and levelling power. It has been shown that depending on the electrode potential, surfactants can preferentially absorb to the surface [52, 53] and influence the deposit microstructure. The absence of surfactants usually leads to the formation of large dendritic crystals and rough deposits.

Surfactants or wetting agents have been used during this research to control the metal content in the alloy deposit as well as to improve the surface microstructure. A non-ionic fluorosurfactant was used in this project since 2008 in very small quantities of 0.01 %vol (30-60 μL/ experiment). The specific surfactant used falls under the classification of perfluorooctane sulfonic acid (PFOS) and its derivatives [54]. In August 2010, PFOS and its derivatives became regulated across Europe under the Persistent Organic Pollutants (POPs) Regulation 850/2004 (as amended) [55]. In general, the production, placing on the market and use of substances, preparations, mixtures, semi-finished products and articles that contain PFOS (at above a certain concentration) is effectively banned. Some materials and uses are exempt from the PFOS ban, but may still be covered by other legal requirements. In particular, the regulation also prescribes how stockpiles containing PFOS must be managed and notified, and how wastes that contain PFOS must be disposed. However, wetting agents for use in controlled electroplating systems are currently exempted from this ban until August 2015.

1.6 Electrodeposition of Tin Alloys

There are two main ways in which one could electrodeposit tin alloys. The first is to deposit each individual metal in its own plating bath and then move it to the second bath to deposit the next metal. For example, fabricating Cu-Sn alloys involves the use of separate baths for each individual metal to successively plate one metal layer on top of the other creating a multilayer that would later be annealed to form an alloy mixture [56]. However, the main problem with this multistep process is that it is time consuming and suffers from difficultly in controlling the relative thickness of the individual tin and copper layers. This can affect the uniformity of the alloy composition across the substrate. The surface also needs to be cleaned when moving from one bath to another as metal oxide layers may form which would have a negative impact on the quality of the deposit. This multiple bath system also increases the production time and costs as unwanted metal oxide layers formed on the substrate needs to be removed before successive layers of metal can be deposited. The fabrication of ternary alloys causes even more problems as there are more steps involved. In order to deposit SAC alloys, one would need to sequentially deposit Ag-Sn on top of Cu-Sn and annealed to obtain the eutectic composition. Reliability and reproducibility would be the main concern as each layer would need to be precisely controlled to obtain the desired composition after annealing.

The second method would be to co-deposit all metals from a single plating bath. However, the single bath method also comes with its own set of problems. This is due to the fact that, depending on the combination, most metals would not readily deposit at the same potential. In general the main strategies used to overcome this problem is to use chelating agents which can bind to selected metals or by the use of surfactants that also absorb on the surface and influence the deposition potentials of each metal.

The electronics industry has designated SAC alloys as the standard lead-free replacement and much research has been carried out with regards to this ternary alloy [57-69]. Although the electrodeposition of ternary alloys such as SAC has been shown to be possible almost a decade ago [57, 70], relatively few studies have been described in literature.

Fukuda et al [59], has described a method in which eutectic Bi-Sn, Cu-Sn, and SAC alloy films were obtained from sulfate baths (operating at 20°C, 20 mA cm^{-2}) which contained 0.004 M of the surfactant polyoxyethylene laurylether (POELE). The bath contained only the surfactant and metal salts; SnSO$_4$ (0.2 M), CuSO$_4$, (0.02 M) and AgNO$_3$ (0.1 M). A chelating agent, thiourea, was only used in SAC baths. It was proposed that POELE initially adsorbs on the deposited Sn during electrodeposition suppressing subsequent deposition of Sn while also providing a surface smoothing effect. POELE could then be easily washed off the surface and is not incorporated into the deposit.

Joseph and Phatak [62] proposed an MSA bath (operating at room temperature, 10 mA cm^{-2}) containing tin methanesulfonate (Sn-MSA), CuSO$_4$, Ag$_2$SO$_4$, and a thiourea chelating agent (0.04 M), iso-octyl phenoxy ethanol (OPPE) surfactant (12 g L^{-1}), and gelatin (2 g L^{-1}). Near eutectic SAC composition (Sn-Ag2.7-Cu0.9) was reported to have been obtained. Thiourea was attributed to have modified the deposition potential of the three metals ions closer together, enabling co-deposition. The additives are also beneficial as they absorb to the electrode surface during deposition improving the film microstructure.

More recently Tsai and Hu [67] have developed a citrate-based bath (operating at 25°C, 3 mA cm^{-2}) to deposit near eutectic compositions of Ag-Sn, Cu-Sn, and SAC (Sn-2.9Ag-0.7Au). The bath contained no additives and only the metal salts SnCl$_2$ (0.15 M), AgNO$_3$ (1.5-10 mM), and CuSO$_4$ (0.5-2.5 mM). It was concluded that plating from citric acid baths was possible and that in this case the citrate ion was an effective chelating agent which facilitated co-deposition. Varying the metal concentrations in the bath also effected the metal composition in the deposit. It was also noted that the Cu$_6$Sn$_5$ IMC was found in Cu-Sn deposits, but not in SAC deposits.

New processes and electrolyte formulation for SAC electrodeposition are still being discovered, but currently it is not clear that they have the potential to become feasible in industrial settings. This is because the electrodeposition of the SAC alloy from a single plating bath is complicated and precise electroplating parameters have to be maintained in order to obtain the eutectic composition (Sn-Ag3.5-Cu0.9 wt%). Although the electrodeposition of SAC is being actively pursued by the industry which is reflected by the increasing number of patent applications, these have become increasingly complex. There are a large number of antioxidants, brighteners, and surfactant

combinations to choose from and each research group naturally aims to promote theirs as the best. For example a patent by Tsuji et al [70] lists over 100 additive variations that can be used to deposit Cu-Sn, SAC, and Bi-Cu-Sn alloys. It was decided that in order to better understand the process of tin alloy deposition one should initially start looking at binary alloys. Therefore, discussions in the next section will be concentrated on various binary Sn alloys and how they have been deposited. The choice of electrolyte system and additives used will be noted to observe whether there are any trends that may help aid their selection.

Cu-Sn alloy deposition

Deposition of binary alloys such as Ag-Sn [63, 67], Au-Sn [71-73], Bi-Sn [59] , and Cu-Sn [67] have been shown to be possible from a single plating bath. However, Cu-Sn represents an interesting candidate for the study of the electrodeposition of binary tin-based alloys due to the relatively low cost of copper metal and its high plating efficiency [74]. A literature survey of Cu-Sn electrodeposition from a single electrolyte shows that they are still recently being carried out in various electrolytes such as alkaline [75], pyrophosphate [40, 76], sulfate [59], and MSA [50, 77, 78].

Taking into account the various advantages and disadvantages of each electroplating system as shown in Table 1-6, we can rule out in alkaline baths due to their incompatibility with microfabrication processes. Pyrophosphate baths can also be eliminated due to their high toxicity. Therefore, the remaining baths that warrant further investigation are sulfate and MSA-based baths. Patents are a good source of information as they can provide details of electrolyte systems that have potential to be used in industrial settings.

Andricacos et al. [77] has proposed a method for depositing Cu-rich Cu-Sn alloys from acid electrolyte solutions. The invention aims to electrodeposit alloys of the two metals that have reversible potentials that are sufficiently separated such that they cannot be readily co-deposited. A typical bath contains a Cu salt and a second salt of a metal less noble than Cu dissolved in acid electrolyte such as MSA. The bath also contains a wetting agent polyethylene glycol (PEG) and a brightener mercaptopropane sulfonic acid. These additives have the effect of shifting the deposition potential of Cu to a more negative potential by slowing down Cu deposition kinetics. This allows the co-deposition of Cu-Sn alloys with low Sn levels to occur. The current densities applied were in the range of 5-50 mA cm^{-2}. Sn^{2+} can be added to the solution in the form of its

sulfate ($SnSO_4$) or methanesulfonate ($Sn(O_3SCH_3)_2$ salts. This invention was able to deposit Cu-Sn alloys, but only having Sn contents of 0.1 to 1.3 at.% and, therefore, would not be suitable for plating Sn-rich Cu-Sn solders.

Tamura [50] describes a more general invention which allowed the electrodeposition of Cu-Sn alloys from MSA-based baths. The bath is composed of Cu and Sn methanesulfonate salts (Cu^{2+} 0.1 g L^{-1} and Sn^{2+} 30 g L^{-1}) dissolved in methanesulfonic acid (200 g L^{-1}) with antioxidants such as catechol or hydroquinone (0.2-10 g L^{-1}), a dispersant or surface active agent such as polyoxyethylene alkyl ethers (1-30 g L^{-1}), and a mixture of two or more brighteners such as formaldehyde or acetylacetone (0.1-10 g L^{-1}). The bath is operated at 10-30°C and 5-200 mA cm^{-2}.

This invention gives information concerning the bath components needed to deposit Cu-Sn alloys and uses a Hull cell to test and evaluate the deposit appearance. However, the aim of this invention was to obtain bright Cu-Sn alloys which might not be preferable for soldering as they are prone to form tin whiskers. No mention of Cu or Sn content in the deposit was given.

Tsuji [70] provided an invention that outlined a very comprehensive list of additives that can be used to plate Cu-Sn from either a sulfate or MSA bath. As an example, a typical MSA bath contained Sn-MSA (0.2 M), CuSO4 (0.0026 M) dissolved in MSA (2 M) containing a brightener such as polyoxyethylene nonylphenyl ether (5 g L^{-1}), and an antioxidant such as hydroquinone (1 g L^{-1}). The baths were operated at 25°C and at two different current densities (5 and 30 mA cm^{-2}) to determine whether the composition of the deposits were dependent on the current density.

It was found that the Cu content of the deposits had low dependency on the current density. The Cu:Sn ratio was similar whether the applied current density was 5 or 30 mA cm^{-2}. However, the Cu:Sn ratio in the deposit was influenced by the amount of copper salt in the bath. Smaller amounts of Cu added to the bath resulted in a lower amount of copper in the deposit and vice versa. This implies that the Cu:Sn ratio in the deposit can be controlled by the amount of each metal salt initially added to the bath. The influence of the non-ionic surfactant in the bath was also determined. In solutions without surfactant, the preferential deposition of Cu at lower current densities was observed. The absence of surfactants also lead to a dendritic surface which was not suitable for practical use. This result was interesting as it shows that brighteners are

not necessarily needed to plate Cu-Sn alloys but that surfactants are a crucial component. The mechanism of how the surfactant facilitates Cu-Sn co-deposition was not mentioned.

Martyak and Seefeldt [31] investigated the role of glycol-type additives in MSA solutions. Sn-MSA (30 g L^{-1}) was dissolved in MSA (130 g L^{-1}) which contained hydroquinone (1 g L^{-1}) and glycol-type additives such as PEG (2.5 g L^{-1}). It was shown that glycol-type additives are effective in minimizing the evolution of hydrogen gas at low over potentials and they helped to refine the deposit microstructure. The glycol molecules are most likely adsorbed to the surface during deposition and the result is a smooth matte tin coating.

More recently Low and Walsh [47, 78], have carried out Cu, Sn, and Cu-Sn electrodeposition in a relatively simple MSA bath containing an antioxidant (hydroquinone) and a fluorosurfactant. The bath was composed of $CuSO_4$ (0.02-0.2 M) and $SnSO_4$ (0.02-0.05 M) dissolved in MSA (1.9-2.3 M) solution containing hydroquinone (0.01 M) and a cationic fluorosurfactant (up to 0.012 vol%). They have shown that in this bath the presence of the surfactant had no effect on the Sn deposition potential. However the surfactant shifted the Cu deposition potential to a more negative value when the copper concentration was low (less than 0.1 M). They have also reported that it was possible to deposit Sn-rich Cu-Sn alloys from this MSA electrolyte at room temperature. A high Sn:Cu ratio in the bath resulted in a low copper content in the deposit. The formation of Cu_6Sn_5 IMCs is present in deposits which had a high Sn content of 96 wt%. It was not specifically mentioned whether the tin rich deposits could be used for soldering purposes as only electrochemical studies using a rotating disk electrode were carried out in their work. The presence or absence of metal oxides which can greatly affect the performance of a Cu-Sn solder alloy was also not discussed.

The current author has published work which has shown that the addition of the surfactant to a similar MSA-based bath minimizes the propensity for tin sludge formation as well as inhibiting the formation of metal oxides [79] (paper attached in Appendix). However, to the author's best knowledge, there have been no reports describing a systematic approach in which the electrolytes and specific plating parameters were selected. This can lead to many problems such as the selection of baths that are not compatible with the microelectronic fabrication process (alkaline

baths would dissolve photoresists) or baths that are not suitable for the plating of specific types of alloys (baths that contain chloride can dissolve Au-based alloys).

1.7   Aims and objectives

The aim of this research project is to document the necessary steps involved in the systematic determination of both electrolyte composition and plating parameters needed to obtain a specific alloy composition. The research project also aims to determine the feasibility of Cu-Sn electrodeposition from MSA electrolytes. This was carried out in the following steps:

1) Preliminary feasibility studies of the effect that antioxidants and surfactants have on the deposit composition and morphology.

2) Electrochemical analysis was carried out to study the current-potential behaviour of copper, tin, and Cu-Sn alloy deposition from MSA electrolytes. Cyclic voltammetry was used to determine the potential at which the individual metals and tin-rich alloys start to deposit. The effect of fluorosurfactant on the reduction potential of tin and copper was also examined. Chronoamperometry and anodic stripping voltammetry were then carried out to study the effect of applied potential and plating time on current efficiency. Based on these results, a basis for depositing tin-rich Cu-Sn alloys by electrodeposition was devised.

3) Thereafter a series of deposition experiments at a current density which produced high tin content were performed. A comparison of the deposit quality and morphology was also made between two different methods of electrodeposition; direct current plating and pulse plating. The surface microstructure and alloy composition of deposited material was examined using a scanning electron microscope and energy dispersive X-ray spectroscopy, respectively. X-ray diffraction analysis was carried out to determine the phases of the deposits and to observe the formation of any IMCs.

2. FUNDAMENTAL THEORY

In order to electrodeposit metals we first need to understand the basic concepts of electrochemistry. An electrochemical reaction involves the transfer of charge across the electrode-electrolyte interface, a region also known as the electrical double layer. The charge carriers in an electrode are electrons while the charge carriers in the electrolyte solution are ionic species. A deposition reaction occurs when a potential is applied across the electrode-electrolyte interface which is enough to overcome the activation energy and thermodynamic barrier needed to drive the reaction.
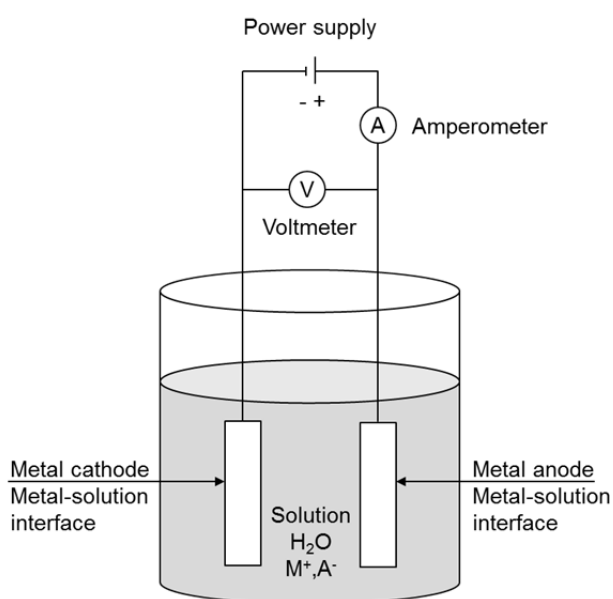
Figure 2-1 A schematic representation of an electrochemical cell

Although a metal reduction reaction can be written simply as $M^{z+} + ze^- \rightarrow M$, the actual process is much more complex and the electrode reaction rate depends on many processes such as [80]:

- mass transport of ions from the bulk solution to the electrode surface
- adsorption, desorption, or crystallization on the electrode surface
- charge transfer reaction at the electrode surface
- incorporation of the metal ion into a growing lattice

Some of these reactions such as electron transfer and electrodeposition are dependent on the potential across the electrochemical double layer.

Electrode-Electrolyte Interface

Whenever an electrode is in contact with an electrolyte an electrochemical double layer is formed as shown in Figure 2-2. There exists a phase boundary between the electrodes and the electrolyte which is called the interphase. The simplest model of the electrochemical double layer is the one proposed by Helmholtz [32]. According to this model the hydrated ions are lined up in the plane at a fixed distance away from the electrode called the outer Helmholtz plane (OHP). This fixed distance is determined by the hydration sphere of the ions. It is defined as the plane of the centre of the hydrated ions. The interface consists of two equal and opposite layers of charge, one on the metal and the other in the solution. It is this separation of charged layers that gives rise to the term electrochemical double layer. In theory it can be thought of as being equivalent to a parallel plate capacitor.
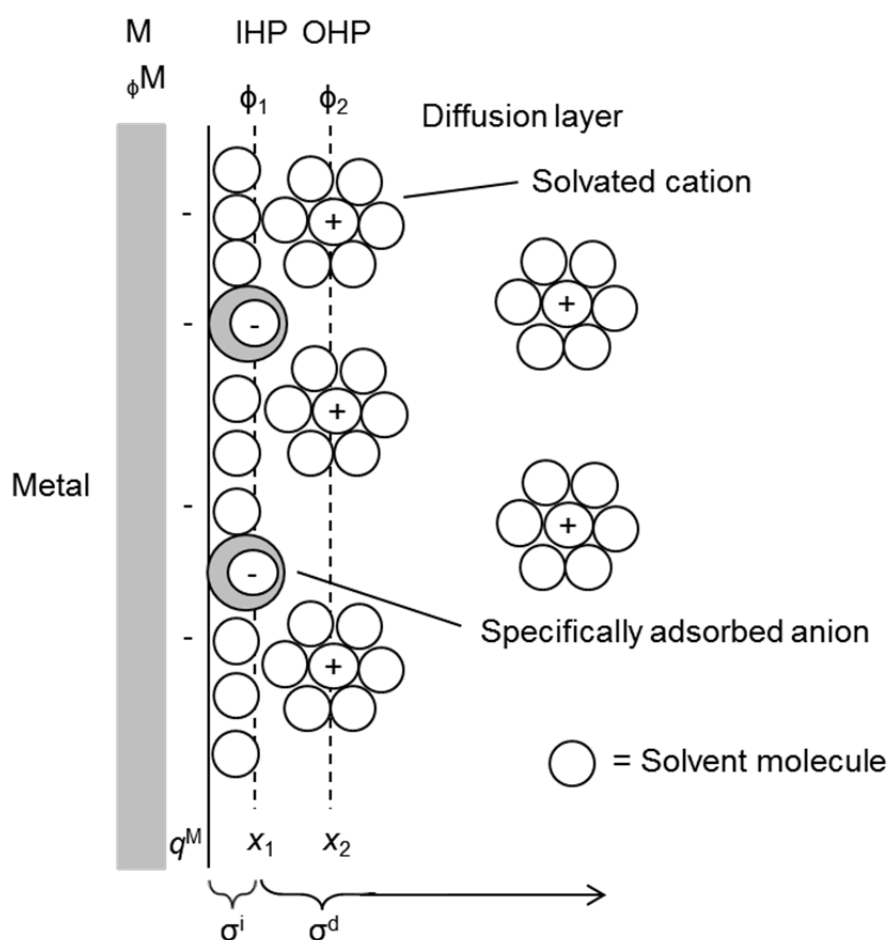
Figure 2-2 Model of the electrochemical double layer showing the Helmholtz layer and the diffuse double layer beyond the outer Helmholtz plane (OHP) [80].

31

It should be noted that when in solution, the metal ions are always surrounded by a hydration sheath of water molecules. Chelating or complexing agents may also bind to metal ions which can have an influence on the stability of the metal complex and in turn the stability of the bath.

An updated model of the Helmholtz fixed double layer is the Gouy-Chapman, and Stern model [32]. According to this model some excess charges are in a fixed (compact) position restricted to a single plane close to the electrode surface, the Helmholtz or Stern layer, and others are statistically distributed into the solution in what is referred to as the diffuse layer. Thus, in this model the double layer is divided into two regions: the compact and the diffuse double layers. The diffuse layer provides an additional capacitance which is dependent on the potential and concentration. The overall capacitance shown in Equation 2.1, therefore, is

$$\frac{1}{C_{dl}} = \frac{1}{C_H} + \frac{1}{C_{diffuse}}$$

(2.1)

Where C_{dl}, C_H, and $C_{diffuse}$ are the capacitances of the double layer, Helmholtz layer, and diffuse double layers respectively. Since most metal deposition is carried out with highly conductive supporting electrolyte contribution of $C_{diffuse}$ can usually be ignored. The thickness of the double layer and concentrated electrolytes is approximately 10 nm [80] and can have very high electric field strengths of up to 10^9 V m^{-1} [32].

Whenever an electric current is applied in order to drive a deposition reaction the current would initially be consumed to charge this double layer. This is referred to as the capacitive current or non-Faradaic current as no charge is transferred across the double layer. The remainder of the current is what actually drives the electrodeposition reaction and is referred to as the Faradaic current. This charge transfer reaction across the electrode solution interface can be described by Faraday's law and is named as such.

The purpose of this fundamental theory chapter is to describe the fundamental theory of metal deposition which includes the understanding of thermodynamics and kinetics of electrodeposition as well as the influence of mass transfer on the deposition rate.

2.1 Thermodynamics

2.1.1 Stability of Electrolyte

Thermodynamics describes the change in energy and entropy during a reaction which is in equilibrium. Thermodynamic data explains why some species exist in electrolyte and others do not. For a general reaction

$$aA + bB \rightarrow cC + dD \tag{2.2}$$

the change in Gibbs free energy (ΔG_{rxn}) of the reaction is defined as

$$\Delta G_{rxn} = [\Sigma(c\Delta G_f^0(C) + \Sigma(d\Delta G_f^0(D)) - \Sigma(a\Delta G_f^0(A) + \Sigma(b\Delta G_f^0(B))] \tag{2.3}$$

Cu species	ΔG^o_f (kJ mol^{-1})	Sn species	ΔG^o_f (kJ mol^{-1})
CuO(c)	-134.0	SnO(c)	-257.0
Cu$_2$O(c)	-148.1	SnO$_2$(c)	-519.9
CuSO$_4$(c)	-663.0	SnSO$_4$(c)	-1055.9
Cu$^+$(aq)	50.3	Sn(SO$_4$)$_2$(c)	-1451.0
Cu^{2+}(aq)	65.7	Sn^{2+}(aq)	-27.2
		SO$_4^{2-}$(aq)	-744.6

Table 2-1 Gibbs standard free energy or formation for various Cu and Sn species [81]. The phases are aqueous (aq) and solid or crystal (c).

For example the reaction of tin(II) sulfate formation

$$Sn^{2+}{}_{(aq)} + SO_4{}^{2-}{}_{(aq)} \rightarrow SnSO_{4\,(c)} \tag{2.4}$$

$$\Delta G_{rxn} = [(\Delta G_f^0(SnSO_4) - (\Delta G_f^0(Sn^{2+}) + (\Delta G_f^0(SO_4^{2-}))]$$
$$\Delta G_{rxn} = (-1055.9) - [(-27.2) + (-744.6)]$$
$$\Delta G_{rxn} = -284.1 \text{ kJ mol}^{-1}$$

In MSA electrolyte, free Sn^{2+} ions can favourably form a complex with sulfate ions. Another example attempts to show the role of sulfate oxidation of stannous (Sn^{2+}) to stannic (Sn^{4+}) ions which proceeds in 3 steps:

$$Sn^{2+} + SO_4^{2-} \rightarrow SnSO_4$$

$$SnSO_4 + H_2O \rightarrow Sn(OH)^+ + HSO_4^-$$ (2.5-2.7)

$$Sn(OH)^+ + H_2O \rightarrow SnO_2 + 3H^+ + 2e^-$$
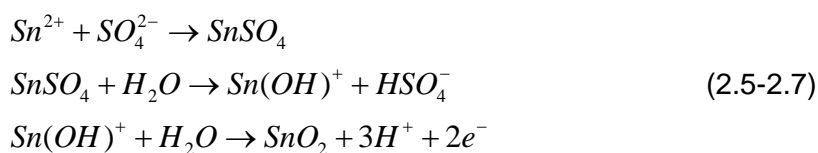
The overall free energy of the combined reactions 2.5-2.7 is ΔG_{rxn} = -27.12 kJ mol^{-1}. This indicates that if $SnSO_4$ is present in the solution, stannic oxide (SnO_2) will be readily formed. Therefore, the loss of tin from the solution and the creation of tin sludge by the mechanism above may be minimized but cannot be completely avoided. One method to mitigate this is to keep the free acid concentration high (low pH) which would shift the equilibrium of Equation 2.7 to the left minimizing SnO_2 formation.

Understanding of thermodynamics can lead one to construct a Pourbaix diagram as shown in Figure 2-3. Although the construction of such a diagram for the specific MSA electrolyte used is beyond the scope of this work, useful information can still be extracted. The Pourbaix or Eh-pH diagram shows the stability area of different redox species in the system according to the potential and pH of the solution.
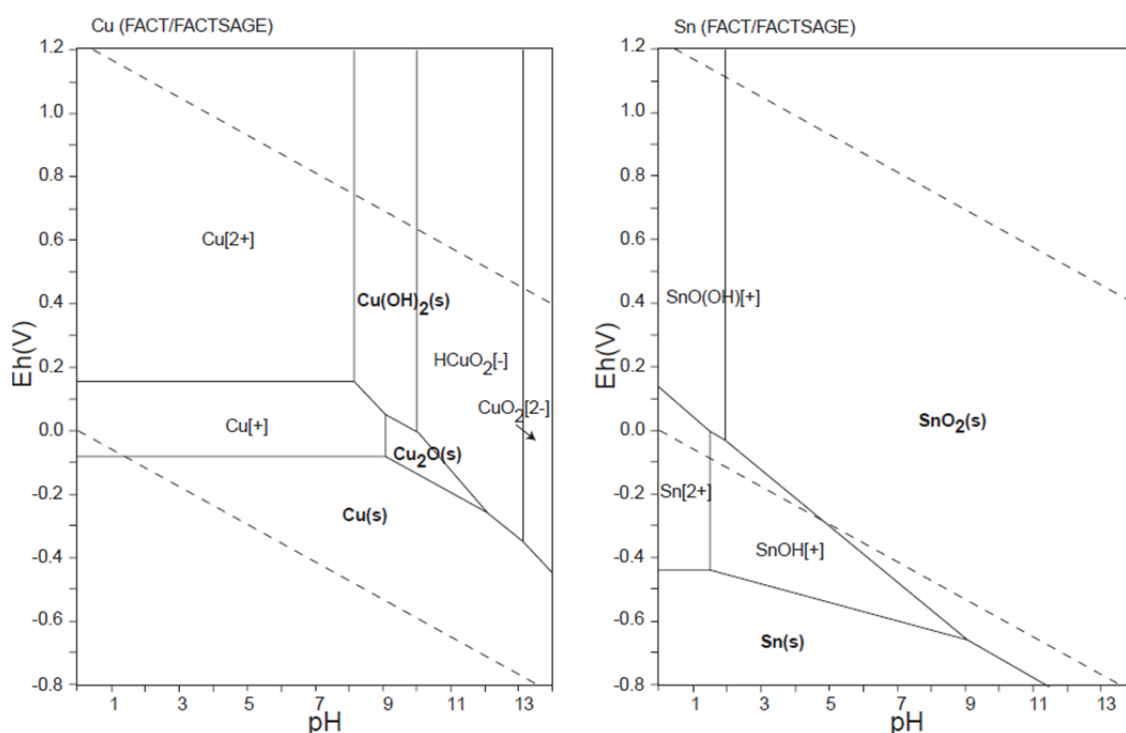
Figure 2-3 Pourbaix diagram of the Cu-O-H and the Sn-O-H system [10].

Cu electrodeposition is feasible in almost all pH ranges as long as the potential is sufficiently negative as shown by the stability of Cu(s) in the bottom right corner of Figure 2-3. The electrodeposition of Sn, on the other hand, is not as straight forward. It can be seen that the precipitation of Sn as SnO_2(s), top right corner of Figure 2-3, can be a major problem for electrolyte systems that have a high pH. This is one of the reasons why it is preferable to deposit Sn and Sn-alloys from acid baths which would minimise the problem of Sn precipitation. This would lead to build up of tin sludge and the need to replenish tin in solution to maintain its concentration, increasing costs.

2.1.2 Standard Electrode Potentials

The equilibrium between a metal and its metal ion in solution is described by the Nernst equation. According to the Nernst equation the equilibrium or reversible potential can be expressed as

$$E_{rev} = E^{\circ} + (\frac{RT}{zF}) \ln Q$$

(2.8)

where E_{rev} is the reversible potential (V), E° is the standard reduction potential (V), R is the universal gas constant $8.315\ J\,K^{-1}\,mol^{-1}$, T is the absolute temperature (K), z is the number of moles of electrons involved in the reaction, F is the Faraday constant ($96,485\ C\,mol^{-1}$), and Q is the reaction quotient. While the reaction quotient is usually expressed in terms of activity, for dilute solutions it is usually expressed in terms of concentration instead.

Table 2-2 lists the standard electrode potentials of selected metals relative to the standard hydrogen electrode (SHE) which by convention is set to zero. As the SHE can be complicated to set up and accurately maintained a more convenient reference electrode that is commonly used is the saturated calomel electrode (SCE). Since the SCE has been used throughout this research, the column on the right in Table 2-2 was created to give an indication of what the standard reduction potentials are on the SCE scale. Note that the conversion is SCE = SHE + 0.241 V.

Half reaction	E° / V vs SHE	E° / V vs SCE
$Ag^+{}_{(aq)} + e^-$ ⇌ $Ag_{(s)}$	0.799	1.020
$Cu^{2+}{}_{(aq)} + 2e^-$ ⇌ $Cu_{(s)}$	0.342	0.583
$Bi^{3+}{}_{(aq)} + 3e^-$ ⇌ $Bi_{(s)}$	0.308	0.549
$Cu^{2+}{}_{(aq)} + e^-$ ⇌ $Cu^+{}_{(aq)}$	0.153	0.394
$Sn^{4+}{}_{(aq)} + 2e^-$ ⇌ $Sn^{2+}{}_{(aq)}$	0.151	0.392
$2H^+ + 2e^-$ ⇌ $H_{2(g)}$	0.00	0.241
$Pb^{2+}{}_{(aq)} + 2e^-$ ⇌ $Pb_{(s)}$	-0.126	0.115
$Sn^{2+}{}_{(aq)} + 2e^-$ ⇌ $Sn_{(s)}$	-0.138	0.103
$2H_2O_{(aq)} + 2e^-$ ⇌ $H_{2(g)} + 2OH^-{}_{(aq)}$	-0.827	-0.586

Table 2-2 Standard electrode potentials of selected electrolyte processes [81].

The electrochemical series gives an indication of the relative ease of which reduction and oxidation for each metal can occur relative to one another. The electrochemical series shown in Table 2-2 is useful as a starting point to determine strategies for depositing metals and metal alloys which would be explained in a later section.

2.1.3   Overpotential deposition

So far we have only discussed reversible equilibrium electrode potentials where there is no net charge or current flow across the electrode-electrolyte interface. In order to drive the equilibrium equation in one direction or the other, a potential above or below the equilibrium potential is applied. In order for electrodeposition to occur we must apply a potential (E) which would shift the electrode potential away from the equilibrium potential (E_{rev}) to drive the deposition process. This driving force for an electrochemical reaction to occur is called the overpotential (η).

$$h = E - E_{rev} = h_{ct} + h_d + h_r + h_c \qquad (2.9)$$

There are four main type of overpotentials; charge transfer (η_{ct}), diffusion (η_d), chemical reaction (η_r), and crystallisation (η_c) overpotentials. In most systems the former two are the first overpotentials which need to be taken into consideration. Other types of

overpotentials such as the nucleation or crystallization overpotentials are also important, but were not intensely examined in this work.

2.2 Kinetics

2.2.1 Charge Transfer Kinetics

Once the electric double layer is fully charged, the charge transfer kinetics will determine the potential at which deposition occurs. Thermodynamic data has provided an indication of which metal would preferably deposit first in the case of alloy deposition. During normal deposition the overpotential would first shift to that of the more noble metal. For example, in the case of Cu-Sn co-deposition thermodynamic data (cf. Table 2-2) indicates that the deposition of copper will occur first followed by the co-deposition of the two metals.

The total current density for a reaction is the sum of the anodic and cathodic currents and can be described by a Butler-Volmer (B-V) type equation

$$j = j_0 \{ \exp(\frac{anF}{RT} h_s) - \exp(-\frac{(1-a)nF}{RT} h_s) \}$$ (2.10)

Where j is the current exchange density, α is the transfer coefficient, n is charge transfer valency, and η_s is the overpotential. The former exponential term described the anodic reaction while the latter describes the cathodic reaction.

For electrodeposition at high negative over potentials the B-V equation is often expressed in the Tafel form:

$$\log \left| \frac{j}{j_0} \right| = -\frac{(1-a)nF}{RT} h_s$$ (2.11)

Where $\eta_s = E_{applied} - E_{rev}$. The plot of log j vs. η is known as the Tafel plot and is useful in evaluating kinetic parameters [80]. By comparing the slopes of the Tafel plot we can comparing the relative kinetics of different metals.

2.2.2   Metal Nucleation

Electrocrystallisation is an electrochemical process describing the nucleation and deposition of the metallic layer on the surface. The overall process of deposition will take place on a single crystal surface through one of two mechanisms, Figure 2-4 (a) and Figure 2-4(b) [32].

In mechanism (a), discharge of ions from the outer Helmholtz plane takes place to give an ad-atom. This ad-atom retains some partial charge and solvation but is confined to the surface. Some ions may be far more mobile than the completely discharged species, and can diffuse rapidly to a step site. The surface gradually forms by extension of the steps. In mechanism (b), there is discharge of the ion directly at the step or kink sites themselves. There is no ad-atom formation or surface diffusion occurring. An additive such as surfactants adsorbs to the surface and can have a great influence on metal nucleation and the final deposit morphology.
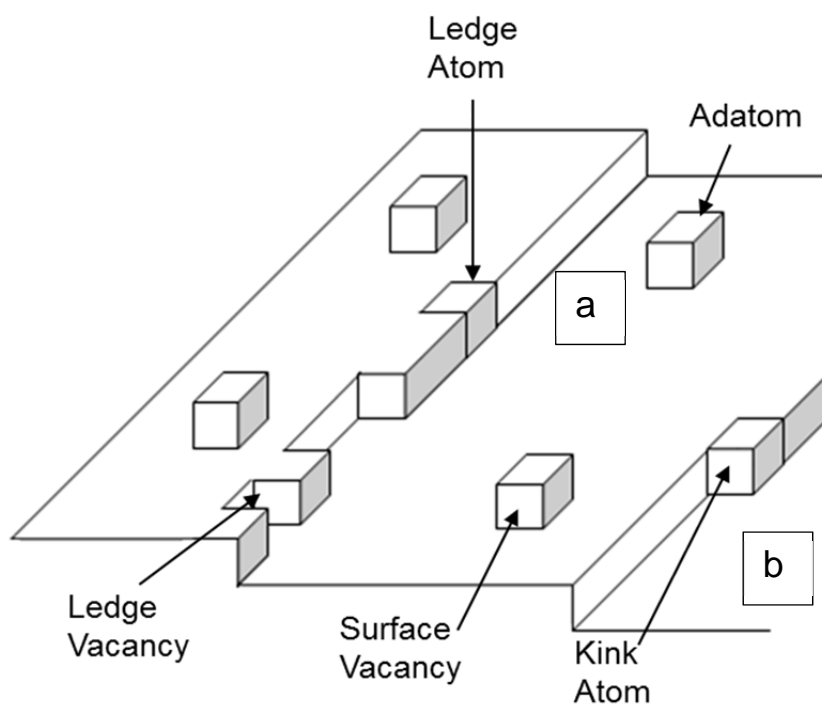
Figure 2-4 Nucleation mechanisms a) discharge of an ad-atom followed by surface diffusion and b) direct discharge at a vacant lattice site [32].

2.3 Mass Transfer

In order for metal deposition to occur the metal ions in the solution have to travel from the bulk electrolyte towards the electrode surface. This mass transport involves the movement of electrochemical species by three methods:

2.3.1 Migration

Migration is the movement of charged species due to the potential gradient and is the mechanism which charge passes through the electrolyte. Migration plays a role in the bulk electrolyte. However, this mode of mass transport often plays only a minor role for the electroactive species of interest. Migration forces are purely electrostatic and hence the charge can be carried out by any ionic species in the solution. The migration flux towards the electrode is usually provided by the supporting electrolyte.

2.3.2 Convection

Convection is the movement of reactants which occur when there is mechanical force acting on the solution. Convection can be divided into natural and forced convection. Natural convection, as its name suggests, occurs in all electrolytes due to natural thermal gradients caused by density differences within the electrolyte solution. This type of convection is generally undesirable as it is random and difficult to predict. Forced convection is achieved by perturbing the solution such as through the pumping or stirring of the solution. In systems such as the rotating disk electrode (RDE), forced convection is well defined and modelled which is one of the main benefits of using such a system.

When a current is applied the concentration of the electroactive species near the electrode starts to decrease from its initial bulk concentration (C_0). Figure 2-5 shows the relationship between the concentration and the distance from the electrode surface, also known as the concentration profile. It can be seen that as time passes, the concentration near the surface gradually decreases to zero (from C_0 à C_s à $C_s=0$).This creates what is called a Nernst diffusion layer or concentration depletion layer. As time passes this layer grows outward in size and can form what is called a stagnant diffusion layer (δ_d). Inside this layer the concentration gradually decreases to zero while outside this layer, moving further away from the surface, the concentration is the bulk concentration which does not significantly fluctuate.
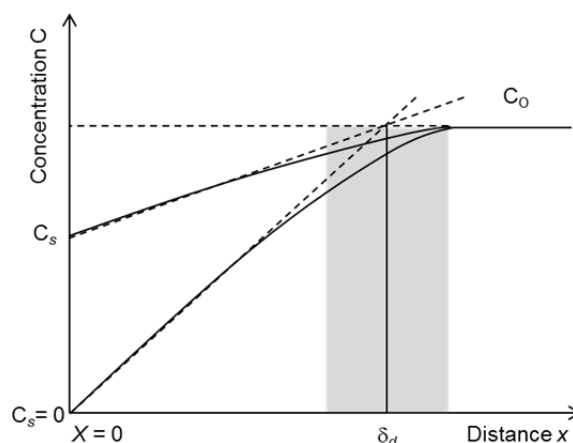
Figure 2-5 Concentration profile showing the evolution of a concentration depletion layer as a function of distance from electrode surface [80].

The rate of metal deposition can be controlled by changing how fast electroactive species move towards the electrode surface. Systems with a large diffusion layer will take longer for the metal ions to cross this layer and deposit at the electrode surface. On the other hand, systems with a small diffusion layer will bring metal ions to the surface faster, increasing the overall deposition rate. Manipulation of the diffusion layer can be controlled by using forced convection, such as an RDE, which will pull the electrolyte towards the electrode surface changing the concentration profile through both convection and diffusion.

2.3.3   Diffusion

Diffusion occurs when there is uneven concentration distribution in the solution and reactants travel down this concentration gradient towards the electrode surface. During normal electroplating the thickness of the diffusion layer can be estimated as a function of time from Equation 2.12.

$$\delta = \sqrt{Dt}$$
$$t = \delta^2 / D$$

(2.12)

Where δ is the diffusion layer thickness, D is the diffusion coefficient, and t is the transition time it takes for surface concentration of the species to reach zero. For example, Cu^{2+} in MSA electrolytes has a diffusion coefficient of 6.5 x 10^{-6} cm^2s^{-1}, and assuming a 50 µm diffusion layer, the transition time would be approximately 3.8 s.

2.4 Alloy Co-deposition Strategy

The main strategies that can be used to modify the reduction potential of metals include:

- Thermodynamics – shifting metal reduction potentials
- Kinetics – changing the kinetics of one metal vs. another
- Nucleation – additive adsorption to the surface influences metal deposition

Thermodynamic control

When two metals are being co-deposited, we can express their reduction potentials as

$$E_1 = E_1^0 + (\frac{RT}{nF})\ln c_{Pb^{2+}}$$

$$E_2 = E_2^0 + (\frac{RT}{nF})\ln c_{Sn^{2+}}$$

(2.13-2.14)

For systems such as Pb-Sn, E_1^0 and E_2^0 are similar, hence the other parameters do not necessary need to be adjusted for co-deposition to occur. For systems such as Cu-Sn, which have very different E_1^0 and E_2^0, modifications to the concentration (c) need to be carried out. It can be seen that by adjusting the concentration of one metal species while keeping the other constant, one can shift the metal reduction potentials of Cu and Sn closer together, facilitating its co-deposition

In order to understand why some tin alloys such as lead-tin (Pb-Sn) are relatively easier to co-deposit from a single bath one must first observe the deposition potential of both metals. The standard reduction potentials (vs. SHE) of copper, lead, and tin are:

$$Cu^{2+} + 2e^- \rightarrow Cu \qquad 0.583V$$
$$Pb^{2+} + 2e^- \rightarrow Pb \qquad 0.103V \qquad (2.15\text{-}2.17)$$
$$Sn^{2+} + 2e^- \rightarrow Sn \qquad 0.115V$$
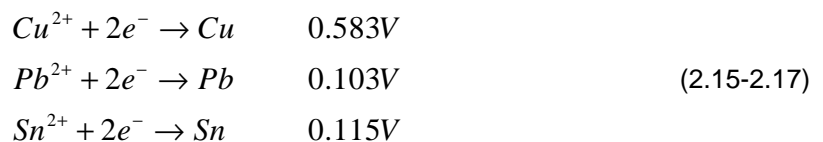
The reduction potentials of lead and tin are approximately 12 mV apart while for copper and tin the difference is 468 mV. Based on this information the deposition of a Cu-Sn alloy does not initially seem possible as when both metal ions are present in the solution the deposition of the more noble metal, copper, would be preferentially carried out.

A possible solution to this problem that has been proposed by other researchers [32] for alloys such as Cu-Co and Cu-Ni which involves maintaining the more noble metal at a relatively lower concentration in the electrolyte. According to the Nernst Equation 2.13-2.14 altering the concentration can result in a change of the reduction potential. This basic strategy is usually employed in order to shift the reduction potentials of individual metals closer together to facilitate co-deposition. This research has shown that by employing the same strategy and using a 1:10 ratio of Cu^{2+}:Sn^{2+} concentration in the electrolyte, Cu-Sn co-deposition could be readily achieved.

Kinetic control

In the case of Cu and Ni, where the deposition of the two metals is independent of each other, the total deposition rate is the sum of all the partial current densities , therefore, $i_{total} = i_{Cu} + i_{Ni}$. Under normal deposition conditions the first layer on the electrode surface would always be a layer of Cu followed by Ni. Here copper is the more noble metal and it will continue to be plated until its concentration near the electrode surface is depleted. Only then can the co-deposition of Cu and Ni occur.
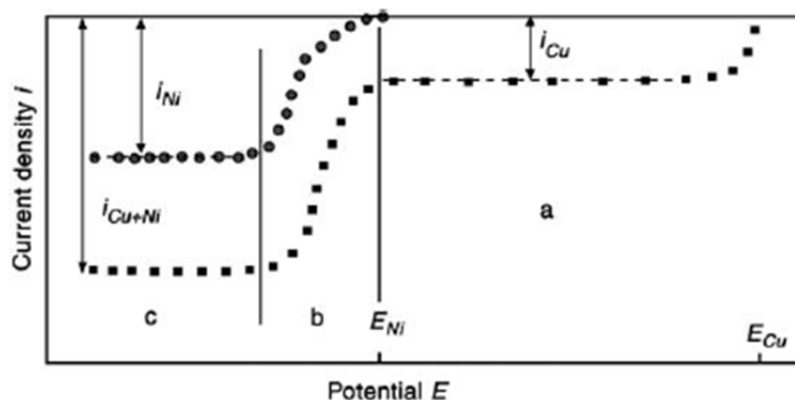
Figure 2-6 Voltammogram of Cu-Ni alloy deposition showing partial currents for Cu and Ni deposition as well as the total deposition current needed to deposit the alloy [82].

According to Brenner's alloy classification, the two main modes of alloy deposition are normal and abnormal. In normal alloy deposition (such as with Cu-Ni) the deposition is as expected according to the E_{rev}. Cu is more noble and has a more positive E_{rev}, therefore it would be expected to deposit first before Ni. Abnormal deposition occurs when the deposition is unexpected or differs from the expected E_{rev}. In this case a less noble metal can deposit such as the preferential deposition of Zn from a Ni-Zn plating bath. While traditionally the Brenner alloy classification has been useful in describing experimental observations, it does not explain the role of charge transfer kinetics and mass transport. A newer approach which better describes alloy deposition was developed by Wagner and Traud and is called the mixed potential theory [82].

In mixed potential theory, alloy deposition can be influenced by manipulating reaction kinetics. Figure 2-7 shows the Evans diagrams for systems with different Tafel slopes. The shaded grey areas are where the less noble metal is preferentially deposited. In this case we would want to decrease the kinetics of the more noble metal A (solid line) compared to metal B in Figure 2-7(a) which is shown by a decrease in the Tafel slope shown in Figure 2-7(b). It can be seen that the reduction potential region in which the less noble metal can deposit has greatly increased. The kinetics and be controlled by the addition of some additives which may bind stronger to the more noble metal which in turn changes its kinetics. This gives the less noble metal which does not bind to the additive as well a chance to deposit more.
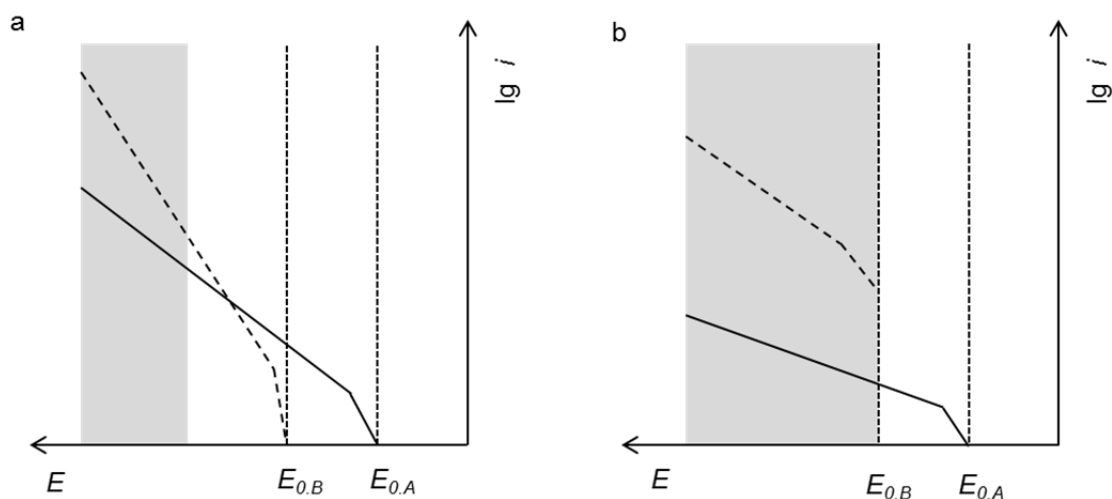
Figure 2-7 Partial current potential diagrams showing systems where (a) A and B are kinetically controlled with different Tafel slope, similar exchange current density and (b) A and B are kinetically controlled with different Tafel slopes and exchange current densities [82].

43

Nucleation control

Additives such as Fluorosurfactants have been shown to absorb on electrode surfaces and suppress hydrogen evolution [52, 53, 83]. At certain electrode potentials they may also cover the electrode surface and block the deposition of specific metal ions. It may be the case that the more noble metal can be suppressed from depositing on the electrode surface. Once the over potential is high enough the less noble metal may deposit and at this stage the co-deposition of both metals can occur.

2.5   Alloy plating – Direct Current

Potentiostatic (constant potential) deposition is not the preferred method to deposit alloys as during co-deposition of alloys with reversible potentials that are considerably far apart there will be a shift in potential during metal deposition. Therefore, galvanostatic (constant current) is commonly used in industry.

During direct current (DC) plating, when the charge is applied it will initially be consumed to charge the double layer. In this stage a very small or zero amount of deposition actually occurs. However since this capacitive charging step is relatively fast the charge lost is negligible and the majority of the charge would go into driving the charge transfer reaction. The time it takes for the concentration of a metal at the electrode surface to reach zero is referred to as the transition time. It should be noted that this is the series of events that occur during normal electrodeposition where the current is applied to the system and left on constantly for the required amount of time to plate the necessary deposit thickness.

However, in pulse plating (PP) the current is continually switched on and off. This means that overpotentials are virtually fixed and only one electrochemical reaction can occur during the on time. There is not enough time for the system to switch between different potentials and so it can be hard to control what is actually depositing when pulse plating is carried out in potentiostatic mode. Therefore, as with DC, galvanostatic deposition is the preferred method.

2.6   Alloy plating – Pulse Current

When applying a charge using a pulse plating technique there is a significant difference on how the charge is being consumed to deposit the metals. As the peak current is applied the current is initially divided into two processes. The first charges the double layer and is denoted the capacitive current (non-Faradaic). In the second step the charge is consumed to drive the charge transfer reaction (Faradaic). It has been found that a minimum time required to charge the double layer is approximately 0.1 to 1ms [84]. Therefore, this is the minimum amount of time that can be set for the pulse on time. Longer deposition times would negate the benefits of PP and are generally avoided.

Figure 2-8 shows a typical waveform of a pulse plating (PP) experiment. The important parameters include:

1) Peak/ average current density (i_p/ i_{avg})

2) Pulse period ($T_{total} = t_{on}/ t_{off}$)

3) Duty cycle ($\theta = t_{on}/ T_{total}$)

As its name implies, during pulse plating (PP) the current is continually switched on and off. Therefore, the actual plating time is dependent on the total time the current is switched on during each pulse cycle. This is commonly referred to as the duty cycle which is a fraction of the pulse on time versus total pulse time. The average current throughout the plating experiment can be calculated by multiplying the peak current with the duty cycle.
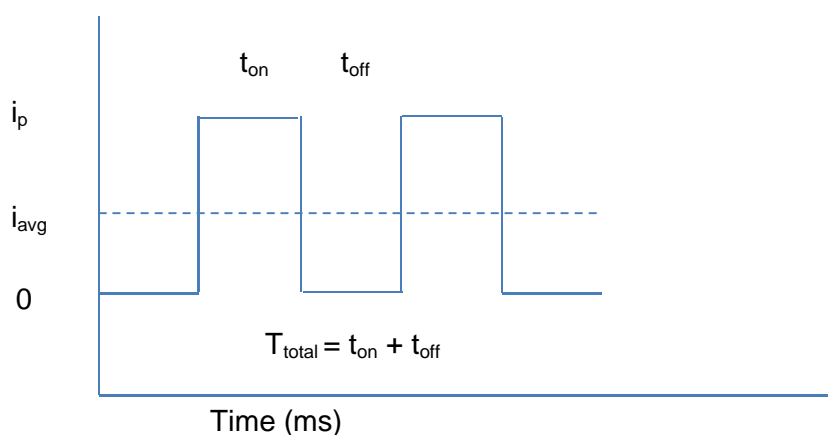
Figure 2-8 Simple pulse plating waveform.

In order to be able to compare the deposit microstructure between DC and PP deposits, the average pulse plating rate is equal to the applied current densities during DC plating. However, in PP the combination of different peak current densities, plating period, and duty cycle can combine to create a very large experimental matrix with many experiments to carry out. This would have greatly increased the amount of samples and time spent analysing the results. It was decided that only two pulse periods (10 and 100 ms) and two duty cycles (0.2 and 0.5) would be studied. Peak current densities in the range of 40-150 mA cm^{-2} (8-30 mA cm^{-2} average current densities) were applied for durations of 20-50 minutes.

The pulse plating limiting current density can be calculated from Equation 2.18 [84].

$$\frac{i_{L,PP}}{i_{L.DC}} = \frac{1 + 2(\frac{i_p}{i_{L,DC}})t_T^* \cdot \sum_{m=1}^{\infty} \frac{\exp(l_m(1-q))-1}{l_m[\exp(l_m)-1]}}{1 - 2t_T^* \cdot \sum_{m=1}^{\infty} \frac{\exp(l_m(1-q))-1}{l_m[\exp(l_m)-1]}} \qquad (2.18)$$

Equation 2.18 allows us to compare the pulse limiting current densities ($i_{L,PP}$) to that of DC limiting current densities ($i_{L,DC}$). The above equation contains two dimensionless terms; t_T^* is the dimensionless pulse period ($t_T^* = D/\delta^2$) and λ_m is the dimensionless summation parameter. For unipolar pulses (no reverse pulses) the peak current (i_p) is set to zero. The second term of the denominator contains the term (1-θ) which allows us to assess the extra material brought to the electrode surface during the off-time. For example, solving for Equation 2.18, it was found that for Cu $i_{L,DC}$ = 3.9 mA cm^{-2}, $i_{L,PP}$ was estimated to be 5.0 mA cm^{-2}; assuming θ = 0.2 and δ = 50 µm.

The influence of short current pulses nucleation and crystallization is a well described phenomenon [84]. PP can favour the formation of new nucleation sites rather than the growth of existing crystals which can lead to grain refinement in the deposit. In comparison, in DC plating it is usually organic additives that are used to provide grain refining and levelling effects. In PP deposits such additives may not be required.

3. EXPERIMENTAL

This chapter describes the experimental apparatus and procedures involved during the three main stages of the research project: electrolyte optimisation study, electrochemical characterization, and electrodeposition experiments. In the first stage, the feasibility of co-depositing copper and tin from a single MSA-based electrolyte was determined. A rotating cylinder Hull (RCH) cell was employed for this purpose. The effects of bath additives on the microstructure and metal content in the deposit were also established. The aim at this stage was to formulate an electrolyte which gave the best deposits that will be used for the remainder of the research project.

After a suitable electrolyte composition was chosen, experiments were carried out to study the electrochemistry of the system in order to better understand and attempt to control the deposition process. This second stage of the research involved the use of a rotating disc electrode (RDE). Parameters such as the deposition potential, limiting current density, and current efficiency of the individual metals and alloys were examined. The aim of these electrochemical experiments was to deduce the appropriate current density range required for alloy co-deposition.

The final stage of the research project involves the actual deposition of the Cu-Sn alloy. Deposition was carried out on an electrode vertically placed in a stagnant solution. Both direct and pulse currents were used to determine which electrodeposition method resulted in better deposit microstructure.

3.1 Electrolytes

Low and Walsh [78] were able to study Cu-Sn alloy deposition from a relatively simple MSA-based electrolyte with only two types of additives; an antioxidant and a surfactant. One of the goals of this research is to determine whether such a simple electrolyte would be able to provide good quality deposits. During initial RCH experiments it was found that a minimum of approximately 0.02 M $CuSO_4$ had to be added to the solution otherwise very thin and uneven deposits were obtained on the cylinder electrodes. For simplicity, the amount of Sn:Cu salt added to the bath was fixed at a ratio of 10:1. This high Sn:Cu metal salt ratio in the electrolyte was used in attempt to determine if this strategy would also lead to a high Sn:Cu ratio in the deposit. However, it was later found that the maximum solubility of tin salt in this specific MSA-based solution at room

temperature was actually around 0.15 M SnSO$_4$. Therefore, the copper and tin concentrations used were later slightly adjusted to 0.015 M and 0.15 M, respectively.

Table 3-1 lists the various analytical grade chemical reagents used to prepare electrolytes for Cu-Sn electroplating. pH and conductivity measurements were taken at 25 ^{O}C with a Mettler Toledo SevenMulti™ meter.

Composition	Concentration		Function
	(M)	(g L^{-1})	
Copper(II) sulfate (CuSO$_4$·5H$_2$O)	0.015 – 0.02	4 – 5	Source of Cu^{2+} ions
Tin(II) sulfate (SnSO$_4$)	0.15 – 0.2	33 – 43	Source of Sn^{2+} ions
Hydroquinone (C$_6$H$_4$(OH)$_2$)	0.01	1	Antioxidant
Methanesulfonic acid (70%) (CH$_3$SO$_3$H)	2.00	192	Supporting electrolyte
Fluorosurfactant (DuPont™ Zonyl® FSN)	0.01 %vol (30-60 µL / experiment)		Wetting agent
density	1.35 x 10^3 g L^{-1}		
kinematic viscosity	1.00 x 10^{-2} cm^2 s^{-1} [85]		
pH	1.17 ± 0.02		
conductivity	389 ± 1 mS cm^{-1}		
temperature	25°C		

Table 3-1 Electrolyte compositions and operating conditions in this research.

Electrolyte Preparation

A typical experiment involved the preparation of 300-600 mL of electrolyte. This was done in three main steps. The first involved pouring 70% MSA into a beaker of de-ionized water. The mixing of acid and water is an exothermic reaction which increased the temperature of the solution to approximately 30°C. In the second step this MSA solution was poured into a separate beaker which contained copper sulfate, tin sulfate, and hydroquinone. The solution was then stirred for approximately 10 minutes to obtain a homogeneous mixture. Only after the solution was properly mixed is the surfactant added. The surfactant was added in the final step because prolonged agitation of the solution containing surfactant can cause excessive froth formation. Experiments were

added. The surfactant was added in the final step because prolonged agitation of the solution containing surfactant can cause excessive froth formation. Experiments were usually carried out when the solution was left to cool to room temperature (25°C). Although hydroquinone was added to suppress oxidation of divalent tin (Sn^{2+}) to tetravalent tin (Sn^{4+}), acidic tin plating baths still exhibit cloudiness due to small amounts of Sn^{4+} formation. These finely dispersed colloidal particles usually do not interfere with electroplating and normally precipitate out of the solution [1]. They can then be removed either through decantation or filtration.

3.2 Electrolyte Optimisation

The classical Hull cell (HC) [86] is a standard experimental apparatus which allows one to observe the effect of current density on the deposit composition and microstructure. It is the instrument metal platers use in research and development to determine the performance of a plating process. This preliminary feasibility study is aimed to prevent potential problems arising from the plating solution itself before mass production in an assembly line can occur. For example, the concentration of primary bath components (metal salts and electrolyte), concentration of additives, lowest current density in which metals can be plated (covering power), and distribution of metal across the surface (throwing power) [87] is usually determined using an HC in laboratories before they are scaled up for production.
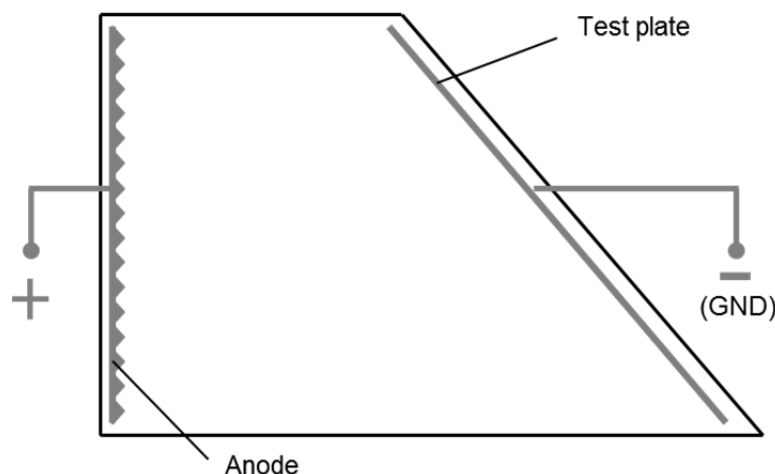
Figure 3-1 Trapezoidal shape of a classical Hull cell.

In the classical HC, as shown in Figure 3-1, the cathode test plate is placed at a slanting angle with respect to the anode. As one moves from the top to the bottom of the cell, the distance between the anode and cathode increases from one end to the other. The distance the current lines have to travel at the top of the cell is shorter leading to a higher current density. The opposite is true at the bottom of the cell where the current lines have to travel a longer distance resulting in a relatively lower current density. This means that for a single applied cell potential a wide range of current densities can, therefore, be obtained and studied in a single experiment [88]. However, due to the trapezoidal geometry of the cell, controlled mass transport conditions cannot be achieved through solution agitation.

3.2.1 Assessment of Electrolyte

More recently, a modified version of the Hull cell, a rotating cylinder Hull cell (RCH) [74], has been developed. Although the basic shape of the RCH is different from that of an HC, the RCH was designed to mimic the current distribution of the HC and this similarity was the basis of the nomenclature of this type of cell. The RCH was used because it allows one to effectively control mass transfer which was not possible with a classical HC. As with the HC, the RCH creates a non-uniform current distribution along the length of the cathode allowing the electroplating of different alloy compositions at various positions along the cylinder cathode. This is due to the varying distance that the current lines have to cover to reach the counter electrode, giving rise to differing ohmic drop in the solution. Figure 3-2 shows a schematic of the RCH instrument used in this research; the HT Rota-Hull (EcoChemie).
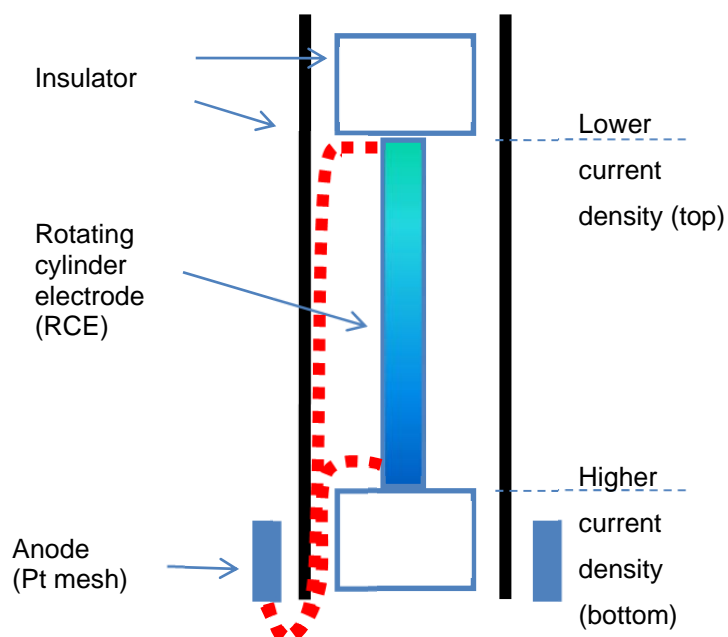
Figure 3-2   Side view schematic of the RCH. The dotted lines (▪ ▪ ▪) denotes varying distance the current lines have to travel between the electrodes.

The RCH is composed of a rotating cylinder electrode (cathode), surrounded by a stationary platinum mesh counter electrode (anode). The cathode cylinder is made of brass (Cu-Zn) with a diameter of 0.6 cm and length of 8.0 cm (active surface area of 15.1 cm^2) fitted to a rotating motor at the top. A concentric insulating wall around the inner cathode is a cylinder made of plexiglass with a diameter of 5.0 cm and height of 15.0 cm. In order to start the experiment the setup shown in Figure 3-2 was immersed in a cylindrical glass cell filled with electrolyte. The normal operating volume is 600 mL which is the amount needed for the cylinder electrode to be fully immersed in the electrolyte. For consistency the rotation speed and deposition time in our experiments were fixed at 400 rev min^{-1} and 600s, respectively.

The theoretical relationship between the average current density applied and the local current density at various positions along the cylinder cathode of the RCH is described in Equation (3.1) [89].

$$\frac{i_{(x/h)}}{i_{ave}} = \frac{0.535 - 0.458(x/h)}{[0.0233 + (x/h)^2]^{0.5}} + 8.52 \times 10^{-5} \times \exp[7.17(x/h)] \qquad (3.1)$$

Where   h   =   length of the cathode

   x / h   =   dimensionless distance along the cathode

   x / h   =   0   corresponds to the position of *highest* current density

   x / h   =   1   corresponds to the position of *lowest* current density

   $i_{(x/h)}$ =   local current density (mA cm^{-2})

   i_{ave} =   average current density applied to the cell (mA cm^{-2})

Figure 3-3 shows a schematic of the cylinder electrode and the section numbering scheme. The ratio of local current density compared to the average applied current density can then be theoretically calculated from Equation 3.1 and is summarised in Table 3-2. In this example, the applied current density to the RCH was 4.7 mA cm^{-2}, but a wide range of local current densities was established starting from 0.85 mA cm^{-2} up to 13.6 mA cm^{-2}. The procedure for selecting the applied current will be described in a following section.
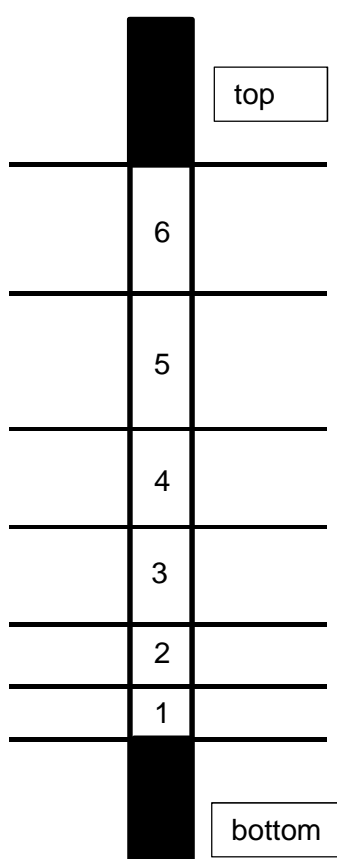
Figure 3-3 Schematic of the cylinder electrode showing section numbers.

Cylinder section	Distance (cm)	$i_{(x/h)}/i_{ave}$	$i_{(x/h)}$ (mA cm^{-2})
1	0.7	2.80	13.16
2	1.5	1.86	8.74
3	2.7	1.03	4.84
4	4.0	0.59	2.77
5	5.8	0.27	1.27
6	7.6	0.18	0.85

Table 3-2 The relationship between the distance along the cylinder electrode and the local current density, $i_{(x/h)}$. The applied current density, i_{ave}, was 4.7 mA cm^{-2}. The solution contained 0.02 M $CuSO_4$, 0.2 M $SnSO_4$, hydroquinone and fluorosurfactant.

Before the start of each experiment, the surface of the cylinder electrodes was marked with lacquer dots. The lacquer was allowed to dry for approximately 10 min. before the cylinder electrode is mounted in the RCH instrument. At the end of each experiment the lacquer dots were removed by washing with acetone. As shown in Figure 3-4, no deposits were plated on the small spots covered by the lacquer. The removal of the lacquer creates small "holes" and the sides of these holes can be used to roughly determine the thickness of the deposits. A profilometer (Dektak) was then run along the whole length of the cylinder to determine the thickness of the deposits at various points. These markings also serve a secondary purpose which is to allow identification of cutting points for cylinder sectioning.

"holes" after lacquer removal
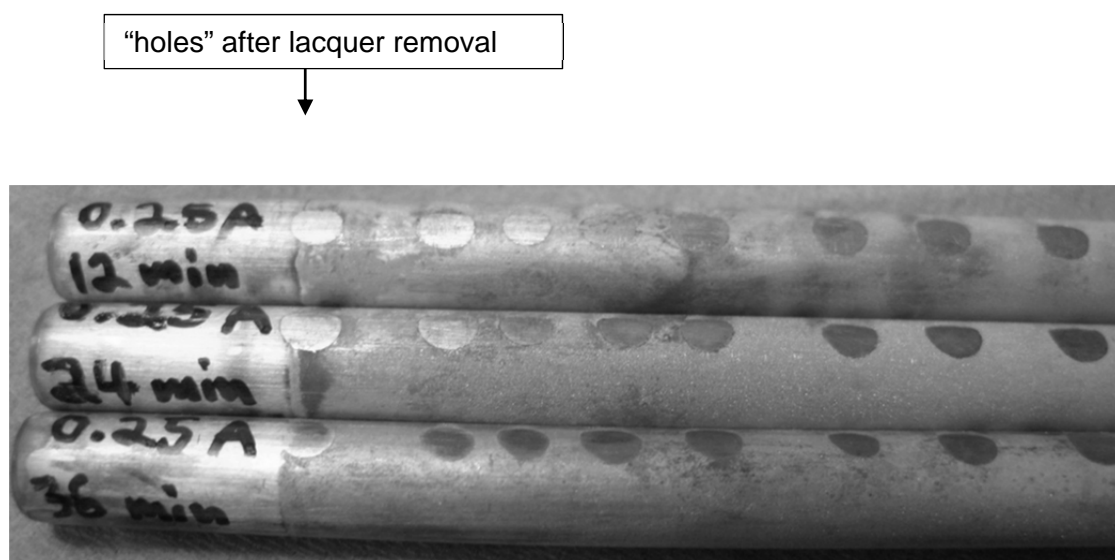
Figure 3-4 After electroplating is completed, markings due to lacquer removal can be used to determine the deposit thickness and mark positions or cylinder sectioning.

The cylinder electrodes were cut into various sections according to the Rota-Hull measuring block found in Figure 3-5. The individual cylinder sections were then mounted in epoxy resin in order to be examined under a microscope. The cross-sections were wet polished by using various successively smoother grade silicon carbide (SiC) sanding paper (1200 -> 2400 -> 4000 grit) while being rinsed with 5% Nital solution (5% nitric acid, 95% ethanol v/v) for 5 s between each grit. The 5% Nital etch was used to expose the cross-section so that it can be better seen. Looking at the cross-section one can also determine the thickness of the deposits in this manner (the thickness of the deposit "ring" surrounding the electrode in the middle). The surface microstructure of each section was studied under a scanning electron microscope

equipped with an energy dispersive X-ray detector which was used to determine the composition of the deposits.

Figure 3-5 Rota-Hull measuring block used to mark positions where the cylinder electrode should be sectioned. The numbers denote $i_{(x/h)}/i_{ave}$ ratios.

As shown in Figure 3-5, quick visual inspection of the deposit can be made and an optimal current density range which results in good quality deposits can be determined. The numbers on the scale are $i_{(x/h)}/i_{ave}$ ratios and their values were calculated from Equation 3.1. At the bottommost position labelled 3 on the measuring block, the local current density is three times the applied current density. At the other end of the scale, at the position labelled 0.11, the local current density is 0.11 times the applied current density.

Degassing of the plating solution

A set of experiments were carried out to determine whether the presence of dissolved oxygen in the plating solution was the cause of the formation of metal oxides in the deposits. Selected electrolyte solutions were degassed with nitrogen for 1 hour prior to

plating while other "normal" plating solutions were not. The deposits obtained from both plating baths were analysed and their elemental compositions compared.

3.2.2 Current Efficiency

The current efficiency was obtained by weighing the cylinder electrode before and after each set of experiments to ascertain the weight of the deposit. The deposit mass obtained was then compared to the theoretical mass that should have been obtained in the case of 100% current efficiency. Equation 3.2 shows that the weight of the deposit is directly proportional to the current applied according to Faraday's law

$$Q = it = \frac{zFW}{M}$$ (3.2)

Where   Q = total charge passed (C)

i = applied current (A)

t = time the current was passed (s)

z = number of electrons involved

F = Faraday constant (96,485 C mol^{-1})

W = weight of the deposit (g)

M = atomic weight of the deposits (g mol^{-1})

As different local current densities are observed along the length of the cathode, different amounts of deposits (local weight and thickness) are also expected at different points. For simplicity, approximations were made as if the cathode was a single piece of homogenous substrate; the atomic weight of the Cu-Sn alloy was approximated to be 91.12 g mol^{-1}, corresponding to an average between that of pure copper (63.54 g mol^{-1}) and that of pure tin (118.69 g mol^{-1}). This approximation had to be carried out as determining the current efficiency at specific points or the current efficiency of each cylinder section was not feasible and could not be reliably determined due to the fact that the weight of the deposits of each cylinder section was very small. The total weight gained due to the deposits was approximately 10 mg.

3.2.3   Choice of Applied Current

The current applied to the RCH was selected by considering the mass transfer limiting current for each metal and Equation 3.3 was used to calculate the limiting current density at the RCH [90].

$$i_{L,RCH} = 0.079 z F c_b d^{-0.3} U^{0.70} \nu^{-0.344} D^{0.644} \tag{3.3}$$

Where $i_{L,RCH}$ =   RCH limiting current density (A cm^{-2}),

   z =   number of electrons in the electrode process,

   F =   Faraday constant (96,485 C mol^{-1}),

   c_b =   bulk concentration of the electroactive species (mol cm^{-3}),

   d =   diameter of the RCE (cm),

   U =   peripheral velocity of the RCE (cm s^{-1}),

   ν =   kinematic viscosity of the electrolyte (cm^2 s^{-1}), and

   D =   diffusion coefficient of the electroactive species (cm^2 s^{-1}).

As the kinematic viscosity of MSA-based electrolytes have not been widely reported in literature, the value used for this calculation, 1.0 x 10^{-2} cm^2 s^{-1}, was initially taken from a study by Low and Walsh concerning the electrodeposition of tin from a methanesulfonic acid bath [85]. The diffusion coefficient of Cu^{2+} and Sn^{2+} ions were assumed to be similar at approximately 7.0 x 10^{-6} cm^2 s^{-1} [91]. The electrolytes used for RCH experiments contained 0.02 M CuSO$_4$ and 0.2 M SnSO$_4$ which corresponds to a limiting current of 4.7 and 47.4 mA cm^{-2}, respectively. The total maximum current that can be applied, assuming that there are no side reactions, is a summation of the partial currents, i.e. 52.1 mA cm^{-2}. In our RCH experiments the applied current was set as the limiting current of copper, 4.7 mA cm^{-2}. This was chosen as the local current density range obtained (0.85 – 13.16 mA cm^{-2}) covers a range below and above the limiting current density of copper.

3.3 Electrochemical Characterisation

Electroanalytical experiments were carried out in a 300 mL cell using a typical three-electrode setup, a schematic of which can be seen in Figure 3-6. The working electrode was a gold tipped rotating disc electrode (RDE) (0.1 cm radius, 0.031 cm^2 surface area) encapsulated in a PTFE holder. A platinum mesh was used as a counter electrode and a saturated calomel electrode (SCE) ($Hg|Hg_2Cl_2$) reference electrode was connected to the electrochemical cell via a Luggin capillary probe placed approximately 0.5 cm from the RDE surface. In order to clean the RDE surface between each experimental run, the RDE was wet polished with 4000 grit SiC paper, etched in 5% Nital solution for 5 s, and then ultrasonically cleaned in deionized water.
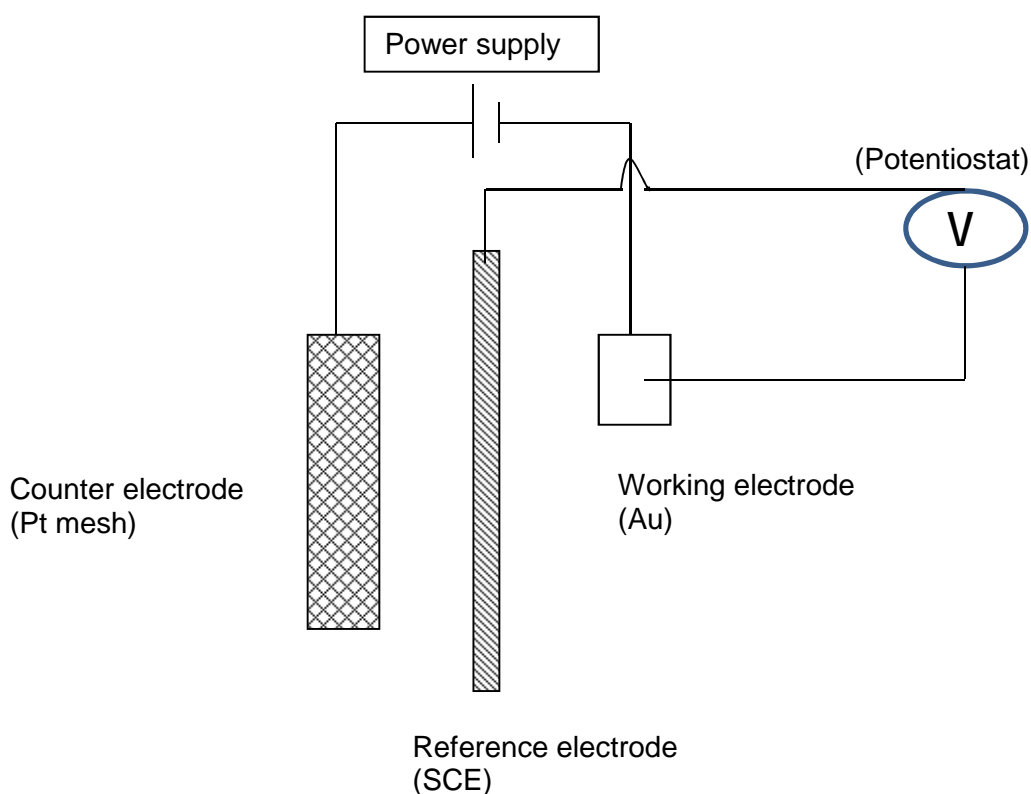
Figure 3-6 Schematic of the three-electrode setup used in electrochemical characterization experiments involving rotating disc electrodes.

The RDE unit (Radiometer, EDI101) was connected to and controlled by a speed control unit (Radiometer, CTV101) which was used to adjust and read the rotation speed with an accuracy of ± 2 rpm. The rotation speeds used in these experiments were between 100 and 2,000 rpm.

Correction of deposition potential

Currents flowing through the electrochemical cell can cause a potential drop in the electrolyte. This potential drop is called Ohmic or i-R drop. The supporting electrolyte, in this case methanesulfonic acid, primarily serves to minimize this i-R drop. In order to minimize this error supporting electrolyte with high conductivity such as MSA is preferred. In the three electrode cell the i-R drop occurs between the working electrode and the reference electrode. Therefore, the reference electrode has to be brought as close to the working electrode as possible. Experimental procedures were suggested to eliminate the i-R drop by using what is known as a Luggin capillary, the tip of which is positioned very close to the working electrode surface. In this research this distance is approximately 0.5 cm. This arrangement leaves only a small uncompensated solution resistance determined by the distance between the electrode surface and capillary tip.

3.3.1 Cyclic Voltammetry

Cyclic voltammetry (CV) was used to determine the different onset potentials at which individual metals started to deposit, when alloy co-deposition occurred, and when significant hydrogen evolution commenced. CV is also a very useful technique as surface processes such as adsorption/desorption and the formation of oxide layers can be studied.

Experiments were carried out using an EcoChemie Autolab potentiostat (μAutolab II) controlled with the NOVA 1.7 software package. The potential window examined was between -0.60 to 0.60 V vs. SCE with a scan rate of 50 mV s^{-1}. The open circuit potential (OCP) was determined to be approximately 0.075 V. Since this value is relatively close to zero and no electrochemical reactions in the MSA electrolyte occur near this potential region, all experiments were carried out with 0.0 V as the starting potential.

Figure 3-7 shows the waveform of a typical CV experiment carried out in this research. The starting potential was at 0.0 V and in the forward sweep the potential was scanned to V_1. In the forward sweep in this negative potential region the onset deposition potentials of the metals can be determined as well as the limiting current density. In the next step the potential is then scanned in the opposite direction towards V_2. In this

reverse sweep in the positive potential region the deposits are stripped from the RDE surface and the stripping currents can be recorded.
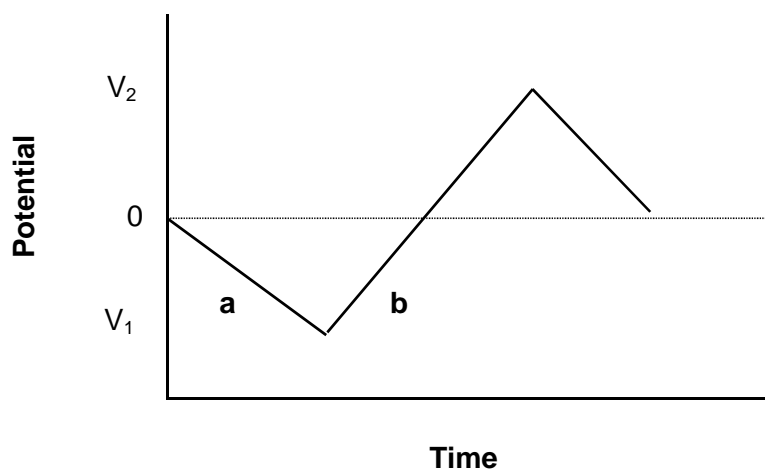
Figure 3-7 Potential-time waveform of a typical cyclic voltammetry experiment. a) is the forward sweep and b) the reverse sweep.

Figure 3-8 is an example of a typical CV plot that is recorded.The onset deposition potential is defined as the potential in which the current density value starts falls below zero. This is referred to as the cathodic current. The initial increase in current is usually followed by a large increase in current density signifying that metal deposition is occurring on the RDE surface. The anodic current or stripping current is defined as the current densities above zero that occur on the reverse scan. The onset deposition potential and the corresponding position of stripping peaks are usually characteristic of different type of metals.

The deposition of metals on the RDE surface only occurs when the potential is great enough to overcome the reversible reduction potential. Once that potential is reached in the scan, the metal deposits on the RDE surface and a current response is observed. The reason that the oxidation or anodic potential is not the same as the reduction potential is because the deposition and stripping of metal ions is not a simple redox process. An extra overpotential is needed to oxidise the metal that has been deposited earlier and therefore the oxidation potential is usually more positive than the reduction potential.
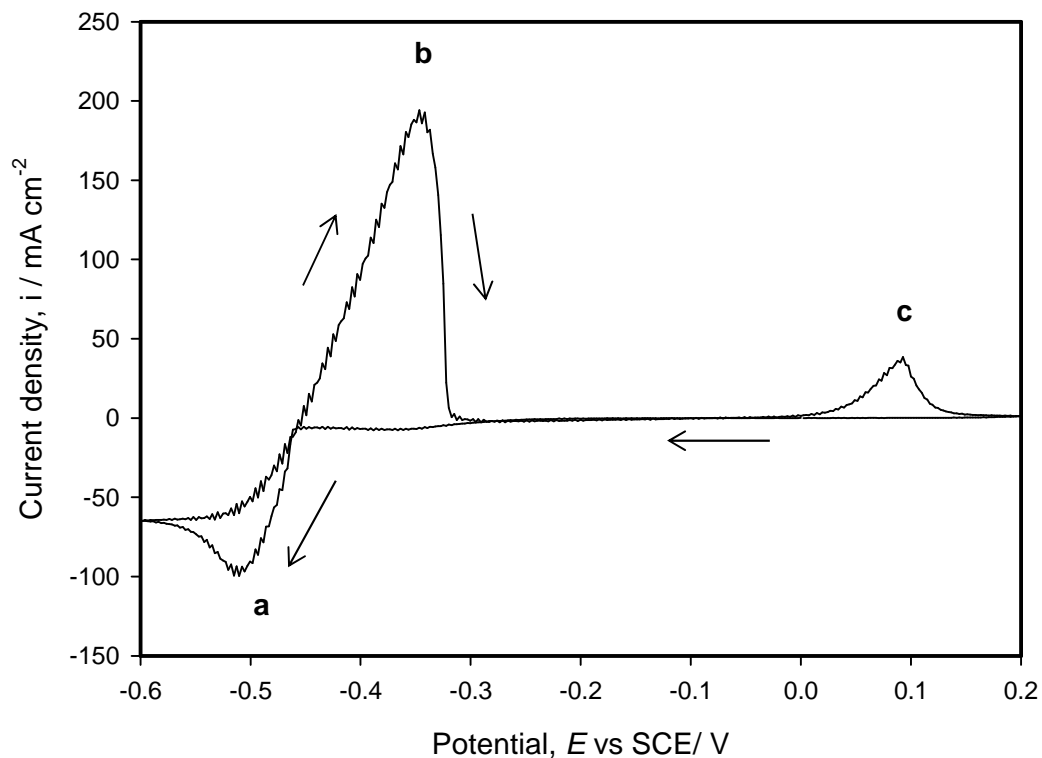
Figure 3-8 A typical cyclic voltammogram (current-potential plot) showing a) deposition peak and two stripping peaks b) and c).

Figure 3-8 is an example of a CV in which the two metals start to co-deposit together on the forward sweep while on the reverse sweep they are stripped from the RDE surface individually giving rise to two stripping peaks. Co-deposition can only occur when their reversible potentials are close to one another otherwise the more noble metal will deposit first followed by a second layer of the less noble metal. The stripping current and corresponding charge consumed for peaks b and c can be compared and the ratio of metals in the alloy can be determined.

The limiting current density at an RDE is given by Equation 3.4 [32].

$$i_{L,RDE} = 0.62 z F C D^{2/3} \nu^{-1/6} \omega^{1/2}$$

(3.4)

Where $i_{L,RDE}$ = RDE limiting current density (A cm^{-2}),

z = number of electrons in the electrode process,

F = Faraday constant (96,485 C mol^{-1}),

C = bulk concentration of the electroactive species (mol cm^{-3}),

D = diffusion coefficient of the electroactive species (cm^2 s^{-1}),

ν = kinematic viscosity of the electrolyte (cm^2 s^{-1}), and

ω = angular velocity (rad s^{-1}).

A literature survey showed that in MSA electrolytes the diffusion coefficient of both copper and tin were roughly of the same magnitude (within 10^{-6} cm^{2}s^{-1}). The variability is due to the fact that the electrolyte compositions are not identical. The metal concentration, diffusion coefficient, and RDE limiting current density are summarized in Table 3-3. The RDE rotation speed was 100 rpm. It can be seen from Equation 3.4 that the limiting current density is directly proportional to the angular velocity which means that higher RDE rotation speeds would lead to higher current densities recorded on a voltammogram.

Metal species	Concentration (M)	Diffusion coefficient (x10^{-6} cm^2 s^{-1})	$i_{L,RDE}$ (mA cm^{-2})
Cu^{2+}	0.015	6.8 [92]	4.5
		7.5 [93]	4.8
Sn^{2+}	0.15	5.4 [47]	38.5
		6.5 [91]	43.6
		8.3 [30]	51.3

Table 3-3 The RDE limiting current density of copper and tin in MSA-based electrolytes.

Diffusion coefficient for Sn in MSA has been widely reported and the value of 6.5 x 10^{-6} cm^{2}s^{-1} was taken to be the average value for Sn.

3.3.2 Chronoamperometry

Chronoamperometry (CA) experiments involve the application of a fixed potential over a period of time while the changes in current density are recorded. Figure 3-9 is an example of a typical CA plot showing two different current responses. A stable current is usually indicative of a stable electrodeposition process. Metal ions are being brought to the electrode surface at a relatively steady rate and good compact deposit growth is expected. On the other hand an increasing current response usually indicates problem with the plating process. The continuous rise in current may be caused by various processes such as hydrogen evolution or it might be due to deposits with a rough microstructure which would increase the surface area resulting in increasing current over a longer period of time.

In our research CA experiments were carried out in the range of -0.41 to -0.50 V with the deposition time of 300 s as longer deposition times resulted in the roughening of the deposit and decrease in current efficiency.
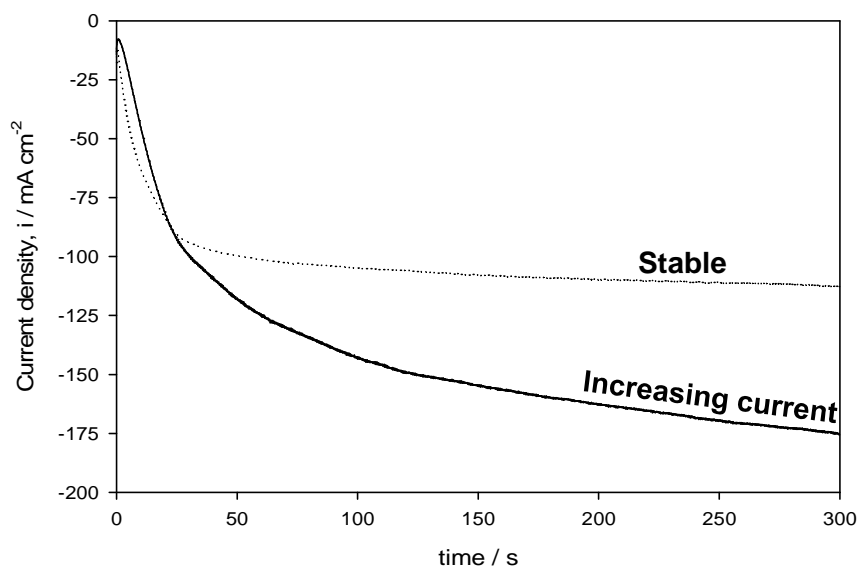
Figure 3-9 A typical chronoamperometry plot (current-time) showing two different current responses.

3.3.3   Anodic Stripping Voltammetry

Anodic stripping voltammetry (ASV) experiments were carried out immediately after each CA experiment at a specific potential. ASV is considered a linear sweep voltammetry technique in which the potential is scanned in a single direction in the potential window where deposited metals are stripped from the electrode surface. As with CV experiments, the stripping current and corresponding anodic charge of each peak can be used to calculate the ratio of individual metals in the alloy.

In this research the ASV starting potential is the same as the corresponding CA potential (-0.41 to -0.50 V). The potential is then scanned in the positive direction stopping at 0.6 V. Both copper and tin metals are stripped from the RDE surface within this potential window region. Scanning to potentials more positive than 0.6 V was not necessary as no significant stripping currents were observed beyond that potential. Figure 3-10 is an example of a typical ASV plot showing two metal stripping peaks.
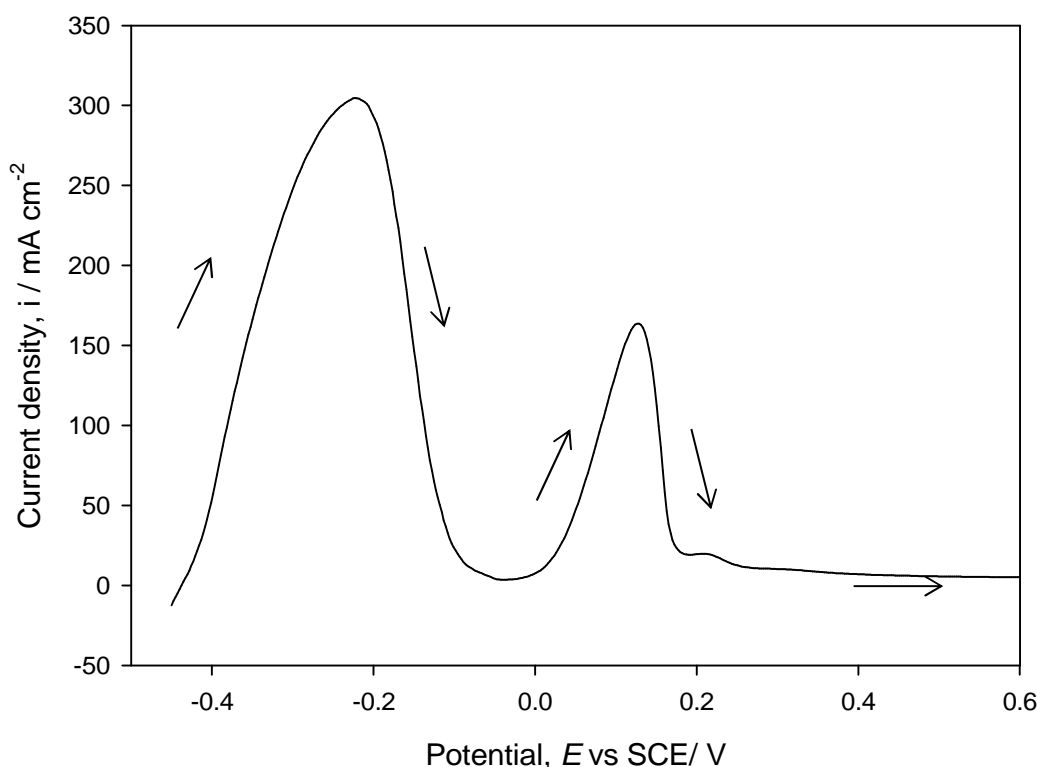
Figure 3-10 A typical anodic stripping voltammetry plot (current-potential).

3.4 Electrodeposition Experiments

In order to examine the deposited material using SEM and XRD techniques, a substrate that is much flatter and thinner than the tip of an RDE was needed. Vitreous carbon was found to be a suitable substrate for these studies. It is a good electrical conductor suitable for SEM, has a very flat surface suitable for XRD analysis, and is amorphous which would minimize the influence of substrate on the deposit (epitaxial growth). Therefore electrodeposition experiments, where material characterization was performed, were carried out with a flat vitreous carbon substrate (GoodFellow). Figure 3-11 shows a schematic of the instrumental setup used in direct current plating.
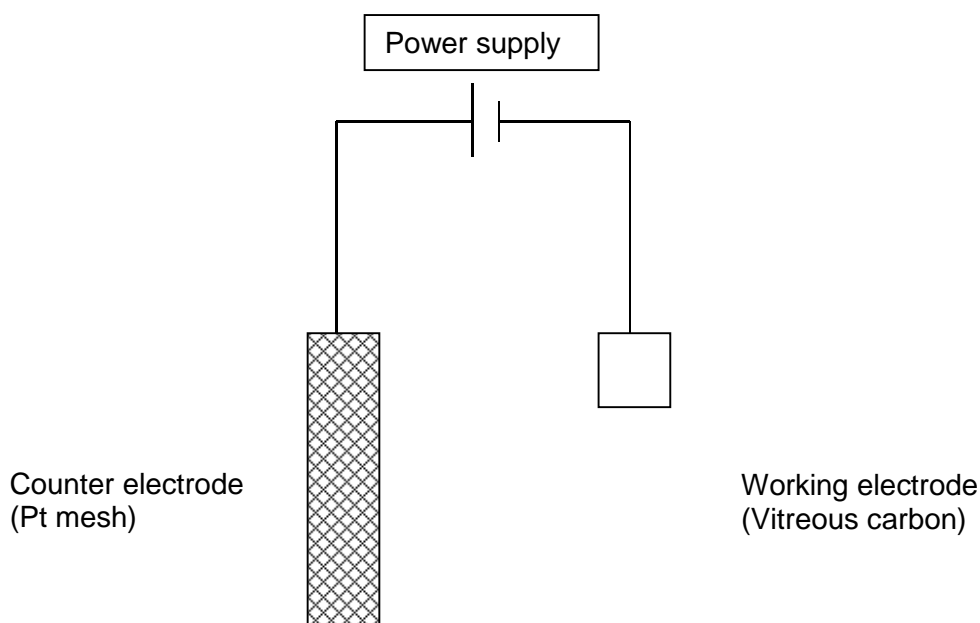
Figure 3-11 Schematic of the two electrode setup used in electrodeposition experiments.

3.4.1 Direct Current Plating

A DC power supply was used to apply current densities in the range of 20-30 mA cm^{-2} and the deposition time was fixed at 600 s. Deposition was carried out on a 1 x 1 cm vitreous carbon working electrode with a platinum mesh as the counter electrode which was positioned approximately 2 cm apart. These experiments were performed using two electrodes (working and counter), in order to simulate conditions in practical industrial situations. A reference electrode was not used in these experiments. The

procedure for choosing the current for electrochemical characterisation data is described in Chapter 6.

The experiments were carried out without added agitation as the limiting current density at a stationary vitreous carbon electrode was comparable to that of the limiting current density at an RDE rotation speed of 100 rpm. The DC limiting current density can be calculated from Equation 3.5 [94].

$$i_{L,DC} = zFD\frac{c_b}{d_s} \tag{3.5}$$

Where $i_{L,DC}$ = DC limiting current density (mA cm^{-2}),

z = number of electrons in the electrode process,

F = Faraday constant (96,485 C mol^{-1}),

D = diffusion coefficient of the electroactive species (cm^2 s^{-1}),

c_b = bulk concentration of the electroactive species (mol cm^{-3}),

δ_s = outer stagnant diffusion layer (cm),

For example for Cu^{2+} with a diffusion coefficient of 6.8 x 10^{-6} cm^{2}s^{-1} and assuming that the diffusion layer is approximately 50 µm (typical thickness in a stirred solution), $i_{L,DC}$ was estimated to be 3.9 mA cm^{-2}. This value is very close to that of $i_{L,RDE}$ = 4.5 mA cm^{-2} (*cf.* table 3.3). Therefore, the limiting current density seen in CA experiments can be used in DC plating experiments.

Current Efficiency

Current efficiency was calculated by using the electrochemical equivalent method and Faraday's law which gives the relationship between the amount of charge consumed and the theoretical weight that should be obtained. The values for copper and tin are 0.329 mg C^{-1} and 0.615 mg C^{-1}, respectively. For example if the deposit contained 88% Cu and 12% Sn the theoretical mass obtained (assuming 100% current efficiency) would be (0.88x0.329) + (0.12x0.615) = 0.363 mg C^{-1} for a Cu88Sn12 alloy.

3.4.2   Pulse Current Plating

A DC pulse reverse power supply (Plating electronic) is connected to the working and counter electrode as shown in Figure 3-12.
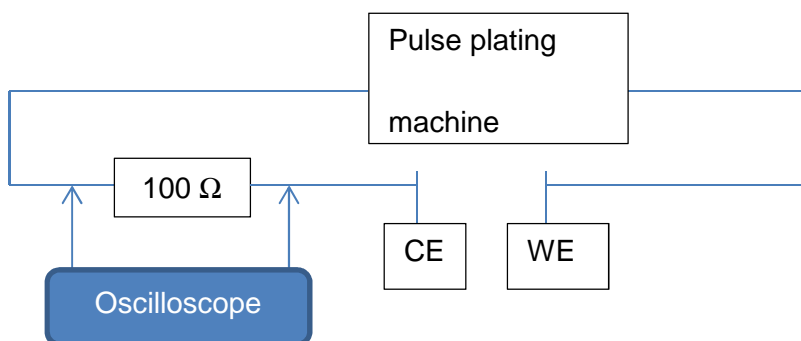
Figure 3-12 Schematic of a pulse current plating instrumental setup.

An external resistor was added to the circuit in order to provide a load to the pulse power supply machine without which incorrect currents would be applied to the plating system. The current is monitored via an oscilloscope which displayed the potential drop across the resistor. The applied current was then determined from this potential drop by using Ohm's law in Equation 3.6.

$$V = IR \qquad\qquad (3.6)$$

Where   V = potential shown on oscilloscope (V)

  I = applied current (A)

  R = resistance (Ω), in this case a standard 100 Ω resistor

For example, setting an applied current of 0.1 A on the pulse plating machine should give a corresponding signal of 10 V on the oscilloscope. We can then monitor both the current and potential changes that occur during electrodeposition. Note that the resistor was not temperature compensated and experiments were carried out at normal room temperatures. During experiments the temperature did not significantly fluctuate and it was made sure that the temperature of the electrolyte was constantly kept near room temperature (25 ^{o}C).

The equivalent PP time can be obtained by multiplying the duty cycle and the DC plating time as shown in Table 3-4. The DC plating time of 10 min. was shown to give satisfactory deposits and the corresponding PP plating time was calculated accordingly.

Duty cycle	Plating time (min.)	
	DC	PC
	10	50
0.2	20	100
	30	150
	10	20
0.5	20	40
	30	60

Table 3-4 Equivalent PC plating time based on duty cycle and DC plating time.

Current densities in the range of 40-150 mA cm^{-2} were applied for durations of 20-50 minutes. The procedure used in selecting the current densities are described in greater detail in Chapter 6.

3.5   Materials Analysis

3.5.1   Optical Microscopy

Deposits on RDE surfaces were initially examined under an optical microscope. As many repeat experiments were carried out, initial visual inspections with an light microscope was performed before samples were studied under a scanning electron microscope. The light microscope (Olympus) was attached to a digital camera. This allowed us to directly save images in digital format. Images were usually captured at 20x magnification depending on the roughness of the surface. Higher magnification on rough surfaces did not yield useful micrographs as they were indistinguishable from one another.

3.5.2   Scanning Electron Microscopy

The deposit microstructure was studied using an optical microscope and two types of SEMs. A low vacuum SEM (Jeol JSM-5300LV) was used mainly for low resolution images and composition analysis. A high vacuum SEM (FEI XL30 ESEM-FEG) was used for higher resolution images needed to observe the cross-section and deposit growth from the substrate. Deposit thicknesses were measured from at least five

different points before being averaged. The thickness was measured before and after annealing of samples from both DC and pulse current modes of deposition. All SEMs were equipped with an Energy Dispersive X-ray (EDX) detector which was used to determine deposit composition.

Signal detection

A special feature of the SEM that sets it apart from light microscopes is that it can provide more information than just the topography of the sample. The various types of signals and the information that the SEM can provide are summarized in Appendix A. The main signals of importance in SEM analysis are secondary electrons and backscattered electrons that requires the use of a special type of detector called the Everhart-Thornley detector which is a scintillator-photomultiplier device. Spectrochemical analysis can also be achieved through EDX.

When the incident beam of electrons from the electron gun hits the sample, it can either pass through the sample, be absorbed by the sample, or become reflected through elastic or inelastic scattering. The interaction between the electron beam and the sample occurs within in a tear drop shaped volume known as the interaction volume which extends to approximately 5 μm below the sample surface.

Elastic scattering

Backscatter electrons (BSE) are signals from elastic scattering which means that the energy of the incident electrons is preserved. This occurs because not all the electrons can flow through the sample and a beam of electrons will be reflected, backscattered from the sample. The BSE signal intensity is dependent on the atomic number and can be used to provide information about the micro-distribution of various elements across the surface [21].

Inelastic scattering

Inelastic scattering occurs when the energy of the incident electron beam is not conserved as it hits the sample. These signals include secondary electrons (SE), auger electrons, characteristic X-rays, and cathodoluminescence radiation. SE are defined as

low energy electrons of less than 50 eV which would only be able to penetrate a few nanometres below the sample surface and can provide topographic information.

Energy Dispersive X-ray Spectroscopy (EDX)

Characteristic X-ray radiation is produced by the interaction of incident electrons with the inner shell electrons of the atoms in the sample. If the incident electron is of sufficient energy it can dislodge a K, L, or M inner shell electrons putting the atom in an excited or ionized state. This leaves an electron hole which can be filled by an electron from an outer shell. When this happens the atom relaxes to its normal ground state and an emission of X-ray radiation occurs. The characteristic X-rays emitted are unique for specific atoms of a given atomic number and therefore can provide information about the elemental composition of the sample.

For each sample EDX measurements were taken from at least three different points spread across the surface to obtain an average elemental composition. The highest accuracy of EDX measurement is approximately ±3% meaning that elemental compositions of less than 3% cannot be accurately guaranteed. The presence of oxides in the deposit was also detected and it should be noted that deposits containing oxides are usually porous and rough which would affect the accuracy of the measurements.

3.5.3   X-Ray Diffraction

X-ray diffraction (XRD) analysis was carried out using a Panalytical X'Pert Pro Multipurpose Diffractometer (Cu Kα, 40 kV, 40 mA). The diffractometer was fitted with an X'Celerator and a secondary monochromator. The X'Celerator is an ultra-fast X-ray detector that uses RTMS (Real Time Multiple Strip) technology and operates as if it were an array of over a hundred detectors simultaneously.

Analyzing the XRD data, one must be aware that the width of a diffraction peak can be influenced by various factors such as instrumental line broadening, lattice defects, the size of the crystallites, and differences in strain of deposits that have different grain sizes or microstrains [95].

To compensate for these factors, the average crystallite size was calculated from the Williamson-Hall method as shown in Equation 3.5.

$$\frac{b\cos q}{l} = h\frac{\sin q}{l} + \frac{K}{L}$$

(3.5)

where   β   =   line broadening at Full Width Half Maximum (FWHM)

       λ   =   x-ray wavelength (nm)

       θ   =   Bragg angle (rad)

       K   =   shape factor (typical value of 0.9)

       L   =   crystallite size (nm)

Rearranging Equation 3.5 we get

$$b\cos q = h\sin q + \frac{Kl}{L}$$

(3.6)

From Equation 3.6 we can see that plotting $\beta\cos\theta$ vs. $\sin\theta$ results in a straight line with slope η (microstrain component) and a y-intercept of $K\lambda/L$ (size of crystallites) [95].

The average crystal size is the average of the three most intense XRD peaks in a particular sample. XRD phase analysis was carried out on samples before and after annealing from both DC and pulse current modes of deposition to determine if any changes in phase or preferred orientation has occurred.

The three most intense peaks were identified and their peak position and FWHM values noted. The crystallite size for each peak is then calculated and an average of the three obtained. Table 3-5 is a summary of crystal properties obtained from a database of standard Powder Diffraction Files (PDF). The X'Pert Pro software automatically matches up the pattern of peaks in an "unknown" sample to the XRD pattern found in the database of the International Centre for Diffraction Data (ICDD) to determine what phases are found in the sample. A perfect match is sometimes not obtained due to factors such as impurities in the sample and the peak list of the PDF may need to be consulted.

Phase name (crystal system)	(PDF #)	Order of peak intensity	Peak (2Θ)	Crystal plane <h k l> notation
Cu (cubic)	00-004-0836	1st	43.30	<1 1 1>
		2nd	50.43	<2 0 0>
		3rd	74.13	<2 2 0>
Sn (tetragonal)	00-004-0673	1st	30.65	<2 0 0>
		2nd	32.01	<1 0 1>
		3rd	44.90	<2 1 1>
Cu$_6$Sn$_5$ (hexagonal)	00-047-1575	1st	30.13	<1 0 1>
		2nd	42.97	<1 1 0>
		3rd	43.28	<1 0 2>

Table 3-5 List of Cu, Sn, and Cu-Sn phase and their crystal properties used for XRD analysis (ICDD database).

3.5.4 Annealing Procedure

Cu-Sn deposits were reflowed in order to observe any microstructure and crystal structure changes that might occur. The deposits were annealed in a curing oven (Despatch Industries) under a nitrogen atmosphere in order to minimize the effect of oxidation. The deposits were put through the temperature profile shown in Figure 3-13. The peak temperature for reflowing was 260°C which was held for 2 min. Since the idling temperature of the oven was 60°C and the maximum ramp up rate was 8°C/min, increasing the temperature from 60 to 260°C took approximately 25 min. The ramp down rate was the same so it took the sample approximately 25 min. to cool down from the peak temperature.
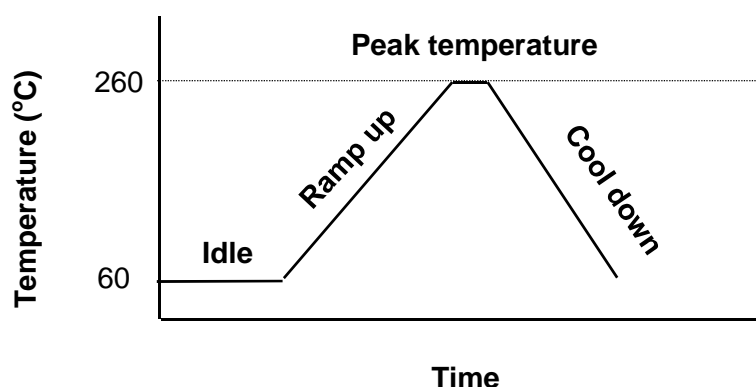
Figure 3-13 Annealing temperature profile. The preheating stage was 25 min. and the reflow stage was approximately 2 min at 260°C.

4.   RESULTS: ELECTROLYTE OPTIMISATION

Preliminary electrolyte optimisation experiments were carried out using a rotating cylinder Hull cell (RCH) in order to select the bath components as well as concentration needed in order to successfully plate Cu-Sn alloys from an MSA electrolyte. The electrolyte composition used in this initial research stage is shown in Table 4-1.

Composition	Concentration		Function
	(M)	(g L^{-1})	
Copper(II) sulfate (CuSO$_4$·5H$_2$O)	0.007	2	Source of Cu^{2+} ions
Tin(II) sulfate (SnSO$_4$)	0.07	15	Source of Sn^{2+} ions
Hydroquinone (C$_6$H$_4$(OH)$_2$)	0.01	1	Antioxidant
Methanesulfonic acid (70%) (CH$_3$SO$_3$H)	2.00	192	Supporting electrolyte

Table 4-1 Preliminary electrolyte composition used for electrolyte optimisation experiments.

To keep the electrolyte chemistry simple, the only additive initially added was hydroquinone after it was found that without it, significant Sn precipitation would occur. Many different CuSO$_4$:SnSO$_4$ ratios added to the bath were tested including 30:70, 20:80, 50:50, and 10:90 all of which resulted in deposits which contained more than 50% Cu. As the goal was to obtain Sn-rich deposits, the 10:90 bath was further developed as it gave the highest amount of Sn in the deposit (47%). This resulted in the bath formulation shown in Table 4-1 where it was decided that for consistency in future experiments the amount of Sn added to the bath would be ten times more than copper (1:10 ratio). This corresponds well with the alloy co-deposition strategy (*c.f.* section 2.4) where the more noble metal (Cu) is kept at a lower concentration than the less noble metal (Sn) in the electrolyte.

The main problem encountered was that the deposits obtained from this bath would always be very thin and uneven with the brass substrate clearly exposed. Test carried out in baths containing only CuSO$_4$ showed that the concentration of Cu initially added was simply too low for good quality deposits to form. Therefore, the amount of Cu and Sn was increased as shown in Table 4-2 and used for all further experiments.

Composition	Concentration		Function
	(M)	(g L^{-1})	
Copper(II) sulfate (CuSO$_4$·5H$_2$O)	0.02	5	Source of Cu^{2+} ions
Tin(II) sulfate (SnSO$_4$)	0.20	43	Source of Sn^{2+} ions
Hydroquinone (C$_6$H$_4$(OH)$_2$)	0.01	1	Antioxidant
Methanesulfonic acid (70%) (CH$_3$SO$_3$H)	2.00	192	Supporting electrolyte
Fluorosurfactant (DuPont™ Zonyl® FSN)	0.01 %vol (30-60 µL / experiment)		Wetting agent

Table 4-2 Final electrolyte composition used for electrolyte optimisation experiments.

4.1 Effect of additives on deposits

Antioxidants are usually added to all acid tin plating baths to prevent oxidation of Sn^{2+} to Sn^{4+} which would ultimately lead to the formation of tin sludge (SnO$_2$). As a result, the concentration of Sn^{2+} in the electrolyte would decrease and would need to be replenished more frequently. A wetting agent is sometimes added to the electrolyte in order to improve the deposit morphology. It was not clear, however, before the preliminary experiments began if the surfactant is a necessary bath component or whether it can be omitted from the electrolyte.

As electrodeposition experiments will be carried out on a cylinder electrode, it is necessary to first determine the nature of this substrate. This is to ensure that EDX signals are arising only from the deposit and not from the substrate. Table 4-3 shows the composition of the cathode cylinder which was made of brass (Cu-Zn alloy).

	% Sn (weight)	% Cu	% Zn	% C	% O	% total
Electrode	-	49	32	14	-	95

Table 4-3 Elemental composition of the brass cylinder electrode substrate.

A pure Cu substrate was available but not used extensively as it quickly corroded not to mention that fact that a Cu substrate would have significantly affected the EDX measurements of Cu-Sn deposits. It would not be possible to obtain an accurate report of the actual Cu content in the deposit as Cu signals arising from the substrate would

also be detected. A brass substrate was used mainly because it provided good adhesion for Sn deposition. The surface was also relatively easy to clean and can be reused in multiple experiments. It should be noted that the brass cylinder is not a pure Cu-Zn alloy and that carbon (approximately 14 wt%) as well as iron (usually less that 5 wt%) was also detected in the substrate. The elemental composition data presented are the average of three separate measurements taken at different random locations across the surface of a single sample. The variation between these measurements was less than 5%, which was the average accuracy of the EDX instrument. The total percentages of individual elements combined lie between 93-98 wt% (the last column in the tables), which is a reflection of the accuracy of these measurements.

It must also be noted that the amount of Cu reported may be a slight overestimation of the actual Cu content in the deposit; this depends on the thickness of the deposit. For thin uneven deposits, the beam of electrons can reach the substrate surface and the total amount of Cu detected is likely due to a combination of Cu found in the deposit as well as Cu from the brass substrate *i.e.* $Cu_{total} = Cu_{deposit} + Cu_{substrate}$. For thicker deposits, the electron beams cannot penetrate deep enough to reach the substrate surface and the total amount of Cu detected is a more accurate estimation of the actual amount of Cu found in the deposit *i.e.* $Cu_{total} = Cu_{deposit}$ only.

4.1.1   Electrolytes without surfactant

The average current density applied was based on limiting current density of 0.02 M Cu which in this case was 4.7 mA cm^{-2}. The current was applied for a period of 600 s. Table 4-4 shows the elemental composition of Cu-Sn deposits obtained from a plating bath without surfactants.

Cylinder section	Distance (cm)	% Sn (weight %)	% Cu	% Zn	% C	% O	% total
1	0.7	35	28	2	12	21	98
2	1.5	33	29	3	9	21	95
3	2.7	25	40	9	5	14	93
4	4.0	24	43	11	4	14	96

Table 4-4 Elemental composition of Cu-Sn deposits from electrolytes without surfactant.

A gradual decrease in Sn content from 35 to 24 wt% (the second column) was seen as the local current density decreases from section 1 to 4. On the other hand, in column three we see that the Cu content increased from 28 to 43 wt% which is to be expected

due to the decrease in current density. The preferential deposition of Cu (the more noble metal) over Sn at lower current densities suggests that this is a normal alloy deposition system.

The additional columns in Table 4-4 show the presence of zinc, carbon and oxygen. The detection of zinc and carbon indicates that the x-rays are penetrating into the substrate layer as the deposits are relatively thin (approximately 4 µm). In addition, the high oxygen content indicates that that the deposit is in the form of metal oxides and, therefore, accurate metal composition cannot be determined.

Figure 4-1 shows the appearance of the Cu-Sn deposit. At relatively lower current densities (cylinder section 6 is in the far right of the figure) we see a deposit that is mainly composed of copper. Visual inspection shows that the deposition of black tin(II) oxide or stannous tin (SnO) which has a distinctive "burnt" appearance can be seen to the far left of the Figure 4-1. This area corresponds to cylinder section 1. Therefore, the formation of metal oxides has been confirmed both visually and by EDX analysis of the rotating cylinder electrode shown in Figure 4-1, the results of which were presented in Table 4-4.
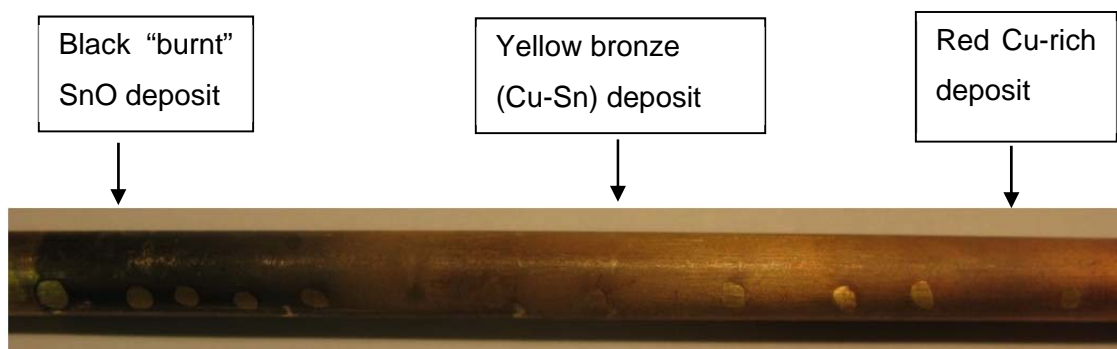
Figure 4-1 Cu-Sn deposit showing the effect of varying Cu:Sn composition along the rotating cylinder electrode surface. The RCH rotation speed was 400 rpm and the average applied current density was 4.7 mA cm^{-2}.

4.1.2 Electrolytes with surfactant added

The surfactant was added to see if it would have any effect on tin content, whether it could be increased, and whether metal oxides were still being formed even with the presence of surfactant. Table 4-5 shows the elemental composition of Cu-Sn deposits obtained from a plating bath with surfactants added.

Cylinder section	Distance (cm)	% Sn (weight %)	% Cu	% Zn	% C	% O	% total
1	0.7	85	3	2	7	-	97
2	1.5	73	9	5	8	-	95
3	2.7	72	12	3	9	-	96
4	4.0	70	13	5	6	-	94

Table 4-5 Elemental composition of Cu-Sn deposit from electrolytes with surfactant added.

A similar trend of decreasing tin content and increasing Cu content is observed (column three) as one moves down the table from section 1 to 4. However, it can be seen for section 1 the tin content has now risen to 85 wt%, while copper content has droped to 3 wt%. Zinc and carbon were still detected owing to the thinness of the deposits. However, no oxygen is detected, showing that the deposit does not contain metal oxides. Indeed, the change in both copper and tin content is corroborated by the SEM images in Figure 4-2, which shows that the deposit microstructure is also different when surfactants are added to the electrolyte. The deposits with low tin content appeared relatively smoother than deposits which have high tin content. Figure 4-2(b) shows the propensity of tin to form crystallites; the higher the Sn content in the deposit, the more porous the deposit.
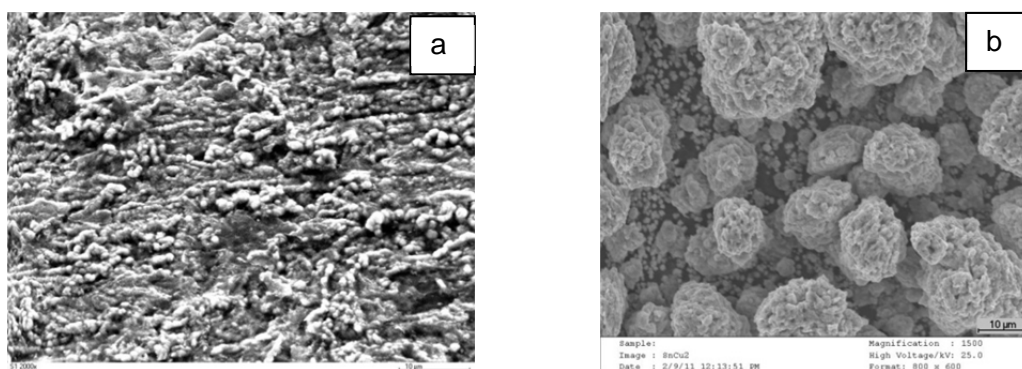
Figure 4-2 Surface microstructure of Cu-Sn deposits a) without surfactant, 35 wt.% Sn and b) with the addition of surfactant, 85 wt.% Sn.

4.1.3 Nitrogen degassing experiments

As mentioned earlier, the antioxidant hydroquinone is known to lower the amount of dissolved oxygen in the electrolyte [1, 31] and was added to all electrolytes. Therefore, any bath with hydroquinone added should not contain metal oxides. The formation of metal oxides was initially thought to be due to the presence of dissolved oxygen in the solution. In theory hydroquinone should have minimised and prevented the formation of metal oxides. If metal oxides were still found in the deposits, it would mean that either hydroquinone is not an effective antioxidant or that its concentration in this specific MSA bath is too low.

In order to test the hypothesis that dissolved oxygen in the solution may be the cause of metal oxide formation, experiments were carried out in two different types of baths, aerated and deareated. As experiments have shown that the deposits with metal oxides were only coming from baths without surfactants, only baths without surfactant were tested. Both types of baths contained the usual Cu and Sn salts with hydroquinone, but the first set was carried out in an open vessel while the second set was deaerated before deposition was carried out. The second set of baths was degassed with nitrogen for 1 hour prior to plating. This was to ensure that the amount of dissolved oxygen in the solution was as low as possible.

EDX analysis showed that the deposit composition was 55% Sn, 19% Cu, 1% Zn, 5% C and 20% oxygen. These set of values is similar to those shown in Table 4-4 (21 % oxygen). It was clear that metal oxides were still being formed even though the electrolyte had very low amounts of dissolved oxygen. It was therefore concluded that the dissolved oxygen in the solution is not the cause for metal oxide formation. It was also observed that when fluorosurfactant are added to any type of bath, deaerated or not, the formation of metal oxides were always inhibited. Therefore, it can be concluded that the surfactant plays an important role in inhibiting oxide formation. The actual cause of metal oxide formation will be discussed in a following section.

The last point to note in this section is that the EDX results showed no significant amounts of carbon detected in the deposits. The possible source of carbon from the MSA electrolyte is either from hydroquinone ($C_6H_4(OH)_2$) or the MSA molecule itself (CH_3SO_3H). Since no trace of sulphur was detected as well, it was concluded that additives were not being incorporated into the deposit.

4.2   Deposit Thickness

Attempts were made to measure to deposit thickness by using various techniques that would eventually fail to give consistent reliable results. Initially before cutting or sectioning the RCE into different sections, the whole cylinder electrode was sent to a colleague in the same research group to perform surface profilometry measurements. A Dektak profilometer was run across the length of the electrode to determine the average thickness of the deposits. This proved to be a very time consuming process and it showed that for tin deposits, a reliable measurement could not be obtained as the deposition layers were very thin not to mention rough.

Examining the cross-section to determine the deposit thickness revealed that the deposits have a very rough microstructure. The process of sectioning the cylinder electrodes and mounting them in epoxy resin would also prove that reliable thickness measurement could not be made. The samples were polished to a smooth finish as this will assist in accurate EDX measurements. Figure 4-3 shows a backscatter electron image (BSI) highlighting common problems such as rough deposit growth and smearing of the outer deposition layer into the brass substrate layer due to polishing (smooth surfaces are necessary for SEM/EDX analysis). BSIs display a contrast between the different elements and are suited to provide information about the elemental distribution across the sample. Heavier elements backscatter electrons more strongly than lighter elements and would appear relatively brighter in a BSI. For example, in Figure 4-3a The brass electrode is a mixture of ^{29}Cu and ^{30}Zn and is displayed as a relatively darker area to the left of the image. The ^{50}Sn deposit with the higher atomic number appears as brighter contrast regions near the edges. Measurements have shown that the average thickness can vary anywhere from 1µm to a maximum of 7 µm within the same sample section.
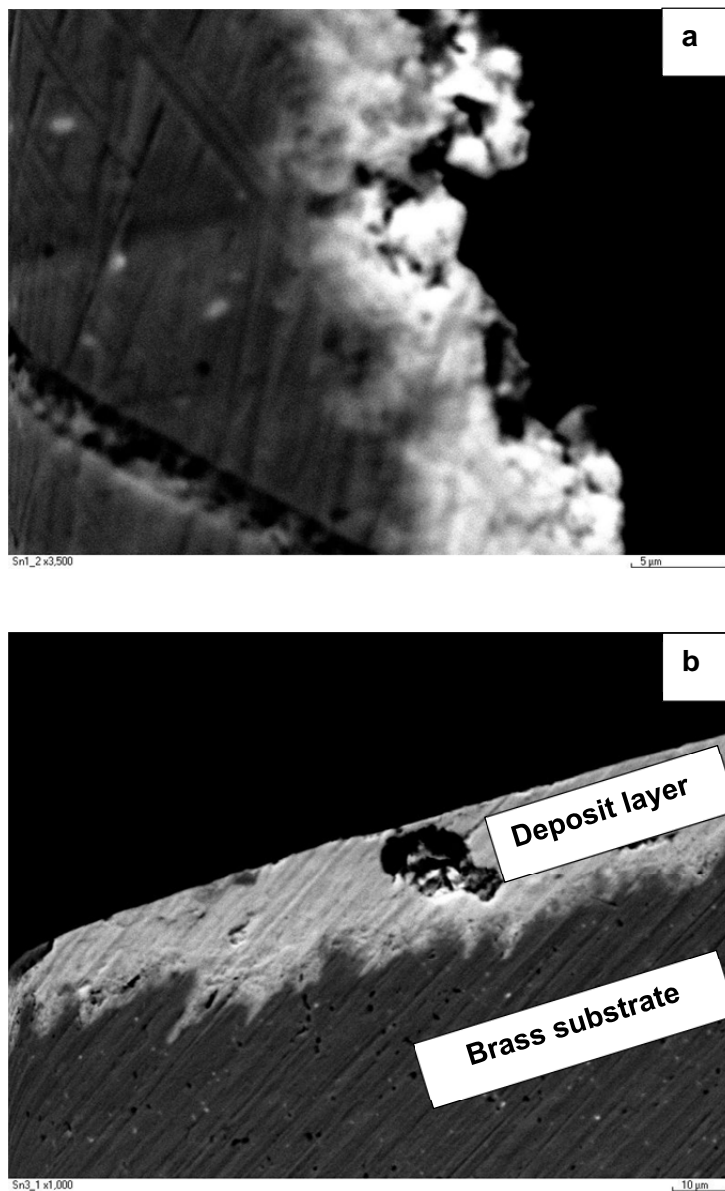
Figure 4-3 Backscatter electron image showing issues preventing accurate deposition thickness measurements from cylinder electrode cross-sections a) rough deposits and b) smearing of the deposition layer into the brass substrate.

The final technique which was employed as an attempt to measure the deposit thickness involves the use of EDX elemental mapping as shown in Figure 4-4. In this type of analysis the distribution of a single element is mapped out across the original SEM image. A band of Sn deposits can be clearly seen in Figure 4-4(b). Once again as the brass substrate is a Cu-Zn alloy the distribution of Cu shows up accordingly in Figure 4-4(c). By drawing two parallel lines across the Sn band in Figure 4-4(b), the average deposit thickness was determined to be approximately 6 μm.
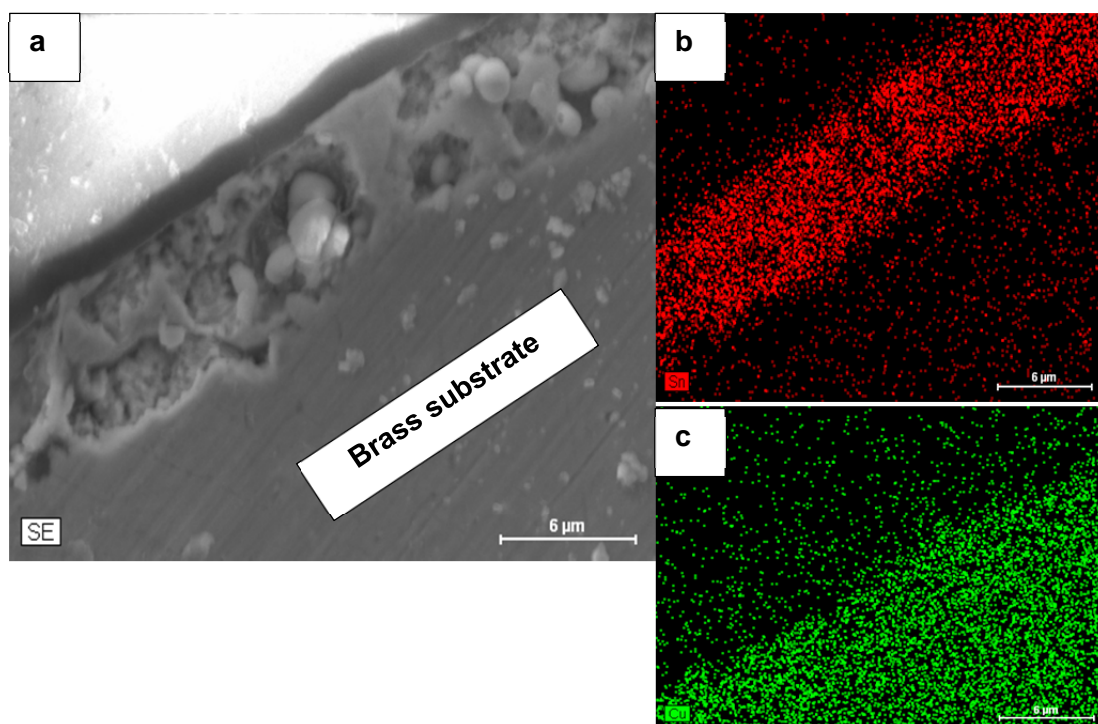
Figure 4-4 Cross section elemental map analysis of Sn deposits on an RCE. a) original SEM image, b) Sn distribution and c) Cu distribution maps.

4.3   Current efficiency

The current efficiency of deposits from the bath without surfactant was found to be 55%. In the presence of surfactant the current efficiency rose to 66%. The lower current efficiency may be attributed to the fact that the current is being consumed in other side reactions, such as hydrogen formation, and not in depositing metals. Cathodic electrodeposition of metal oxides has been reported [96-100]. It has been shown that tin oxides can form when the hydrogen reaction proceeds at the electrode surface resulting in local pH changes as shown in Equation 4.1.

$$2H_3O^+ + 2e^- \rightleftharpoons H_2 + 2H_2O \tag{4.1}$$
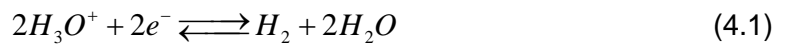
As protons are being reduced the local pH near the electrode surface increases. Pourbaix diagrams, such the one in Figure 4-5 show that the rise of the pH of the electrolyte very close to the electrode surface through Equation 4.1 can lead to the formation of tin oxides [10, 31, 101, 102].
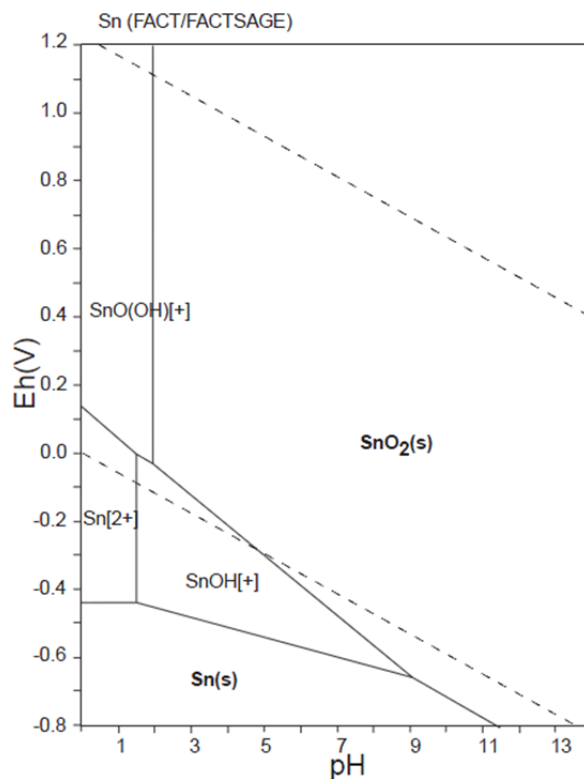
Figure 4-5 Pourbaix diagram of the Sn-O-H system [10].

It is known that fluorosurfactants can inhibit hydrogen evolution by adsorbing at the electrode surface [52, 53, 83]. Therefore, we can infer that the fluorosurfactant is crucial in the suppression of hydrogen thereby limiting or minimizing pH changes and enabling the deposition of metals. Based on these findings, it can be concluded that oxide formation in the deposit can be minimized by adding fluorosurfactants into the electrolyte.

4.4 Discussion

Hydroquinone has been found to be a crucial component of the plating bath due to its antioxidant properties [51, 91]. As shown in Figure 4-6, hydroquinone is a redox molecule that can donate electrons to Sn^{4+} ions in solution and reduce them to Sn^{2+}. This process helps to reduce the amount of Sn^{4+} ions in solution that would otherwise form white tin(IV) oxide or stannic oxide (SnO_2). These colloidal particles are the cause of solution turbidity which if left to settle, would precipitate and sink to the bottom of the tank forming what is known as tin sludge [51].
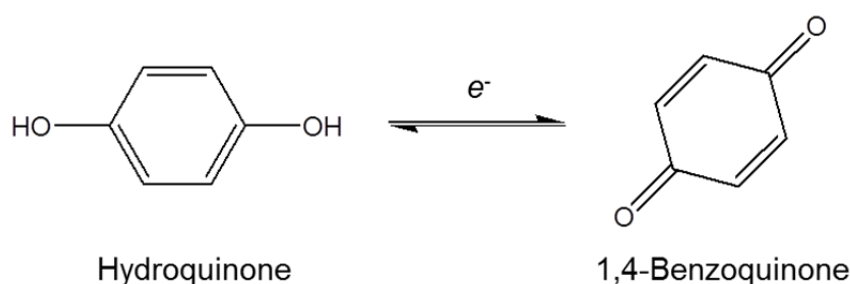
Figure 4-6 Hydroquinone antioxidant is a redox molecule.

RCH experiments have shown that the major problem which arose with MSA-based electrolytes was the formation of metal oxides. Dissolved oxygen is inevitable for electrodeposition carried out in open vessels (such as in the plating tank of a factory) and, therefore, antioxidants are a crucial component of every electrolyte. The antioxidant hydroquinone used in this research was shown to be a good candidate as it could maintain bath stability over a reasonable period of time (3 weeks) [91]. However, the concentration of Sn used in the mentioned work is relatively low (0.05 M) while in this research the Sn concentration was much higher (0.20 M). It is proposed that due to

the high concentration of Sn in solution, some oxidation of Sn^{2+} to Sn^{4+} still occurs which can be seen by a thin layer of tin sludge at the bottom of the plating vessels. This loss of tin is not uncommon and is expected when plating from an acidic bath [2]. The tin sludge sinks to the bottom and does not interfere with the electrodeposition process. It can simply be removed by decanting or by filtering the solution.

4.5   Conclusion

Important findings of the experiments with the RCH in this chapter have concluded that:

- A high Sn:Cu ratio in the electrolyte corresponds to a high Sn:Cu ratio in the deposit.
- Without the surfactant electrodeposits contain metal oxides.
- Dissolved oxygen in the solution is not the cause of metal oxide formation in the deposit as shown by nitrogen degassing experiments.

5.   RESULTS: ELECTROCHEMICAL CHARACTERISATION

In the previous Chapter 4, preliminary experiments with the RCH showed that the MSA electrolyte used was capable of depositing Sn-rich Cu-Sn deposits without the formation of any metal oxides. This chapter will be concentrating on various electrochemical analysis techniques namely cyclic voltammetry (CV), chronoamperometry (CA), and anodic stripping voltammetry (ASV) which were employed to better understand the electrochemistry of the electrodeposition system containing surfactants. The ultimate aim of these experiments was to establish the potential and current region where Sn-rich Cu-Sn alloys could be deposited with reasonable current efficiency and acceptable morphology.

Table 5-1 summarizes the electrolyte composition used in electrochemical characterisation experiments. Note that this differs from the composition used for RCH experiments (*c.f.* Table 4-2) in that slightly less Cu and Sn concentrations were added. This is because additional analysis of the electrolyte showed that the saturation point of $SnSO_4$ in the MSA electrolyte was 0.15 M. Therefore, any additional Sn added would simply be wasteful as it would just precipitate as Sn sludge. The Cu concentration was also adjusted accordingly to maintain a Cu:Sn ratio of 1:10. CVs were carried out using electrolytes that contained Cu, Sn, or both metal salts. There were two main types of plating solutions; with and without surfactant. This was carried out to observe the effect that the surfactant had on the current-potential behaviour.

Composition	Concentration		Function
	(M)	(g L^{-1})	
Copper(II) sulfate ($CuSO_4 \cdot 5H_2O$)	0.015	4	Source of Cu^{2+} ions
Tin(II) sulfate ($SnSO_4$)	0.15	33	Source of Sn^{2+} ions
Hydroquinone ($C_6H_4(OH)_2$)	0.01	1	Antioxidant
Methanesulfonic acid (70%) (CH_3SO_3H)	2.00	192	Supporting electrolyte
Fluorosurfactant (DuPont™ Zonyl® FSN)	0.01 %vol (30-60 µL / experiment)		Wetting agent

Table 5-1 Electrolyte composition used in electrochemical characterisation experiments.

5.1   Cyclic Voltammetry

All CV experiments in this section were carried out as described in Section 3.3 with Au RDE as the working electrode, Pt mesh as the counter electrode, and SCE as the reference electrode; all potential values reported were vs SCE. The first set of CV experiments was carried out in an electrolyte containing no metal salts. The scan started at a potential of 1.0 V and was scanned in the negative direction towards -0.6 V at a rate of 50 mV s^{-1}. The scan was then reversed and stopped at 0.0 V.

Figure 5-1 shows that this "background" electrolyte did not show any reduction or oxidation peaks between 1.0 to -0.60 V, a potential region where Cu and Sn were expected to deposit. The insert in Figure 5-1 shows that a negligible current density of less than 1 mAcm^{-2} was observed. Therefore, no signals from the background electrolyte were expected to interfere with signals observed during metal deposition experiments. It was found that significant hydrogen evolution began at potentials more negative than -0.60 V leading to a significant current density change, as was observed by other researchers [51].

Based on these findings, all CV experiments henceforth started with a forward *cathodic* sweep to -0.60 V, after which the scan direction was reversed. On the reverse *anodic* sweep the potential was swept up to 0.60 V and then back to 0.0 V.
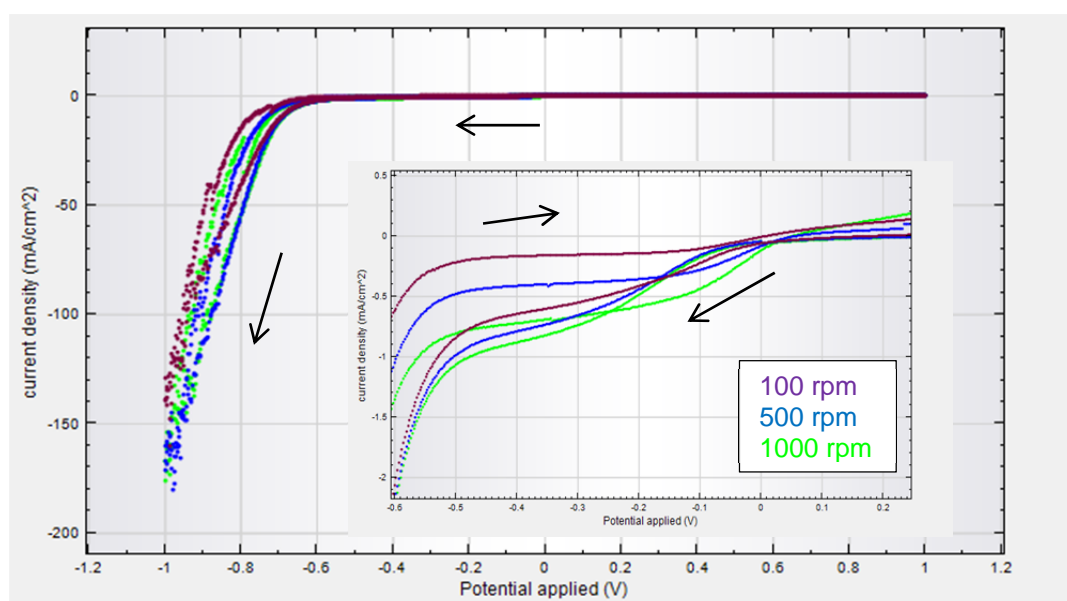
Figure 5-1 Cyclic voltammetry of the background electrolyte shows that significant hydrogen evolution start to occur at a potential of -0.6 V vs SCE.

In Figure 5-1 the RDE rotation speed varied between 100-2000 rpm to change the mass transport rate and determine if it affected the current-potential behaviour. The reduction potential of each metal, Cu and Sn, in its own corresponding electrolyte containing only a single metal ion was determined first. This was then compared to the reduction potential observed in the electrolyte containing both metal ions to determine the potential at which Cu-Sn was being co-deposited.

5.1.1   Copper

Figure 5-2 shows the cyclic voltammogram for the reduction of 0.015 M $CuSO_4$ with and without surfactant. As the reversible potential could not be seen clearly in the figure, a zoomed inset is provided. The reversible potential was estimated to be the position where a corresponding distinct change in current density was observed, i.e. where the curve starts drop from the baseline (in this case 0.0 V). The potential where deposition starts to occur is also referred to as the onset potential.

However, as Figure 5-2 shows, it can sometimes be difficult to determine exactly where the onset potential lies and so a systematic selection method was employed. This involved estimating where the current density starts to noticeably change and then drawing a horizontal line from the y-axis towards the graph curves. At the point along the curves where this horizontal line intersects, a vertical line is drawn towards the x-axis and this is designated as the onset potential.

With no surfactant, the reduction of Cu^{2+} ions to Cu^0 metal started at approximately -0.13 V. However, with the addition of the surfactant the reduction potential shifted to -0.18 V; a change of -0.05 V (50 mV) towards a more negative potential. On the reverse scan only one stripping peak, corresponding to the oxidation of Cu^0 to Cu^{2+} was observed. The anodic stripping peak for Cu is also displaced towards more positive potentials showing that the addition of surfactant affects both reduction and oxidation of Cu^{2+} ions.

It was noted that although the reduction of Cu^{2+} to Cu^+ (one electron transfer process) is theoretically possible, Cu^+ ions are unstable and would not be significantly present. If any Cu^+ were formed, a distinctive second onset potential would have been observed in Figure 5-2. Since only one reversible potential was observed, it was concluded that the only reduction reaction occurring was Cu^{2+} to Cu^0 (two electron transfer process).

Figure 5-2 Cyclic voltammetry of 0.015 M $CuSO_4$ in 2.0 M MSA and hydroquinone antioxidant with and without surfactant. The scan rate was 50 mV s^{-1} and the RDE rotation speed was 100 rpm.

Figure 5-3 shows the effect of varying RDE rotation speeds on the current response. The limiting current plateau region can be clearly seen at all rotation speeds and as the rotation speed increases so does the limiting current density. According to the Levich equation, the fact that the limiting current density is directly proportional to the rotation speed indicates that Cu is under mass transport diffusion control. From Figure 5-3b, the limiting current density at 100 rpm was determined to be around -4.5 mA cm^{-2}.

Cu on Au underpotential deposition (UPD) is a well-known phenomenon [82] and the stripping peaks at 100 and 500 rpm RDE speeds exhibit a slight shoulder to the right of the main stripping peak, Figure 5-3c. The stripping of a single phase would be seen as a single stripping peak with no shoulders. This shoulder is indicative of the stripping of a second phase of Cu close to the surface. Although it is not conclusive evidence, it suggests that UPD may have occurred, albeit a very small amount otherwise a larger and more distinct shoulder or a second stripping peak would have been observed.
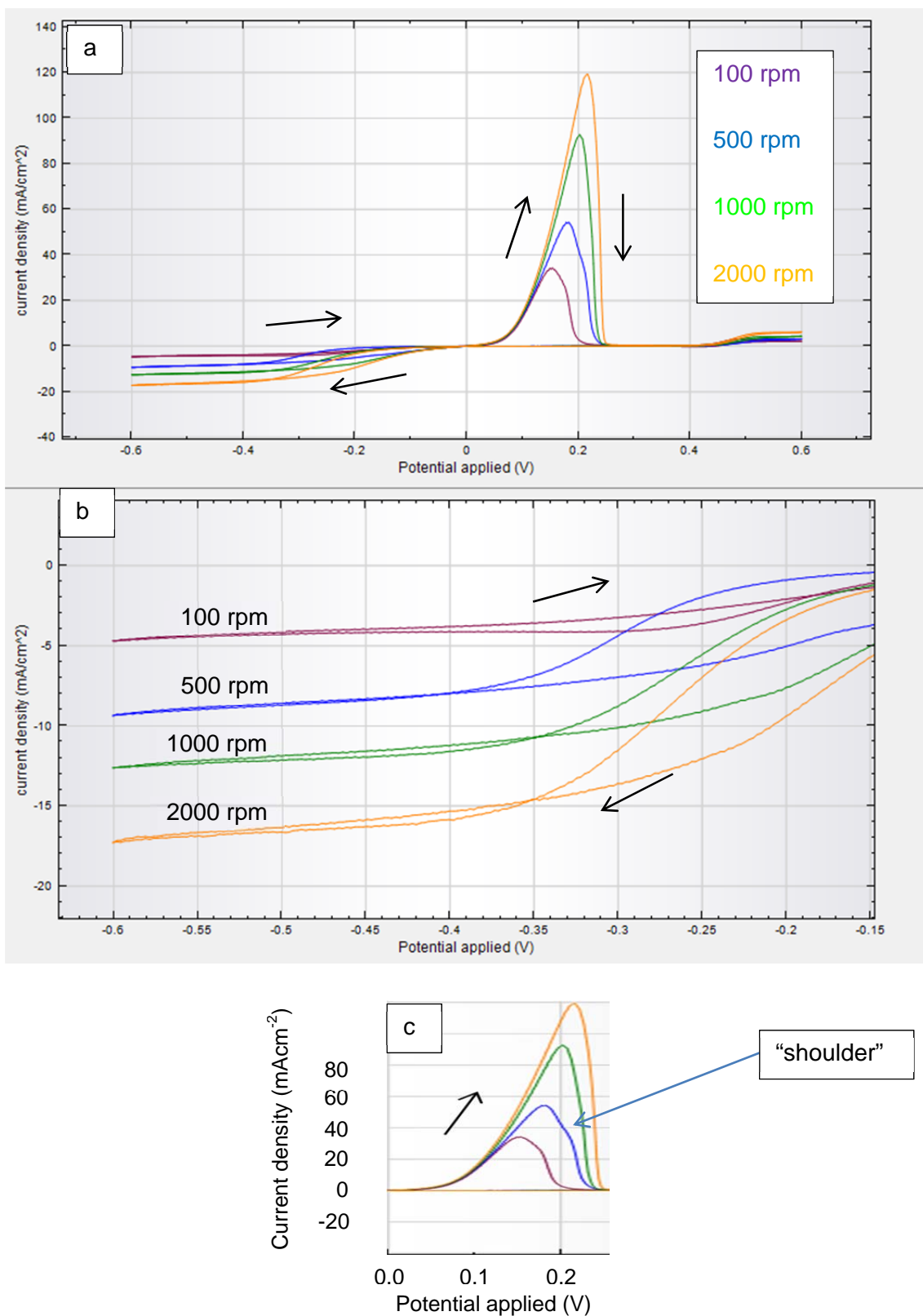
Figure 5-3 Cyclic voltammetry of 0.015 M CuSO$_4$ with surfactant. The scan rate was 50 mV s^{-1} and the RDE rotation speed was between 100 to 2000 rpm. a) whole scan region. b) zoom of Cu deposition region and c) zoom of Cu stripping region.

5.1.2 Tin

Figure 5-4 shows the cyclic voltammogram for the reduction of 0.15 M $SnSO_4$ with and without surfactant. The potential was scanned from 0.0 V to -0.60 V at a scan rate of 50 mV s^{-1} and the RDE rotation speed was 100 rpm. In the absence of the surfactant, the reduction of Sn^{2+} ions to Sn^0 metal starts to occur at approximately -0.45 V. With the addition of surfactant, the reduction potential remained at -0.45 V showing that the surfactant did not alter Sn onset deposition potential. This is in agreement with work carried out by Low and Walsh [78]. It should be noted that two anodic stripping peaks are observed during the reverse scan. The larger stripping peak is the oxidation of Sn^0 to Sn^{2+} that was observed at all rotation speeds. The significantly smaller stripping peak is most likely due to the stripping of Sn UPD near the electrode surface.
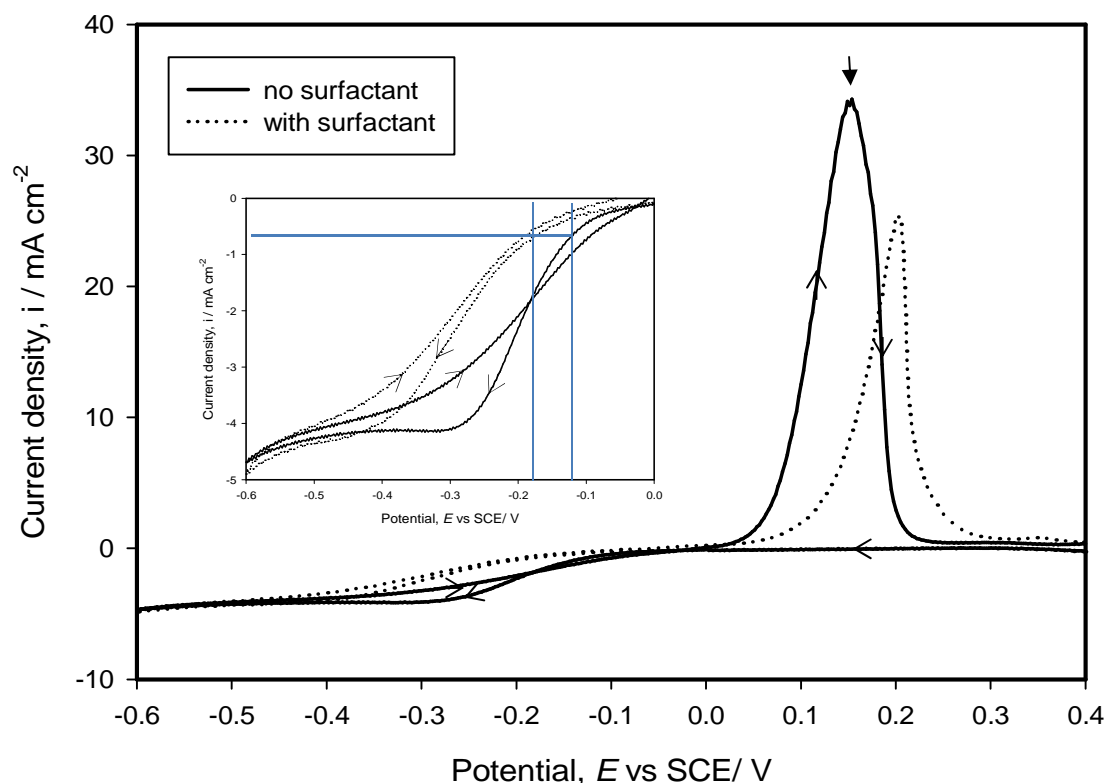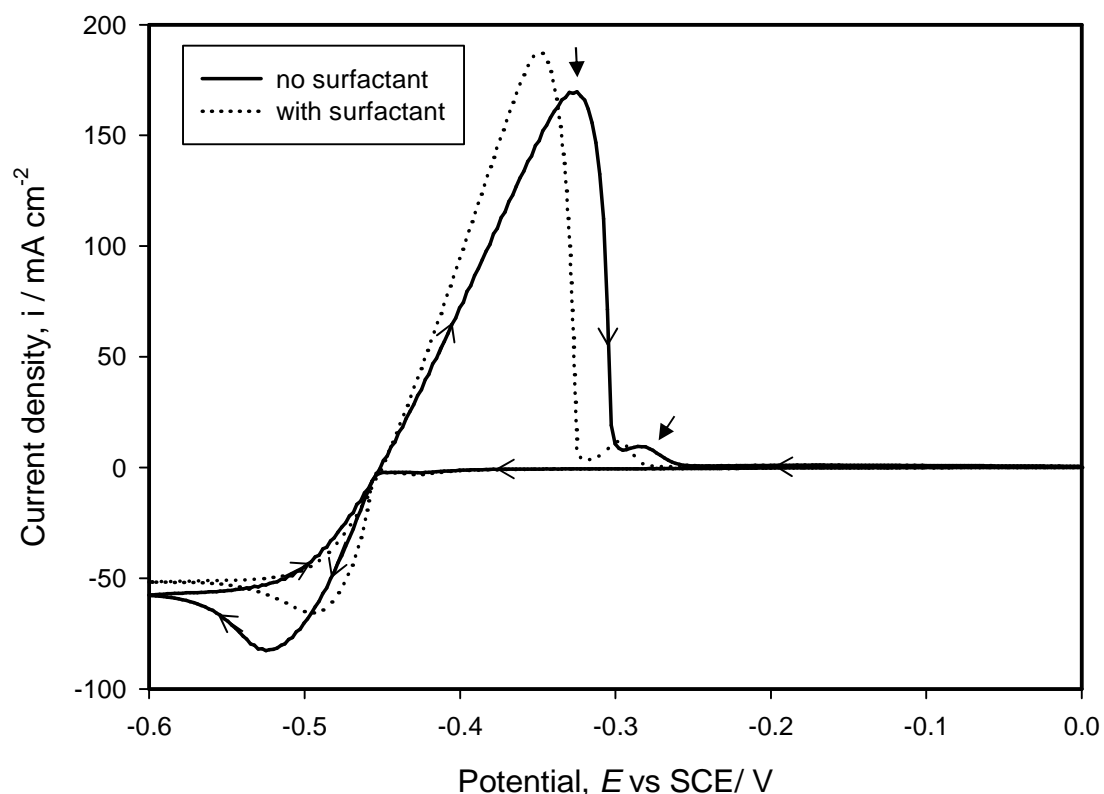

Figure 5-4 Cyclic voltammetry of 0.15 M $SnSO_4$ in 2.0 M MSA and hydroquinone antioxidant with and without surfactant. The scan rate was 50 mV s^{-1} and the RDE rotation speed was 100 rpm.

Upon closer inspection of the Sn CV, as shown in Figure 5-5b and Figure 5-6b, it can be seen that there are two distinct Sn deposition regions. In the first region, approximately -0.40 to -0.43 V, there appears to be slight Sn on Au UPD at a low current density of -2 to -6 mA cm^{-2}. This is seen more clearly in surfactant containing electrolytes, Figure 5-6b. The current density then gradually drops to -4 mA cm^{-2} as the potential is swept from -0.43 to -0.45 V. The main or "bulk" deposition of Sn then occurs when the potential is more negative than -0.45 V as seen by the large increase in current density. Figure 5-5a shows that the current density keeps on increasing as the potential is swept to -0.60 V, never reaching a limiting current density plateau indicating that the deposition of Sn is not completely diffusion controlled, but rather by mixed kinetics and mass transport controlled.

Figure 5-5c shows that on the reverse anodic sweep, a small stripping peak is observed most prominently for 100 rpm and less so for 500 and 1000 rpm, which appear as small shoulders masked by the main stripping peak. Similar to Cu, this second smaller stripping current is due to the removal of a second layer of Sn close to the electrode surface. This secondary stripping current can be seen more clearly in electrolytes containing surfactant; Figure 5-6c.

These CVs of individual metals show that the addition of surfactant increases the overpotential for deposition and stripping of Cu. On the other hand the surfactant does not affect Sn onset deposition potentials. Without the surfactant, the reduction potential of Sn and Cu were -0.45 V and -0.13 V, respectively; a reduction potential gap of 0.32 V. With the surfactant, the reduction potential of Sn and Cu were -0.45 V and -0.18 V, respectively, thereby diminishing the gap to 0.27 V; approximately 30% reduction. Therefore the inclusion of surfactant would facilitate co-deposition by lowering the difference in reduction potentials of the two individual metals. This result is similar to the findings of Low and Walsh [78]. It is proposed that the surfactant facilitates the UPD deposition of Sn, which would in turn block the deposition of Cu in that potential region; before -0.45 V.
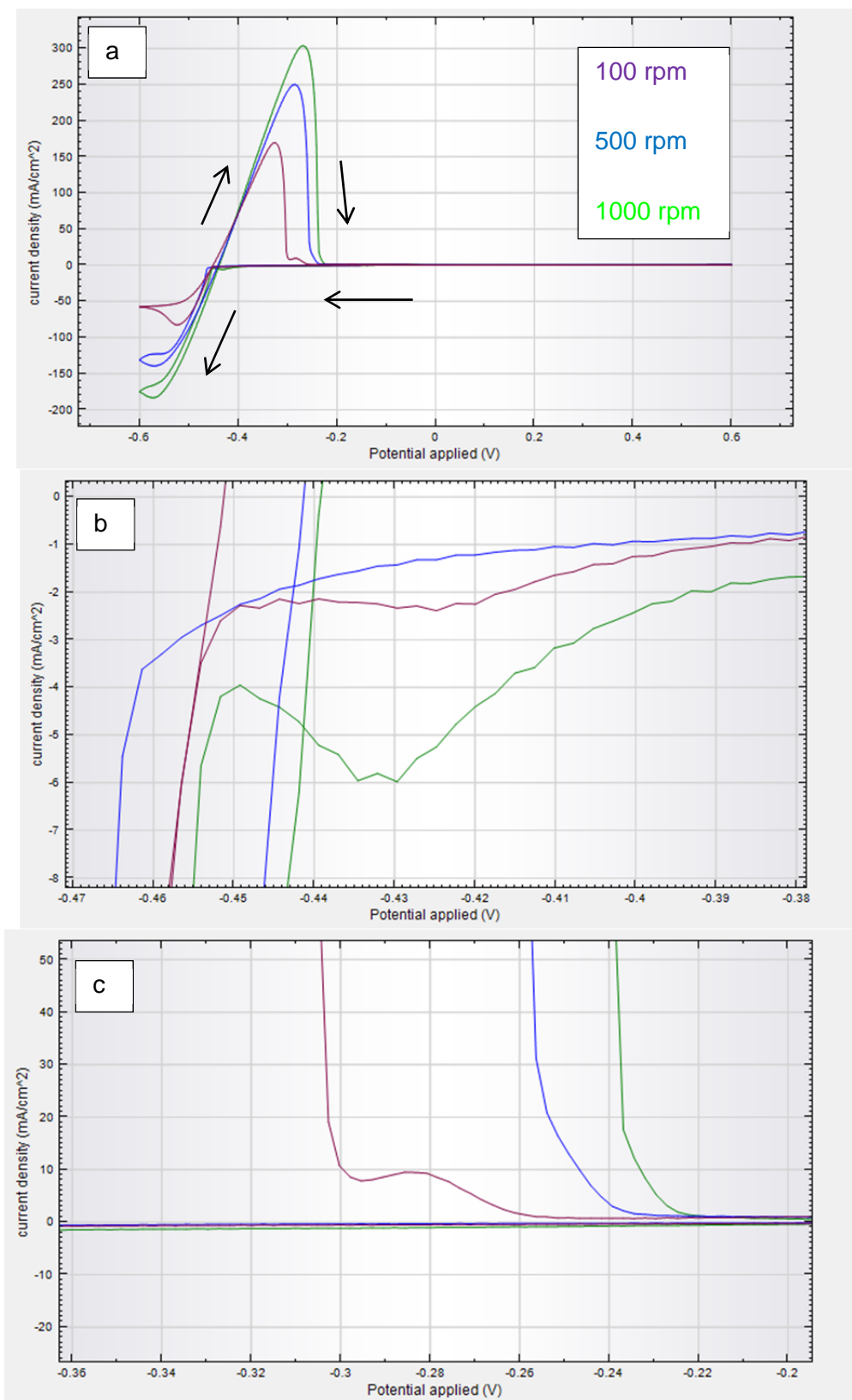
Figure 5-5 Cyclic voltammetry of 0.15 M SnSO$_4$ without surfactant. Scan rate was 50 mV s^{-1} and the RDE rotation speed was 100, 500, 1000 rpm. a) whole scan region b) under potential deposition of Sn and c) corresponding stripping peak for Sn under potential deposition.
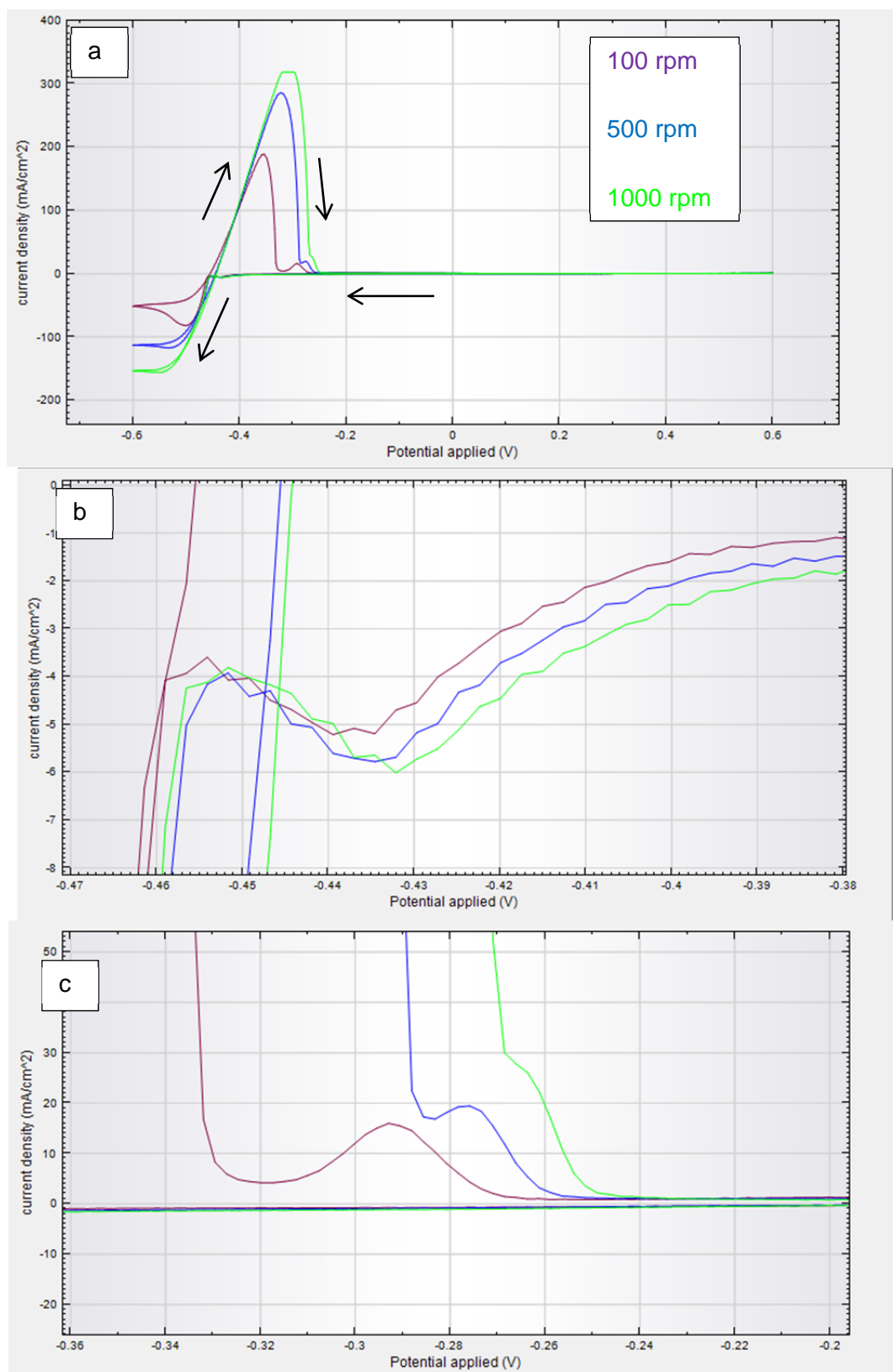
Figure 5-6 Cyclic voltammetry of 0.15 M SnSO$_4$ with surfactant. The scan rate was 50 mV s^{-1} and the RDE rotation speed was 100, 500, 1000 rpm. a) whole scan region b) under potential deposition of Sn and c) corresponding stripping peak for Sn under potential deposition.

5.1.3 Copper-Tin

Figure 5-7 shows the cyclic voltammogram for a solution containing 0.015 M CuSO$_4$ and 0.15 M SnSO$_4$. The potential was scanned from 0.20 to -0.60 V to cover the entire range of metal deposition and dissolution. The scan rate was 50 mV s^{-1} and the RDE rotation speed was varied between 100 to 2000 rpm. It can be seen that metal ion reduction commenced at a potential of approximately -0.32 V. The low current density at this potential is similar to that found in the deposition of Cu (cf.Figure 5-3 b). The current does not increase significantly within the potential window of -0.30 to -0.45 V. Once the potential reaches -0.45 V, a current-potential behaviour similar to that of Sn (cf. Figure 5-6) is observed. The absence of a limiting current density plateau suggests that, once again, Cu-Sn deposition is kinetically controlled.
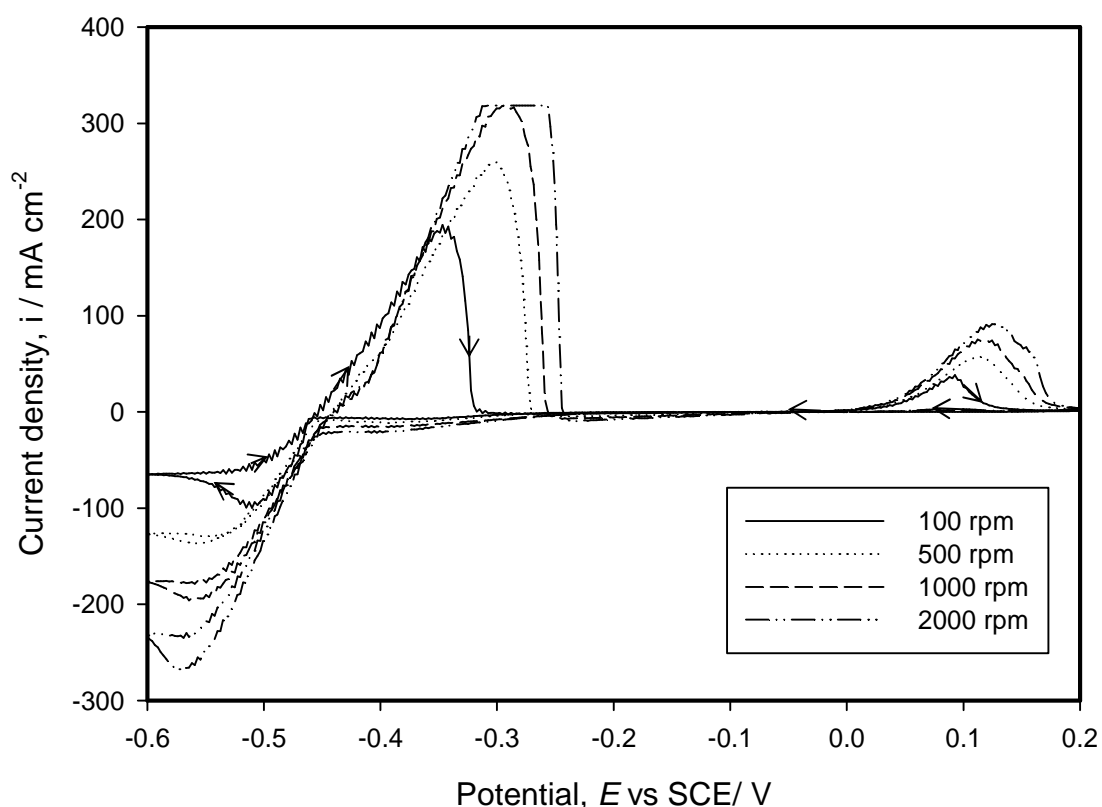
Figure 5-7 Cyclic voltammetry of Cu-Sn alloy on a Au RDE from an electrolyte composed of 0.15 M SnSO$_4$, 0.015 M CuSO$_4$, 0.01 M hydroquinone, 2.0 M methanesulfonic acid, and 0.01% vol DuPont™ Zonyl® FSN surfactant. The scan rate was 50 mV s^{-1} and the effect of varying RDE rotational speed from 100 to 2000 rpm shown.

The reverse scan shows that a large stripping peak is observed commencing at -0.45 V and ending at -0.25 V which is in the same regime as the stripping potential of Sn found in Figure 5-6. It should be noted that a Sn UPD stripping current next to the main Sn stripping current is not observed here because the deposit is Cu in the -0.30 to -0.45 V region. A smaller stripping current positive to 0.05 V was observed, which corresponds to the pure Cu oxidation peak similar to that in Figure 5-3a.

Based on these CV results, it was concluded that a potential more negative than -0.45 V was needed if one is attempting to co-deposit a Cu-Sn alloy. Progressive increase in Sn content can be expected as the deposition potential becomes more negative. It should be noted that for CV scans such as that in Figure 5-7, a layer of Cu would first be deposited which is then followed by a layer of Sn as the scan progresses and the potential becomes more negative. Strictly speaking this is deposition of multilayers forming an alloy (above -0.45 V) followed by co-deposition (below -0.45 V). The similarity in electrochemical behaviour of Cu-Sn deposition and that of the individual Cu and Sn metals indicates that this is an independent alloy plating system (c.f. Section 2.4, Figure 2-6).

5.1.4   Current Efficiency Measurements

There are two main methods in which the current efficiency of the Cu-Sn deposition process can be determined.

- direct weight measurement of the deposit
- charge balance analysis

Assuming 100% current efficiency, the theoretical weight that the deposit should have is directly proportional to the amount of charge passed and the total deposition time as described by Faraday's law. The actual weight of the deposit obtained during experiments can then be compared to this theoretical value and the current efficiency calculated accordingly.

However, as the RDE has a very small active surface area in which the metals can actually be deposited, the amount and weight of deposits is very small. In most cases approximately only 1 mg of deposit was observed and it was difficult to compare the

current efficiency across different set of experiments. Therefore, it was concluded that an alternative current efficiency evaluation method was needed.

A charge balance analysis was carried out with data obtained from the cyclic voltammograms to determine the current efficiency of the deposition process. This was done by integrating the current vs. time data of the CVs in forward and reverse scans presented in Figure 5-7. In order to calculate the charge consumed, one has to realise that the potentiostat data acquisition rate varies depending on the scan rate. This "time constant" is named as such because it remains constant at a specific scan rate. The time constant is defined as the interval of time between two adjacent data points, i.e. how long the machine pauses before the next data point is recorded. Data acquisition steps can be visualised as:

[data point n]…time constant…[data point n+1]...time constant…[data point n+2]…

The time constant is automatically set by the potentiostat depending on the scan rate and their relationship is summarized below in Table 5-2.

Scan rate (mV s^{-1})	Time constant (s)
15	0.16
25	0.10
50	0.05
100	0.02

Table 5-2 Scan rate and corresponding time constant.

For example, this means that at a scan rate of 50 mV s^{-1} the current measured at each data point is measured for 0.05 s before moving on to the next data point. The charge (Q), therefore, is the product of the current (i) measured at each data point and the time constant (t), i.e. $Q = it$. The total charge is the summation of all the individual charges throughout the whole scan range. Any current or charge with a negative value (below zero on the y-axis) is defined as cathodic while those with positive values are defined as anodic.

The forward scan corresponds to the total cathodic charge (Q_{cc}) that was consumed to deposit the metals on the RDE. The reverse scan shows the total combined anodic charge (Q_{ac}) needed to strip the metal deposits back into the electrolyte. The current efficiency is calculated as:

$$\text{Current efficiency (\%)} \ = \frac{\text{total deposition charge} \ (Q_{cc})}{\text{total stripping charge} \ (Q_{ac})} x100 \qquad (5.2)$$

Using current data from Figure 5-7, the plot of charge consumed vs. time can be created and is shown in Figure 5-8 . The current efficiency of the Cu-Sn deposition, as derived for the potential window between 0.20 V and -0.60 V, ranged between 87% and 92%.
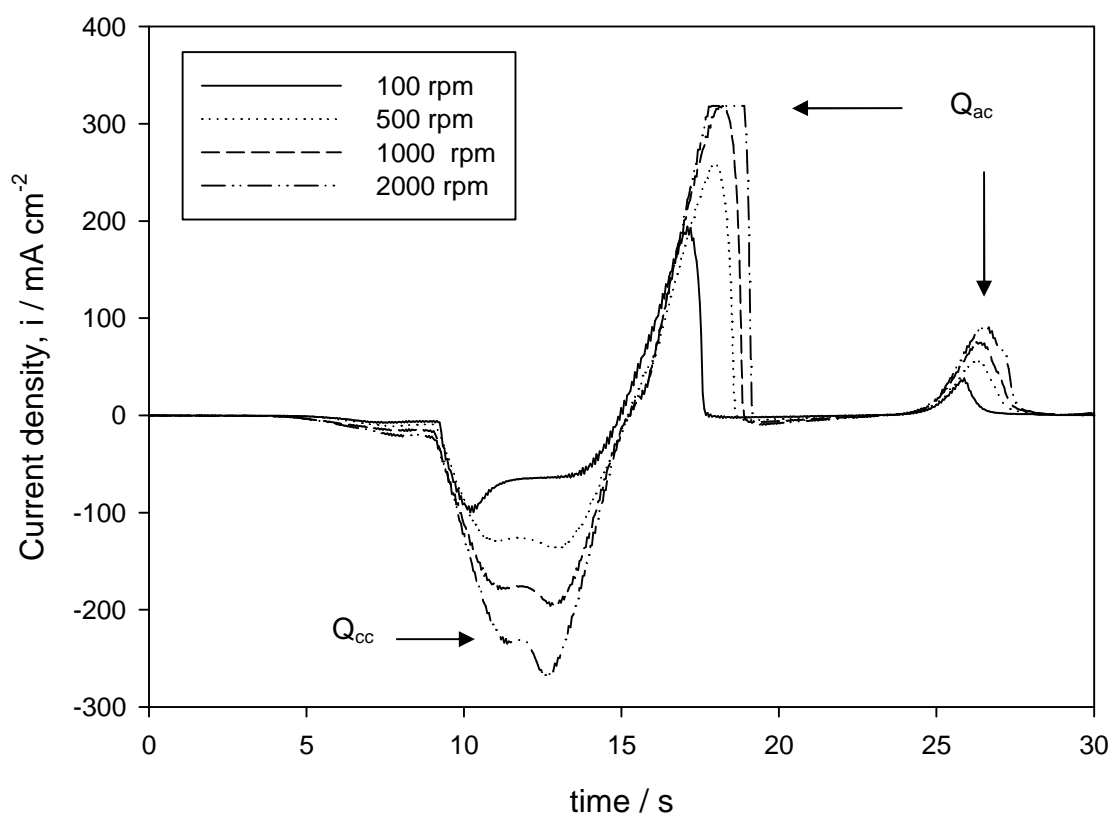
Figure 5-8 Current efficiency of Cu-Sn alloy plating calculated by comparing the anodic charge (Q_{ac}) to the cathodic charge (Q_{cc}) vs. time. A maximum current efficiency of 92% could be obtained at the RDE rotation speed of 1000 rpm. The scan rate was 50 mV s^{-1} and the effect of varying RDE rotational speed is shown.

5.2 Chronoamperometry

Once the potential range in which the co-deposition of Cu-Sn alloys has been established, chronoamperometry (CA) was carried out to determine the current densities that should be applied to obtain acceptable deposits. Potentiostatic deposition in the range of -0.30 to -0.50 V were conducted for these chronoamperometry experiments and the deposition current noted. Anodic stripping voltammetry was then carried out to determine the amount of metal deposited by sweeping anodically from -0.45 to 1.0 V.

Once it was determined that co-deposition of the two metals could be carried out with relatively high current efficiency, CA was carried out in the region of -0.41 to -0.50 V, the potential window where both Cu and Sn are reduced. In these CA experiments, the potentials were fixed at each chosen potential, i.e. between -0.41 V and -0.50 V, in decrements of -0.10 V, and electrodeposition was then carried out for 300 s. The disc rotation speed in these experiments was set at 100 rpm. Plots of current density vs. time for each of these experiments are shown in Figure 5-9 and can be divided into three main potential regions:

- Region a, -0.41 to -0.44 V
- Region b, -0.45 to -0.47 V
- Region c, -0.48 to -0.50 V

5.2.1 Region a, -0.41 to -0.44 V

Figure 5-9a shows the current transient as a function of time as well as the deposit microstructure, obtained through a light microscope. At -0.41 V the current transient steadily decreases, reaching a value of approximately -2.7 mA cm^{-2} after 300 s. The appearance of the deposit was red, indicative of Cu deposition. Interestingly, as the potential is made increasingly cathodic, i.e. lowered to -0.42, -0.43 and -0.44 V, the current drops to a very small value, about -0.4 mA cm^{-2}, showing that surface reactions are inhibited in this potential regime. As the potential is progressively lowered to -0.42, -0.43 and -0.44 V, the deposit appears thin and uneven, revealing the underlying surface of the RDE. These images confirm CA data which shows that Cu deposition is impeded in this potential region.

An initial raising current transient trace can be seen in the first few seconds of Figure 5-9a. This can be explained by the fact that at the very beginning of the experiment there is a relatively large potential jump from the open circuit potential to the applied potential of -0.41 V. The current recorded in this early stage quickly decays towards zero unless it is being consumed to deposit any Cu. This is the reason why over a longer period of time the current transient for -0.41 V eventually drops as Cu is being deposited. However, for -0.42 to -0.44 V, the region where the surfactant is blocking the electrode surface, the current transient does not change as no significant amount of Cu is depositing.

5.2.2 Region b, -0.45 to -0.47 V

Figure 5-9b shows the CA data at potentials below -0.45 V. A current density just below -15 mA cm^{-2} is obtained at -0.45 V, greater than the limiting current for Cu reduction. The deposit was grey showing that Sn was being co-deposited. As the potential was lowered further to -0.46 and -0.47, higher currents were observed reaching up to -90 mAcm^{-2}. The micrographs corroborate with CA data which shows that deposits obtained between -0.45 to -0.47 V cover the entire surface of the electrode, as would be expected when the deposition current is higher than that those observed between -0.42 to -0.44 V (Figure 5-9a).

5.2.3 Region c, -0.48 to -0.50 V

At still lower cathodic potentials, the current transient continued to increase with time as is shown in Figure 5-9c. At -0.48 and -0.49 V, the cathodic current increased up to -175 mA cm^{-2} over the 300 s deposition period, never reaching a plateau, as was observed for -0.47 V (Figure 5-9b). As the potential was decreased further to -0.50 V, the current transient appears to level out and stabilise at approximately -112 mA cm^{-2}. The deposits for this potential range, i.e. -0.48 V to -0.50 V were visibly rough and a detailed microstructural analysis was not feasible.
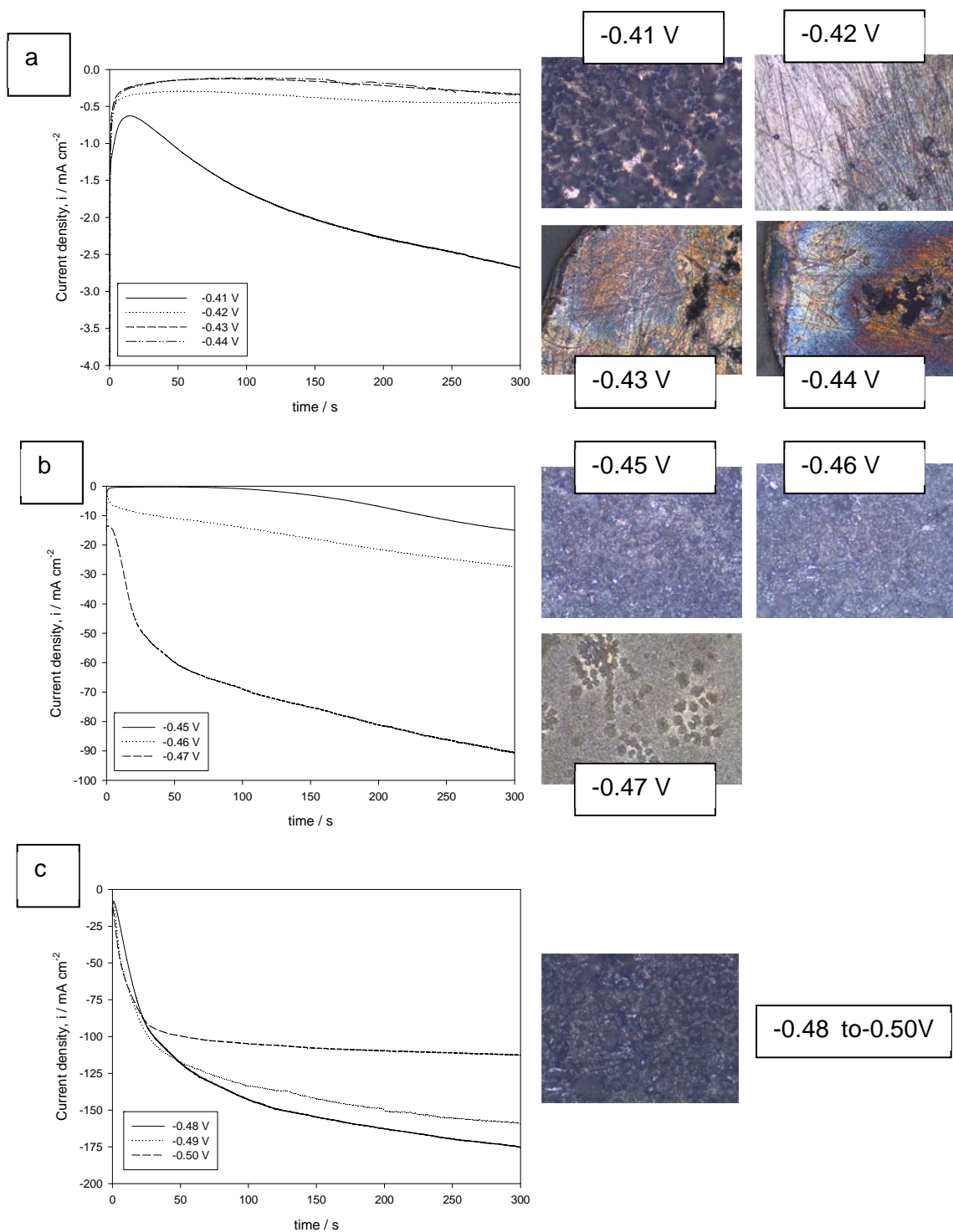
Figure 5-9 Chronoamperometry showing metal deposition at various fixed potentials from a) -0.41 to -0.44 V b) -0.45 to -0.47 V and c) -0.48 to -0.50 V carried out for 300 s. RDE rotation speed 100 rpm.

5.3   Anodic Stripping Voltammetry

Anodic stripping voltammetry experiments were carried out to determine the relative content of Cu and Sn in the alloy and the current efficiency of deposition in the experiments shown in Figure 5-9a and b. This was done by integrating the charge under the Cu and Sn stripping peaks and comparing them to the total charge consumed during the CA experiments. The method used was the same as that described earlier in Section 5.1.4 to find the current efficiency from Figure 5-8. Typical stripping peaks for the deposit obtained in the CA experiments are shown in Figure 5-10. As shown in Figure 5-10, only Cu stripping peaks are observed up to potentials of -0.44 V. The stripping peak as well as the area underneath the peak is much greater for -0.41 V. The stripping currents for Cu between -0.42 to -0.44 V are roughly similar, but are much lower than that at -0.41 V. The curve for -0.45 V is different in that stripping peaks for both Sn and Cu are observed and Cu deposition rates are also increased at this potential.
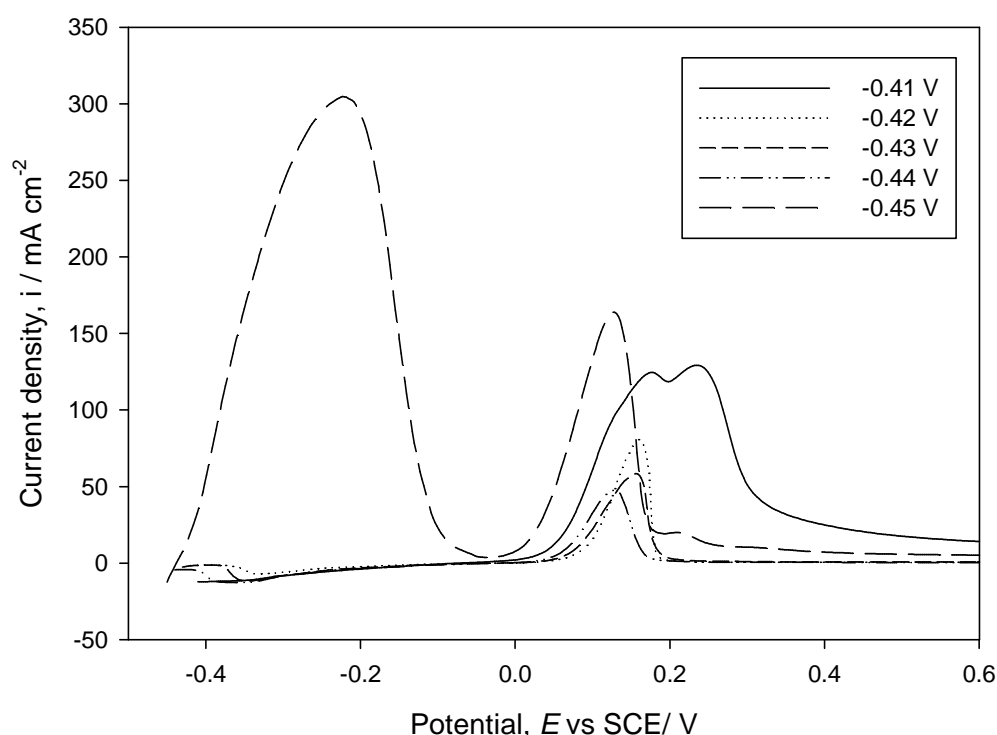
Figure 5-10   Anodic stripping voltammetry of the deposits obtained at fixed potentials from chronoamperometry experiments. The scan rate was 15 mV s^{-1} and the RDE rotation speed was 1000 rpm.

Results in Figure 5-10 correlate with those in Figure 5-9 and they confirm the validity of one another on two main issues. The first is that the surfactant is binding to the electrode surface and suppressing Cu deposition in the potential range of -0.42 to -0.44 V. Low current transients in Figure 5-9a is consistent with relatively small Cu stripping peaks in Figure 5-10. The second is that onset Sn deposition and Cu-Sn co-deposition occur at -0.45 V. Decreasing current transient in Figure 5-9b is consistent with a large Sn stripping peak and relatively large Cu stripping peak as well.

Table 5-3 compares the stripping charge associated with each metal in columns 3 and 4 to the total deposition charge in column 2 in order to calculate the current efficiency of deposition in the CA experiments. The current efficiency is calculated by dividing the combined total stripping charge for both metals by the charge consumed during deposition. Additional information of these calculations can be found in Appendix A. Columns 3 and 4 show typical charges consumed in CA experiments while the current efficiency and charge consumed by each metal in columns 5-7 are averages of three separate CA experiments. Calculations from these data showed that the current efficiency for Cu ranges between 43% - 58% in the region of -0.41 to -0.44 V. These results indicate that not only is Cu deposition suppressed within this potential range, but also that the current is being consumed by other surface reactions, even though at a very low rate (because the currents are small). The current efficiency increases to 92% when Sn co-deposition, commences, i.e. at -0.45 V. The current efficiency remains high, i.e. up to 95%, even when higher overpotentials of -0.46 and   -0.47 V are used.

Potential (V)	Charge consumed during deposition $(C\ cm^{-2})$	Stripping charge $(C\ cm^{-2})$		Current efficiency (%)	Contribution of deposition charge consumed by each metal (%)		Cu/Sn content in alloy $(\pm 3\%)$
		Cu	Sn		Cu	Sn	
-0.41	0.56	0.24	-	43±8	100	-	100/0
-0.42	0.12	0.07	-	58±9	100	-	100/0
-0.43	0.06	0.03	-	50±2	100	-	100/0
-0.44	0.06	0.03	-	50±3	100	-	100/0
-0.45	1.49	0.13	1.24	92±3	8±1	77±3	9/91
-0.46	5.50	0.14	5.11	95±2	2±1	88±3	2/98
-0.47	6.34	0.44	5.52	94±4	7±3	82±2	8/93

Table 5-3   Charge consumed for the deposition and stripping of Cu and Sn during chronoamperometry experiments with potentials in the range of -0.41 to -0.47 V. The RDE rotation speed was 100 rpm and the deposition time was 300 s.

Alloy composition, as shown in the last column of Table 5-3, was determined from the individual metal stripping charges divided by the combined total stripping charge of columns 6 and 7. Between -0.41 to -0.44 V the deposit consists solely of Cu. At -0.45 V an alloy containing 89% Sn is obtained. At -0.46 and -0.47 V the Sn content in the alloy rises to 97 and 93 wt%, respectively. Based on these findings, it can be concluded that a high Sn:Cu ratio, i.e.90% and above, can be obtained if the potential were set more negative than -0.45 V.

6. RESULTS: ELECTRODEPOSITION

Electrochemical characterisation carried out in Chapter 5 provided insights into the potential as well as current density ranges where the co-deposition of Cu-Sn alloys occur. Electrodeposition can be carried out through either potentiostatic (fixed potential) or galvanostatic (fixed current) methods. However, in commercial industrial settings the galvanostatic technique is preferred since the deposit thickness can be controlled according to Faraday's law; the amount of metal deposited is directly proportional to the charge applied. Therefore, galvanostatic deposition was the technique used in this last stage of research where an industrially useful methodology for Cu-Sn deposition is developed. The aim of this chapter is to determine whether acceptable Cu-Sn deposits could be obtained from MSA electrolytes through direct current (DC) plating and pulse plating (PP) methods.

6.1 Galvanostatic Electrodeposition Strategy

The current densities recorded from chronoamperometry experiments in Chapter 5 were used as a guide to determine the current densities that should be applied for galvanostatic electrodeposition. However, those experiments were carried out at an RDE, which is an instrument used mainly in laboratory settings only. In industry, actual electrodeposition would be carried out on a flat stationary electrode. Current densities recorded from a rotating electrode would not be directly comparable. In order to directly translate the current density from RDE experiments to those of a stationary electrode, the RDE speed can be set to zero (not spinning at all) to make it a stagnant stationary electrode system as well.

Unfortunately, this zero speed RDE option was ruled out due to the nature of the experimental instrument. The RDE unit contains small spring-loaded contact brushes inside the rotating shaft. These brushes provide electrical contact with the rotating shaft which is in turn connected to the removable RDE tip. In normal operation modes the shaft rotates and this electrical contact is maintained. However, when the shaft is not rotating a constant electrical contact is not maintained which would lead to incorrect measurements being obtained. Therefore, it is not advisable to run RDE experiments at zero rotation speed, i.e. an RDE spinning at whatever speeds (low or high) is better than it being stationary at zero rpm.

It was concluded that the RDE should be rotating at a minimum speed which would allow accurate measurements to be made. To fulfill this requirement, the RDE speed should also result in limiting current densities that would be comparable to that of a stagnant electrode system.

The RDE speed (ω, angular velocity) affects the limiting current that will be observed according to equation 6.1

$$i_{L,RDE} = 0.62zFCD^{2/3}v^{-1/6}\omega^{1/2}$$

(6.1)

The limiting current density for an RDE at 100 rpm was calculated to be approximately 4.4 mA cm^{-2}. This was determined by using values of z = 2, F = 96485 C mol^{-1}, C = 0.015 M, D = 6.5 x 10^{-6} cm^2 s^{-1}, v = 1.0 x 10^{-2} cm^2 s^{-1}, and ω = 100 rpm.

The limiting current density at a stagnant vertical electrode can be determined from equation 6.2

$$i_{L,DC} = zFD\frac{c_b}{d_s}$$

(6.2)

Studies at vertical electrodes have shown that the diffusion layer δ_s is approximately 50 μm [94]. The limiting current density at the stagnant 1x1 cm long electrode was calculated to be approximately 3.9 mA cm^{-2}, which is similar to that of the RDE rotating at 100 rpm. Since the strategy is to determine which RDE rotation speed would give a limiting current density that would be comparable to a stationary electrode, it was concluded that RDE experiments carried out at 100 rpm gave limiting current densities that were comparable to a stagnant electrode system.

Previous chronoamperometry data suggested that Cu-Sn co-deposition occurs when the applied current density is greater than 20 mA cm^{-2} (*cf.* Figure 5-9b). At lower current densities (Figure 5-9a) only copper was plated while at higher current densities (Figure 5-9c) the deposit became rough and powdery and did not adhere well to the electrode surface. However, it must be noted that the deposits obtained in chronoamperometry experiments were through potentiostatic deposition. In order to assess whether the same current densities can be used in galvanostatic DC plating, preliminary deposition experiments on vitreous carbon were carried out, which are shown in Figure 6-1.
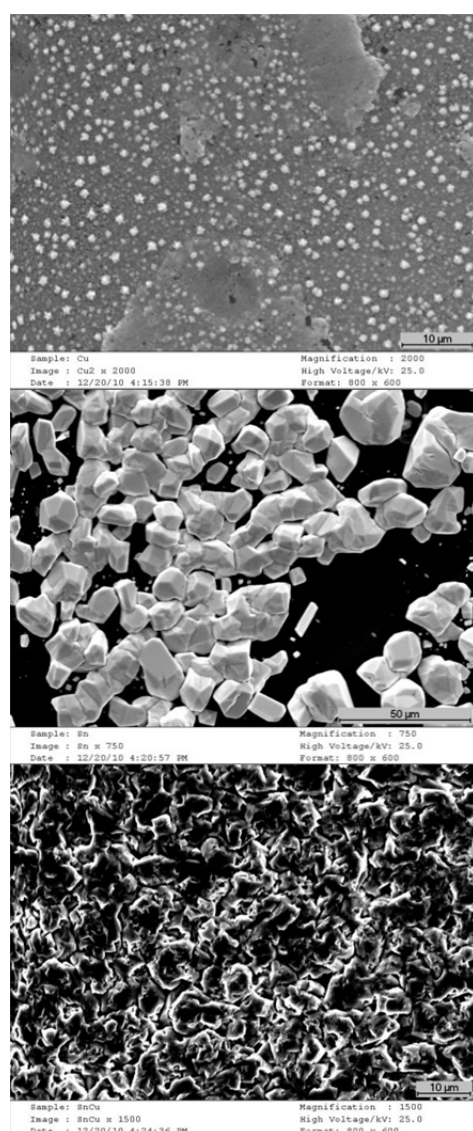
a) Bright Cu from Cu only bath

b) Sn crystals from Sn only bath

c) Matte Cu-Sn from Cu-Sn bath

Figure 6-1 SEM images of a) Cu, b) Sn, and c) Cu-Sn deposits on vitreous carbon. The plating time was 600s and the current densities were 3, 20, and 25 mA cm^{-2}, respectively.

Figure 6-1 confirms that the current densities measured at an RDE with the rotation speed of 100 RPM are comparable to and can be used to plate Cu-Sn alloys on stationary vitreous carbon electrodes. Cu, Sn, and Cu-Sn were depositing at the same current densities in both chronoamperometry and electrodeposition at a stationary electrode. Figure 6-1a shows that bright Cu deposits with strong surface adhesion can be deposited on vitreous carbon. Figure 6-1b, on the other hand, shows a very important characteristic of Sn deposition which is its propensity to form large crystals on an amorphous substrate such as vitreous carbon. This leads to poor surface coverage as the Sn crystals de-adhere from the surface when washed and the underlying substrate can be seen as dark contrast regions. The microstructure of Cu-Sn as seen in Figure 6-1c is drastically different from the other two cases and was used as a quick visual confirmation that co-deposition of Cu-Sn has occurred.

It should be noted that the working electrode or substrate used for deposition should not interact chemically with the electrolyte or the metal deposits themselves. For this reason, inert materials such as Au, Pt, and vitreous carbon are usually used. Vitreous carbon is a commonly a good choice due to its relatively low cost and ease of cleaning which creates a very reproducible surface.

Vitreous carbon is also known as glassy carbon as its surface has a glass-like appearance. This substrate has proven to be a good choice for Cu, but not for Sn deposition due to their different modes of nucleation and growth (c.f. Section 2.2.2, Metal Nucleation). It is proposed that on a very flat and smooth surface such as glassy carbon, the progressive nucleation of Cu is followed by rapid surface diffusion. This surface diffusion results in a smooth and uniform growth of Cu deposit across the whole substrate, as seen in Figure 6-1a.

On the other hand, Sn has a propensity towards instantaneous nucleation and surface diffusion is limited. This means that Sn would preferentially nucleate and grow on top of each other and not diffuse across the whole substrate. Sn crystals would continue to grow bigger on top of existing nucleation sites leading to poor surface coverage as seen in Figure 6-1b. However, in the case of Cu-Sn where the two metals co-deposit, a combination of nucleation and growth effects are seen which results in complete surface coverage but at the cost of surface smoothness; Figure 6-1c.

6.2 Direct Current Plating

Further experiments were carried out to determine the optimal applied current density in order to achieve acceptable deposits both in terms of thickness and microstructure. Table 6-1 summarizes the effect of increasing current density on the quality of the deposits.

Current Density (mA cm^{-2})	Sn (wt%)	Cu (wt%)	Thickness (µm)	Remarks
3	-	Cu only	1	Bright Cu
20	Sn only	-	N/A	Sn crystals
22	96	4	8.00	Best deposit
24	96	4	7.36	Rough
26	97	3	2.59	Patchy
28	96	4	2.95	Powdery

Table 6-1 Variation of deposit thickness and microstructure as a function of applied current density in the range of 3-28 mA cm^{-2}.

From Table 6-1 it was determined that the ideal current density for DC plating is 22 mA cm^{-2} as it resulted in matte deposits with even coverage. At a slightly higher current density, 24 mA cm^{-2}, large black Sn crystals started to form along the edges of the vitreous carbon electrode. This is indicative of the applied current density being higher than the limiting current density which would result in loose individual crystals. In some cases, these crystals eventually grew sufficiently larger and fell off the edges to bottom of the glass cell. This phenomenon is due to the fact that the current at the edge is usually higher. As expected, in this case it can be seen that the deposits are growing much faster along the edges compared to growth perpendicular to the electrode surface.

At 26 mA cm^{-2} and beyond the deposits became rough and more powdery, and were washed off during the cleaning stage. Over the entire electrode surface underneath the rough deposit, a shiny adherent metallic Sn layer was observed on the surface even when these large crystals were washed off. It must be noted that current efficiency data is not shown in this table as most of the tin deposits did not adhere well enough and some portion of the deposit was lost due to washing. A meaningful interpretation, therefore, was not possible. Earlier RDE experiments indicated that a 90% current efficiency is normally obtained during Cu-Sn co-deposition.

6.2.1 DC Deposit Thickness

Figure 6-2 shows cross-section SEM images of the co-deposited Cu-Sn alloy at a vitreous carbon electrode. It can be seen in Figure 6-2a that after a deposition time of 600 s the deposit has a polycrystalline structure with an average thickness of 8 μm. Longer deposition times of 1800 s (Figure 6-2b) resulted in increased thickness of up to 28 μm which was rough and less compact.

Four repeats of the deposition experiments were carried out to test the reproducibility of these galvanostatic experiments. The deposit microstructure was found to be very similar to those shown in Figure 6-1a and 6b for the two different deposition times. The tin content in the deposits was found to be consistently at 96±1 wt.% for all cases. The thickness of Cu-Sn for the two different deposition times were found to be 8±1 μm and 28±2 μm.
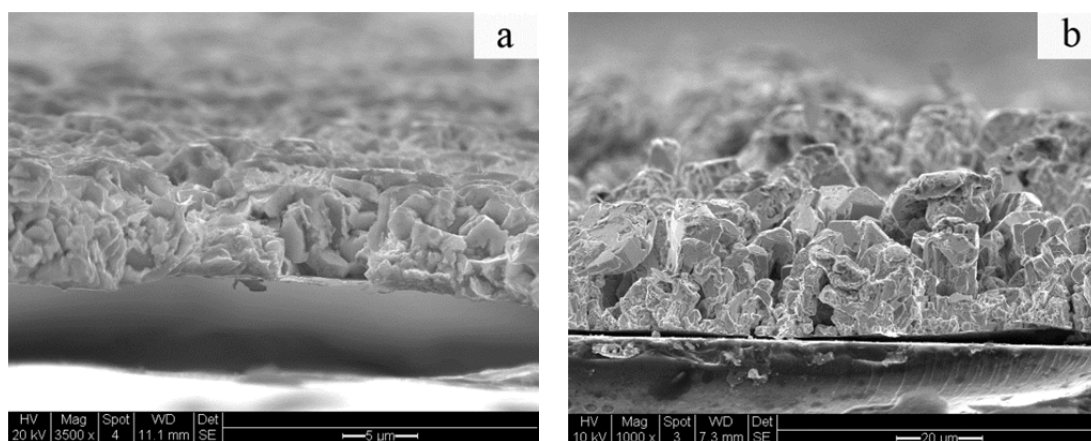
Figure 6-2 Cross section of Cu-Sn deposited on vitreous carbon at 22 mA cm^{-2} for a) 600 s, 8 μm thick and b) 1800 s, 28 μm thick.

Taking into account the reproducibility of the deposit microstructure, composition, and thickness, deposition carried out at 22 mA cm^{-2} could be scaled up for industrial processes.

6.2.2 DC Crystalline Structure

Figure 6-3 is the XRD pattern of vitreous carbon showing a broad peak due to the amorphous nature of the substrate. The three main broad peaks can be seen at approximately 2Θ = 25, 43, and 79°. It was found that for XRD analysis the deposit has

to be sufficiently thick (at least 5 μm) otherwise signals arising from the vitreous carbon substrate is detected. Therefore, to ensure that XRD signals are only arising from the deposit and not the vitreous carbon substrate, the deposition time was set to 1800 s for all samples that would undergo XRD analysis. It should also be noted here that vitreous carbon, Cu, Sn, and Cu-Sn all share a common peak which is at approximately $2\Theta = 43°$, and therefore other peaks should be used to identify the presence or absence of each individual metal and alloy.
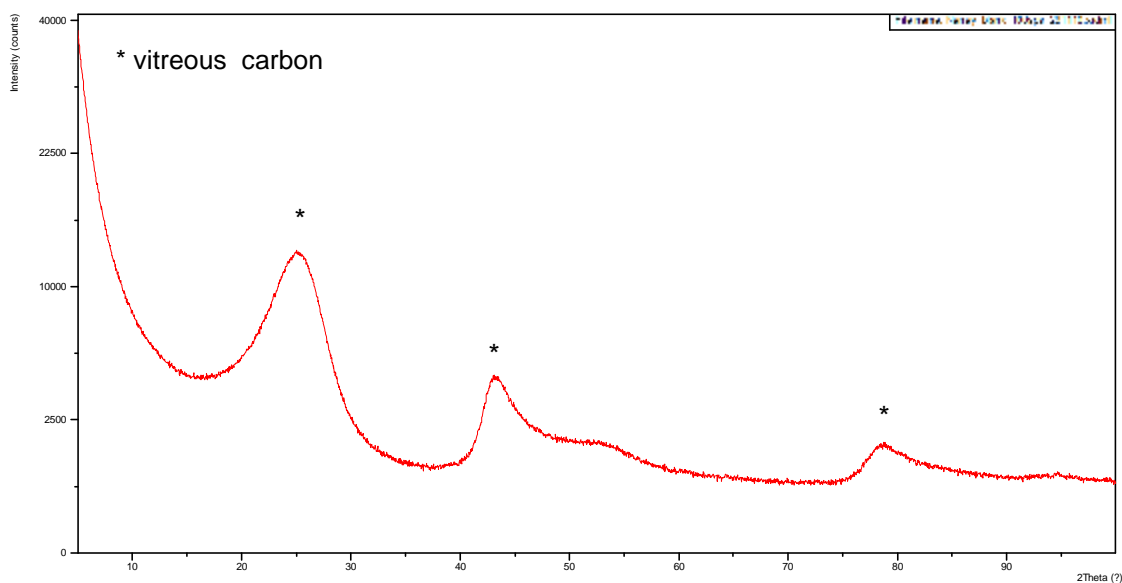
Figure 6-3 XRD pattern of vitreous carbon. The broad wide peaks are indicative of the amorphous nature of the substrate.
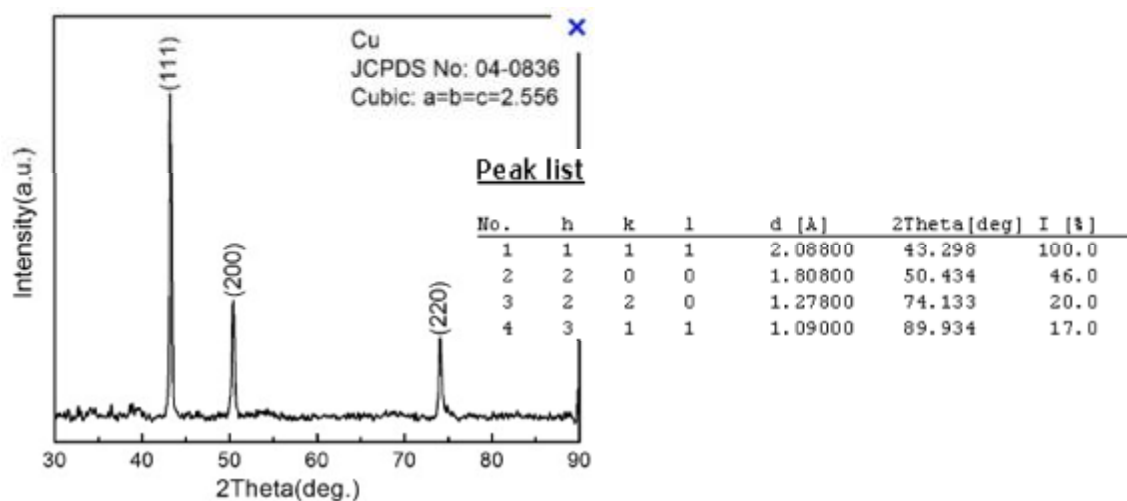
Figure 6-4 Cu XRD pattern from International Centre for Diffraction Data (ICDD) database.

110

Figure 6-4 shows the XRD pattern of pure Cu taken from the ICDD database which indicates that Cu deposits are very crystalline with three main sharp peaks. The simplicity of the Cu XRD pattern means that the presence of Cu can be easily identified in any sample.

Figure 6-5shows the XRD pattern of a) Cu b) Sn, and c) and d) Cu-Sn deposits in their corresponding electrolytes containing individual metal salts and both salts, respectively. All bath components were the same except that only either copper (0.015 M) or tin (0.15 M) was added to the electrolyte for individual metal deposition. The concentration of the individual metals reflects the concentration of the metals found in the final bath used for Cu-Sn co-deposition.
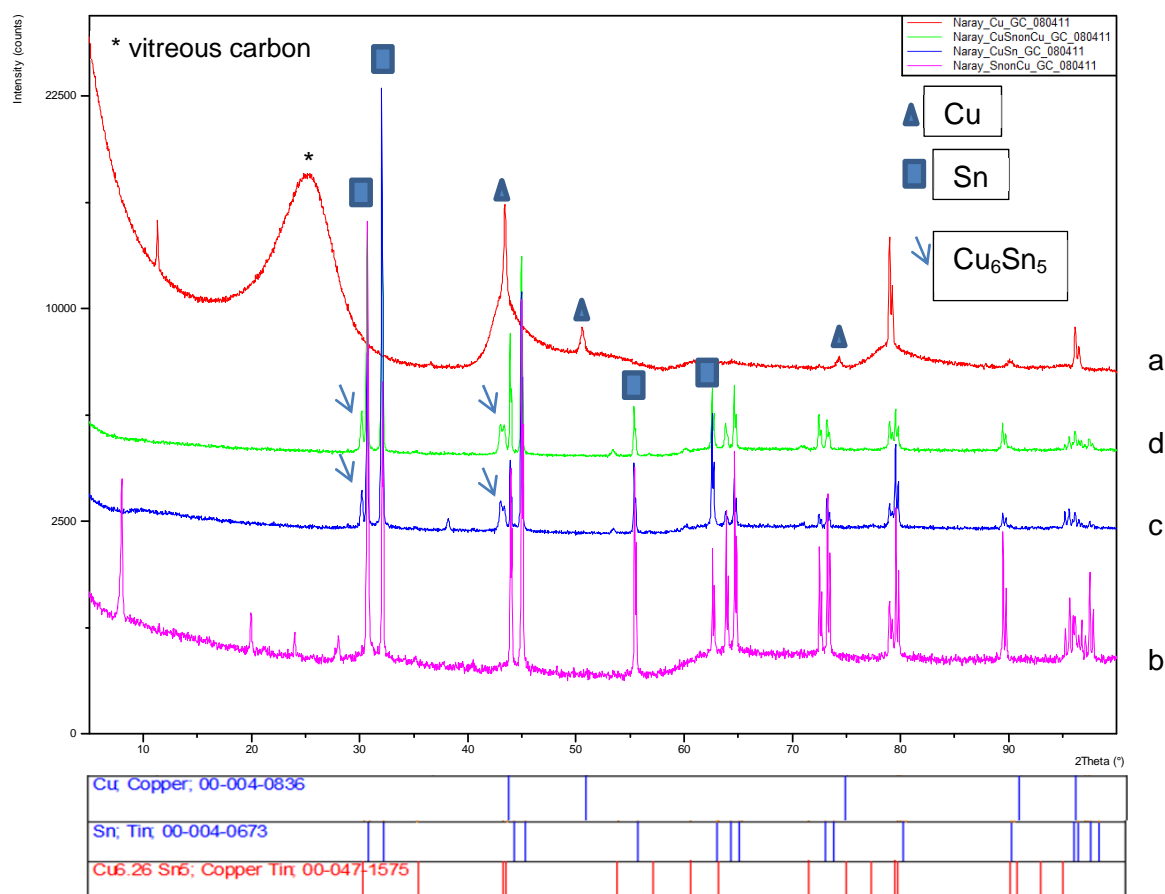
Figure 6-5 XRD pattern of DC plated a) Cu b) Sn on Cu c) Cu-Sn on vitreous carbon and d) Cu-Sn on Cu. Characteristic Cu_6Sn_5 peaks are denoted by arrows.

A current of 3 mA cm^{-2} for copper, 20 mA cm^{-2} for Sn, and 22 mA cm^{-2} Cu-Sn was used in these experiments. Cu and Cu-Sn could be deposited directly onto the vitreous carbon surface. Tin, however, did not adhere to vitreous carbon. In order to solve this

problem, a base layer of copper was plated for 1800 s before tin deposition was plated on top of this Cu layer. Cu-Sn was also deposited on copper to observe whether this copper underlayer would have any influence on the crystal structure of the deposits.

Cu XRD pattern shown in Figure 6-5a exhibits many broad peaks due to the fact that the maximum Cu deposit thickness that could be obtained was relatively thin at 3 μm. It was earlier noted that ideally the deposit thickness for XRD analysis should be at least 5 μm otherwise signals arising from the substrate will be observed which is the case here for Cu deposition. We were not able to deposit very thick Cu layers even after 1800 s. This is most likely due to the fact that Cu can only be deposited at low current density (3 mA cm^{-2}) and hence a very low deposition rate. Cu deposits may be dissolved back into the deposit at a similar rate, hence the thickness cannot grow. Sn and Cu-Sn are deposited at a much higher current density (>20 mA cm-2) and higher deposition rate so this thickness growth was not a problem.

The broad peaks observed in the Cu XRD pattern are characteristic Cu on amorphous glassy carbon substrate. Sn and Cu-Sn deposits show very sharp peaks indicative of a high degree of crystallinity. Broader peaks of the amorphous carbon substrate were not observed in these cases because these deposits were significantly thicker, i.e., >8 μm. The three main Cu peaks at 2Θ = 43, 50, and 74° can be seen in Figure 6-5a. However, due to the relative thinness of the copper deposit, the copper XRD signal at 2Θ = 25° has been completely masked by the broad vitreous carbon peak. At 2Θ = 43° both Cu and vitreous carbon peaks can be seen overlaid on top of each other resulting in a wide base with a sharp peak. At 2Θ = 50 and 74° the Cu peaks are still present but at a much lower intensity compared to data from the ICCD database.

Sn XRD pattern shown in Figure 6-5b indicates that tin has the tendency to form crystals during deposition and is not influenced by the substrate underlayer. There are no broad peaks arising from vitreous carbons and no copper peaks from the underlayer were visible. The crystalline structure of Sn was not influenced by the Cu underlayer. It should also be noted that an impurity was present, which lead to the four peaks below 2Θ = 30°. This impurity, $FeCl_3$, was the chemical used to clean the deposit off the glassy carbon surface. In this case it was not properly washed off and a small amount was still present in the deposit. No significant peaks above 2Θ = 30° due to $FeCl_3$ were detected in this sample that would have interfered with the analysis. A complete XRD peak list of the impurity can be found in Appendix B.

Cu-Sn XRD pattern shown in Figure 6-5 signal c and signal d indicates that Cu-Sn deposits are composed of two main phases; tin and a Cu_6Sn_5-like phase. No other Cu-Sn intermetallics were identified in the Cu-Sn samples. Peak intensity analysis shows that the deposit is composed mainly of tin and approximately 5% Cu-Sn intermetallic. No Cu XRD peaks were found and it is assumed that pure copper is not present in the deposit. Data from EDX analysis showed that copper content in the deposit is only 3-4% so it would appear that almost all of the Cu found is in this Cu_6Sn_5-like phase. The peaks assigned to Cu_6Sn_5 have much lower peak intensities than peaks assigned to Sn. Therefore, it can be said that the composition data are in good agreement with the results of the phase analysis.

Copper deposited from the MSA electrolyte has a face centered cubic crystal structure, tin was tetragonal, and the Cu_6Sn_5-like phase had a hexagonal crystal structure. The different types of crystal structures are shown in Figure 6-6 and their crystallographic parameters or physical dimensions of their unit cells are summarized in Table 6-2.

| Cu | Sn | Cu-Sn |
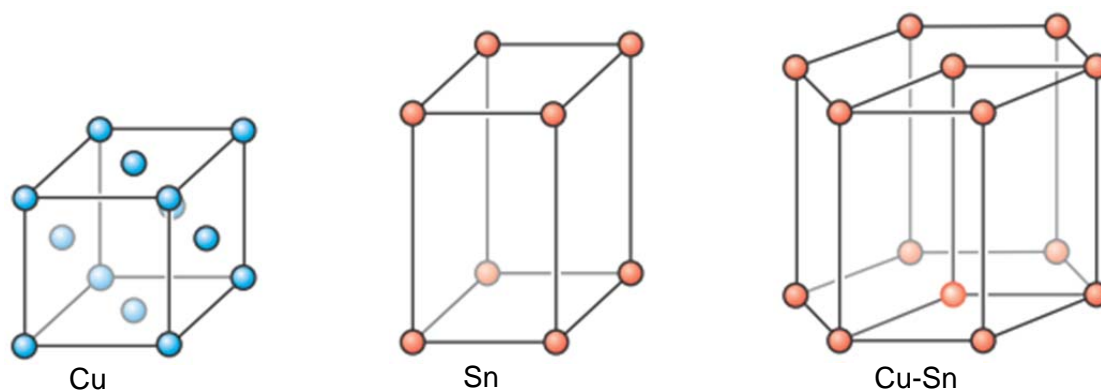
Figure 6-6 Crystal structures of Cu (face-centered cubic), Sn (tetragonal), and Cu_6Sn_5 (hexagonal) intermetallic phase [19].

Unit cell	a	b	c	α, β, γ	Volume (x10^6 pm^3)
Cu	3.6	3.6	3.6	90,90,90	47
Sn	5.8	5.8	3.1	90,90,90	108
Cu_6Sn_5	4.2	4.2	5.1	90,90,120	78

Table 6-2 Crystallographic parameters of Cu, Sn, and Cu_6Sn_5 unit cells (ICDD database).

Table 6-3 summarizes the average crystallite sizes for copper, tin, and Cu-Sn deposits. The Williamson-Hall method was used to account for microstrains that can have an influence on the x-ray peak width (as described in Section 3.5.3, X-Ray Diffraction). More details of this calculation are provided in the Appendix. The large difference in crystallite sizes between pure Cu and Sn vs Cu-Sn indicates that the co-deposition of Cu and Sn has an effect on the nucleation mechanism. This would also influence the crystallite size in Cu-Sn deposits which is significantly different to those of the individual metal deposits.

Deposit	Crystallite size (nm)
Cu	43±12
Sn	70±15
Cu-Sn	128±36

Table 6-3 Average crystallite sizes of Cu, Sn, and Cu-Sn deposited on vitreous carbon.

6.3   Pulse Current Plating

Although DC plating was shown to provide Cu-Sn deposits which were highly reproducible, its optimal limiting current density of 22 mA cm^{-2} limits the plating rate to approximately 0.8 µm/min. Increasing the applied current density would result in higher deposition rates but at the expense of poor deposit quality. Therefore, an alternative plating technique, pulse plating (PP), was explored to determine whether it can provide higher deposition rates without compromising deposit quality. Chin has shown that pulse limiting currents could be up to three magnitudes higher for very small pulse times (<1 ms) and duty cycles ($\Theta < 10^{-3}$) [103].

6.3.1   Pulse Plating Parameters

Initial experiments were carried out in the 40-150 mA cm^{-2} peak current density range to determine the onset current density for Cu-Sn co-deposition. The average current density is the product of the peak current density and the duty cycle and was in the 8-75 mA cm^{-2} range. Table 6-4 summarizes the pulse plating parameters that were used.

It was found that for the peak current density of 100 mA cm^{-2}, depending on the duty cycle (0.2 or 0.5), the average current density is in the range of 20-50 mA cm^{-2} which is comparable to the current densities being applied during DC plating where one would expect to see Cu-Sn co-deposition; 20 mA cm^{-2} onwards.

Peak current (mA cm^{-2})	$i_{L,PP}$ (mA cm^{-2})	Duty cycle	Average current (mA cm^{-2})	$i_{L,PP}$ (mA cm^{-2})	T_{total} (ms)	Plating time (min.)
40	50	0.2	8	47	10	50
50	55	0.2	10	47	10	50
60	62	0.2	12	47	10	50
80	80	0.2	16	47	10	50
100	100	0.2/0.5	20-50	47-50	10-100	20-50
150	150	0.2/0.5	30-75	47-75	10-100	20-50
N/A (DC plating)	-	-	3-30	-	-	10-30

Table 6-4 Comparison of pulse and direct current plating parameters.

The pulse plating limiting current densities ($i_{L,PP}$) were calculated from Equation 3.7. It must be noted that at peak/ average current density below 40/8 mA cm^{-2}, nothing deposited on the electrode surface. In DC plating experiments the limiting current density of copper was approximately 3 mA cm^{-2}. However, during pulse plating the average current density needed to be as high as 8 mA cm^{-2} before copper deposition could occur. This may be due to the fact that for relatively low current densities, for example, 20/4 or 30/6 mA cm^{-2}, most of the charge was initially consumed to charge the electric double layer.

6.3.2 PP Deposit Composition

Table 6-5 shows the deposit microstructure and relative tin and copper content as well as the current efficiency of PP deposition. It can be seen in the first row that even with peak/ average current density as low as 40/8 mA cm^{-2}, Sn can be found in the deposit. The microstructure suggests that tin crystals are being deposited on a thin layer of copper. This is due to the fact that the surface is relatively smooth (similar to copper only deposits seen in DC plating) with "islands" of tin deposits spread sparsely across the surface.

As the peak and average current densities gradually increase we observe a corresponding increase in tin content in the deposit. It is only when the current density reaches 100/20 mA cm^{-2} do we see the highest amount of tin being deposited as well as a significant change in the microstructure. The change in microstructure gives a good visual indication that Cu-Sn alloys are being formed.

As the current density is increased further to 150/30 mA cm^{-2}, the copper and tin content remained the same. However, the microstructure became noticeably rougher, more porous and current efficiency of the deposition process decreased by approximately 13%. This is indicative of hydrogen evolution at high over potentials which would lead to powdery deposits. The current efficiency was calculated using Faraday's law. The electrochemical equivalent [2]of copper is 0.3293 mg C^{-1} and for tin it is 0.615 mg C^{-1}. Using this method the actual deposit weight obtained can be compared to the expected weight assuming 100% current efficiency and actual current efficiency can be calculated accordingly. The results of this calculation are shown in Table 6-5 and Table 6-6.
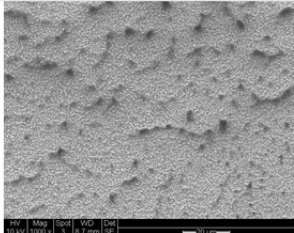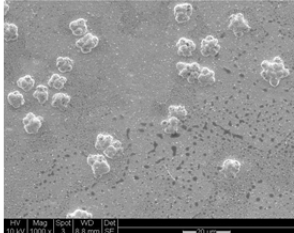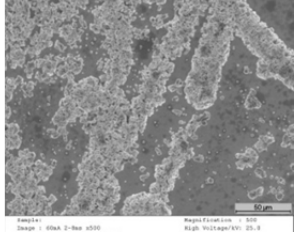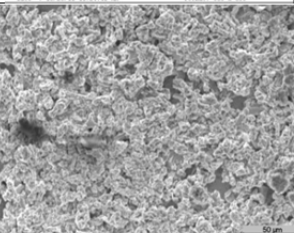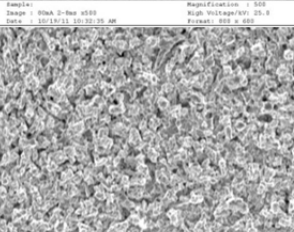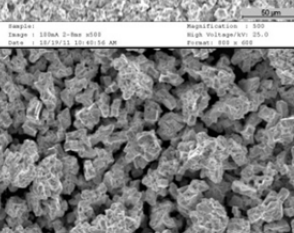
Peak/ average current density (mA cm^{-2})	Microstructure	Sn (wt%)	Cu (wt%)	Current efficiency (%)
40/8		12	88	8
50/10		39	61	12
60/12		82	18	18
80/16		84	16	52
100/20		94	6	66
150/30		95	5	56

Table 6-5 Microstructure, composition, and current efficiency of PP deposits ($\Theta = 0.2$)

Peak/ average current density (mA cm^{-2})	Sn (at %)	Cu (at %)	Expected weight (mg)	Actual weight (mg)
40/8	12	88	7.9	0.6
50/10	25	75	8.9	1.1
60/12	71	29	13.7	2.5
80/16	74	26	17.8	9.2
100/20	84	16	21.1	14.0
150/30	88	12	31.0	17.3

Table 6-6 The expected deposit weight assuming 100% current efficiency calculated from Faraday's law and the electrochemical equivalent method. The atomic % was obtained for EDX measurements.

For example, when an average current density of 8 mA cm^{-2} is applied, the electrochemical equivalent is $(0.615 \times 0.12) + (0.3293 \times 0.88) = 0.365$ mg C^{-1}. It should be noted that the current efficiencies found in PP are very low ranging from 8-66%. This might be an indication that the charge is being consumed in other electrochemical processes. The current might be consumed as non-Faradaic charge (such as the charging of the electrochemical double layer) or the absorption of other species on the electrode surface may be blocking the surface leading to lower current efficiencies.

It was also revealed that the pulse period, whether it was 10 ms or 100 ms, did not result in any changes in deposit composition which remained the same in both cases. However, Figure 6-7 shows that a longer duty cycle of 0.5 resulted in deposits that appeared more porous and rough leading to poor surface coverage and adhesion on the vitreous carbon electrodes. The long er t_{on} = 5 ms means that the tin deposition time is twice as long as t_{on} = 2 ms and tin was given enough time to nucleate and grow into larger crystals, resulting in deposits that were more porous with some crystals de-adhering from the surface during washing.
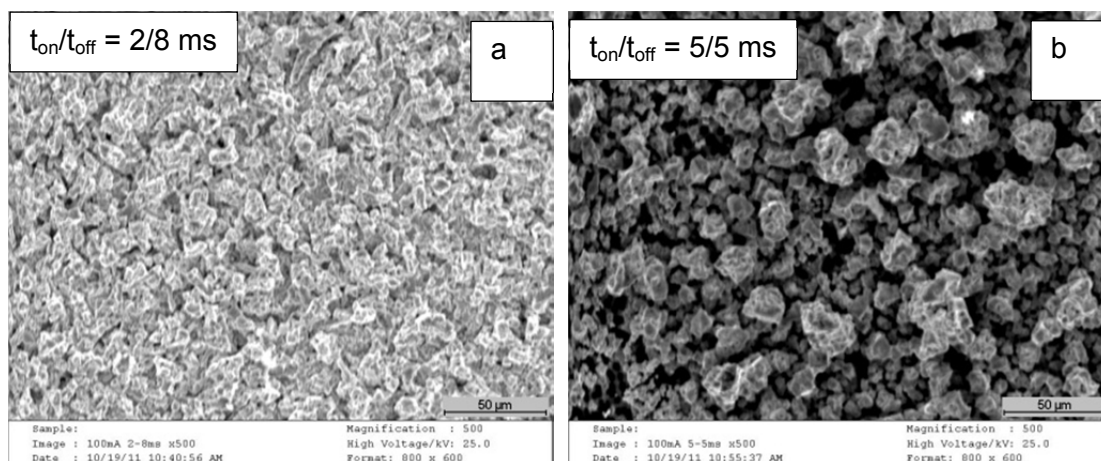
Figure 6-7 Comparison of the deposit microstructure obtained with a) Θ = 0.2 and b) Θ = 0.5. The peak current density was 100 mA cm^{-2} and deposition time was 50 min.

Although the surfactant made a significant impact on DC deposits by acting as a levelling agent and reducing the surface roughness of the deposit, this levelling effect was not clearly seen when the PP technique was used. Surfactant molecules may have been absorbing to the surface at lower current densities (below 50/10 mA cm^{-2}) blocking the deposition of tin. However, at higher current densities (80/16 mA cm^{-2} and above) the potential might be great enough to overcome the suppression caused by the surfactant leading to large amounts of tin being deposited. It appears that the levelling action of surfactants are different when metal is deposited under DC and PP conditions. It was proposed that optimum levelling would occur when t_{on} is less than the transition time of the additive. The transition time is defined as the time required for the concentration of the reaction to fall to zero at the electrode surface. Beyond the transition time, the current cannot be sustained and a potential shift to another value allowing other electrodes reactions or in this case the deposition of Sn to occur. It is possible that our plating time exceeds the transition time of the additive.

6.3.3 PP Deposit Morphology

Table 6-7 is a cross section comparison of PP deposits as a function of time. The problem was that with longer deposition times the deposits became significantly rougher and more porous due to the growth of tin crystals branching out on top of one another. The deposit thickness and growth rate cannot be accurately determined due to the roughness and uneven growth of the deposit on the substrate, but in all deposits the thickness was >20 µm.
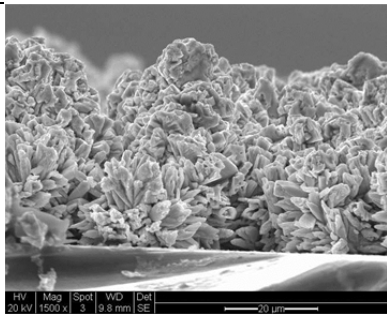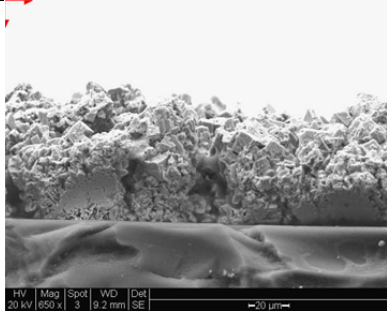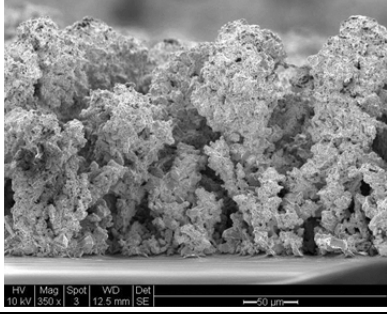
Peak/ average current density (mA cm⁻²)	Deposition time	SEM cross section
100/20	30 min	
100/20	50 min	
100/20	150 min	

Table 6-7 Thickness comparison of PP deposits as a function of time (Θ = 0.2).

Therefore, it was concluded that the best Cu-Sn deposits obtained from PP is at 100/20 mA cm⁻², duty cycle = 0.2, T_{total} = 10 ms and a total plating time of 50 min. All PP deposits from this section on were carried out under these parameters.

6.3.4   PP Crystalline Structure

Figure 6-8 shows the XRD pattern of Cu-Sn deposits obtained from PP plating. The absence of any broad peaks indicates that no signals from the vitreous carbon substrate are being detected. The presence of sharp peaks with small line broadening also indicates that the deposits are crystalline in nature corresponding well with the microstructure seen in Table 6-7. Similar to the XRD pattern obtained from DC plating, the top three highest peak intensities were arising from tin crystal planes.
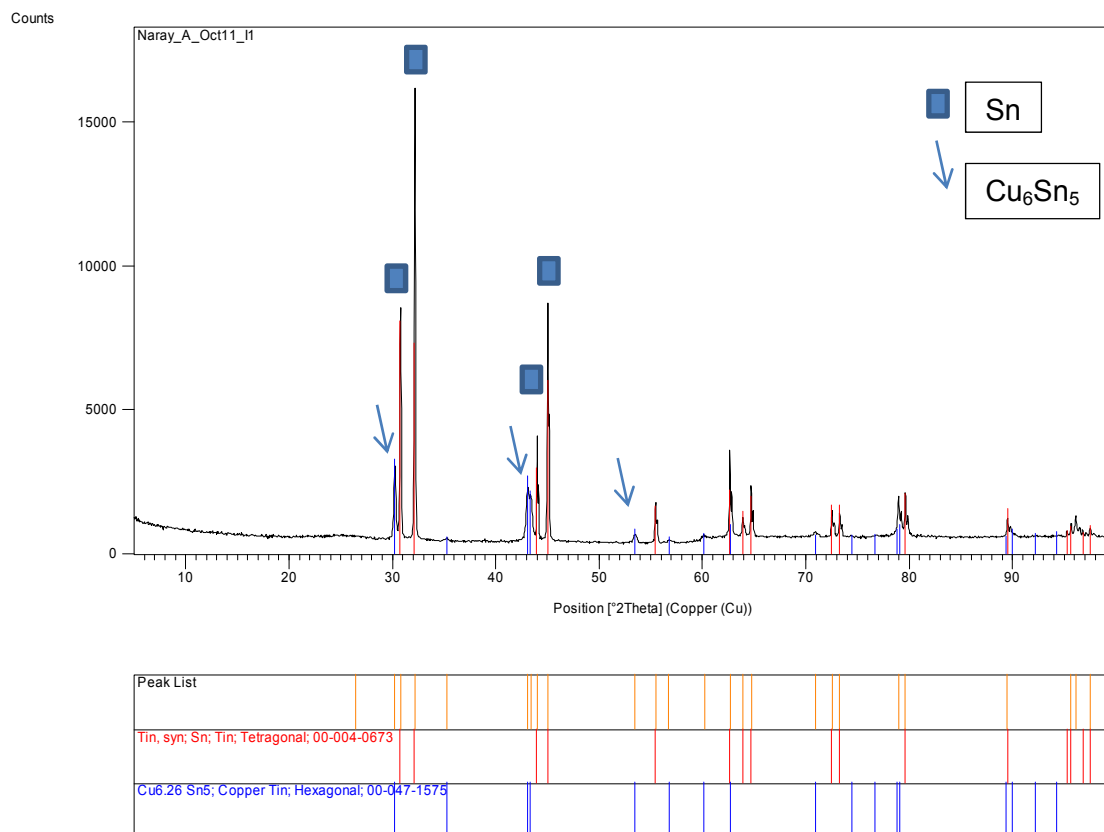
Figure 6-8 XRD pattern of Cu-Sn deposits from PP plating. $\Theta = 0.2$, $T_{total} = 10$ ms, $i_p = 100$ mA cm^{-2}.

In order to test the reproducibility of deposits obtained from PP, XRD analysis were carried out on three different samples under the same PP condition. Even though EDX composition analysis has confirmed that the pulse period (Ttotal = 10 or 100 ms) had no effect on the amount of copper and tin found in the deposit it was unclear whether longer periods would affect the crystal structure of the deposits.

Figure 6-9 shows that all samples deposited with $\Theta = 0.2$ resulted in similar phases as the XRD pattern was nearly identical. It should be noted that the peak intensities cannot be directly compared between samples as they are relative peak intensities that can only be compared with other peaks in the same XRD pattern. The four peaks with the highest intensities were still arising from Sn which combined with EDX analysis, confirms that the main phase in the deposit is Sn.
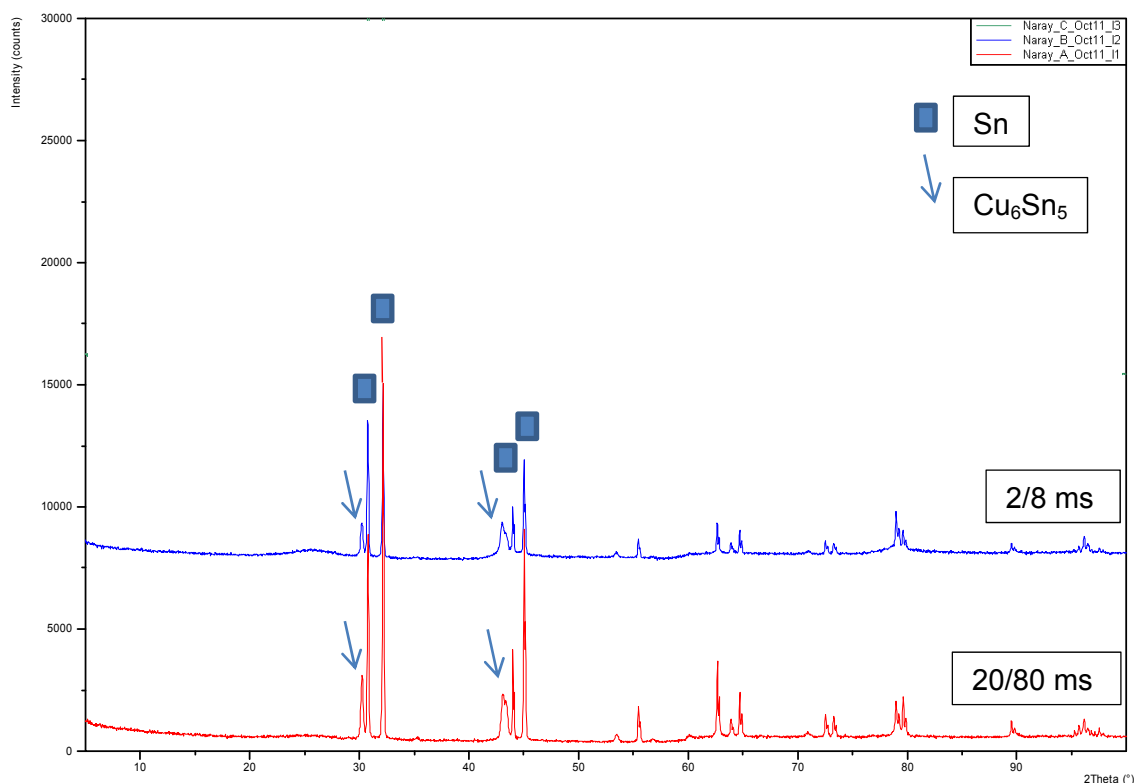
Figure 6-9 XRD pattern showing reproducibility of Cu-Sn deposits obtained via PP plating. Average current density 22 mA cm^{-2}, Θ = 0.2.

It should be noted that on some occasions when the vitreous carbon electrodes are being cleaned, by dissolving the deposit in Nitric acid, a very thin and smooth underlayer of copper can be seen. This indicates that under PP conditions Cu will always reach its mass transfer limit first and forms the first layer on top of the electrode surface. Sn would then deposit on top of this layer and interact with Cu to form the Cu_6Sn_5 intermetallic; this would be the second layer of the deposit. The top layer of will comprise of mostly tin as it forms larger crystals during the t_{on} time. During t_{off} the system relaxes and it is expected that this process would repeat itself although the Cu and Cu_6Sn_5 layers may be too thin to be observed under SEM in our experiments.

6.4   Annealed Deposits

As the Cu-Sn deposit fabricated in this research has the potential to be used as a soldering material, annealing experiments above reflow temperature (227 ^{o}C) were carried out to determine the usability of such deposits. According to the Cu-Sn phase diagram, deposits such as the ones obtained in this research (96%Cu-4%Sn) should be able to melt and completely reflow at temperatures above 250 ^{o}C. In industry, the reflow temperature of the Cu-Sn alloy is usually set to 30°C higher than the eutectic point; proximately 250-260 ^{o}C. In our annealing experiments the temperature was set to 260 ^{o}C to ensure that the deposit did indeed completely reflow. The procedure carried out for annealing experiments were detailed in Chapter 3.

During PP deposition it was proposed that a multilayer of Cu//Cu$_6$Sn$_5$//Sn was being deposited during each PP cycle. As the t$_{on}$ time was relatively short (2 ms), the Cu and Cu$_6$Sn$_5$ layers that are being formed would be too thin to be observed under SEM. One would expect to see random scattering of the Cu$_6$Sn$_5$ phase across the surface. However, when the deposit completely melts during annealing, rearrangement of Cu and Sn atoms can occur when the melt is in the liquid phase.

This means that the Cu$_6$Sn$_5$ phase was also expected to increase in annealed samples compared to non-annealed samples. However, this change would not be detected through EDX analysis as the copper and tin content in the deposit would remain the same. XRD analysis should provide us with information as to whether an increase in Cu$_6$Sn$_5$ is observed. Although it has not been observed in any deposits so far, formation of CuSn$_3$ is also a possibility after samples are annealed. However, since there is a limited amount of Cu in the deposit, it is expected that Sn-rich Cu$_6$Sn$_5$ would still be the main IMC formed.

6.4.1   Annealed Deposit Microstructure

Figure 6-10 shows that both DC and PP deposit became less porous after annealing. The DC deposit thickness decreased from 8 to 3 µm (63% decrease) while the PP deposit thickness decreased from 57 to 31 µm (46% decrease). The DC deposits seem to be less porous than PP deposits after annealing. Solder balls were formed when excess material melted and upon cooling was present only on DC deposits (cf. Figure 6-9c). This is most likely due to the fact that the DC deposits first collapsed to

form a dense liquefied mass. For PP deposits the formation of solder balls were not observed.
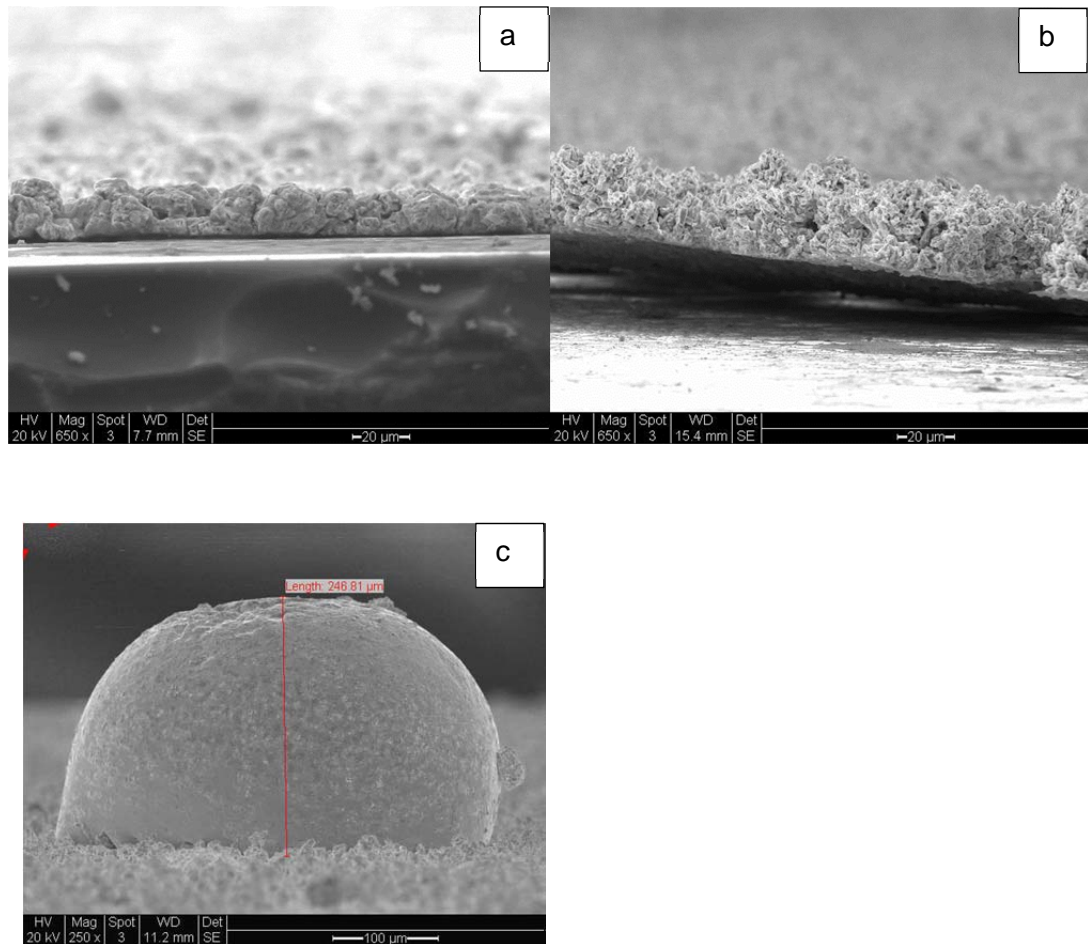
Figure 6-10 Microstructure of annealed deposits from a) DC and b) PP methods. Solder balls c) are observed only in DC deposits.

It can be concluded that for soldering purposes Cu-Sn deposits obtained through DC would be preferable to those obtained through PP plating. The formation of solder balls in Figure 6-10c for annealed DC deposits is an indication that the deposit has completely reflowed. Wetting on glassy carbon is poor, hence the formation of solder balls as the molten solder cools. Usually for soldering purposes the solder layer that is approximately 10 μm would be sufficient to join microelectronic devices. Therefore if Cu-Sn deposition through PP were to be developed farther, plating times of less than 50 min. would be sufficient.

6.4.2 Crystalline Structure of Annealed Deposit

Figure 6-11 shows the increasing peak intensity which indicates that more of the Cu_6Sn_5-like phase has been formed after annealing. The increase of Cu_6Sn_5-like phase can also be seen in the XRD pattern as shifts in crystal orientation planes. A broad peak to the left of the XRD pattern arises from the amorphous vitreous carbon substrate. This is due to the fact that DC deposits are very thin (3 µm) and for accurate XRD analysis it is recommended that the deposits be at least 5 µm thick. It must be noted that since the deposit is not thick enough peak intensity analysis cannot be used to quantitatively determine the amount of Cu_6Sn_5 intermetallic in the deposit. The only conclusion we can make from the XRD pattern is that there is an increase in the Cu_6Sn_5-like phase as now the highest peak intensity is arising from this phase.
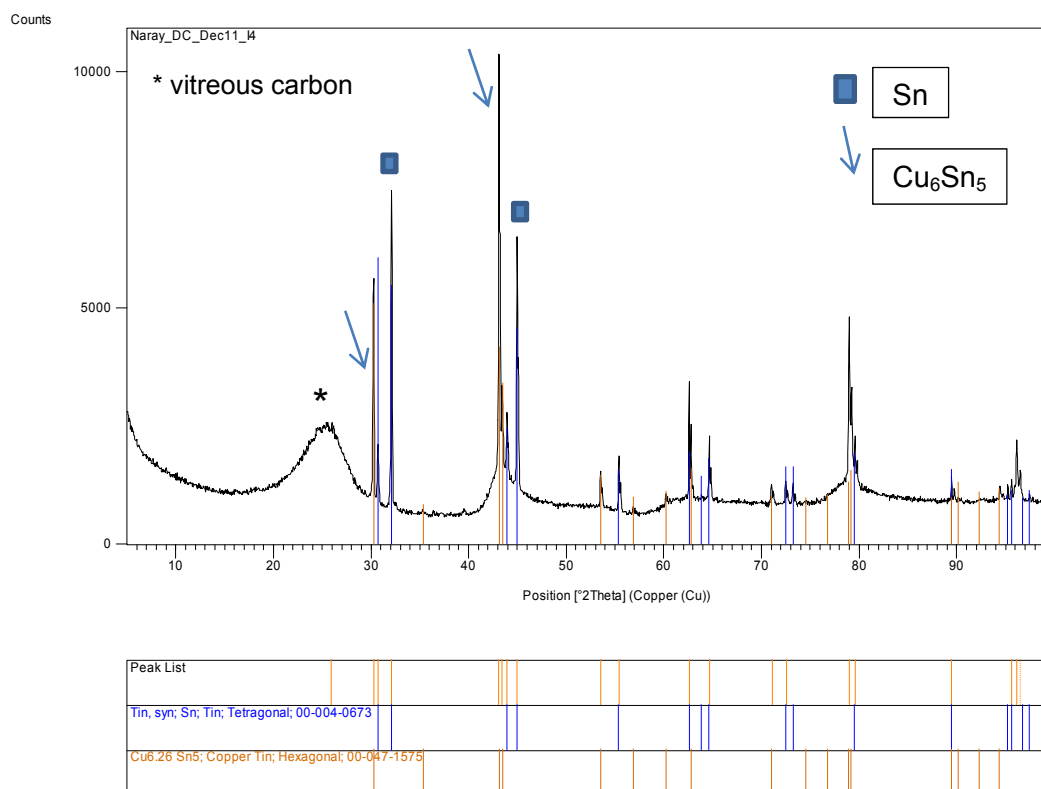
Figure 6-11 XRD pattern of annealed DC deposit.

Figure 6-12 shows no line broadening or peaks below $2\Theta = 30^{\circ}$ due to the fact that the annealed PP deposit is still relatively thick compared to annealed DC deposits. Increase in peak intensities assigned to the Cu_6Sn_5-like phase for both DC and PP deposits have been summarised in Table 6-8.
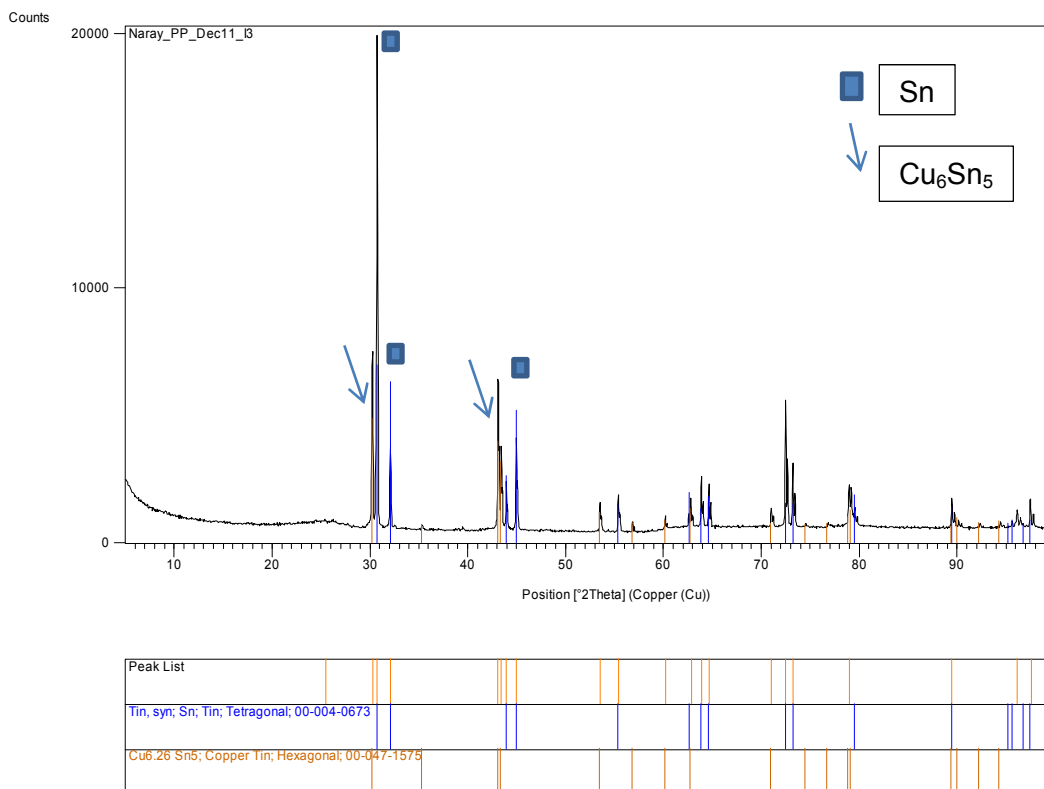
Figure 6-12 XRD pattern of annealed PP deposit.

Table 6-8 summarizes the change in peak intensity of various crystal planes after annealing. Note that there has been no shift in peak positions, only their intensities relative to one another have changed, indicating a slight change in phase composition, i.e. more Cu_6Sn_5.

Deposition method	Peak intensity	Before annealing	After annealing
DC	1st	Sn <2 0 0>	Cu_6Sn_5 <1 3 2>
DC	2nd	Sn <2 1 1>	Sn <2 0 0>
DC	3rd	Sn <1 0 1>	Sn <2 1 1>
PP	1st	Sn <2 0 0>	Sn <2 0 0>
PP	2nd	Sn <2 1 1>	Sn <2 1 1>
PP	3rd	Sn <1 0 1>	Cu_6Sn_5 <1 3 2>

Table 6-8 Change in XRD peak intensity before and after annealing.

Before annealing both DC and PP deposits were mainly composed of Sn. This is shown by the fact that the three highest peak intensities found in their XRD patterns were those of Sn. However, after annealing it can be seen that a new preferred crystal orientation plane Cu_6Sn_5 <1 3 2> has become one of the peaks with the highest peak intensity; Sn is still the main phase in all annealed deposits.

The average crystallite sizes before and after annealing of DC and PP deposits are summarized in Table 6-9. Note that due to time constraints only one set of annealing experiments were carried out, therefore, standard deviation values for annealed deposits were not available.

Deposition method	Crystallite Size (nm)	
	Before annealing	After annealing
DC	128±36	171
PP	83±36	257

Table 6-9 Average crystallite sizes of DC and PP deposits before and after annealing.

The increase in crystallite size (+43 nm for DC and +174 nm for PP deposits) is mainly due to the effect of grain growth, which is normally expected when samples are annealed. However, since the magnitude of this growth is different for DC and PP deposits, there may have been some additional factors involved. One possibility was that when the deposit reflows, further mixing of Sn and Cu (which could have been present as a first underlayer) would have resulted in the formation of additional Cu_6Sn_5-like phase. Since very little amount of unreacted copper would have been present in the deposit, this small increase in Cu_6Sn_5 would only have had a minor influence on the crystallite size. The most likely explanation is that DC and PP deposits reflowed and recrystallized differently as their thickness and microstructure before annealing were different to begin with.

There have been reports in literature that the Cu_3Sn intermetallic can also be present after annealing [2, 24]. However, it was found that the only IMC present in our results was the Cu_6Sn_5 IMC. Although in our experiments only one annealing cycle was attempted due to time constraints. It has been reported that the presence of the brittle Cu_3Sn intermetallic usually occurs after multiple annealing cycles or after long aging experiments. However, this is usually only for the case where deposits were on a Cu substrate. Cu from the substrate layer has been reported to diffuse into the deposit layer forming a Cu-rich Cu_3Sn layer on top of the substrate, but below the deposit

[104]. In this research a glassy carbon substrate was used, therefore, the initial amount of Cu is limited and changes in phase composition would also be limited.

From these annealing experiments it can be concluded that tin whiskers have not been formed. Tin whiskers can also form after the solder has been exposed to air for long periods of time or after multiple annealing. The annealed samples were left exposed to air in a close container for a few weeks before SEM/EDX analysis was performed and during that period of time no Cu_3Sn intermetallic or tin whiskers had been formed. Further aging experimentation would need to be carried out to determine whether they will appear.

7. DISCUSSION: LESSONS LEARNT

7.1 Rotating Cylinder Hull Cell experiments

Co-deposition of Cu-Sn alloys cannot be readily achieved due to the fact that the reduction potentials of the two individual metals are far apart; the standard reduction potential of Cu^{2+} is +0.340 V while for Sn^{2+} it is -0.130 V. A possible solution to this problem that has been proposed by other researchers for alloys such as Cu-Co and Cu-Ni [82] involves maintaining a relatively low concentration of the more noble metal in the electrolyte. According to the Nernst equation altering the concentration would also result in a change of the reversible reduction potential. This basic strategy is usually employed in order to shift the reduction potentials of individual metals closer together to facilitate co-deposition. This research has shown that by employing the same strategy and using a 1:10 ratio of Cu:Sn concentration in the electrolyte, Cu-Sn co-deposition could be readily achieved.

However, RCH experiments have shown that the fixing of initial metal salt concentrations alone is not enough and only fixes part of the problem. Another major problem which arose was the formation of metal oxides. Dissolved oxygen is inevitable for electrodeposition carried out in open vessels, such as in large plating tanks found in industrial electrodeposition. Therefore, antioxidants are a crucial component of every electrolyte. The antioxidant hydroquinone used in this research was shown to be a good candidate as it could maintain bath stability over a reasonable period of time (3 weeks). However, the concentration of Sn used in the mentioned work is relatively low (0.05 M) while in this research the Sn concentration was much higher (0.15 M). It is proposed that due to the high concentration of Sn in solution, some oxidation of Sn^{2+} to Sn^{4+} still occurs which can be seen by a thin layer of tin sludge at the bottom of the plating vessels. This loss of tin is not uncommon and is expected when plating from an acidic bath. The tin sludge sinks to the bottom and does not interfere with the electrodeposition process. It can simply be removed by decanting or by filtering the solution.

The formation of metal oxides was initially thought to be due to the presence of dissolved oxygen in the solution. The antioxidant hydroquinone was added in order to minimise and prevent the formation of metal oxides. If metal oxides were still found in the deposits, it would mean that either hydroquinone is not an effective antioxidant or

that its concentration in this specific MSA bath is too low. To test this hypothesis a set of RCH experiments were carried out in a bath which contains hydroquinone, but no surfactant was added. The bath was then deaerated with nitrogen gas for 1 hour before deposition in order to eliminate as much oxygen in the solution as possible. EDX results from this research show that metal oxides are still found in the deposit when plating from deaerated solutions. It was therefore concluded that the dissolved oxygen in the solution is not the cause for metal oxide formation. However, when fluorosurfactant are added to any type of solution, deaerated or not, the formation of metal oxides were always inhibited. This clearly established that fluorosurfactant eliminates oxide formation.

Fluorosurfactant inhibits oxide formation by eliminating the evolution of hydrogen near the electrode by absorbing on the surface and displacing water molecules. The surfactant blocks protons from being reduced to hydrogen gas near the electrode surface. The depletion of protons at the electrode surface results in a decrease in proton reduction. According to Sn Pourbaix diagrams, proton reduction would lead to an increase in pH which in turn would lead to the formation of tin oxides.

7.2   Voltammetry Experiments

Once it was determined that the fluorosurfactant is also a crucial component of the electrolyte, there was a need to explain its role in electrodeposition. Voltammetry experiments were carried out to observe the effect that fluorosurfactants have on the reduction potential of the individual metals and how co-deposition is facilitated. This research has shown that fluorosurfactant is important for Cu-Sn alloy deposition for two reasons. Firstly, it is proposed that the fluorosurfactant may suppress hydrogen evolution close to the electrode surface and in turn inhibit the formation of SnO_2 (*cf.* Chapter 4 RCH). Secondly, the presence of fluorosurfactant in solution shifts the metal reduction potential of copper closer to tin greatly increasing the chance of the two metals plating together.

Data from voltammetry experiments help us to determine what effect additives can have on the deposition of individual copper and tin metals as well as the Cu-Sn alloy. Both the potential and current density are recorded which will be useful during actual

plating of Cu-Sn alloys. It should be noted that voltammetry techniques such as CV and ASV are only useful in determining the electrochemistry of the system. They are not intended to be used to study actual deposition or deposit growth on the electrode surface. The RDE surface area of 0.031 cm^2 is too small to be used to study the deposit microstructure and crystalline phases. Potentiostatic (constant potential) deposition carried out is also not very useful in actual plating as potentials can vary at different stages of the deposition process. The deposition potential onto a "clean/fresh" surface in the beginning (nucleation overpotential) is usually different to the potential observed in later stages of the deposition process when plating is occurring at a constant rate. Galvanostatic deposition is the preferred plating method carried out in real industrial settings as a constant current density can be more easily controlled.

Potentiostatic analysis, CA and ASV experiments, provide information about the current densities needed in order to deposit Cu-Sn alloys of different compositions. At relatively low RDE rotation speed of 100 rpm, the current density recorded can be directly translated to current densities that should be applied at stationary vitreous carbon electrode. Theoretical calculations have shown that the limiting currents of both systems should be in the same order of magnitude. (cf. Chapter 3 comparing limiting currents of RDE and stationary systems). This has been confirmed by experimental verification that tin deposition is only seen when average current densities are greater than 20 mA cm^{-2} in both sets of experiments. The Sn compositions in both experiments were also similar, showing that the rates of copper and tin deposition were also similar.

7.3   Electrodeposition experiments

Constant current densities in an optimal range were predetermined from voltammetry experiments and later fine-tuned in actual electroplating on vitreous carbon electrodes. The current density needed to obtain a combination of high tin content, high current efficiency, and acceptable deposit microstructure was determined. It was found that tin has a propensity to form large crystals and that deposition at high current densities should be avoided as the deposits would become significantly more crystalline and porous. It was also found that once a certain current density threshold is reached there is no increase in tin content in the deposit.

Both DC and PP modes of deposition were carried out to ascertain whether one would be preferable to the other. It was shown that for equivalent deposition times (DC 10 min. and PP 50 min.) PP deposits were much more porous making accurate thickness measurements difficult (*cf.* Table 6-6). On the other hand, the crystallite sizes for DC and PC deposits were relatively similar at 57 nm and 59 nm, respectively. XRD analysis also showed that for both deposition modes the preferred crystal orientation planes were also relatively similar.

However, upon annealing it was found that the characteristics of both deposits were quite different. XRD peak intensities also indicated that an increase in the formation of the Cu_6Sn_5-like phase was found more in DC deposits compared to PP deposits. This may be due to the fact that the thickness of annealed DC deposits is much less than that of PP deposits making the deposit easier to reflow. Although meaningful quantification of the actual thickness is not meaningful as they are both still very porous. It should be noted that for soldering purposes the deposits should be at least 10 μm thick.

The most important difference is the fact that solder balls were observed on the surface of DC deposits while none were found on PP deposits. This indicates that the thinner DC deposits have completely reflowed, while PP deposits have not. Based on these findings, it is recommended that DC plating be the preferred deposition method for the fabrication of Cu-Sn solder alloys.

This research has shown that MSA-based electrolytes are stable over a short period of time. A one week old solution can be still be successfully used for deposition. It was found that the formation of tin sludge is inevitable, albeit occurring at a very slow rate in the first few days. This agrees with the theoretical thermodynamic calculations in Chapter 2 that the presence of $SnSO_4$ in solution would lead to the formation of SnO_2.

Since our results show that Sn-rich Sn-Cu alloys can be deposited from this MSA electrolyte, the possibility of developing a process for plating was examined. The greatest impediment was anticipated to be the slow precipitation of tin sludge from electrolyte. In fact, it to precipitate consists of copper the material which is present in small quantities constant bath monitoring and control would be required. Loss of Cu and Sn metals in solution only occurs initially as tin sludge is formed. The concentrations were relatively constant after the first week. This may be due to the fact

that the solution was not agitated and therefore the amount of dissolved oxygen did not increase significantly. It has been reported [105] that in similar MSA electrolyte (Sn^{2+} and MSA concentrations were 30 and 130 g L^{-1}, for this work that value was 33 and 192 g L^{-1}, respectively) the change in Sn^{2+} concentration over a nine week period showed a loss of about 15% from the original concentration

.

8. CONCLUSIONS

•   A 1:10 ratio of Cu:Sn concentration in the plating solution can be used to co-deposit Sn-rich Cu-Sn alloys. Initially the more noble metal, in this case copper, would be deposited on the electrode surface. As the copper concentration is relatively low, it is quickly depleted and the rest of the charge is now consumed in the deposition of tin. Therefore, a low copper concentration added to the electrolyte results in a corresponding low copper content in the deposit. This in turn ensures the formation of Sn-rich deposits.

•   EDX results showed that the additives fluorosurfactant and hydroquinone were not incorporated into the deposit as no trace of carbon or sulfur was found in the deposit. Since the deposits were relatively thin (6 μm) the elements copper, carbon, zinc and trace amount of iron were detected by EDX. Therefore, it must be kept in mind that the actual copper content reported in RCH experiments might actually be lower than that reported; although we cannot say quantitatively by how much.

•   Cu-Sn alloy deposition from MSA-based electrolytes must contain two important additives, an antioxidant and a fluorosurfactant. The antioxidant minimises the oxidation of Sn^{2+} to Sn^{4+}. A low Sn^{4+} concentration in solution also prevents the formation of tin sludge which sinks to the bottom of the plating tank. Although tin sludge does not interfere with electrodeposition, its formation is an irreversible process resulting in the loss of Sn^{2+} in solution. Therefore, without an antioxidant, Sn^{2+} would need to be constantly replenished at a relatively higher rate. The fluorosurfactant is also crucial as it inhibits the formation of metal oxides. One main indication that oxides are being formed is the drop in current efficiency. Deposits that contain metal oxides usually have a lower current efficiency due to the fact that the charge is not being efficiently consumed to deposit Cu-Sn alloys.

•   The fluorosurfactant serves two main purposes for successful Cu-Sn alloy co-deposition; inhibiting formation of metal oxides and shifting the reversible reduction potential of copper to a more negative value. The fluorosurfactant suppresses the formation of hydrogen near the electrode surface which can result in a local pH change. Pourbaix diagrams of Sn show that an increase in pH can lead to formation of tin oxides. CV experiments showed that in the presence of the fluorosurfactant, the reversible reduction potential of Sn did not shift and stayed at -0.45 V vs SCE.

However, for Cu its reduction potential shifted from -0.13 to -0.18 V vs SCE. These changes facilitate co-deposition of Cu-Sn alloys as their reduction potentials are now relatively closer to each other than before.

- CA experiments showed that for Cu-Sn co-deposition to occur, a current density greater than 20 mA cm^{-2} is needed. ASV experiments indicate that a current efficiency of 93% and a Sn content of up to 97% can be expected during Cu-Sn co-deposition. It is the ratio of charge consumed during deposition compared to charge consumed during stripping that is used to determine the current efficiency as well as the metal composition. As indicated earlier, low current efficiencies are observed when metal oxides are formed. Therefore, with high current efficiencies (>90%) seen in voltammetry experiments it can be concluded that no metal oxides are being formed in voltammetry experiments as well.

- The same current densities obtained during CA experiments can be used in DC plating on vitreous carbon electrodes. This is due to the fact that the limiting current density for RDEs rotating at 100 rpm is comparable to the limiting current density observed in systems with stationery electrodes. The best DC deposits were obtained when the current density was set to 22 mA cm^{-2} for 10 min. The tin composition was 96% and longer deposition times only resulted in the deposit becoming more porous. Due to poor wetting characteristics of vitreous carbon, small amounts of deposits were usually washed off during cleaning. Therefore, the current efficiency data was not accurately obtained but was estimated to be similar to those found in voltammetry experiments; >90%.

- Before annealing, both DC and PP deposits had similar preferred crystal orientation planes. After annealing DC and PP deposit differ in their preferred crystal orientation planes. Only one Cu-Sn intermetallic, Cu_6Sn_5, is observed in all cases.

- After annealing loose, solder balls found on top of DC deposits while none were found in PC deposits. The formation of solder balls may be dependent on the thickness and porosity of the deposits. Since annealed DC deposits were very thin (3 µm) and showed a propensity for reflowing, it may prove practical for soldering purposes.

9. FUTURE WORK

• Due to instrumental limitations, only preliminary annealing experiments have been attempted. Actual temperature profiles found in industrial reflow or wave soldering could not be replicated. The DC and PP deposits on vitreous carbon electrodes were put in a relatively simple curing oven where complicated temperature profiles could not be programmed. Therefore, the temperature ramp up and cool down times were relatively slow (tens of minutes) which may have affected the formation of different crystallite phases. Due to time constraints only one annealing cycle was carried out. In future experiments more accurate temperature profiles should be carried out using a Differential Scanning Calorimeter (DSC) where the annealing time and ramp up (heating) and ramp down (cooling) times can be more finely tuned (range of a few seconds). The shorter timescales for each annealing stage would more accurately reflect how solder annealing is actually carried out in real world industrial settings.

• In order to ascertain whether the Cu-Sn deposits obtained from this research is suitable for soldering purposes further annealing test and aging experiments should be carried out to determine their susceptibility to tin whisker formation. In microfabrication, PCBs may undergo multiple annealing cycles which have been reported to be the cause of tin whisker formation. Aging experiments where the annealed deposits are left exposed to the atmosphere for prolonged periods of time can also be tested as it has also been reported that phase changes can also occur over extended periods of time. Tin whiskers can cause unwanted electrical contacts that will lead to short circuits and the failure of the electronic product and should be further explored.

• Actual deposition on other substrates should also be carried out. In this research the substrate used was vitreous carbon which has very low wettability. Cu-Sn alloy deposition on copper substrates should be carried out for comparison as other processes such as epitaxial growth may be observed and have influences on deposit growth. Multiple annealing cycles may cause the diffusion of Sn into the Cu substrate and formation of multiple Cu-Sn alloy phases; currently only Cu_6Sn_5 is found. Formation of other phases that have detrimental mechanical properties such as Cu_3Sn may be observed. If only Cu_6Sn_5 was still found, the superiority of MSA-based electrolytes for solder fabrication may be validated.

REFERENCE

1. Jordan, M. (1999) *The Electrodeposition of Tin and its Alloys.* Eugen G. Leuze: Saulgau, Germany.
2. Schlesinger, M. and Paunovic, M. (2010) *Modern Electroplating, 5th ed.* John Wiley & Sons: Hoboken.
3. Organization, W. H. (2005) *Tin and Inorganic Tin Compounds.*
4. US_Geological_Survey. (2011) *Mineral Commodity Summaries 2011.* Reston, Virginia:
5. ITRI. (2011) *6th Annual Tin Use and Recycling Survey.*
6. Barker, T. C. (1977) *The glassmakers : Pilkington : the rise of an international company, 1826-1976.* Weidenfeld and Nicolson: London.
7. Merck. (2006) *The Merck Index, 14th ed.* John Wiley: Whitehouse Station, N.J.
8. Jordan, M. (2003) 'Lead-free tin alloys - Laboratory curiosities or capable processes?', *Metal Finishing,* 101, (1), pp. 8-16.
9. Arnold, S. M. (1966) 'Repressing the growth of tin whiskers', *Plating,* 53, pp. 96.
10. Takeno, N. (2005) *Atlas of Eh-pH diagrams Intercomparison of thermodynamic databases.* National Institute of Advanced Industrial Science and Technology
11. JIETA. (2002) *Lead-free Roadmap 2002: Roadmap 2002 for Commercialization of Lead-free Solder.* Lead-Free Soldering Roadmap Committee
12. OJEU. (2003) 'Directive 2002/95/EC', *Official Journal of the European Union,* L37, pp. 19-23.
13. Chen, S. W., Wang, C. H., Lin, S. K. and Chiu, C. N. (2007) 'Phase diagrams of Pb-free solders and their related materials systems', *Journal of Materials Science: Materials in Electronics,* 18, (1-3), pp. 19-37.
14. Lau, J. H. and Liu, K. (2004) 'Global Trends in Lead-free Soldering part I of A II-part series on lead-free', *Advanced Packaging,* 13, (1), pp. 27-30.
15. Rae, A. and Handwerker, C. (2004) 'NEMI's Lead-Free Alloy', *Circuits Assembly,* 15, (4), pp. 20-25.
16. Abtew, M. and Selvaduray, G. (2000) 'Lead-free solders in microelectronics', *Materials Science and Engineering R: Reports,* 27, (5), pp. 95-141.
17. Exchange, L. M. Available at: http://www.lme.com (Accessed: 15 July 2011).
18. SankaGanesan and Pecht, M. (2006) *Lead-free Electronics.* John Wiley & Sons, Inc.
19. Askeland, D. R., Fulay, P. P. and Wright, W. J. (2011) *The Science and Engineering of Materials, Sixth Edition.* Cengage Learning: Stamford.
20. Saunders, N. and Miodownik, A. P. (1990) 'The Cu-Sn (Copper-Tin) system', *Alloy Phase Diagrams,* 11, (278).
21. Roberts, P. C. (2000) 'Soldering 101', Assembly Magazine,
22. Prasad, R. P. (1997) *Surface mount technology 2nd ed.* Chapman & Hall: New York.
23. Strauss, R. (1998) *SMT Soldering Handbook.* Newnes: Oxford.
24. Rickett, B., Elmgren, P., Flowers, G., Gale, S. and Suhling, J. (2005) 'Whisker formation potential in Pb-free electroplated connector finishes', *Circuits Assembly,* 16, (2), pp. 52-59.
25. NEMI (2000) *NEMI Group Recommends Tin/Silver/Copper Alloy as Industry Standard for Lead-Free Solder Reflow in Board Assemblies.* Available at: http://www.solderconnection.co.uk/lead_free_tech_articles/pr012400.htm (Accessed: 29 July 2011).
26. Indium_Corporation (2011) *Solder Preforms.* Available at: http://www.indium.com/products/solderfabrications/preforms.php (Accessed: 29 July 2011).

27. Geng, H. (2005) *Semiconductor manufacturing handbook.* McGraw-Hill: United States of America.
28. The_Open_University (2011) *Physical vapour deposition.* Available at: http://openlearn.open.ac.uk/mod/resource/view.php?id=198424#FIG056 (Accessed:
29. Health_and_Safety_Executive. (1997) 'Controlling health risks from rosin (colophony) based solder fluxes', in *INDG 249L.*
30. Yau, Y. H. (2000) 'Effect of process variables on electrotinning in a methanesulfonic acid bath', *Journal of the Electrochemical Society,* 147, (3), pp. 1071-1076.
31. Martyak, N. M. and Seefeldt, R. (2004) 'Additive-effects during plating in acid tin methanesulfonate electrolytes', *Electrochimica Acta,* 49, (25), pp. 4303-4311.
32. Paunovic, M. and Schlesinger, M. (2006) *Fundamentals of Electrochemical Deposition, 2nd ed.* John Wiley & Sons: Hoboken, New Jersey.
33. Price, J. W. (1983) *Tin and Tin Alloy Plating.* The Anchor Press Ltd: Tiptree.
34. Oplinger, F. F. and Bauch, F. (1941) 'Alkaline Tin Plating', *Transactions of The Electrochemical Society,* 80, (1), pp. 617-629.
35. Monk, R. G. and Ellingham, H. J. T. (1935) 'Electrodeposition of tin alloys from alkaline stannate baths', *Transactions of the Faraday Society,* 31, pp. 1460-1468.
36. Stout, L. E. and Baum, A. H. (1937) 'The Electrodeposition of Tin', *Transactions of The Electrochemical Society,* 72, (1), pp. 429-446.
37. Stout, L. E. and Erspamer, A. (1935) 'The Electrodeposition of Tin and Its Alloys', *Transactions of The Electrochemical Society,* 68, (1), pp. 483-492.
38. Venkatasamy, V., Riemer, S. and Tabakovic, I. (2011) 'Electrodeposition of eutectic Sn96.5Ag3.5 films from iodide-pyrophosphate solution', *Electrochimica Acta,* 56, (13), pp. 4834-4840.
39. Vaid, J. and Char, T. L. R. (1957) 'Tin Plating from the Pyrophosphate Bath', *Journal of The Electrochemical Society,* 104, (5), pp. 282-287.
40. Arai, S., Funaoka, Y., Kaneko, N. and Shinohara, N. (2001) 'Electrodeposition of Sn-Cu alloy from pyrophosphate bath', *Electrochemistry,* 69, (5), pp. 319-323.
41. Pine, P. R. (1941) 'Electrodeposition of Tin from Acid Solutions', *Transactions of The Electrochemical Society,* 80, (1), pp. 631-644.
42. Tam, T. M. (1986) 'Electrodeposition Kinetics for Tin, Lead, and Tin-Lead Fluoborate Plating Solutions', *Journal of The Electrochemical Society,* 133, (9), pp. 1792-1796.
43. Radovic, D. (1989) 'Lead-tin alloy plating with hydroquinone as an additive in fluoborate baths', *Plating and Surface Finishing,* 76, (1), pp. 52-57.
44. Balaji, R. and MalathyPushpavanam. (2003) 'Methanesulphonic acid in electroplating related metal finishing industries', *Transactions of the Institute of Metal Finishing,* 81, (5), pp. 154-158.
45. Gernon, M. D., Wu, M., Buszta, T. and Janney, P. (1999) 'Environmental benefits of methanesulfonic acid', *Green Chemistry,* 1, pp. 127-140.
46. Greef, R. A. T. D. and Janssen, L. J. J. (2001) 'Electrochemical dissolution of tin in methanesulphonic acid solutions', *Journal of Applied Electrochemistry,* 31, (6), pp. 693-702.
47. Low, C. T. J. and Walsh, F. C. (2008) 'Normal and anomalous electrodeposition of tin-copper alloys from methanesulphonic acid bath containing perfluorinated cationic surfactant', *Transactions of the Institute of Metal Finishing,* 86, (6), pp. 315-325.
48. Arkema *Methanesulfonic acid.* Available at: http://www.arkema-inc.com/index.cfm?pag=127 (Accessed: 26 July 2011).

49. BASF. (2008) 'New applications involving methanesulfonic acid', in *EMV 0101 e 2008*.

50. Tamura, T. Nippon MacDermid Co., Ltd. (Kanagawa-Ken, JP) (2002) *Bright tin-copper alloy electroplating solution*.

51. Martyak, N. M. and Seefeldt, R. (2006) 'On the role of sulfate ion in acid tin methanesulfonate electrolytes', *Galvanotechnik,* 97, (1), pp. 48-55+iv.

52. Cachet, C., Keddam, M., Mariotte, V. and Wiart, R. (1992) 'Adsorption of perfluorinated surfactants on gold electrodes-I. Comparison of non-ionic compounds', *Electrochimica Acta,* 37, (12), pp. 2377-2383.

53. Cha, C. S. and Zu, Y. B. (1998) 'Behavior of perfluorinated surfactants at the electrode/solution interface', *Langmuir,* 14, (21), pp. 6280-6286.

54. OECD. (2007) 'Lists of PFOS, PFAS, PFOA, PFCA, related compounds and chemicals that may degrade to PFCA', *ENV/JM/MONO(2006)15*.

55. OJEU. (2004) 'Regulation (EC) No 850/2004', *Official Journal of the European Union,* L158, pp. 7-49.

56. Doyle, C., Brown, N. and Bardizeh, M. (2002) 'Factors Influencing the Solderability of Lead-Free Electrodeposits', *Metal Finishing,* 100, (1), pp. 10-17.

57. Arai, S. and Kaneko, N. (1997) 'Electrodeposition of Sn-Ag-Cu alloys', *Electrochemistry,* 65, (12), pp. 1102-1106.

58. Fukuda, M., Imayoshi, K. and Matsumoto, Y. (2002) 'Effects of thiourea and polyoxyethylene lauryl ether on electrodeposition of Sn-Ag-Cu alloy as a Pb-free solder', *Journal of The Electrochemical Society,* 149, (5), pp. C244-C249.

59. Fukuda, M., Imayoshi, K. and Matsumoto, Y. (2003) 'Effect of adsorption of polyoxyethylene laurylether on electrodeposition of Pb-free Sn alloys', *Surface and Coatings Technology,* 169-170, pp. 128-131.

60. Han, C., Liu, Q. and Ivey, D. G. (2009) 'Electrochemical composite deposition of Sn-Ag-Cu alloys', *Materials Science and Engineering B: Solid-State Materials for Advanced Technology,* 164, (3), pp. 172-179.

61. Joseph, S. and Phatak, G. J. (2008) 'Effect of surfactant on the bath stability and electrodeposition of Sn-Ag-Cu films', *Surface and Coatings Technology,* 202, (13), pp. 3023-3028.

62. Joseph, S. and Phatak, G. J. (2010) 'Effect of additives on the co-electrodeposition of Sn-Ag-Cu lead-free solder composition', *Materials Science and Engineering B: Solid-State Materials for Advanced Technology,* 168, (1), pp. 219-223.

63. Ozga, P. (2006) 'Electrodeposition of Sn-Ag and Sn-Ag-Cu alloys from thiourea aqueous solutions', *Archives of Metallurgy and Materials,* 51, (3).

64. Qin, Y., Liu, C., Wilcox, G. D., Zhao, K. and Wang, C. (2009) *11th Electronic Packaging Technology Conference, EPTC 2009.* Singapore,

65. Qin, Y., Liu, C., Wilcox, G. D., Zhao, K. and Wang, C. (2010) Las Vegas, NV,

66. Qin, Y., Wilcox, G. D. and Liu, C. (2010) 'Electrodeposition and characterisation of Sn-Ag-Cu solder alloys for flip-chip interconnection', *Electrochimica Acta,* 56, (1), pp. 183-192.

67. Tsai, Y.-D. and Hu, C.-C. (2011) 'Composition control of the eutectic Sn-based alloys: Sn-Ag, Sn-Cu, Sn-Ag-Cu, from simple plating baths', *Journal of The Electrochemical Society,* 158, (8), pp. D527-D534.

68. Zhang, J., An, M. and Chang, L. (2009) 'Study of the electrochemical deposition of Sn-Ag-Cu alloy by cyclic voltammetry and chronoamperometry', *Electrochimica Acta,* 54, (10), pp. 2883-2889.

69. Zhang, J., An, M., Chang, L. and Liu, G. (2008) 'Effect of triethanolamine and heliotropin on cathodic polarization of weakly acidic baths and properties of Sn-Ag-Cu alloy electrodeposits', *Electrochimica Acta,* 53, (5), pp. 2637-2643.

70. Tsuji, K., Obata, K., Takeuchi, T., Nawafune, H. and Nishikawa, T. Daiwa Fine Chemicals Co., Ltd (2003) *Plating Bath and Processes for Depositing Alloy Containing Tin and Copper.*

71. Hradil, G. (2007) *Proceedings of the International Symposium and Exhibition on Advanced Packaging Materials Processes, Properties and Interfaces.* Atlanta, GA,

72. Bozzini, B., Fanigliulo, A., Giovannelli, G., Natali, S. and Mele, C. (2003) 'Electrodeposition of Au-Sn alloys from acid Au(III) baths', *Journal of Applied Electrochemistry,* 33, (8), pp. 747-754.

73. Bozzini, B., Giovannelli, G., Natali, S., Serra, M. and Fanigliulo, A. (2002) 'Electrodeposition of Au-Sn alloys from alkaline baths', *Journal of Applied Electrochemistry,* 32, (2), pp. 165-171.

74. Madore, C., Landolt, D., Habenpflug, C. and Hermann, J. A. (1995) 'Application of the rotating cylinder hull cell to the measurement of throwing power and the monitoring of copper plating baths', *Plating and Surface Finishing,* 82, (8), pp. 36-41.

75. Finazzi, G. A., de Oliveira, E. M. and Carlos, I. A. (2004) 'Development of a sorbitol alkaline Cu-Sn plating bath and chemical, physical and morphological characterization of Cu-Sn films', *Surface and Coatings Technology,* 187, (2-3), pp. 377-387.

76. Correia, A. N., Façanha, M. X. and de Lima-Neto, P. (2007) 'Cu-Sn coatings obtained from pyrophosphate-based electrolytes', *Surface and Coatings Technology,* 201, (16-17), pp. 7216-7221.

77. Andricacos, P. C., Chang, I.-c., Deligianni, H. and Horkans, W. J. International Business Machines Corporation (Armonk, NY) (1995) *Acid electrolyte solution and process for the electrodeposition of copper-rich alloys exploiting the phenomenon of underpotential deposition.*

78. Low, C. T. J. and Walsh, F. C. (2008) 'Electrodeposition of tin, copper and tin-copper alloys from a methanesulfonic acid electrolyte containing a perfluorinated cationic surfactant', *Surface and Coatings Technology,* 202, (8), pp. 1339-1349.

79. Pewnim, N. and Roy, S. (2011) 'Effect of Fluorosurfactant on Copper-Tin Reduction from a Methanesulfonic Acid Electrolyte', *Transactions of the Institute of Metal Finishing,* 89, (4), pp. 206-209.

80. Bard, A. J. and Falkner, L. R. (2001) *Electrochemical Methods.* John Wiley & Sons: New York.

81. Bard, A. J., Parsons, R. and Jordan, J. (1985) *Standard Potentials in Aqueous Solution.* Dekker: New York.

82. Plieth, W. (2008) *Electrochemistry for Materials Science.* Elsevier: Hungary.

83. Cachet, C., Keddam, M., Mariotte, V. and Wiart, R. (1994) 'Influence of perfluorinated and hydrogenated surfactants upon hydrogen evolution on gold electrodes', *Electrochimica Acta,* 39, (18), pp. 2743-2750.

84. Hansal, W. E. G. and Roy, S. (2012) *Pulse Plating.* Leuze Verlag: Bad Saulgau.

85. Low, C. T. J. and Walsh, F. C. (2008) 'The influence of a perfluorinated cationic surfactant on the electrodeposition of tin from a methanesulfonic acid bath', *Journal of Electroanalytical Chemistry,* 615, (2), pp. 91-102.

86. Hull, R. O. (1939) *Technical Proceedings of the American Electroplater's Society,* 27, pp. 52.

87. Dargis, R. (2005) *The Hull Cell: Key to Better Electroplating.* Available at: http://www.pfonline.com/articles/the-hull-cell-key-to-better-electroplating-part-i (Accessed: 17/1/2012).

88.   Schloetter (2012) *Hull Cells & Plating Test Equipment.*   Available at: http://www.schloetter.co.uk/plating-equipment/Hull-cells-and-plating-test-equipment.htm (Accessed: 17/1/2012).

89.   Low, C. T. J., De Leon, C. P. and Walsh, F. C. (2005) 'The Rotating Cylinder Electrode (RCE) and its application to the electrodeposition of metals', *Australian Journal of Chemistry,* 58, (4), pp. 246-262.

90.   Low, C. T. J., Roberts, E. P. L. and Walsh, F. C. (2007) 'Numerical simulation of the current, potential and concentration distributions along the cathode of a rotating cylinder Hull cell', *Electrochimica Acta,* 52, (11), pp. 3831-3840.

91.   Low, C. T. J. and Walsh, F. C. (2008) 'The stability of an acidic tin methanesulfonate electrolyte in the presence of a hydroquinone antioxidant', *Electrochimica Acta,* 53, (16), pp. 5280-5286.

92.   Hasan, M. and Rohan, J. F. (2010) 'Cu Electrodeposition from Methanesulfonate Electrolytes for ULSI and MEMS Applications', *Journal of The Electrochemical Society,* 157, (5), pp. D278-D282.

93.   Quickenden, T. I. and Xu, Q. (1996) *Journal of The Electrochemical Society,* 143, pp. 1248.

94.   Cheh, H. Y. (1971) 'The limiting rate of deposition by P-R plating', *Journal of the Electrochemical Society,* 118, (7), pp. 1132-1134.

95.   Guinebretiere, R. (2007) *X-ray Diffraction by Polycrystalline Materials.*

96.   Karuppuchamy, S., Nonomura, K., Yoshida, T., Sugiura, T. and Minoura, H. (2002) 'Cathodic electrodeposition of oxide semiconductor thin films and their application to dye-sensitized solar cells', *Solid State Ionics,* 151, (1-4), pp. 19-27.

97.   Peulon, S. and Lincot, D. (1996) 'Cathodic electrodeposition from aqueous solution of dense or open-structured zinc oxide films', *Advanced Materials,* 8, (2), pp. 166-170.

98.   Peulon, S. and Lincot, D. (1998) 'Mechanistic study of cathodic electrodeposition of zinc oxide and zinc hydroxychloride films from oxygenated aqueous zinc chloride solutions', *Journal of the Electrochemical Society,* 145, (3), pp. 864-874.

99.   Yoshida, T., Komatsu, D., Shimokawa, N. and Minoura, H. (2004) 'Mechanism of cathodic electrodeposition of zinc oxide thin films from aqueous zinc nitrate baths', *Thin Solid Films,* 451-452, pp. 166-169.

100. Dahms, H. and Croll, I. M. (1965) 'The Anomalous Codeposition of Iron-Nickel Alloys', *Journal of the Electrochemical Society,* 112, pp. 771-775.

101. Buckle, R. and Roy, S. (2008) 'The recovery of copper and tin from waste tin stripping solution. Part I. Thermodynamic analysis', *Separation and Purification Technology,* 62, (1), pp. 86-96.

102. Chase, W. T., Notis, M. and Pelton, A. D. (2007) *METAL 07, ICOM-CC Metal Working Group triennial conference.* Amsterdam (The Netherlands), 17-21 September 2007.

103. Chin, D.-T. (1983) 'Mass Transfer and Current-Potential Relation in Pulse Electrolysis', *Journal of The Electrochemical Society,* 130, (8), pp. 1657-1667.

104. Tamura, N., Oshita, R., Fujimoto, M., Fujitani, S., Kamino, M. and Yonezu, I. (2002) 'Study on the anode behavior of Sn and Sn-Cu alloy thin-film electrodes', *Journal of Power Sources,* 107, pp. 15-55.

105. Martyak, N. M. and Seefeldt, R. (2005) 'On the Oxidation of Tin (II) in Methanesulfonate Solutions and the Role of Sulfate', *Galvanotechnik,* 96, (3), pp. 594-601.

Appendix A: Supplemental Theory and Calculations

Radiation type	Signal	Location	Information
Reflection	Backscattered electrons	1-2 μm of surface	Nature of specimen
Emission	Secondary electrons	Within 5 μm of surface	Topography
Transmission	Transmitted electrons	Thin foils and films	Thickness and composition
Beam induction	Current in external circuit	Within specimen	Semiconductors
X-rays	X-rays of selected wavelengths	Within specimen	Spectrochemical analysis
Auger	Auger electrons	Auger electrons	Chemical elements
Cathodoluminescence	Photons of selected wavelength	Light emission	Various phases

Table A-1 Various types of signal produced through SEM analysis and the information they provide.

Current efficiency calculations

a) Current efficiency and alloy content calculations (for Table 5-3)

In order to calculate the current efficiency of deposition in the CA experiments we need to compare the stripping charge associated with each metal in columns 3 and 4 to the total deposition charge in column 2 as shown:

Current efficiency = (Column 3 + Column 4)/ Column 2

For example

for -0.41 V,   current efficiency = (0.24 + 0) / 0.56 = 43%

for -0.45 V,   current efficiency = (0.13 + 1.24) / 1.49 = 92%

Alloy composition (column 8) was determined from the individual metal stripping charges (column 6 or column 7 individually) divided by the combined total stripping charge (columns 6 + 7) as shown:

Cu content = column 6 / (column 6 + column 7)

Sn content = column 7 / (column 6 + column 7)

For example

for -0.45 V,   Cu content = 8 / (8+77) = 9%

Sn content = 77 / (8+77) = 91%

for -0.46 V,   Cu content = 2 / (2+88) = 2%

Sn content = 88 / (2+88) = 98%

b) Amount and phase of Cu in Sn-rich deposits

EDX measurements showed that Sn-rich deposits contained 96 wt% Sn and 4 wt% Cu. However, EDX provides no information on whether Cu or Sn is present in their elemental form or as Cu_6Sn_5. Additional phase analysis via XRD needed to be carried out and peak intensity analysis indicates that the deposits contained approximately 95% Sn and 5% Cu_6Sn_5. Taking this into consideration, the EDX data can be re-interpreted and the amount of Sn, Cu, and Cu_6Sn_5 is approximately:

$$96\% \text{ Sn} = 92\% \text{ as Sn} + 4\% \text{ as } Cu_6Sn_5$$

$$4\% \text{ Cu} = 4\% \text{ as } Cu_6Sn_5$$

ASV data from Table 3 corroborates this (within the experimental error) as the Cu/Sn content in the alloy (column 8) is in the same range (>91% Sn and <9% Cu).

Williamson-Hall plot for XRD analysis

In a Williamson-Hall plot (c.f. Experimental section 3.5.3), a line of best fit can be drawn which provides us with information about the microstrains in a sample. The slope value gives us an indication of the amount of strain, while the y-intercept provides information about the crystallite size.
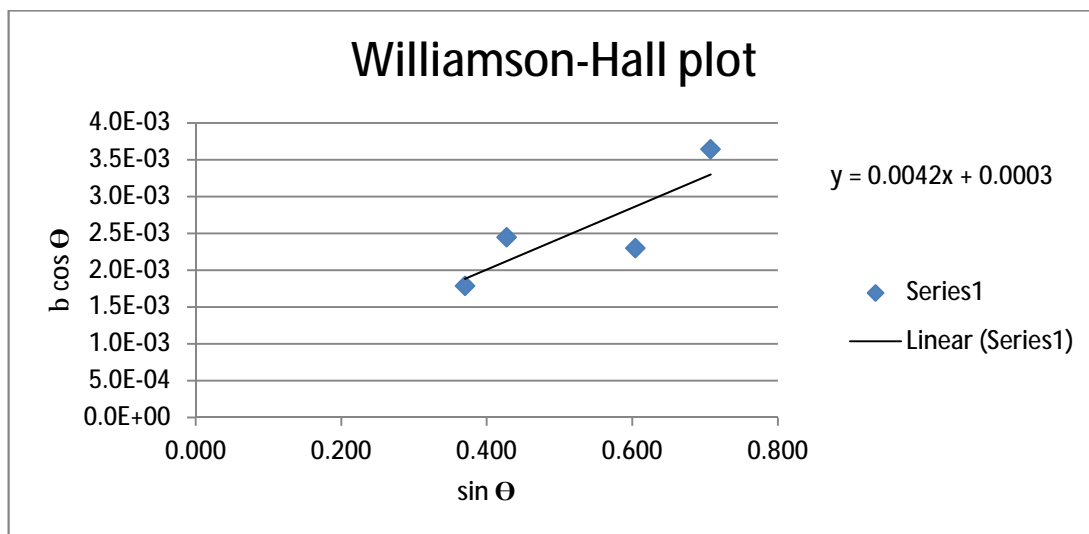
Figure A-1 Example of a Williamson-Hall plot used in XRD analysis.
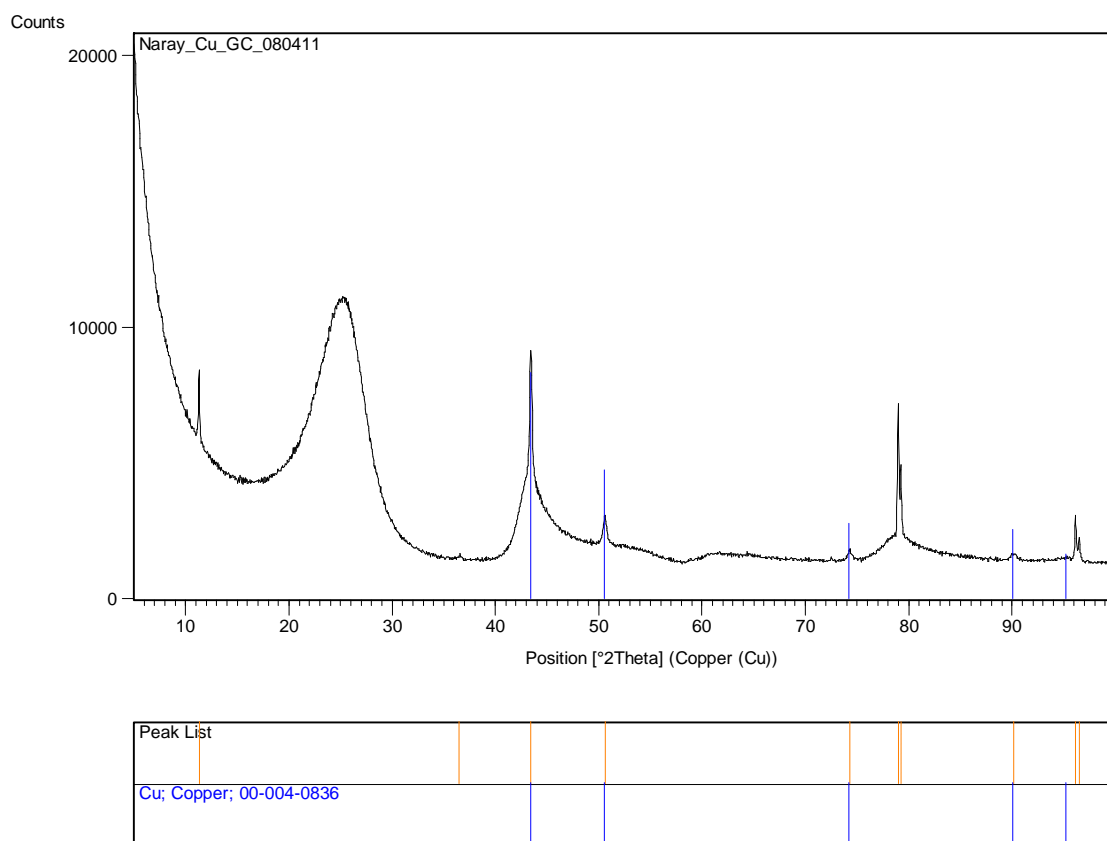
Appendix B: Additional XRD patterns

Figure B-1 XRD pattern of DC plated Cu on vitreous carbon.
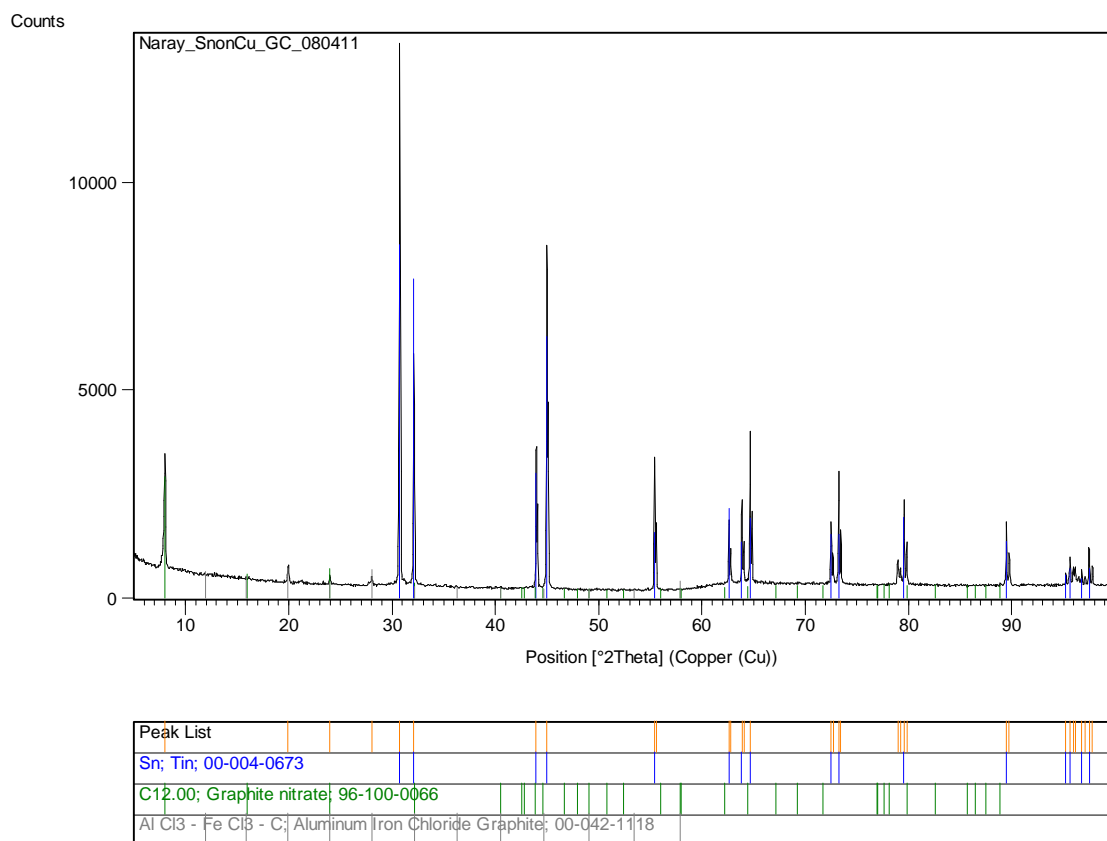
Figure B-2 XRD pattern of DC plated Sn on vitreous carbon (Cu base layer). AlCl$_3$ impurity present.
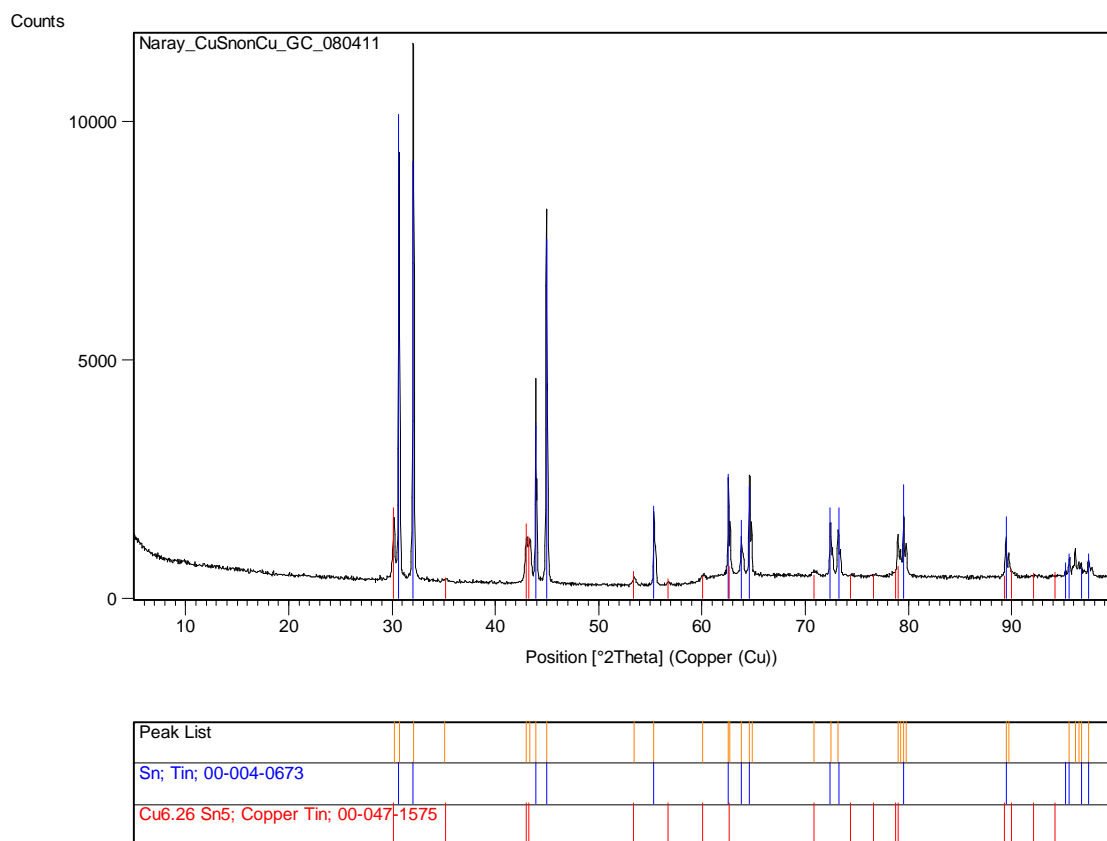
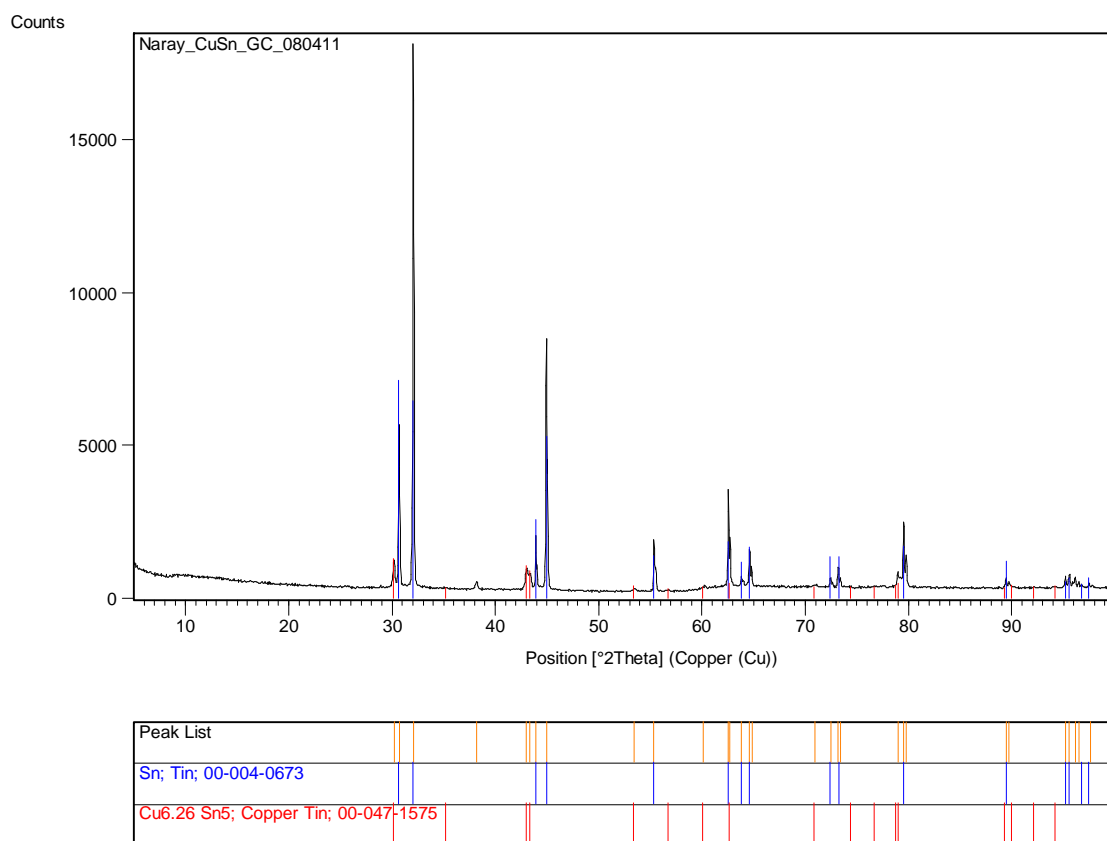**Figure B-3** XRD pattern of DC plated Cu-Sn on vitreous carbon (Cu base layer).

Figure B-4 XRD pattern of DC plated Cu-Sn on vitreous carbon.

Appendix C: Publications

Effect of fluorosurfactant on copper–tin reduction from methanesulphonic acid electrolyte

N. Pewnim* and S. Roy

In this study, methanesulphonic acid electrolytes have been used to electrodeposit copper–tin alloys of different compositions to examine the effect of a fluorosurfactant additive on deposit composition. Experiments have been carried out at a rotating cylinder Hull cell as it allows the deposition of many alloy compositions over a wide range in a single experiment. The relative amounts of tin and copper in the deposit were controlled by fixing the ratio of copper to tin in the electrolyte as well as the addition of hydroquinone and a non-ionic fluorosurfactant additive. It was found that without the surfactant, metal oxides with a tin content of 35 wt-% were deposited. The addition of the surfactant eliminated metal oxides and deposits with a tin content of up to 85 wt-% could be plated.

Keywords: Copper–tin, Hydroquinone, Methanesulphonic acid, Rotating cylinder Hull cell, Surfactant

Introduction

Copper–tin (Cu–Sn) alloys or tin bronzes are of particular interest due to their various applications including use as a decorative finishing in jewellery products, as a coating to improve corrosion and wear resistance for machinery parts such as gears and bearings,[1] and also as a lead-free soldering material in electronic packaging.[1–5] Traditionally the most important electrolyte for Cu–Sn deposition has been the alkaline cyanide system,[1,5] mainly because tin is dissolved more easily as stannate salt. Electrodeposition of tin and its alloys from acidic baths is based on fluoborate,[5,6] sulphate[1] and phenolsulphonic acids.[5] The problem with acidic baths, such as sulphate, is that tin oxide is precipitated out and the deposit can be a metal oxide[5,7] while phenolsulphonate baths contain phenol, which can be toxic. To obviate these problems, various additives and complexing agents[8–10] have been used to control the quality of deposits in industry, and are recommended by some suppliers.[11]

More recently, attempts have been made to develop sulphonate baths with low toxicity: the methanesulphonic acid (MSA) based system.[9,12–19] Studies have shown that MSA can be used to electrodeposit copper and tin from a bath containing an antioxidant, hydroquinone, and a fluorosurfactant.[16] These researchers have demonstrated that a low copper content in the alloy can be obtained from a bath with a high tin to copper ratio. They have also suggested that there was a reduction in the amount of dissolved oxygen in the background

electrolyte in the presence of the surfactant.[8] It remains unclear, however, if MSA baths plate metals or metal oxides, which can often be a crucial criterion in choosing electrolytes, especially when Cu–Sn alloys are used for electronic applications.[3,4]

In this study, the authors have attempted to determine the additive agent which can minimise oxides in the deposit such that metallic alloys can be electrodeposited. Similar to other researchers,[16] only two additives were used – hydroquinone and a fluorosurfactant, DuPont Zonyl FSN. It is generally accepted that hydroquinone, an antioxidant, lowers the amount of oxygen in the electrolyte, and can eliminate spontaneous oxidation of divalent stannous tin (Sn^{2+}) to tetravalent stannate tin (Sn^{4+}).[1,9] The fluorosurfactant, on the other hand, is known to reduce hydrogen evolution which can occur during Cu–Sn co-deposition.[20] The useful MSA concentration in the electrolyte range has been found to be between 0·7 to 2·0M; it is reported that a high acid concentration depresses the solubility of the tin salt.[1]

In this work, we have co-deposited copper and tin from an MSA electrolyte with the aforementioned additive agents at a rotating cylinder Hull (RCH) cell to determine if metals or metal oxides are plated during the co-deposition process. Deposits have been plated at a wide range of current densities, which enabled the examination of a wide range of deposit composition. Deposit composition has been ascertained by energy dispersive X-ray (EDX) analysis and experimental findings have been used to deduce the additive agents required to obtain oxide-free deposits.

The experimental approach in this study involved the use of a Hull-type cell. The Hull cell[21] is a standard experimental apparatus which allows the determination of the effect of current density on the composition, microstructure and crystalline structure of electrodeposits.

School of Chemical Engineering and Advanced Materials, Merz Court, Newcastle University, Newcastle upon Tyne, NE1 7RU, UK

*Corresponding author, email naray.pewnim@ncl.ac.uk
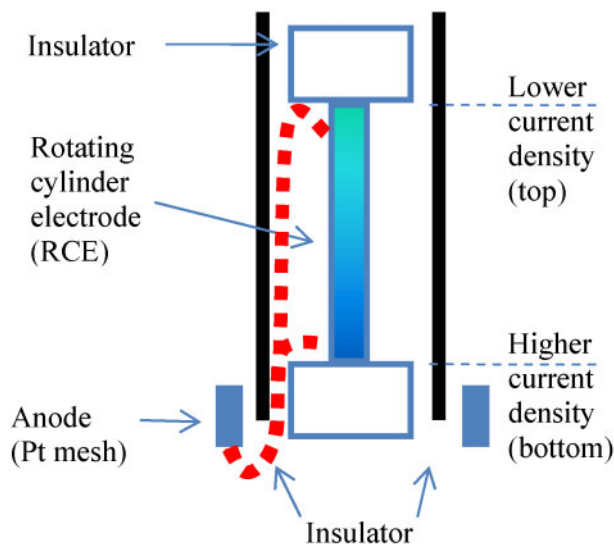
1 Side view of the rotating cylinder Hull cell showing the platinum mesh anode surrounding the cylinder cathode; dotted lines denote the distance between the electrodes. The greater distance between the top and bottom of the cylinder and the anode affects current distribution, giving rise to different local current densities along the length of the cylinder cathode

More recently, a modified version of the Hull cell has been developed, a rotating cylinder Hull cell,[22] RCH, which also allows the fixing of mass transfer conditions. The RCH cell creates a non-uniform current distribution along the length of the cathode allowing the electroplating of different alloy compositions at various positions along the cylinder cathode. This is due to the varying distance that the current lines have to cover to reach the counter electrode, giving rise to differing ohmic drop in the solution.

Experimental

The electroplating bath was prepared by dissolving 0.2 mol dm^{-3} SnSO$_4$ (Prolabo) and 0.02 mol dm^{-3} CuSO$_4$.5H$_2$O (AnalaR) into a solution of 2 mol dm^{-3} 70% methanesulphonic acid (Alfa Aesar) and distilled water. A volume of 600 mL, the normal operating volume of the RCH cell, was used in the experiments. The additives were 0.01 mol dm^{-3} hydroquinone (Merck) and 0.01 vol.-% non-ionic fluorosurfactant (DuPont Zonyl FSN). The solution was heated on a hot plate to about 303 K to aid the dissolution of tin salt and left to cool to room temperature before experiments were initiated.

Electrodeposition was carried out at an RCH cell from EcoChemie (HT Rota-Hull), a schematic of which is shown in Fig. 1. The RCH cell is composed of a cathode which is a rotating cylinder electrode, surrounded by a stationary anode which is a platinum mesh counter electrode. The cathode cylinder was made of brass with a diameter of 0.6 cm and length of 8.0 cm (active surface area of 15.1 cm^2) and fitted to a rotating motor at the top. A concentric insulating wall around the inner cathode is a cylinder made of plexiglass with a diameter of 5.0 cm and height of 15.0 cm. The rotation speed and deposition time were fixed at 400 rev min^{-1} and 600 s respectively.

Equation (1) gives the relationship between the average (applied) and the local current at the RCH cell[23]

$$\frac{i_{(x/h)}}{i_{ave}} = \frac{0.535 - 0.458(x/h)}{[0.0233 + (x/h)^2]^{0.5}} + 8.52 \times 10^{-5} \exp[7.17(x/h)] \tag{1}$$

where h is the length of the cathode, x/h is the dimensionless distance along the cathode, $x/h=0$ corresponds to the position of highest current density, $x/h=1$ corresponds to the position of lowest current density, $i_{(x/h)}$ is the local current density, and i_{ave} is the average current density applied to the cell. The average current applied to the cathode was determined by the approach of mass transfer limiting current for each metal. Equation (2) was used to calculate the limiting current density at the RCH cell[24]

$$i_{lim} = 0.079 zFc_b d^{-0.3} U^{0.70} v^{-0.344} D^{0.644} \tag{2}$$

where i_{lim} is the limiting current density (A cm^{-2}), z is the number of electrons in the electrode process, F is the Faraday constant (96 485 C mol^{-1}), c_b is the bulk concentration of the electroactive species (mol cm^{-3}), d is the diameter of the RCE (cm), U is the peripheral velocity of the RCE (cm s^{-1}), v is the kinematic viscosity of the electrolyte (cm^2 s^{-1}), and D is the diffusion coefficient of the electroactive species (cm^2 s^{-1}).

For a bath composition such as the 1 : 10 wt-% Cu–Sn bath, the limiting current densities for tin and copper were then calculated from equation (2) to be 4.7 and 47.4 mA cm^{-2} respectively. The total maximum current that can be applied (assuming that there are no side reactions) is a summation of the partial currents, i.e. 52.1 mA cm^{-2}. In these experiments the applied current density was fixed to the limiting current of copper, 4.7 mA cm^{-2}. Table 1 shows the actual local current density along the electrode which covered a wide range that is lower and higher than the limiting current density of copper, i.e. ranging from 2.77 to 13.2 mA cm^{-2} but never exceeding the sum of the limiting current densities of the two metals, i.e. 52.1 mA cm^{-2}. This reduces the possibility of hydrogen reaction due to the approach towards mass transfer controlled conditions.

The current efficiency was obtained by weighing the cylinder electrode before and after each set of experiments. The actual deposit mass obtained was then compared to the theoretical mass for 100% current efficiency. The deposit weight is directly related to the applied current according to Faraday's law

$$Q = it = \frac{nFW}{M} \tag{3}$$

where Q is the total charge passed (C), i is the applied current (A), t is the time the current was passed (s), n is the number of electrons involved, F is the Faraday

Table 1 Local current density as a function of distance along cathode of RCH cell. Average current density applied was 4.7 mA cm^{-2}

Distance/cm	$i_{(x/h)}/i_{ave}$	$i_{(x/h)}/$mA cm^{-2}	Cylinder section no.
0.7	2.80	13.2	1
1.5	1.86	8.74	2
2.7	1.03	4.84	3
4.0	0.59	2.77	4

Table 2 Elemental composition of brass cylinder electrode substrate*/wt-%

Cylinder	Sn	Cu	Zn	C	O	%total
Brass	...	49	32	14	...	95

constant (96 485 C mol^{-1}), W is the weight of the deposit (g), and M is the atomic weight of the deposits (g mol^{-1}). As the RCH cell applies different local currents along the length of the cathode, different amounts of deposits are also expected at different points. For simplicity, approximations were made as if the cathode was a single piece of homogenous substrate; the average applied current of 4·7 mA cm^{-2}, corresponded to a total applied current of 0·07 A, and the atomic weight of the Cu–Sn alloy was approximated to be 91·12 g mol^{-1}, corresponding to an average between that of pure copper (63·54 g mol^{-1}) and that of pure tin (118·69 g mol^{-1}).

After deposition, the cylinder electrode was sectioned into various pieces at fixed distances and each cylinder section labelled accordingly as shown in Table 1. Knowing the exact distance along the electrode, the local current density at each section could then be determined. The surface microstructure of each section was studied under a scanning electron microscope (SEM; Jeol JSM-5300LV) equipped with an EDX detector which was used to determine the composition of the alloy.

Results and discussion

Tables 2–4 show the compositions of the cathode cylinder, and the composition of deposits obtained from two different baths with and without the fluorosurfactant, respectively; all other bath components remained the same. The data presented in the tables are the average of three separate measurements at different locations carried out on a single sample. The variation between these measurements was less than 5%, which was the accuracy of the instrument. The total percentages of individual elements combined lie between 93 and 98 wt-% (the last columns in the Tables 2–4), which is a reflection of the accuracy of these measurements.

Table 2 shows the composition of the cathode cylinder which was made of brass (Cu–Zn alloy). It should be noted that the brass cylinder is not a pure Cu–Zn alloy and that carbon, approximately 14 wt-%, was also detected in the substrate. In Table 3, the second column shows a gradual decrease in tin content from 35 to 24 wt-% as the local current density decreases from section 1 to 4. In column three we see that the copper content increased from 28 to 43 wt-% which is to be

expected due to the decrease in current density. The additional columns show the presence of zinc, carbon and oxygen. The detection of zinc and carbon indicates that the X-rays are penetrating into the substrate layer as the deposits are relatively thin (approximately 4 μm). In addition, the high content of oxygen shows that the deposit is in the form of metal oxides.

In Table 4, the bath with the surfactant added, a similar trend of decreasing tin content and increasing copper content was observed moving down the table from section 1 to 4. However, it can be seen at the top of columns 2 and 3 that the tin content rose to 85 wt-%, while copper content dropped to 3 wt-%. Zinc and carbon were still detected owing to the thinness of the deposits. However, no oxygen was detected, showing that the deposit does not contain metal oxides. Indeed, this change is corroborated by the SEM images shown in Fig. 2, which shows that the microstructure is completely different.

The current efficiency of the bath without surfactant was found to be 55%. In the presence of surfactant it rose to 66%. It is known that perfluorinated surfactants can minimise hydrogen evolution.[20] The results here show that inclusion of surfactant in the solution raises the current efficiency and reduces hydrogen evolution. As all plating solutions contain hydroquinone, the ability to plate oxide-free deposits cannot be attributed to its addition in solution. However since it lowers the amount of dissolved oxygen in the electrolyte,[1,9] the appearance of deposits containing oxides is unexpected. In order to verify that dissolved oxygen in the solution is not the cause of metal oxide formation, a separate set of plating experiments was carried out where the solution containing only hydroquinone was degassed with nitrogen for 1 h prior to plating. The current efficiency for this plating experiment was 55%. The EDX analysis showed that the deposit composition was 55Sn–19Cu–1Zn–5C–20O. This set of values is similar to those shown in Table 3. This indicated that dissolved oxygen did not contribute to the oxide content within the deposit.

Based on these findings, it can be inferred that the addition of the surfactant minimised oxide formation in the deposit. Cathodic electrodeposition of metal oxides has been reported before.[25–29] It has been shown that tin oxides can form when the hydrogen reaction proceeds at the electrode surface resulting in local pH changes as shown

$$2H_3O^+ + 2e^- = H_2 + 2H_2O \qquad (4)$$

Pourbaix diagrams show that the rise in the pH of the electrolyte very close to the electrode surface through equation (4) can lead to the formation of tin

Table 3 Composition of deposit obtained from 1:10 (Cu–Sn) bath without surfactant*/wt-%

Cylinder section	Sn	Cu	Zn	C	O	%total
1	35	28	2	12	21	98
2	33	29	3	9	21	95
3	25	40	9	5	14	93
4	24	43	11	4	14	96

*The average current density applied was 4·7 mA cm^{-2} for 600 s. The local current density is the highest in cylinder section 1 and lowest in section 4.

Table 4 Composition of deposit obtained from 1:10 (Cu–Sn) bath with addition of surfactant*/wt-%

Cylinder section	Sn	Cu	Zn	C	O	%total
1	85	3	2	7	...	97
2	73	9	5	8	...	95
3	72	12	3	9	...	96
4	70	13	5	6	...	94

*The average current density applied was 4·7 mA cm^{-2} for 600 s. The local current density is the highest in cylinder section 1 and lowest in section 4.
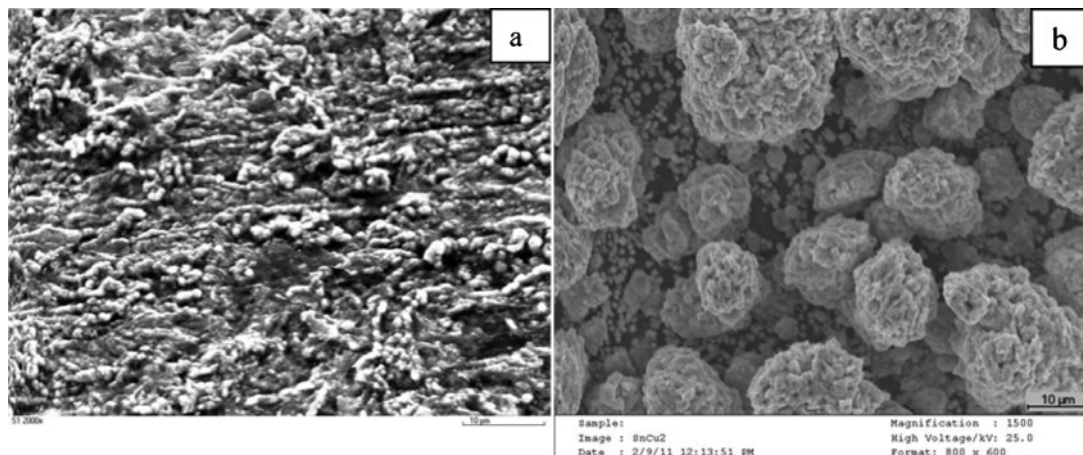
2 Surface microstructure of Cu–Sn deposits *a* without surfactant, 35 wt-%Sn and *b* with addition of surfactant, 85 wt-%Sn

oxides.[7,9,30,31] Perfluorinated surfactants can inhibit hydrogen evolution by adsorbing[20,32,33] at the electrode surface or by removing water from it. Thus, we can infer that a non-ionic fluorosurfactant such as DuPont Zonyl FSN is crucial to the suppression of hydrogen thereby limiting pH changes and enabling the deposition of metals.

Conclusion

An experimental study on Cu–Sn alloy deposition from MSA electrolytes containing tin and copper sulphates with the addition of hydroquinone and DuPont Zonyl FSN non-ionic fluorosurfactant has been carried out. An RCH cell was employed to obtain a variety of current densities. It was found that:

1. Metal oxides were plated from a solution containing the hydroquinone antioxidant.

2. Copper and tin were co-deposited without any oxides when the solution contained both an antioxidant and a fluorosurfactant.

3. Dissolved oxygen in solution is not the cause of metal oxide formation in the deposit.

4. The surfactant is a crucial electrolyte component which reduces hydrogen evolution from proton reduction, thereby promoting the co-deposition of metals.

Acknowledgements

References

1. M. Jordan: 'The electrodeposition of tin and its alloys', 155–162; 1999, Saulgau, Eugen G. Leuze.
2. C. Doyle, N. Brown and M. Bardizeh: *Met. Finish.*, 2002, **100**, 10–17.
3. M. Jordan: *Met. Finish.*, 2003, **101**, 8–16.
4. J. H. Lau and K. Liu: *Adv. Packag.*, 2004, **13**, 27–30.
5. M. Schlesinger and M. Paunovic: 'Modern electroplating', 5th edn, 139–199; 2010, Hoboken, NJ, John Wiley & Sons, Inc.
6. S. Hirsch and C. Rosenstein: *Met. Finish.*, 2007, **105**, 260–271.
7. R. Buckle and S. Roy: *Sep. Purif. Technol.*, 2008, **62**, 86–96.
8. C. T. J. Low and F. C. Walsh: *J. Electroanal. Chem.*, 2008, **615**, 91–102.
9. N. M. Martyak and R. Seefeldt: *Electrochim. Acta*, 2004, **49**, 4303–4311.
10. Y. Qin, A. Wassay, C. Liu, G. D. Wilcox, K. Zhao and C. Wang: Proc. 2009 Int. Conf. on 'Electronic packaging technology and high density packaging', Beijing, China, August2009, IEEE, 772–777.
11. Schloetter: 'Lead-free plating processes', http://www.schloetter.co.uk/pcb/PCB-Lead-Free.htm
12. R. Balaji and M. Pushpavanam: *Trans. Inst. Met. Finish.*, 2003, **81**, 154–158.
13. M. D. Gernon, M. Wu, T. Buszta and P. Janney: *Green Chem.*, 1999, **1**, 127–140.
14. C. T. J. Low, M. De La Toba Corral and F. C. Walsh: *Trans. Inst. Met. Finish.*, 2011, **89**, 44–50.
15. C. T. J. Low, C. Kerr, B. D. Barker, J. R. Smith, S. A. Campbell and F. C. Walsh: *Trans. Inst. Met. Finish.*, 2008, **86**, 148–152.
16. C. T. J. Low and F. C. Walsh: *Surf. Coat. Technol.*, 2008, **202**, 1339–1349.
17. C. T. J. Low and F. C. Walsh: *Trans. Inst. Met. Finish.*, 2008, **86**, 315–325.
18. S. Rekha, K. N. Srinivasan and S. John: *Trans. Inst. Met. Finish.*, 2010, **88**, 215–219.
19. Y. H. Yau: *J. Electrochem. Soc.*, 2000, **147**, 1071–1076.
20. C. Cachet, M. Keddam, V. Mariotte and R. Wiart: *Electrochim. Acta*, 1994, **39**, 2743–2750.
21. R. O. Hull: *Proc. Am. Electroplat. Soc.*, 1939, **27**, 52.
22. C. Madore, D. Landolt, C. Habenpflug and J. A. Hermann: *Plat. Surf. Finish.*, 1995, **82**, 36–41.
23. C. T. J. Low, C. P. De Leon and F. C. Walsh: *Aust. J. Chem.*, 2005, **58**, 246–262.
24. C. T. J. Low, E. P. L. Roberts and F. C. Walsh: *Electrochim. Acta*, 2007, **52**, 3831–3840.
25. H. Dahms and I. M. Croll: *J. Electrochem. Soc.*, 1965, **112**, 771–775.
26. S. Karuppuchamy, K. Nonomura, T. Yoshida, T. Sugiura and H. Minoura: *Solid State Ionics*, 2002, **151**, 19–27.
27. S. Peulon and D. Lincot: *Adv. Mater.*, 1996, **8**, 166–170.
28. S. Peulon and D. Lincot: *J. Electrochem. Soc.*, 1998, **145**, 864–874.
29. T. Yoshida, D. Komatsu, N. Shimokawa and H. Minoura: *Thin Solid Films*, 2004, **451–452**, 166–169.
30. W. T. Chase, M. Notis and A. D. Pelton: Proc. METAL 07, ICOM-CC Metal Working Group Triennial Conference, Amsterdam, The Netherlands, September2007, ICOM-CC.
31. N. Takeno: 'Atlas of Eh-pH diagrams Intercomparison of thermodynamic databases', Geological Survey of Japan Open File Report No. 419, National Institute of Advanced Industrial Science and Technology, 2005.
32. C. Cachet, M. Keddam, V. Mariotte and R. Wiart: *Electrochim. Acta*, 1992, **37**, 2377–2383.
33. C. S. Cha and Y. B. Zu: *Langmuir*, 1998, **14**, 6280–6286.

Corresponding Author: Mr Naray Pewnim,

Corresponding Author's Institution: Newcastle University

First Author: Naray Pewnim

Order of Authors: Naray Pewnim; Sudipta Roy, PhD

Abstract: A systematic approach for the selection of electrochemical parameters for the electrodeposition of tin-rich copper-tin alloys has been performed. This was enabled by using a Cu:Sn ratio of 1:10 in the electrolyte. The effect of this metal ion ratio in the electrolyte and surfactants on the tin content in the deposit was examined using a rotating disk electrode. Cyclic voltammetry showed that inclusion of surfactant in the electrolyte had no effect on the reduction potential of tin which remained at -0.45 V. However, the reduction potential for copper decreased from -0.13 to -0.18 V, thereby making alloy deposition more facile. Chronoamperometry and anodic stripping voltammetry showed that current efficiency for copper-tin deposition ranged from 92-95%. Electrodeposition experiments to obtain high Sn content were carried out at constant current using vitreous carbon electrodes. Deposits containing up to 96 wt.% tin were obtained. Cu-Sn alloys consisted of two phases, tetragonal tin and a hexagonal Cu_6Sn_5 intermetallic compound.

School of Chemical Engineering and Advanced Materials
Newcastle University
Newcastle upon Tyne, NE1 7RU

Date: 13 December 2012

Ms. Ref. No.: SS12-315

RE: SS12-315R1 revised submission

[Electrodeposition of Tin-rich Cu-Sn Alloys from a Methanesulfonic Acid
Electrolyte], by N. Pewnim, S. Roy.

Dear Editor

We would like to submit a second revision of our manuscript (SS12-315) along with
replies to reviewer #1 who has advised us to correct our manuscript again for the 2nd
time.

Thank you for considering our resubmission. I look forward to hearing from you.

Yours sincerely

Naray Pewnim

Electrodeposition of Tin-rich Cu-Sn Alloys from a Methanesulfonic Acid Electrolyte

N. Pewnim[1,*], S. Roy[2]

School of Chemical Engineering and Advanced Materials

Merz Court, Newcastle University, Newcastle upon Tyne, NE1 7RU, UK

Abstract

A systematic approach for the selection of electrochemical parameters for the electrodeposition of tin-rich copper-tin alloys has been performed. This was enabled by using a Cu:Sn ratio of 1:10 in the electrolyte. The effect of this metal ion ratio in the electrolyte and surfactants on the tin content in the deposit was examined using a rotating disk electrode. Cyclic voltammetry showed that inclusion of surfactant in the electrolyte had no effect on the reduction potential of tin which remained at -0.45 V. However, the reduction potential for copper decreased from -0.13 to -0.18 V, thereby making alloy deposition more facile. Chronoamperometry and anodic stripping voltammetry showed that current efficiency for copper-tin deposition ranged from 92-95%. Electrodeposition experiments to obtain high Sn content were carried out at constant current using vitreous carbon electrodes. Deposits containing up to 96 wt.% tin were obtained. Cu-Sn alloys consisted of two phases, tetragonal tin and a hexagonal Cu_6Sn_5 intermetallic compound.

Keywords: Chronoamperometry; Cyclic voltammetry; Copper-tin alloy; Electrodeposition; Surfactant

*Corresponding author.Tel.: +44 0191 222 5457; fax: +44 0191 222 5292.

Email address: naray.pewnim@ncl.ac.uk

[1] ISE student member, [2] ISE member.

1. Introduction

Historically, one of the most important alloy systems has been those of tin. Archeological evidence shows that soft solders such as tin-lead were used since Roman times [1, 2]. Binary systems of tin alloyed with bismuth, cadmium, cobalt, copper, lead, nickel, and zinc have been chosen by commercial manufacturers depending on factors such as mechanical, thermal, and electrical properties of the alloys and the environment in which they will be used [1, 2]. One of the applications of Sn-based alloys has been in solder fabrication, the main candidate for which has been Sn-Pb alloys. Over the past decade lead-free systems have become more important due to a ban of lead based solders [3]. This has led to a variety of investigations of Sn and Sn-based alloys [4-14] to replace solders containing lead. Among the various lead-free alternatives, the copper-tin (Cu-Sn) alloy is of particular interest due to the relatively low cost of the parent metals.

Since electrodeposition is a relatively inexpensive technique it has the potential for fabrication of Cu-Sn alloys. In industry, fabricating Cu-Sn alloys involves the use of separate baths to plate individual metal layers followed by annealing to form an alloy [15]. However, this multistep process can be time consuming and controlling the relative thickness of individual tin and copper layers is difficult. This can also affect the composition across the substrate. Undesirable metal oxide layer can also form on the substrate requiring removal before successive layers of metal are deposited. All these problems can be alleviated by electrodepositing an alloy from a single plating bath [16-19].

Commercial tin plating had been carried out using a variety of different electrolytes involving different chemistries which can be roughly divided into two categories: acidic and alkaline baths. In acid baths, stannous tin (Sn^{2+}) is the main metal cation while in alkaline

baths stannic tin (Sn^{4+}) is predominant. Acid baths include sulfate [20-26], fluoroborate [27-29], and methanesulfonate [30-33] while alkaline baths include stannate/cyanide [34-38] and pyrophosphate-based formulations [5, 39-43]. Although copper can be plated from various electrolytes such as alkaline cyanide [44, 45], pyrophosphate [46-50] and acid fluoborate [47, 51] systems, problems with high costs, toxicity, and waste treatment has prevented them from gaining significant market share [2, 45]. By far the most widespread copper plating system used commercially today is acid sulfate electrolytes [1, 2, 45, 52]. Since tin is relatively insoluble in acid electrolytes [53], it is difficult to find electrolytes where both copper and tin can be solubilised in reasonable quantities. Therefore, in the past, almost all bronze (Cu-Sn) plating was carried out in alkaline cyanide baths.

In the past two decades, increasing environmental regulations have led to the development of environmentally benign electrolytes where copper and tin can be dissolved in reasonable quantities, such as methanesulfonic acid (MSA) [30-33, 54-56]. MSA is an interesting supporting electrolyte with many desirable properties such as high salt solubility, high conductivity, low toxicity and low corrosivity which enables better waste management [30, 31, 57, 58]. Being an acidic electrolyte has the added benefit of being compatible with photoresist materials. Various additives or complexing agents such as brighteners, antioxidants, and surfactants are commonly used to stabilize the bath and improve the quality of deposits [1, 2, 12, 59]. It has been shown that plating parameters influencing the composition of the deposit includes current density, agitation, operating temperature, pH, and the concentration of metal ions [2, 33, 60, 61].

Cu-Sn electrodeposition in a relatively simple MSA bath containing an antioxidant and a fluorosurfactant has been carried out previously [56, 62]. The antioxidant, hydroquinone, was

added to counter the spontaneous oxidation of divalent stannous tin (Sn^{2+}) to tetravalent stannic tin (Sn^{4+}) [12, 60], thereby limiting stannic oxide sludge [63]. A fluorosurfactant was also added to the solution, reducing hydrogen evolution [64, 65] by adsorbing on the electrode and lowering surface tension [64, 66]. The inclusion of these two additives shifted the metal reduction potential of Cu in the cathodic direction, thereby facilitating the co-deposition of the Cu-Sn alloy [54]. A high tin to copper ratio in the bath resulted in a high tin content in the deposit. It was shown that deposits containing 91-97 wt% Sn could be obtained from this electrolyte [56].

A recent study by the current authors using this electrolyte showed that the addition of the fluorosurfactant not only shifts the copper reduction potential, but also serves another purpose - it suppresses the formation of metal oxides [67]. Metallic Cu-Sn alloys were obtained only when both additives were included in the electrolyte. The authors suggested that non-ionic fluorosurfactants suppress hydrogen evolution and thereby pH changes close to the electrode surface, resulting in deposition of metals rather than metal oxides.

The aim of this work is to further examine if this simple electrolyte can be used to fabricate Sn-rich Cu-Sn deposits. An optimized bath containing a fixed ratio of metal ions with hydroquinone and fluorosurfactant as additives were used for this purpose. Electrochemical analysis was carried out to study the current-potential behaviour during Cu, Sn, and Cu-Sn co-deposition from the MSA electrolytes. Cyclic voltammetry was used to determine the potential at which the individual metals and tin-rich alloys start to deposit. Chronoamperometry and anodic stripping voltammetry were carried out to study the effect of applied potential and plating time on current efficiency. Based on these results, optimized current densities for the electrodeposition of tin-rich Cu-Sn alloys were determined.

Thereafter a series of galvanostatic alloy deposition experiments, using a current range where high tin content would be obtained, were performed. The surface microstructure and alloy composition of deposited material was examined using a scanning electron microscope (SEM) and energy dispersive X-ray (EDX) spectroscopy, respectively. X-ray diffraction (XRD) experiments were carried out to determine the phases of the deposits.

2. Experimental

The composition of the electroplating bath used to deposit Cu-Sn alloys is shown in Table 1. It was found that the maximum solubility of tin salt in solution was 0.15 mol dm^{-3} (33 g dm^{-3}) and the minimum copper concentration of 0.015 mol dm^{-3} (4 g dm^{-3}) was required for an acceptable deposit [67], based on which the ratio of Cu:Sn in the bath was fixed as shown in the table. To ensure complete dissolution of SnSO$_4$, the solution was agitated at 30°C until all the metal salt was dissolved. The solution was then left to cool down to room temperature (25°C) before electrochemical or deposition experiments were carried out.

2.1 Electrochemical Analysis

Electroanalytical experiments were carried out in a 300 mL glass cell using a typical three-electrode setup. The working electrode was a gold tipped rotating disc electrode (RDE) (0.1 cm radius, 0.031 cm^2 surface area). A platinum mesh was used as a counter electrode. A saturated calomel electrode (SCE) served as reference and was connected to the cell via a Luggin capillary probe placed approximately 0.5 cm from the RDE surface. The RDE surface was wet polished with 4000 grit silicon carbide paper, etched in 5% Nital (5% nitric acid, 95% ethanol) solution for 5 s, and then ultrasonically cleaned in deionized water between sets of experiments.

Cyclic voltammetry (CV) was used to determine the potentials at which individual metals started to deposit, when alloy co-deposition occurred, and when significant hydrogen evolution commenced. Experiments were carried out using an EcoChemie Autolab potentiostat (μAutolab II) controlled with the NOVA 1.4 software package. The potential window examined was between -0.60 to 0.60 V *vs*. SCE. The experiments started at open circuit potential with a forward cathodic sweep to -0.60 V, after which the scan direction was reversed. On the reverse anodic sweep the potential was swept up to 0.60 V and then back to 0.0 V.

CVs were carried out using solutions containing metals salts with and without surfactant as well as a background electrolyte containing only MSA. The scan rate was set at 50 mV s^{-1} while the RDE rotation speed varied between 100-1000 rpm. The reduction potential of each metal, copper and tin, in its own corresponding electrolyte containing only a single metal ion was determined. These were then compared to the reduction potential observed in the electrolyte containing both metal ions to determine the potential at which Cu-Sn was being co-deposited.

Once the potential range in which the co-deposition of Cu-Sn alloys has been established, chronoamperometry was carried out to determine the current densities that should be applied to obtain acceptable deposits. Potentiostatic deposition in the range of -0.30 to -0.50 V were conducted for these chronoamperometry experiments and the deposition current noted. An RDE speed of 100 rpm was chosen in this stage because it mimics a stagnant system (stationary vitreous carbon electrode) which was used in electrodeposition experiments. Anodic stripping voltammetry was then carried out to determine the amount of metal deposited by sweeping anodically from -0.45 to 1.0 V at (15 mV s^{-1}) at 1000 rpm.

2.2 Electrodeposition Experiments

Vitreous carbon (GoodFellow) was used as a substrate for SEM and XRD techniques as it

a good electrical conductor suitable for SEM, has a very flat surface suitable for XRD

analysis, and is amorphous which would minimize the influence of substrate on the deposit.

Deposition was carried out on a 1 x 1 cm working electrode with a platinum mesh as the

counter electrode positioned approximately 2 cm apart. The applied current density was in

the range of 20-30 mAcm^{-2} and the deposition time was fixed at 600 s. The surface

microstructure of these deposits was studied using an optical microscope and SEM (Jeol

JSM-5300LV and FEI XL30 ESEM-FEG) equipped with an EDX detector which was used

to determine deposit composition. For phase analysis, XRD data were obtained using a

PANalytical X'Pert Pro diffractometer (Cu Kα, 40 kV, 40 mA). The average crystallite size

of the Sn-Cu deposits were calculated from Scherrer's formula:

$$\tau = \frac{K\lambda}{\beta\cos\theta}$$

where τ is the average crystallite size, K is the shape factor (0.9), λ is the x-ray wavelength, β

is the line broadening at Full Width Half Maximum (FWHM), and θ is the Bragg angle (rad).

3. Results and Discussion

3.1 Deposition of Individual Metals

Figure 1a shows the effect of fluorosurfactant on the reduction potential of tin. In the

absence of the surfactant, the reduction of Sn^{2+} ions to Sn metal starts to occur at

approximately -0.45 V. With the addition of surfactant, the reduction potential remained at

-0.45 V showing that the surfactant did not alter tin deposition potential. This is in agreement

with work carried out by other researchers [54, 60]. Two anodic stripping peaks

corresponding to the oxidation of Sn^0 to Sn^{2+} are observed during the reverse scan. The

smaller stripping peak to the right of the main Sn stripping peak seen in Fig. 1a is most likely arising from the stripping of an underlayer of Sn.

Cu deposition potential, shown in Figure 1b, was found to be affected by surfactant. The deposition potential was estimated to be where current density was significantly greater than the resolution of the instrument, i.e. -0.8 mA cm^{-2}, as shown in the inset of Figure 1b. The corresponding electrode potential, therefore, shows that with no surfactant the reduction of Cu^{2+} ions to Cu^0 metal started at approximately -0.13 V. However, with the addition of the surfactant the reduction potential shifted to -0.18 V; a change of -0.05 V towards a more negative potential. On the reverse scan only one stripping peak, corresponding to the oxidation of Cu^0 to Cu^{2+}, was observed. The anodic stripping peak for copper was also displaced towards more positive potentials showing that the addition of surfactant affects both oxidation of Cu^0 to Cu^{2+} ions.

Without the surfactant, the reduction potential of tin and copper were -0.45 V and -0.13 V, respectively; a reduction potential gap of 0.32 V. With the surfactant, the reduction potential of tin and copper were -0.45 V and -0.18 V, respectively, thereby diminishing the gap to 0.27 V. Therefore, the inclusion of surfactant facilitates the co-deposition by lowering the difference in reduction potentials of the two individual metals. This result is similar to the findings of Low and Walsh [54].

Cu-Sn alloys cannot be readily co-deposited due to the fact that the reduction potentials of the two individual metals are far apart. This has been partially resolved by maintaining a low concentration of the more noble metal in the solution as our approach of using a Cu^{2+}:Sn^{2+} concentration of 1:10 demonstrates. This strategy has been proposed by other researchers for

systems such as Cu-Ni and Cu-Co, where the deposition potentials of the two reducing ions are separated by a large potential gap [68-70]. A second strategy to facilitate co-deposition is to shift the reduction potentials closer together by utilizing additives such as fluorosurfactants, which adsorb on the surface, as has been used here [64-66].

3.2 Co-deposition of Copper and Tin

Figure 2 shows the cyclic voltammogram for a solution containing both copper and tin ions. The potential was scanned from 0.20 to -0.60 V to cover the entire range of metal deposition and dissolution. It can be seen that metal ion reduction commenced at a potential of approximately -0.32 V. The low current density at this potential is similar to that found in the deposition of copper (*cf.* Figure 1b). The current does not increase significantly within the potential window of -0.30 to -0.45 V, in the region Cu^{2+} was observed to reduce (*cf.* Fig 1b). In this region, therefore, the deposit is expected to be copper. An increase in the cathodic current is observed at potentials more negative than -0.45 V, with a current-potential behavior similar to that of tin (*cf.* Figure 1a). In this region both copper and tin co-deposit, since these potentials exceed the reduction potentials of both copper and tin.

The reverse scan shows a large stripping peak commencing at -0.45 V and ending at -0.25 V which is in the same regime as the stripping potential of tin (*cf.* Figure 1a). A smaller stripping current positive to 0.05 V was observed, which corresponds to the copper oxidation peak similar to (*cf.* Figure 1b). It can be concluded that co-deposition of the two metals proceeds at potentials below -0.45 V. The similarity in electrochemical behaviour of the individual metals with that of co-deposition is indicative of an independent alloy plating system.

A charge balance analysis was carried out with data obtained from the cyclic voltammograms to determine the current efficiency of the deposition process by comparing the charge consumed during the forward and reverse scans. Figure 3 shows a plot of charge consumed vs. time using data from Figure 2. Table 2 summarizes the charges consumed, in the potential window between 0.20 V and -0.60 V, at different rotation speeds as well as the Cu:Sn ratio in the deposit. The current efficiency of Cu-Sn deposition was shown to be between 85-89% and the Sn content ranges 84-87 %.

3.3 Electrochemical Analysis Using Chronoamperometry

Once it was determined that co-deposition of the two metals could be carried out with relatively high current efficiency, chronoamperometry (CA) was carried out in the region of -0.41 to -0.50 V, the potential window where both Cu and Sn are reduced. In these CA experiments, the electrode was polarized to a fixed potential, i.e. between -0.41 V and -0.50 V, in decrements of -0.10 V. Plots of current density vs. time for each of these experiments are shown in Figure 4 a-c.

Figure 4a shows that at -0.41 V a current transient steadily decreases, reaching a value of approximately -2.7 mA cm^{-2} after 300 s. The appearance of the deposit was red, indicative of copper deposition. Interestingly, as the potential is made increasingly cathodic, *i.e.* lowered to -0.42, -0.43 and -0.44 V, the current drops to a very small value, about -0.4 mA cm^{-2}, indicating that surface reactions are inhibited in this potential regime. Figure 4a also shows the deposit structure, obtained by a light microscope, of the deposits on the gold RDE surface. At -0.41 V, the deposit consists of copper only. As the potential is lowered to -0.42 V, -0.43V and -0.44 V, the surface of the RDE can be seen. These results corroborate that

copper deposition is impeded at the lower applied potentials and is indicative of

fluorosurfactant blocking copper deposition within -0.42 V and -0.45 V.

Figure 4b shows that a current just below -15 mA cm^{-2} is obtained at -0.45 V, greater than

the limiting current for copper reduction. The deposit appearance was grey showing that tin

was co-deposited. As the potential was lowered further to -0.46, -0.47, and -0.48 V, higher

deposition currents were observed, reaching up to -90 mAcm^{-2}. Deposits obtained between

-0.45 to -0.47 V cover the entire surface of the electrode (Figure 4b), as is expected when the

deposition current is higher than that those observed between -0.42 to -0.44 V (Figure 4a).

At still lower cathodic potentials between -0.48 and -0.49 V, the cathodic current

increased up to -175 mA cm^{-2} over the 300 s deposition period (Figure 4c), never reaching a

plateau, as was observed for -0.47 V (Fig. 4b). At -0.50 V, the current transient stabilized at

approximately 112 mA cm^{-2}. The deposits for this potential range, i.e. -0.48 V to -0.50 V,

were visibly very rough (Figure 4c) and therefore a detailed microstructural analysis was not

feasible.

The relative content of copper and tin in the alloy and the current efficiency of deposition

in the experiments shown in Figure 4a and 4b was obtained by integrating the charge under

the copper and tin stripping peaks and comparing them to the total charge consumed during

the CA experiments. Typical stripping peaks for the deposit obtained in the CA experiments

are shown in Figure 5. At a potential of -0.41 V two copper stripping peaks are observed,

indicative of two different phases of copper deposited. The stripping peak at the more noble

potential could be due to UPD deposition of Cu on Au [71-72].

Decreasing the potential to -0.42, -0.43 and -0.44 V one observed only copper stripping peaks. In addition, it is interesting to note that only one stripping peak is observed at these potentials instead of the two peaks for -0.41 V. It should also be noted that the area underneath the peak is much greater for -0.41 V than for -0.42 to -0.44 V. This suggests that the fluorosurfactant is blocking copper UPD at the lower overpotentials (c.f Figure 4a).

The data for -0.45 V is different in that stripping peaks for both tin and copper are observed, which confirms that tin is deposited at these potentials. Interestingly, the UPD peak for copper reappeared and the area underneath the copper stripping peaks also increased. This suggests that the blocking effect of the fluorosurfactant is reduced at -0.45 V.

In Table 3 the current efficiency (column 5) and alloy composition of the deposits (column 8) obtained in CA experiments are summarized. The method for determination of current efficiency is shown in Appendix 1a. The current efficiency for copper ranges between 43% - 58% in the region of -0.41 to -0.44 V which indicates that not only is copper deposition suppressed within this potential range, but also that the current is being consumed by other surface reactions, even though at a very low rate (as the currents are small). The current efficiency increases to 92% when Cu-Sn co-deposition, commences, i.e. at -0.45 V. The current efficiency remains high, i.e. up to 95%, when higher overpotentials of -0.46 and -0.47 V are applied. The alloy composition (column 8) shows that between -0.41 to -0.44 V the deposit consists solely of copper. At -0.45 V an alloy containing 91% Sn is obtained while at -0.46 and -0.47 V the Sn content in the alloy rises to 98 and 93%, respectively. Based on these findings, it can be concluded that a high tin content, *i.e.* more than 90%, can be obtained if a potential more negative than -0.45 V was applied.

Since deposits containing >90% Sn were obtained only at potentials more negative than -0.45 V, or when the plating current was approximately 20 mA cm^{-2} (*c.f.* Fig. 4b), a set of deposition experiments were tested in the current range between 20 to 30 mA cm^{-2}. It was found that deposits of reasonable thickness (up to 8 µm) could be obtained at 22 mA cm^{-2} while higher current densities led to powdery non-adherent deposits. Therefore, co-deposition experiments were carried out only at 22 mA cm^{-2}.

3.4 Galvanostatic Co-deposition Experiments

SEM images of the cross-section of the co-deposited Cu-Sn alloy at a vitreous carbon electrode show that after a deposition time of 600 s the deposit had an average thickness of 8 µm (Figure 6a). A longer deposition time of 1800 s resulted in deposit thickness of up to 28 µm (Figure 6b), but was rough and non-adherent. Four repeats of the deposition experiments were carried out to test the reproducibility of these galvanostatic experiment which revealed similar microstructures. The tin content in the deposits was found to be consistently at 96±1 wt% for all cases, i.e., for both 8±1µm and 28±2 µm thicknesses.

Figure 7 shows the XRD pattern of a) copper, b) tin, and c) Cu-Sn deposits in their corresponding electrolytes containing individual metal salts and both salts, respectively. A current of 3 mA cm^{-2} for copper, 20 mA cm^{-2} for tin and 22 mA cm^{-2} for Cu-Sn was used in these experiments. Copper and Cu-Sn could be deposited directly onto the vitreous carbon surface. Tin, however, did not adhere well to vitreous carbon. In order to solve this problem, a base layer of copper was plated for 1800 s before tin deposition.

Figure 7a exhibits many broad peaks due to the fact that copper deposits were relatively thin (3 µm) compared to that of tin deposits. These XRD patterns are characteristic of the

amorphous glassy carbon substrate. Thicker Sn and Cu-Sn deposits show very sharp peaks indicative of their crystalline structure. Copper deposited from the MSA electrolyte has a face centered cubic crystal structure while deposited tin has a tetragonal structure. The Cu-Sn alloy shows the presence of two phases; tetragonal tin and a hexagonal Cu_6Sn_5 intermetallic.

Peak intensity analysis shows that the deposit is mostly tin with approximately 5% Cu_6Sn_5 intermetallic. When the composition and phase analysis measurements are compared, the data suggest that copper is present in the Cu-Sn deposit as Cu_6Sn_5 (see Appendix 1b). The average crystallite size for copper, tin, and Cu-Sn alloy were 33±24, 57±3, and 56±4 nm, respectively. The larger error in calculating the crystal size for copper is due to the broadness of the peaks which was only observed for Cu deposits and not for deposits of Sn and Sn-Cu alloys.

4. Conclusion

An experimental study on Cu-Sn alloy co-deposition from MSA electrolytes containing tin and copper sulfate, hydroquinone, and non-ionic surfactant has been carried out to pre-determine the current density where acceptable Cu-Sn deposits are obtained. A rotating disk electrode has been used to determine the potential where tin-rich alloys are obtained at a reasonable current density. The salient findings of this study are:

1. Co-deposition of Cu-Sn alloys from methanesulfonic acid electrolyte can be carried out from a solution containing 0.15 mol dm^{-3} $SnSO_4$, 0.015 mol dm^{-3} $CuSO_4$, hydroquinone antioxidant, and a non-ionic fluorosurfactantn, namely, DuPont™ Zonyl® FSN.

2. The fluorosurfactant shifted the reduction potential of copper by approximately

-0.05 V to a relatively more negative value. The reduction potential of tin, however, was not affected.

3. Potentiostatic experiments showed that the surfactant suppresses copper deposition in the region of -0.41 V and -0.44 V while allowing tin deposition to proceed at potentials more negative than -0.45 V which facilitates tin-rich Cu-Sn alloy deposition.

4. The optimal plating current density is approximately 22 mAcm^{-2} and alloys of up to 96 wt% Sn can be deposited.

5. A deposition period of 600 s resulted in deposits approximately 8 μm thick. Increasing the deposition time to 1800 s increased the thickness to 28 μm, but led to poor deposits.

6. The tin-rich Cu-Sn deposits consisted mainly of tetragonal tin with up to 5% hexagonal Cu_6Sn_5 intermetallic.

Appendix 1

a) Current efficiency and alloy content calculations (for Table 3)

In order to calculate the current efficiency of deposition in the CA experiments we need to compare the stripping charge associated with each metal in columns 3 and 4 to the total deposition charge in column 2 as shown:

Current efficiency = (Column 3 + Column 4)/ Column 2

For example

for -0.41 V,   current efficiency = (0.24 + 0) / 0.56 = 43%

for -0.45 V,   current efficiency = (0.13 + 1.24) / 1.49 = 92%

Alloy composition (column 8) was determined from the individual metal stripping charges (column 6 or column 7 individually) divided by the combined total stripping charge (columns 6 + 7) as shown:

$$Cu \text{ content} = \text{column } 6 / (\text{column } 6 + \text{column } 7)$$

$$Sn \text{ content} = \text{column } 7 / (\text{column } 6 + \text{column } 7)$$

For example

for -0.45 V,   Cu content = 8 / (8+77) = 9%

Sn content = 77 / (8+77) = 91%

for -0.46 V,   Cu content = 2 / (2+88) = 2%

Sn content = 88 / (2+88) = 98%

b) Amount and phase of Cu in Sn-rich deposits

EDX measurements showed that Sn-rich deposits contained 96 wt% Sn and 4 wt% Cu. However, EDX provides no information on whether Cu or Sn is present in their elemental form or as Cu_6Sn_5. Additional phase analysis via XRD needed to be carried out and peak intensity analysis indicates that the deposits contained approximately 95% Sn and 5% Cu_6Sn_5. Taking this into consideration, the EDX data can be re-interpreted and the amount of Sn, Cu, and Cu_6Sn_5 is approximately:

$$96\% \text{ Sn} = 92\% \text{ as Sn} + 4\% \text{ as } Cu_6Sn_5$$

$$4\% \text{ Cu} = 4\% \text{ as } Cu_6Sn_5$$

ASV data from Table 3 corroborates this (within the experimental error) as the Cu/Sn content in the alloy (column 8) is in the same range (>91% Sn and <9% Cu).

References

[1] M. Jordan, The Electrodeposition of Tin and its Alloys, Eugen G. Leuze, Saulgau, 1999.

[2] M. Schlesinger, M. Paunovic, Modern Electroplating, 5th ed., John Wiley & Sons, Hoboken, 2010.

[3] OJEU, L37 (2003) 19.

[4] M. Abtew, G. Selvaduray, Mater. Sci. Eng. R 27 (2000) 95.

[5] A.N. Correia, M.X. Façanha, P. de Lima-Neto, Surf. Coat. Technol. 201 (2007) 7216.

[6] J. Horkans, I.C.H. Chang, P.C. Andricacos, H. Deligianni, J. Electrochem. Soc. 142 (1995) 2244.

[7] M. Jordan, Met. Finish. 101 (2003) 8.

[8] J.H. Lau, K. Liu, Adv. Packag. 13 (2004).

[9] A. Rae, C. Handwerker, Circuits Assembly 15 (2004).

[10] M.-S. Suh, C.-J. Park, H.-S. Kwon, Surf. Coat. Technol. 200 (2006) 3527.

[11] W. Sun, D.G. Ivey, J. Mater. Sci. 36 (2001) 757.

[12] T. Tamura, U.S. Patent No. 6,372,117 (2002).

[13] Y.-D. Tsai, C.-C. Hu, J. Electrochem. Soc. 158 (2011) D527.

[14] Schloetter, Lead-Free Plating Processes, available at http://www.schloetter.co.uk/plating-processes/Lead-Free.htm. Accessed: 13 Dec 2012.

[15] C. Doyle, N. Brown, M. Bardizeh, Met. Finish. 100 (2002) 10.

[16] S. Arai, H. Akatsuka, N. Kaneko, J. Electrochem. Soc. 150 (2003) C730.

[17] N. Kaneko, M. Seki, S. Arai, N. Shinohara, Electrochemistry 71 (2003) 791.

[18] Y. Qin, A. Wassay, C. Liu, G.D. Wilcox, K. Zhao, C. Wang, ICEPT-HDP 2009, Beijing, 8-11 Aug., 2011; (2009) 772.

[19] C. Han, Q. Liu, D.G. Ivey, Electrochim. Acta 54 (2009) 3419.

[20] I.A. Carlos, E.D. Bidoia, E.M.J.A. Pallone, M.R.H. Almeida, C.A.C. Souza, Surf. Coat. Technol. 157 (2002) 14.

[21] I.A. Carlos, C.A.C. Souza, E.M.J.A. Pallone, R.H.P. Francisco, V. Cardoso, B.S. Lima-Neto, J. Appl. Electrochem. 30 (2000) 987.

[22] C.A. Dischee, F.C. Mathers, J. Electrochem. Soc. 102 (1955) 387.

[23] D. Padhi, S. Gandikota, H.B. Nguyen, C. McGuirk, S. Ramanathan, J. Yahalom, G. Dixit, Electrochim. Acta 48 (2003) 935.

[24] I. Petersson, E. Ahlberg, J. Power Sources 91 (2000) 143.

[25] P.R. Pine, J. Electrochem. Soc. 80 (1941) 631.

[26] M.J. Liew, S. Roy, K. Scott, Green Chem. 5 (2003) 376.

[27] T.M. Tam, J. Electrochem. Soc. 133 (1986) 1792.

[28] D. Radovic, Plat. Surf. Finish. 76 (1989) 52.

[29] S.M. Silaimani, M. Pushpavanam, K.C. Narasimham, Plat. Surf. Finish. 83 (1996) 48.

[30] R. Balaji, MalathyPushpavanam, Trans. Inst. Met. Finish. 81 (2003) 154.

[31] M.D. Gernon, M. Wu, T. Buszta, P. Janney, Green Chem. 1 (1999) 127.

[32] R.A.T.D. Greef, L.J.J. Janssen, J. Appl. Electrochem. 31 (2001) 693.

[33] Y.H. Yau, J. Electrochem. Soc. 147 (2000) 1071.

[34] G.A. Finazzi, E.M. de Oliveira, I.A. Carlos, Surf. Coat. Technol. 187 (2004) 377.

[35] R.G. Monk, H.J.T. Ellingham, Trans. Faraday Soc. 31 (1935) 1460.

[36] F.F. Oplinger, F. Bauch, J. Electrochem. Soc. 80 (1941) 617.

[37] L.E. Stout, A.H. Baum, J. Electrochem. Soc. 72 (1937) 429.

[38] L.E. Stout, A. Erspamer, J. Electrochem. Soc. 68 (1935) 483.

[39] S. Arai, Y. Funaoka, N. Kaneko, N. Shinohara, Electrochemistry 69 (2001) 319.

[40] A. Hrussanova, I. Krastev, J. Appl. Electrochem. 39 (2009) 989.

[41] K. Johannsen, D. Page, S. Roy, Electrochim. Acta 45 (2000) 3691.

[42] J. Vaid, T.L.R. Char, J. Electrochem. Soc. 104 (1957) 282.

[43] V. Venkatasamy, S. Riemer, I. Tabakovic, Electrochim. Acta 56 (2011) 4834.

[44] N. Mandich, Met. Finish. 103 (2005) 30.

[45] L.M. Weisenberger, B.J. Durkin, ASM Handbook Volume 5, Surface Engineering, ASM International, 1994, Copper Plating, pp. 167-176.

[46] D. Tench, C. Ogden, J. Electrochem. Soc. 125 (1978) 194.

[47] B.F. Rothschild, J. Electron. Packaging 15 (1975) 102.

[48] O. Radovici, C. Vass, I. Solacolu, Electrodeposition Surf. Treat. 2 (1974) 263.

[49] A.C. Hamilton Jr, Plat. Surf. Finish. 90 (2003) 12.

[50] S.B. Feng, S.B. Shang, Plat. Surf. Finish. 92 (2005) 38.

[51] D.N. Lee, S. Kang, J. Yang, Plat. Surf. Finish. 82 (1995) 76.

[52] S. Rekha, K.N. Srinivasan, S. John, Trans. Inst. Met. Finish. 88 (2010) 215.

[53] R. Buckle, S. Roy, Sep. Purif. Technol. 62 (2008) 86.

[54] C.T.J. Low, F.C. Walsh, Surf. Coat. Technol. 202 (2008) 1339.

[55] C.T.J. Low, F.C. Walsh, Electrochim. Acta 53 (2008) 5280.

[56] C.T.J. Low, F.C. Walsh, Trans. Inst. Met. Finish. 86 (2008) 315.

[57] Arkema, Methanesulfonic acid, Available at http://www.arkema-inc.com/index.cfm?pag=127. Accessed: 6 Feb. 2012.

[58] BASF, New applications involving methanesulfonic acid, EMV 0101e, 2008.

[59] S. Hirsch, C. Rosenstein, Met. Finish. 105 (2007) 260.

[60] N.M. Martyak, R. Seefeldt, Electrochim. Acta 49 (2004) 4303.

[61] M. Paunovic, M. Schlesinger, Fundamentals of Electrochemical Electrodeposition, 2nd ed., John Wiley & Sons, Hoboken, New Jersey, 2006.

[62] C.T.J. Low, F.C. Walsh, J. Electroanal. Chem. 615 (2008) 91.

[63] N.M. Martyak, R. Seefeldt, Galvanotechnik 97 (2006) 48.

[64] C. Cachet, M. Keddam, V. Mariotte, R. Wiart, Electrochim. Acta 37 (1992) 2377.

[65] C. Cachet, M. Keddam, V. Mariotte, R. Wiart, Electrochim. Acta 39 (1994) 2743.

[66] C.S. Cha, Y.B. Zu, Langmuir 14 (1998) 6280.

[67] N. Pewnim, S. Roy, Trans. Inst. Met. Finish. 89 (2011) 206.

[68] S. Roy, M. Matlosz, and D. Landolt, J. Electrochem. Soc. 141 (1994) 1509.

[69] P. Bradley, S. Roy, and D. Landolt, J. Chem. Soc. Faraday Trans. 92 (1996) 4015.

[70] S. Roy, Surf. Coat. Technol. 105 (1998) 202.

[71] Budevski, E., Staikov, G., Lorenz, W.J, Electrochimica Acta 45 (2000) 2559.

[72] Herrero, E., Buller, L.J., Abruña, H.D., Chemical Reviews 101 (2001) 1897.

Figure 1 Cyclic voltammetry of a) 0.15 mol dm^{-3} SnSO$_4$ and b) 0.015 mol dm^{-3} CuSO$_4$ in 2.0 mol dm^{-3} MSA and hydroquinone antioxidant with and without surfactant. The scan rate of 50 mV s^{-1} and the RDE rotation speed was 100 rpm.

Figure 2. Cyclic voltammetry of copper-tin alloy on a gold RDE from an electrolyte composed of 0.15 mol dm^{-3} SnSO$_4$, 0.015 mol dm^{-3} CuSO$_4$, 0.01 mol dm^{-3} hydroquinone, 2.0 mol dm^{-3} methanesulfonic acid, and 0.01% vol DuPont™ Zonyl® FSN surfactant. The scan rate was 50 mV s^{-1} and the RDE rotation speed was varied between 100 to 1000 rpm.

Figure 3. Current efficiency of copper-tin alloy plating calculated by comparing the anodic charge (Q$_{ac}$) to the cathodic charge (Q$_{cc}$) *vs.* time. The cathodic charge was consumed to deposit the metals while the anodic charge was consumed to strip the metal.

Figure 4 a b c. Chronoamperometry showing metal deposition at various fixed potentials from a) -0.41 to -0.44 V b) -0.45 to -0.47 V and c) -0.48 to -0.50 V *vs.* SCE. Electrodeposition was carried out for 300 s at a rotation speed of 100 rpm.

Figure 5. Anodic stripping voltammetry of the deposits obtained at fixed potentials from chronoamperometry experiments.

Figure 6. Cross section of Cu-Sn deposited on vitreous carbon at 22 mA cm^{-2} a) 600 s deposition time, 8 μm thickness b) 1800 s deposition time, 28 μm thickness.

Figure 7. XRD pattern of a) copper, b) tin, and c) Cu-Sn deposited on vitreous carbon for 1800 s at 3, 20, and 22 mA cm^{-2} from electrolytes containing a) $CuSO_4$, b) $SnSO_4$, and c) both $CuSO_4$ and $SnSO_4$, respectively, along with MSA and fluorosurfactant.

TABLES

Table 1. Electrolyte composition and operating condition for Cu-Sn co-deposition experiments.

Composition	Concentration		Function
	(mol dm^{-3})	(g dm^{-3})	
Copper(II) sulfate (CuSO$_4$·5H$_2$O)	0.015	4	Source of Cu^{2+} ions
Tin(II) sulfate (SnSO$_4$)	0.15	33	Source of Sn^{2+} ions
Hydroquinone (C$_6$H$_4$(OH)$_2$)	0.01	1	Antioxidant
Methanesulfonic acid (CH$_3$SO$_3$H)	2.00	192	Supporting electrolyte
DuPont™ Zonyl® FSN	0.01 %vol (30 μL)		Fluorosurfactant
pH	1.17 ± 0.02		
conductivity	389 ± 1 mS cm^{-1}		
temperature	25 ^{o}C		

RDE speed	Total deposition charge (C)	Total stripping charge (C)	Current efficiency (%)	% Cu	% Sn
100 rpm	3.76×10^{-1}	3.20×10^{-1}	85	13	87
500 rpm	6.29×10^{-1}	5.61×10^{-1}	89	16	84
1000 rpm	8.55×10^{-1}	7.56×10^{-1}	88	16	84

Table 3. Charge consumed for the deposition and stripping of copper and tin during chronoamperometry experiments with potentials in the range of -0.41 to -0.47 V. The RDE rotation speed was 100 rpm and the deposition time was 300 s.

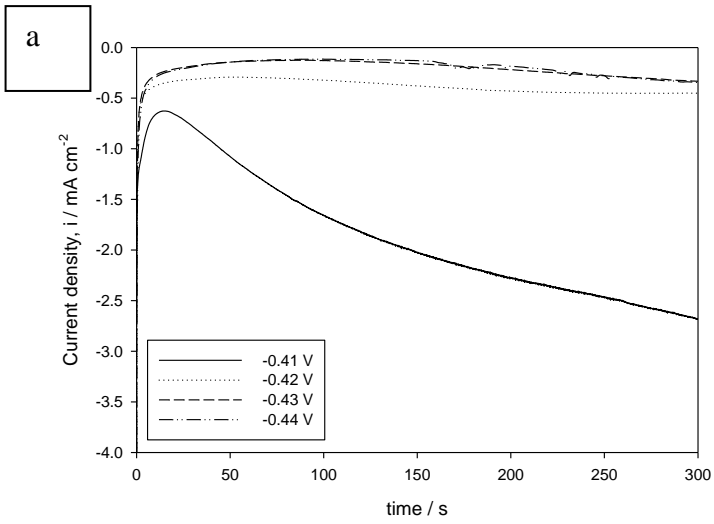| Column 1	2	3	4	5	6	7	8
Potential (V)	Charge consumed during deposition (C cm-2)	Stripping charge (C cm-2)		Current efficiency (%)	Contribution of deposition charge consumed by each metal (%)		Cu/Sn content in alloy (±3%)
		Cu	Sn		Cu	Sn	
-0.41	0.56	0.24	-	43±8	100	-	100/0
-0.42	0.12	0.07	-	58±9	100	-	100/0
-0.43	0.06	0.03	-	50±2	100	-	100/0
-0.44	0.06	0.03	-	50±3	100	-	100/0
-0.45	1.49	0.13	1.24	92±3	8±1	77±3	9/91
-0.46	5.50	0.14	5.11	95±2	2±1	88±3	2/98
-0.47	6.34	0.44	5.52	94±4	7±3	82±2	8/93

Figure 1.
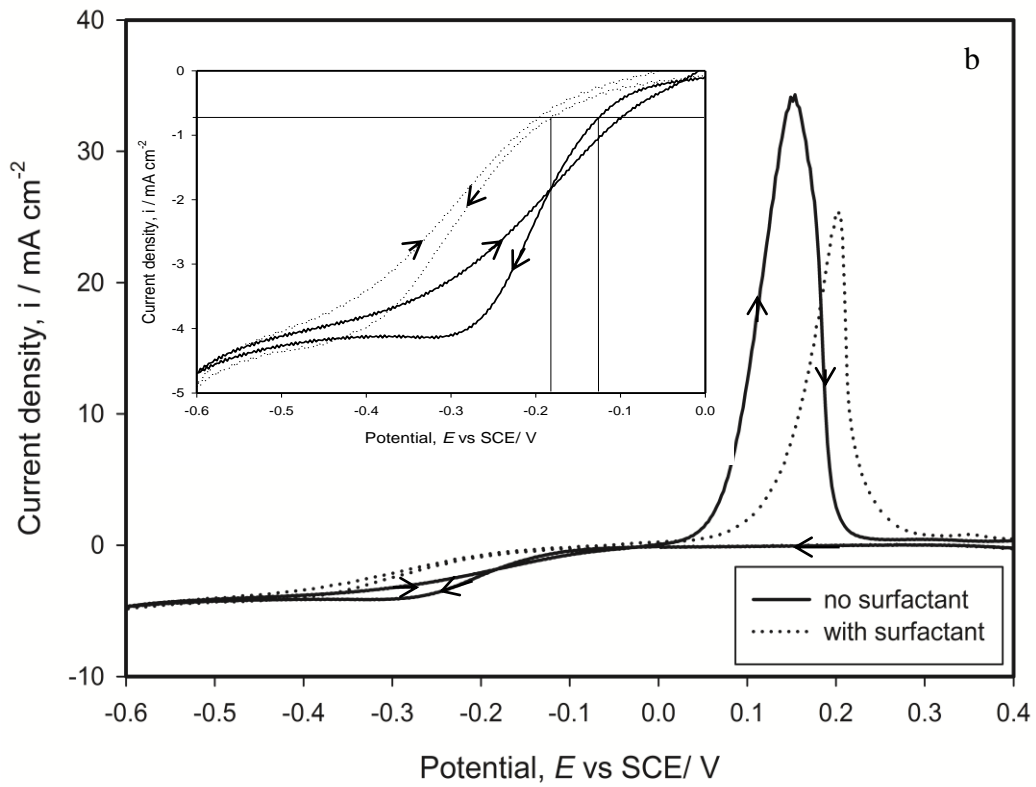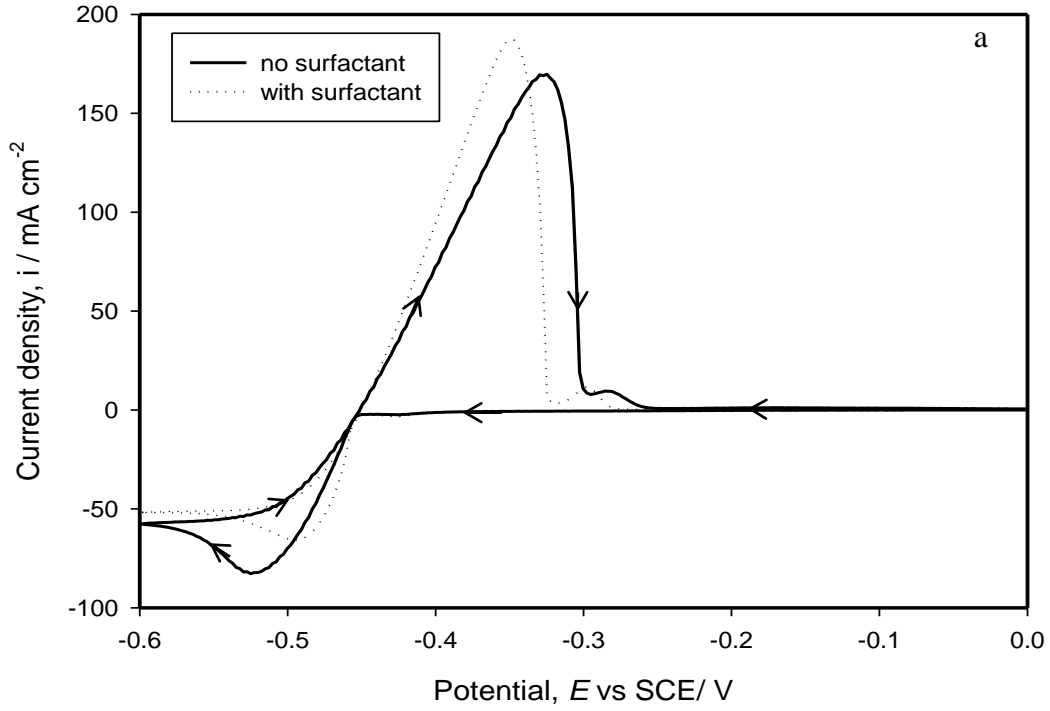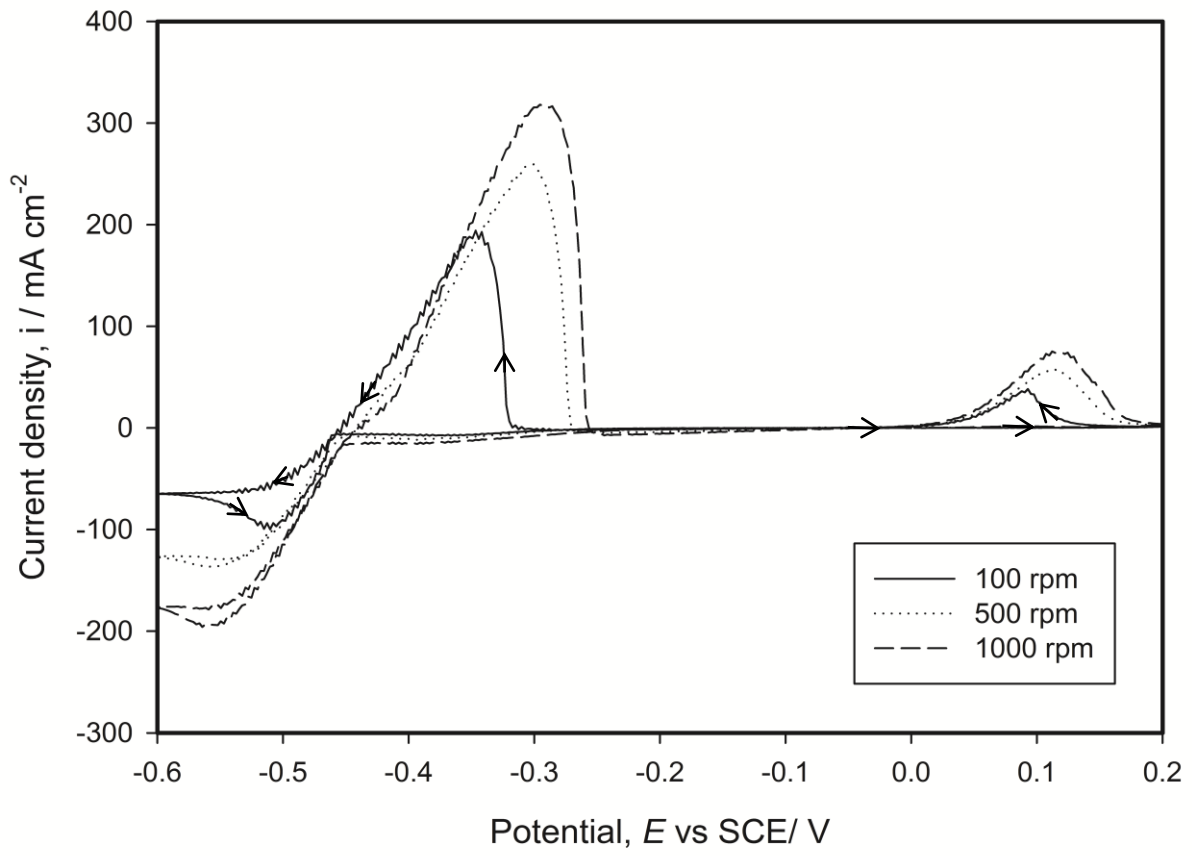
Figure 2.

Figure 3.
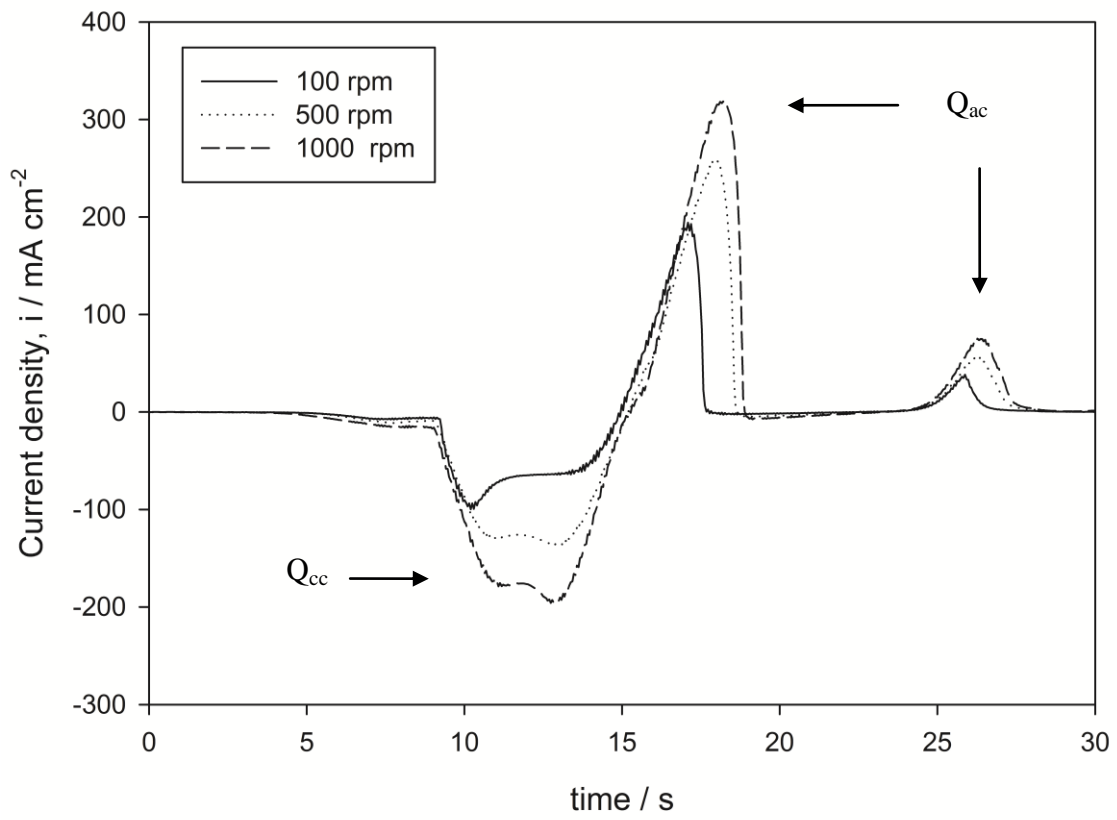
Figure 4.
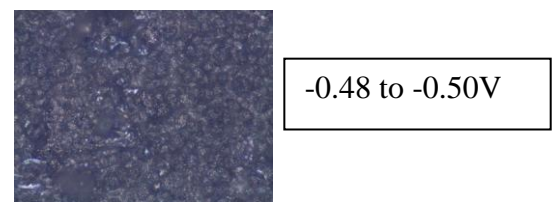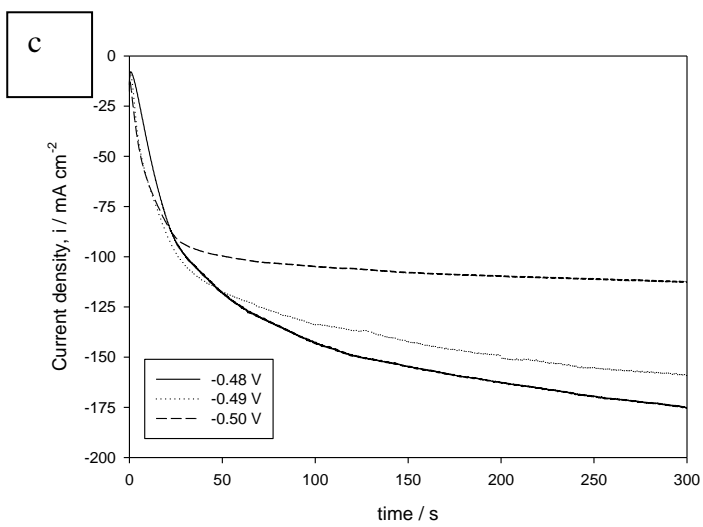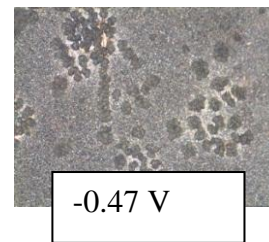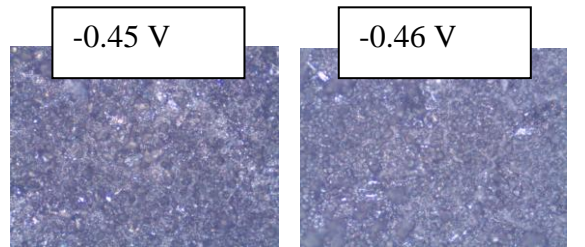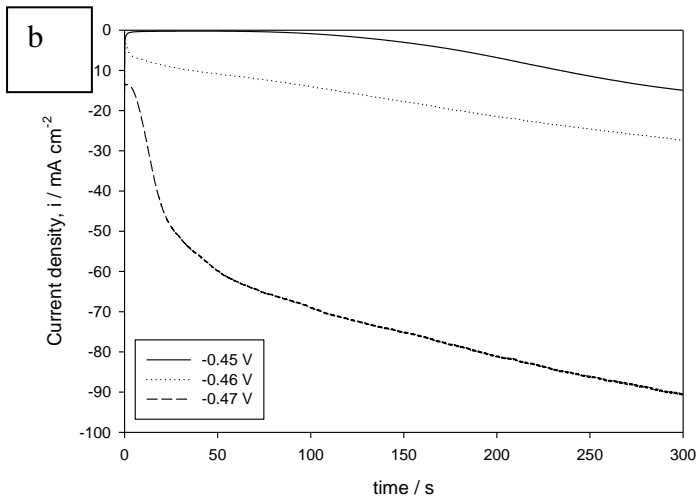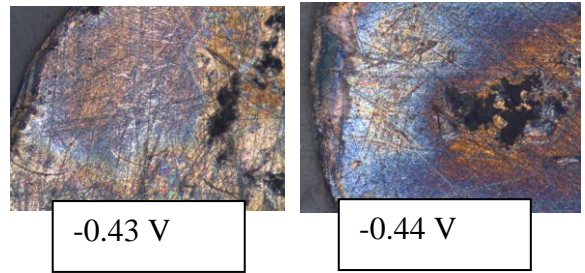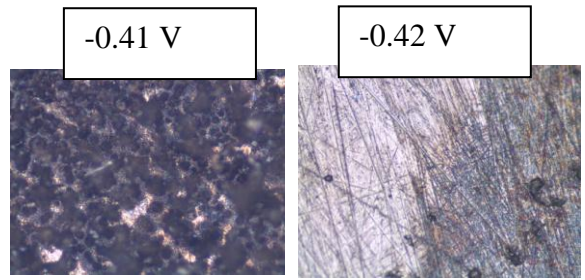
Figure 5.

Figure 6.

Figure 7.